First-principles based theory for chemical substitution in electronic materials

---

Zur Erlangung des akademischen Grades eines

Doktors der Naturwissenschaften

von der KIT-Fakultät für Physik
des Karlsruher Instituts für Technologie

genehmigte

Dissertation

von

Lars Lauke, M. Sc.
aus Mannheim

Tag der mündlichen Prüfung: 29.01.2021

Referent: Prof. Dr. Jörg Schmalian
Korreferent: Prof. Dr. Matthieu Le Tacon

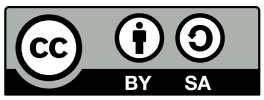

It is really quite impossible to say anything with absolute precision, unless that thing is so abstracted from the real world as to not represent any real thing

Richard Feynman

To my parents and siblings

who always supported me,
even though they never truly understood
what I was talking about.

To Sophie

for her endless love and support,
and for putting up with all my quirks.

Introduction

The beauty of solid state physics, first and foremost, arises from the idealization of crystalline solids: their perfect periodicity, and the translational invariance it entails, allows us to describe them in terms of simple and elegant mathematics. However, the real world is neither ideal nor perfect, and the same holds for crystals. Regardless of the extent to which we improve crystal growth methods, they always contain some sort of imperfection - be it defects, deficiencies, impurity atoms or grain boundaries. The fact that these are randomly distributed all over the crystal introduces disorder into our system.

One of the most prominent consequences of imperfect crystals is finite electrical conductivity. Without the scattering of electrons on impurities, the world as we know it would be quite different. And although at first it may seem as a nuisance, disorder affecting the underlying physical properties and dynamics is responsible for numerous fascinating and technologically valuable phenomena.
Thus, it seems apparent to deliberately make use of disorder to tune physical systems to our desire and need. One possibility to achieve this is via chemical substitution by which a specific atomic type in the host material is replaced by another to some degree. And indeed, mankind has been doing so for decades: among other applications, by doping semiconductors we can induce a spatial dependence of electronic properties and construct complex semiconductor devices - computers.

Apart from this famous example, in many material classes magnetic, structural, superconducting, and even topological phases are governed by substitutional disorder. Hence, disorder provides us with a powerful tool to fabricate complex materials with beneficial properties. However, this comes at a cost: while translational symmetry is the foundation on which the success of solid state theory is in large parts based, it is inherently not preserved in a disordered system. Thus, we lose the ability to describe our system with the simple mathematics we are used to. The absence of full translational symmetry forces us to leave pen and paper behind and resort to the power of numerical methods and computers. Even in the well established field of first principle electronic structure calculations, the description of substitutional disorder is a challenging task. Especially the treatment of arbitrary concentrations is far from trivial.

Many theoretical frameworks have been developed to describe substitutional disorder. Among them, the supercell approach is widely applied. Here, disorder is incorporated by enlarging the unit cell to such an extend as to accommodate for partial occupation. Physical observables are then gained by averaging over a finite number of configurations in an attempt to approximate the thermodynamic limit. However, this method is computationally feasible only for very specific concentrations, as unit cells must be extended ever further. Consequently, arbitrary concentrations remain out of reach.
A more promising route to their description is given by the so-called effective medium theories. Among them, the virtual crystal approximation (VCA) can be regarded as the most rudimentary method, in which the atomic potentials are replaced by a concentration weighted average. Although it has supplied good results for a limited set of problems, it is unable to fully capture the random nature of disorder, neglecting environmental disorder effects.

One of the most sophisticated representatives of effective medium theories in the context of substitutional disorder is the coherent potential approximation (CPA) [1–3], best known within the Kohn-Korringa-Rostocker (KKR) framework [4, 5]. In this work, we shall focus on a more recent version

of the CPA within a pseudopotential density functional theory (DFT) framework as developed by A. Herbig [6], based on the CPA formalism due to Blackman, Esterling and Berk (BEB) [3].
A significant portion of the work conducted for this thesis has gone into the extension of the base CPA formalism [6] to include spin polarization, the description of vacancies, and spin-orbit coupling. Both the SOC and vacancy extension were essential to the central topics of this thesis outlined below. Beyond these specific fields of interest, the enhanced versatility of the formalism enables a broad application of the CPA in the context of materials design with respect to a multitude of systems, providing a powerful tool for future works.

We have already emphasized the potential of intentionally induced disorder via chemical substitution for manufacturing new materials tailored to our needs. With the CPA at our disposal we are not restricted to purely academic considerations but can in fact provide guidance to experiment. This is an overarching objective of this work - to initiate a feedback loop between theory and experiment. A promising target material class in this context, which has received enormous scientific attention since its discovery in 2008 [7], are the iron-based superconductors. They provide a rich hunting ground for our intentions, as they possess highly diverse phase diagrams [8–11] with structural, magnetic and superconducting phase transitions. As superconductivity is most prominently characterized by vanishing resistivity at low temperatures, it holds great technological prospect. After the discovery of the cuprates [12], the iron-based superconductors extended the realm of compounds with high superconducting transition temperature [13–15], adding to their attractiveness for materials design.
While most quantum phase transitions in condensed matter physics (such as structural transitions, paramagnet-ferromagnet transitions and superconductivity) can be explained by Landau's theory of phase transitions [16] in terms of broken symmetry, in recent years another class of phase transitions has entered the arena. With the discovery of the quantum Hall effect [17] in 1980, it became apparent that a new type of order had emerged which was beyond the limits of Landau's theory. The changes in the quantized value of the Hall conductance with varying magnetic field implied quantum phase transitions without breaking of symmetries.

It was realized by Thouless, Kohmoto, Nightingale, and den Nijs [18] that the distinct phases of the quantum Hall effect were in fact not a consequence of symmetry but rather of *topology*. Considering two phases with a gap in the vicinity of the Fermi surface, we can consider them topologically distinct (with respect to a given set of symmetries) if there exists no continuous deformation that respects the symmetries and transforms one phase into the other without closing the gap. We refer to a system as topologically nontrivial if it is topologically distinct from the vacuum. As a consequence, such a system will exhibit gapless modes at its boundary, with fascinating physical properties.
This subject has since drawn immense scientific interest from the condensed matter community, and many system with "topological order" have since been identified and proposed. Among them are topologically nontrivial superconductors - candidates for which are expected to be found among the iron-based superconductors.

This thesis will be concerned with all three aspects mentioned above - disorder, iron-based superconductors, and topology. We will to a large extent focus on $FeSe_{0.5}Te_{0.5}$ which is proposed to be a topological superconductor [19]. This system exhibits a band crossing point along the high symmetry line ΓZ at which spin-orbit coupling (SOC) opens a direct gap. The topological nature of the bandstructure leads to the emergence of a surface Dirac cone (SDC) inside this gap that could host exotic anyonic surface states at the core of vortices in the superconducting phase. These Majorana zero modes are subject to non-Abelian exchange statistics [20] and constitute promising candidates for fault-tolerant scalable quantum computers [21].
However, the aforementioned SDC is located well above the Fermi level and model calculations predict

a topological superconducting phase only to be realized if the latter crosses the SDC [22]. Furthermore, the position of the SDC prevents access of experimental techniques such as surface transport measurements which are of great interest in the context of topological surface states. It will be the main task of this work to devise a strategy which employs chemical substitution in order to bring the SDC into the vicinity of the Fermi level.

By band engineering $FeSe_{0.5}Te_{0.5}$ via the CPA we will identify viable substitutional candidates which introduce additional electrons into our system, thus raising the Fermi level towards the SDC. Specifically, we will consider two hypothetical substituted crystals of the form $Fe_{1-y}TM_ySe_{0.5}Te_{0.5}$ and $FeSe_{1-y-x}Ha_yTe_x$, respectively. Here, *TM* denotes transition metal substitution at the Fe site with concentration y, while *Ha* denotes halogen substitution at the Se site.
Simultaneously, we will investigate the broadening effects resulting from the additional disorder to ensure that the SOC gap (and subsequently the SDC) persists - a task for which the CPA is ideally suited, as it naturally provides the necessary spectral information.

In addition to the central topic of this thesis, we will apply the CPA in the context of partial occupation of the interstitial site in $FeSe_{0.5}Te_{0.5}$ with iron. This excess iron, which naturally occurs to varying degree in grown samples, is intricately connected to the suppression of superconductivity in the system under consideration. Hence, it has great bearing on the fabrication of a crystalline platform for the realization of Majorana zero modes. We will asses the impact of impurity scattering by comparing the effect of interstitial iron to other substitutions which are known to suppress superconductivity.

The analysis presented in this thesis is structured as follows: we begin the first part of this thesis with an introduction to the field of electronic structure calculations. We recapitulate the fundamental theoretical framework of disorder theory in Chapter 1 and give an overview of the field of substitutional disorder in solid state systems and some of the most commonly used methods. In particular, we will present the coherent potential approximation (CPA) in the BEB-formalism and briefly discuss its practical implementation. All further technical details concerning the program package, as well as its usage, and details of individual calculations are documented in Appendices A-J.
The powerful extensions to the base formalism and program [6] are presented and discussed in Chapter 2. As a proof of concept of our theoretical approach, each extension is validated with an appropriate case study.
In the second part of this thesis (Chapter 3), the *ab-initio* CPA will be applied to $FeSe_{0.5}Te_{0.5}$, focusing on band engineering the material's surface Dirac cone. A detailed analysis of doping and disorder effects is presented by exploring the substitutional phase space. Accordingly, an optimal doping strategy is developed with the goal of raising the Fermi level towards the surface Dirac cone while preserving the spin-orbit coupling gap, thus creating the necessary conditions for topological superconductivity and Majorana zero modes.
Our investigations into $FeSe_{0.5}Te_{0.5}$ are concluded in Chapter 4, where the connection between interstitial iron content and the suppression of superconductivity due to impurity scattering is examined. Finally, a summary of the work presented in this thesis is given, together with concluding remarks and an outlook on possible improvements and future work.

Contents

Introduction v

1 Fundamentals: electronic structure calculations and disorder 1
1.1 Density functional theory . . . 1
1.1.1 The many-body problem . . . 1
1.1.2 Hohenberg-Kohn theorems . . . 2
1.1.3 The mixed-basis pseudopotential framework . . . 3
1.2 Disorder through chemical substitution . . . 4
1.2.1 A brief overview of disorder . . . 4
1.2.2 The coherent potential approximation . . . 5
1.2.3 The Blackman, Esterling and Berk formalism . . . 9
1.2.4 *Ab-initio* implementation of the pseudopotential framework in an orbital basis . 11
1.3 CPA work flow and charge self-consistency . . . 16
1.3.1 Charge self-consistency . . . 16

2 Extensions to the original CPA formalism - Proof of concept 21
2.1 Fermi sheets and surfaces extension . . . 21
2.1.1 Proof of principle - Fermi surface of copper . . . 22
2.1.2 Fermi surface of a disordered alloy . . . 23
2.2 Vacancy extension . . . 26
2.2.1 Proof of principle - turning body centered cubic Fe into simple cubic Fe . . . 26
2.2.2 Band structure and density of states . . . 27
2.3 Spin polarization extension . . . 30
2.3.1 $Fe_{1-x}Co_x$ as benchmark . . . 30
2.3.2 Band structure of spin polarized clean Fe and Co . . . 30
2.3.3 Evolution of the magnetic moment in $Fe_{1-x}Co_x$ . . . 32
2.4 Full *ab-initio* spin-orbit coupling extension . . . 35
2.4.1 Band structure and Fermi surface of bcc Fe with spin-orbit coupling . . . 35

3 Band engineering of Dirac cones in iron chalcogenides 39
3.1 A brief introduction to iron-based superconductors . . . 40
3.2 The iron chalcogenides - FeSe, FeTe, Fe(Se,Te) . . . 41
3.3 The origin of the surface Dirac cone in Fe(Se,Te) . . . 43
3.4 Band structure and Fermi surface of FeSe . . . 46
3.4.1 The influence of the lattice parameters on the band structure of FeSe . . . 49
3.5 The effect of Te-substitution . . . 51
3.6 Inclusion of Spin-orbit coupling . . . 52
3.7 Electron doping via chemical substitution - shifting the Fermi level . . . 54
3.7.1 3*d* transition metal substitution at the Fe site . . . 54

3.7.2 Halogen substitution at the Se site . . . 56
3.8 Conclusion and outlook . . . 61

4 Interstitial iron in $Fe_{1+y}Se_{0.5}Te_{0.5}$ and its possible impact on superconductivity 63
4.1 Superconductivity in FeSe and Fe(Se,Te) . . . 63
4.2 Iron interstitial in Fe(Se,Te) . . . 64
4.3 Impact of excess iron on DOS, band structure, and Fermi surface . . . 65
4.4 Impurity scattering and the suppression of superconductivity . . . 68
4.5 Conclusion and outlook . . . 70

Summary and Conclusion 71

Bibliography 75

List of Figures 87

Acronyms 89

Acknowledgments 91

A *Ab-initio* CPA program 93
A.1 Code extensions . . . 93
A.2 Program file structure . . . 93
A.3 Mode of operation . . . 95
A.4 Output file structure . . . 103

B Basis set and overlap matrix elements 107
B.1 Orbital representations . . . 107
B.1.1 Localized orbitals in real space . . . 107
B.1.2 Localized orbitals in reciprocal space . . . 108
B.1.3 Translation of localized orbitals . . . 108
B.2 Useful properties of cubic harmonics and other relations . . . 109
B.3 Overlap matrix elements . . . 109
B.3.1 Onsite overlap . . . 110
B.3.2 Offsite overlap . . . 110

C The electronic density 113

D CPA matrix elements of the Hamiltonian 117
D.1 Potential contributions . . . 117
D.1.1 The Pseudopotential . . . 117
D.1.2 The full local potential . . . 118
D.1.3 The Hartree potential . . . 119
D.1.4 The exchange and correlation potential . . . 120
D.1.5 The mixing potential . . . 123
D.2 The Hamiltonian matrix elements . . . 124
D.2.1 Onsite matrix elements of the Hamiltonian . . . 125

D.2.2 Offsite matrix elements of the Hamiltonian . . . 126

E Spin-orbit matrix elements **129**
E.1 Relativistic norm-conserving pseudopotentials . . . 129
E.2 Matrix elements of spin-orbit interaction . . . 132
E.3 Implementation of the spin-orbit coupling Hamiltonian . . . 134

F Symmetrization **137**

G Green's function for a nonorthogonal basis **143**
G.1 Field operators in a local basis . . . 143
G.2 Field operators in the Bloch basis . . . 144
G.3 The retarded Green's function . . . 145
G.4 The Bloch spectral function . . . 147
G.5 Projected spectral function . . . 148
G.5.1 Green's function integrations . . . 148

H Implementation of the CPA cycle **151**

I CPA GUI documentation **153**

J Crystal structures and calculational details **155**
J.1 Fermi surface calculations for fcc Cu, Ni, and $Cu_{1-x}Ni_x$ . . . 156
J.2 Vacancy calculations - turning bcc Fe into sc Fe . . . 157
J.3 Spin polarized calculations in bcc Fe, Co, and $Fe_{1-x}Co_x$ . . . 158
J.4 Spin-orbit coupling in bcc Fe . . . 159
J.5 $FeSe_{0.5}Te_{0.5}$ and substitutions . . . 160
J.6 Interstitial iron in $Fe_{1+y}Se_{0.5}Te_{0.5}$ . . . 164

Chapter 1

1 Fundamentals: electronic structure calculations and disorder

1.1 Density functional theory

The most prominent and successful theory applied in electronic structure calculations to date is undoubtedly density functional theory (DFT). Its application ranges from solid state physics over chemistry [23] to biology [24]. The importance of the electronic density $n(\boldsymbol{r})$ for the ground state properties of atoms was first realized by Fermi and Thomas resulting in the Thomas-Fermi-Theory [25, 26]. With the electronic density as its only input, the kinetic energy was approximated as that of the uniform electron gas and repulsive interactions treated in terms of the classical electrostatic Coulomb potential. Later on, Dirac was able to show how to incorporate exchange effects [27]. The greatest leap forward was made possible by the work of Hohenberg and Kohn [28] in 1964, which we shall take a closer look at in Sec. 1.1.2.
Despite its great success, especially in solid state physics, it has proven to be an insufficient description in some cases. Numerous extensions and methods have been developed (and are still being developed) to overcome these challenges. Aside from issues with strongly correlated electron systems, DFT is not well suited for the treatment of disordered crystals - a fact of particular interest for this work.
Nevertheless, DFT still provides a solid basis for more sophisticated methods when dealing with real materials. This includes the Coherent potential approximation (CPA) used within this work for the treatment of substitutional disorder and so we will begin with a comprehensive introduction to density functional theory. The following brief review is largely based on the work of Ref. [6], which provided the underlying program further developed in this work.

1.1.1 The many-body problem

In solid state physics, we are typically interested in the properties and dynamics of systems composed of a large number of electrons and nuclei. To describe the interactions between all these particles, we can express the Hamiltonian of the system in the general form

$$H = T_{\text{el}} + T_{\text{nuc}} + V_{\text{el-el}} + V_{\text{el-nuc}} + V_{\text{nuc-nuc}}. \tag{1.1}$$

The kinetic terms of electrons and nuclei are represented by T_{el} and T_{nuc}, respectively, while Vs denote interactions between particles. We must consider interactions between electrons themselves ($V_{\text{el-el}}$),

between electrons and nuclei ($V_{\text{el-nuclei}}$), and those between nuclei and nuclei ($V_{\text{nuc-nuc}}$). Unfortunately, such many-body problems cannot be solved exactly, due to the enormous number of particles involved and consequently enormous number of degrees of freedom to consider. Luckily, we may often help ourselves with approximations that greatly reduce the problem complexity down to a manageable extent while still giving astonishingly accurate results.
The most essential approximation to electronic structure calculations, neglecting lattice dynamics, is the so-called Born-Oppenheimer approximation. Recognizing that the mass of a nucleus is orders of magnitude greater than that of an electron ($M_{\text{nuc}} \gg m_{\text{e}}$) and that consequently the motion of an electron will instantaneously follow that of the nuclei, we can decouple their dynamics. We are thus left with independently solving two Schrödinger equations

$$(T_{\text{el}} + V_{\text{el-el}} + V_{\text{el-nuc}}) \left|\Psi\right\rangle = E_{\text{el}}(\{\boldsymbol{R}_I\}) \left|\Psi\right\rangle \tag{1.2}$$

$$(T_{\text{nuc}} + V_{\text{nuc-nuc}} + E_{\text{el}}(\{\boldsymbol{R}_I\})) \left|\varphi\right\rangle = E_{\text{tot}} \left|\varphi\right\rangle, \tag{1.3}$$

where E_{el} signifies the total energy of the electrons which only depends parametrically on the ionic positions $\boldsymbol{R}_I$. We have hereby greatly simplified the electronic problem, yet the many-body nature is still present in $V_{\text{el-el}}$ and requires further approximations.

1.1.2 Hohenberg-Kohn theorems

In contrast to the prevalent wave function based ansatz typically applied in physics, DFT takes on a different approach: as the fundamental quantity we identify the electronic density $n(\boldsymbol{r})$. This approach is based on the theorems derived by Hohenberg and Kohn [28]. Quantum mechanics tells us that an external potential $v_{\text{ext}}(\boldsymbol{r})$ uniquely defines the ground state and thus the electronic density

$$v_{\text{ext}}(\boldsymbol{r}) \to H \to \left|\Psi\right\rangle \to n(\boldsymbol{r})$$

where in the context of solids this external potential is identified as the ionic background. It was shown by Hohenberg and Kohn that this argumentation may be reversed, i.e., the electronic density defines the external potential up to a constant

$$n(\boldsymbol{r}) \to v_{\text{ext}}(\boldsymbol{r}) + C$$

and thus all properties of the system, including the Hamiltonian and the many-body wave function. Consequently, a density functional $F[n(\boldsymbol{r})]$ exists such that

$$E_{\text{el}}[n(\boldsymbol{r})] = F[n(\boldsymbol{r})] + \int \mathrm{d}^3 r \, n(\boldsymbol{r}) v_{\text{ext}}(\boldsymbol{r}) \tag{1.4}$$

is minimal for the ground state density. This provides a variational principle from which we may determine the ground state energy. In most modern applications, the energy functional in Eq. (1.4) is not minimized directly. Following the work of Kohn and Sham [29], instead of studying a system of interacting particles we turn to a fictitious system of non-interacting particles with an effective potential $v_{\text{eff}}(\boldsymbol{r})$ that produces the same ground state density. This ansatz leads to the Kohn-Sham-equations:

$$\left(\frac{\hbar^2}{2m}\Delta + v_{\text{eff}}(\boldsymbol{r})\right) \varphi_i(\boldsymbol{r}) = \epsilon_i \varphi_i(\boldsymbol{r}) \tag{1.5}$$

$$v_{\text{eff}}(\boldsymbol{r}) = v_{\text{ext}}(\boldsymbol{r}) + v_{\text{Hartree}}[n(\boldsymbol{r})] + v_{\text{XC}}[n(\boldsymbol{r})] \tag{1.6}$$

$$n(\boldsymbol{r}) = \sum_{i=1}^{N} |\varphi_i(\boldsymbol{r})|^2. \tag{1.7}$$

In this picture, ϕ_i are the Kohn-Sham orbitals with eigenenergies ϵ_i. The effective potential that was introduced to map the interacting system onto a non-interacting one is comprised of three contributions: the ionic potential v_{ext} of the crystal lattice, the Hartree potential

$$v_{\text{Hartree}}(\boldsymbol{r}) = \frac{e^2}{2} \int \mathrm{d}^3 r' \, \frac{n(\boldsymbol{r}) n(\boldsymbol{r}')}{|\boldsymbol{r} - \boldsymbol{r}'|} \tag{1.8}$$

to describe density-density interactions and the exchange and correlation (XC) potential v_{XC}. Absorbed within the XC potential are all other relevant many-body interactions beyond the Hartree term. According to Kohn and Sham we may thus reduce the complexity of the insoluble many-body problem to an effective single-particle problem. As simplifications often do, this comes at a price: Eqs. (1.5)-(1.7) must be solved self-consistently. If we wish to determine the orbitals φ_i we must solve the single-particle Schrödinger Eq. (1.5) which is governed by v_{eff}. However, the external potential in turn consists of the Hartree- and XC-potential, which both depend on the electronic density $n(\boldsymbol{r})$. But the electronic density itself is determined by φ_i according to Eq. (1.7).
Usually, such a system of self-consistent equations is solved iteratively by starting from an initial guess of the effective potential or the density. In order to arrive at a single-particle problem we condensed all electronic correlations into the XC potential for which no exact expression exists. Consequently, we must again resort to approximations: among the most commonly used are the local-density approximation (LDA) and generalized gradient approximation (GGA), of which the former is used within this work. To this day, no single approximation has been found that is capable of describing (strongly) correlated electron systems to a sufficient degree of accuracy.

1.1.3 The mixed-basis pseudopotential framework

Now that we have introduced the main concepts of DFT calculations we can turn to the actual implementation. Generally speaking, most DFT programs are tasked with self-consistently solving a set of equations similar to Eqs. (1.5)-(1.7). The route to this solution, however, may differ with regards to the approaches chosen. We shall concentrate here on two main ingredients of an implementation and the possible distinctions between DFT codes: the electron-ion potential v_{ext} and the basis in which to express the Kohn-Sham orbitals φ_i.
There are two main approaches to treat the electron-ion interaction: the all-electron and the pseudopotential approach. Within the former, v_{ext} is taken to be the bare potential of a nucleus and, consequently, the self-consistent equations must be solved for all electrons. The associated immense computational cost can be drastically reduced by resorting to the pseudopotential approach. Instead of having to treat all electrons on an equal footing, we may restrict ourselves to the valence electrons if we take v_{ext} to be an effective nucleus potential screened by the core electrons.
As to the choice in basis set: most implementations make use of plane waves which provide a simple and elegant mathematical treatment. However, this comes at the cost of slow convergence for elements with strongly localized electrons such as $3d$ transition metals. Such elements may be more efficiently described by employing a set of atom centered functions. Yet they are a poor choice for the description of quasi-free electrons and require a more sophisticated mathematical treatment. It seems natural to combine the advantages of both basis set schemes by employing a basis set comprised of a linear combination of plane waves and a few localized atomic functions. This approach was implemented in the mixed-basis pseudopotential (MBPP) [30, 31] code referred to in this work which further makes use of norm-conserving pseudopotentials constructed after Vanderbilt [32]. Together, this allows for an efficient treatment of elements with strongly localized electrons and guarantees computational

feasibility, as discussed above.
The version of the MBPP used within this work is an adaptation of the original approach developed by Steven Louie and co-workers [33] and was completely reformulated and implemented by Bernd Meyer and co-workers [30]. It was adapted by Rolf Heid and Alexander Herbig to supply all necessary quantities needed for the treatment of substitutionally disordered systems, i.e., it provides the input to the CPA program (see Sec. 1.3).

1.2 Disorder through chemical substitution

Before we focus on the method used within this work to describe substitutional disorder we give a brief overview of disorder and present a few early electronic structure methods.

1.2.1 A brief overview of disorder

The fundamental property of an ideal solid which allows an elegant mathematical description is perfect periodicity. For such an idealized crystal we may restrict ourselves to a single unit cell from which we may straightforwardly derive all bulk properties. As it turns out, nature is not ideal and perfect, and so crystals themselves are not ideal: they do not exhibit perfect periodicity, but rather randomly distributed impurities. These lead to disorder effects which manifest themselves in the electronic properties of our crystals. Although at first this may seem as a great downside, we can make use of this imperfection and the entailed physical effects to tune our systems to exhibit desired effects and properties.
In contrast to unwanted but inevitable defects such as vacancies and boundaries, disorder by chemical substitution provides a powerful tool to access the physics of solid state system. Within this work we will concentrate on this type of *wanted* disorder. The changes we can induce by exchanging specific atomic types in the crystal structure are manifold: we can drive phase transitions, enhance or diminish magnetism and superconductivity, make an insulting material conductive (and *vice versa*) or even induce topological properties. Disorder is often responsible for the phase diagrams of many material classes (such as the iron pnictide superconductors or the high-T_c cuprates)
In a disordered crystal certain host atom types are replaced by a substituent type or left unoccupied randomly, i.e., we are faced with a non-periodic occupation of crystallographic sites and consequently the periodicity of the system is broken. As such, the properties of the system will, strictly speaking, be determined by the distribution of the different atoms onto the disordered lattice sites.
Although modern day DFT is capable of treating up to a few hundred atoms with reasonable computational effort, generic substitutional disorder is beyond its limits, due to broken translational symmetry. Given the enormous amounts of atoms in a real crystal (of the order of 10^{23}), we cannot expect to give an exact treatment, and so we must resort to meaningful approximations and theories capable of treating arbitrary substitutional disorder in the thermodynamic limit.
We shall now briefly discuss some early approaches to disorder before we focus on the specialized DFT based method used within this work.

Supercell method

A straightforward approach to substitutional disorder can be made by recognizing that most physical quantities can be obtained to a reasonable degree of accuracy by averaging over only a finite number of configurations.

This fact is the underlying principle of the supercell approach: the unit cell of the host lattice is enlarged to accommodate partial occupation. Then, according to the impurity concentration, a fraction of the host sites is occupied by the substituent species. In order to fully account for the random nature of substitutional disorder, the average over several configurations must be taken. The quality of the thermodynamic average introduces an additional computational cost factor. Obviously, only a small set of substitutional concentrations are practical within this approach (e.g. 50%, 25%, 12.5%), as even they lead to large supercells and considering huge numbers of configurations to acquire accurate thermodynamic averages - making calculations sumptuous. An arbitrary concentration would thus require an enormous supercell.
Given these drawbacks, the supercell approach is only viable for a limited set of cases and is not suited as a tool to describe generic disorder. Nonetheless, supercell methods have provided valuable insight and produced sophisticated algorithms for supercell construction.
However, as there are a number of material classes that exhibit fascinating physics at low substitutional concentrations, a tool for generic disorder is highly desirable. The class of methods capable of dealing with these arbitrary concentrations are usually termed *effective medium theories*.

Virtual crystal approximation

The simplest of these methods is the virtual crystal approximation (VCA), where the host atomic potential at a certain site is replaced by an average over host and impurity potential, weighted by their respective concentrations:

$$\{V_A(\boldsymbol{R}_i), V_B(\boldsymbol{R}_i)\} \rightarrow V_{\mathrm{VCA}}(\boldsymbol{R}_i) = c_i^A V_A(\boldsymbol{R})_i + c_i^B V_B(\boldsymbol{R}_i). \tag{1.9}$$

Here, $V_{A(B)}$ is the atomic potential of atom type $A(B)$ and $c_i^{A(B)}$ is the atomic concentration of species $A(B)$ at site i. Even though the VCA is rather simple, it has provided good results in some areas, e.g. lattice dynamics. However, it comes at no surprise that this basic treatment of disorder fails in many scenarios. One example is the split band limit of an alloy: with increasing impurity concentration a formerly single band splits into two individual bands, as is the case in $Cu_{1-x}Zn_x$ alloys (see Ref. [6]). The VCA fails here because it neglects the inhomogeneity of the electronic density in a real disordered $A_{1-x}B_x$ alloy. Due to the random distribution of potentials of types A and B, the probability of finding an electron near A differs from that of finding it near B. This behavior cannot be reproduced by averaging the potentials as is done in the VCA.

1.2.2 The coherent potential approximation

One of the most successful and sophisticated theories to deal with substitutional disorder is the *coherent potential approximation* (CPA). Early applications were widely based on the multiple-scattering formalism of the Korringa-Kohn-Rostoker CPA (KKR-CPA) - and are still in use today [34, 35]. Newer versions, such as the tight-binding-linear-muffin-tin-orbital CPA (TB-LMTO-CPA) [36] and linear-combination-of-atomic-orbitals CPA (LCAO-CPA) [6, 37, 38], are computationally less demanding and capable of dealing with complex unit cells and even surfaces and interfaces [37].
The subsequent derivation of the CPA is largely based on Ref. [6], which provided the foundation for the work presented in this thesis.
In developing a theory of disorder in solid state systems, the most convenient starting point is to consider onsite energies ϵ_i randomly distributed among sites i. In a localized framework we may

describe this situation by a single-particle Hamiltonian of the form

$$\hat{H} = \sum_{ij} t_{ij} c_i^\dagger c_j + \sum_i \epsilon_i c_i^\dagger c_i. \tag{1.10}$$

Here, $c_i^\dagger(c_i)$ represent fermionic creation (annihilation) operators and t_{ij} denote the hopping matrix elements of an electron between sites i and j.
The incorporation of disorder via the onsite energy term is included in the conventional CPA, yet disorder of the surrounding sites is only treated on average. Thus, the approach neglects correlations of a given site with the disordered environment - a short-coming of this simple theory that was resolved by Blackman, Esterling and Berk [3], as we will see in Sec. 1.2.3. The problem described by Eq. (1.10) can be solved by taking the onsite energies ϵ_i as perturbations, leading to a Born's series for the Green's function in frequency domain

$$G_{ij}(\omega) = G^0_{ij}(\omega) + \sum_k G^0_{ik}(\omega)\epsilon_k G^0_{kj}(\omega) + \sum_{kl} G^0_{ik}(\omega)\epsilon_k G^0_{kl}(\omega)\epsilon_l G^0_{lj}(\omega) + \cdots \tag{1.11}$$

with the Green's function of the unperturbed Hamiltonian $G^0_{ij}(\omega) = \left[(\omega - t)^{-1}\right]_{ij}$ that is solely determined by the hopping elements t_{ij} and assumed to be known. In the closed formulation of a Dyson's equation this can be rewritten as

$$G_{ij}(\omega) = G^0_{ij}(\omega) + \sum_k G^0_{ik}(\omega)\epsilon_k G_{kj}(\omega). \tag{1.12}$$

As the physical observables of a disordered system are thermodynamic averages, we can take the configurational average of each term in Eq. (1.11):

$$\langle G_{ij}(\omega)\rangle = G^0_{ij}(\omega) + \sum_k G^0_{ik}(\omega)\langle\epsilon_k\rangle G^0_{kj}(\omega) + \sum_{kl} G^0_{ik}(\omega)\langle\epsilon_k G^0_{kl}(\omega)\epsilon_l\rangle G^0_{lj}(\omega) + \cdots \tag{1.13}$$

$$= G^0_{ij}(\omega) + \left(G^0(\omega)\Sigma(\omega)\langle G(\omega)\rangle\right)_{ij}. \tag{1.14}$$

In the last step of Eq. (1.13) we have absorbed all repeated averaging processes into a complex, frequency dependent self-energy $\Sigma(\omega)$ that can only be treated approximately. One of the simplest possible simplification is to take it as a single-site quantity $\Sigma_{ij} = \Sigma_i\,\delta_{ij}$, as proposed independently by Soven [1] and Taylor [2].
Before diving into the mathematical derivation of the CPA, it is instructive to first consider the underlying idea sketched in Fig. 1.1 for a two-dimensional A-B-alloy: we replace the actual sites of a disordered crystal by an initially unknown effective medium. This effective medium is associated with an effective medium Green's function, that is in turn determined by an effective medium self-energy. Then an arbitrary site in the effective medium is replaced by a real impurity with a well defined onsite energy. Due to the single-site nature of the CPA it does not matter which site is replaced.
We then perform the replacement with every species allowed to be substituted at the aforementioned site and demand that these replacements must not change the medium on the average. This provides us with a self-consistency condition for the CPA resulting in an iterative scheme to determine the initially unknown medium.
Having briefly outline the underlying idea, we can now derive equations that mathematically express the CPA self-consistency condition in the so-called locator framework.

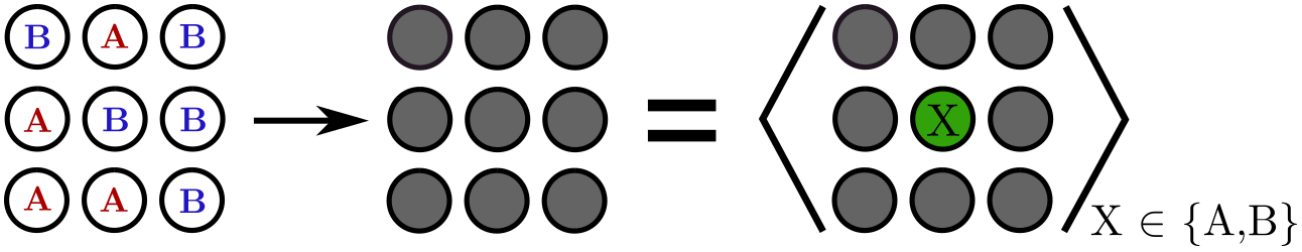

Figure 1.1: Illustration of the CPA principle: The random A-B-alloy is replaced by an effective medium (shaded circles) which must be equal to the average over all replacements with real impurities in the effective medium. Schematic drawing in the style of Fig. 2.1 in Ref. [6] taken from Ref. [39].

We here closely follow the outline given in Ref. [6], which relies on the derivation presented by Ref. [40]. By introducing the so-called locator $g_i(\omega) = (\omega - \epsilon_i)^{-1}$ [41], we may write Eq. (1.11) as

$$G_{ij}(\omega) = g_i(\omega)\,\delta_{ij} + \sum_{k\neq i} g_i(\omega) t_{ik} G_{kj}(\omega). \tag{1.15}$$

This formulation is equivalent to Dyson's equation Eq. (1.12), with the sole distinction that here we have started from the Green's function $g(\omega)$ of a localized state with energy ϵ_i and taken hopping t as the perturbation.
We can now simplify Eq. (1.11) by removing the sum restriction. To this end, we need to introduce the so-called *interactor* [42]

$$\Delta_i = \sum_{j\neq i} t_{ij} g_j t_{ji} + \sum_{j\neq i}\sum_{k\neq i} t_{ij} g_j t_{ki} + \cdots . \tag{1.16}$$

As we shall see along the derivation, we will be able to remove it from our equations after it has served its purpose. The interactor allows us to reformulate the locator equation of motion Eq. (1.15) for the diagonal elements into a form similar to Eq. (1.14) and we find

$$G_{ii} = \left(g_i^{-1} - \Delta_i\right)^{-1}. \tag{1.17}$$

At this point, we have found a mathematical formulation which makes it convenient to introduce the effective CPA-medium via the self-energy $\Sigma(\omega)$ and the effective medium Green's function $\Gamma(\omega)$. Using the effective medium interactor $\bar{\Delta}$ and the effective medium locator

$$\gamma_i(\omega) = \big(\omega - \Sigma_i(\omega)\big)^{-1} \tag{1.18}$$

we find

$$\Gamma_{ii}(\omega) = \left(\gamma_i^{-1}(\omega) - \bar{\Delta}_i(\omega)\right)^{-1} \tag{1.19}$$

from Eq. (1.17).
As we have discussed above, within the CPA-scheme a real impurity is to be inserted into the effective medium and we may define a corresponding impurity Green's function ${}^{q}G(\omega)$. By introducing an

impurity locator $g_i^q(\omega) = (\omega - \epsilon_i^q)^{-1}$ with species dependent onsite energy ϵ_i^q and replacing γ in Eq. (1.19) we arrive at

$$ {}^qG_{ii} = \left((g_i^q)^{-1} - \bar{\Delta}_i(\omega) \right)^{-1} = \left(\Gamma_{ii}^{-1} + \Sigma_i - \epsilon_i^q \right)^{-1} . \tag{1.20} $$

In combining Eqs. (1.19) and (1.18), we have here removed $\bar{\Delta}$ which only served to simplify our description.
The CPA condition depicted in Fig. 1.1 can now be formulated mathematically with the use of the impurity Green's function: the effective medium Green's function must be equal to a concentration weighted sum of the impurity Green's function over impurity species, i.e.,

$$ \Gamma_{ii}(\omega) \stackrel{!}{=} \sum_q c_i^q \, {}^qG_{ii}(\omega) \tag{1.21} $$

with c_i^q being the atomic concentration of species q at site i. We may now make the connection between the effective medium and the configurationally averaged Green's function $\langle G \rangle$ of Eq. (1.13): as the former was introduced in order to approximate the latter, Γ and $\langle G \rangle$ must coincide. Consequently, the same holds for the self-energy and Dyson's equation. Inserting G_{ii}^0 and rearranging Eq. (1.14) finally yields

$$ \Gamma_{ii} \stackrel{!}{=} \langle G_{ii} \rangle = \left[(G_{ii}^0)^{-1} - \Sigma_i \right]^{-1} = \left[\omega - t_{ii} - \Sigma_i \right]^{-1} . \tag{1.22} $$

Since the effective medium exhibits the full translational symmetry of the parent compound we can obtain $\Gamma_{ii}(\omega)$ from the $\boldsymbol{k}$-space representation via Fourier transformation. Detailed information on the definitions and conventions chosen for the Fourier transformation of matrix elements can be found in App. D. Here, we simply state the Fourier transform of the hopping matrix elements:

$$ t_{st}(\boldsymbol{k}) = e^{-\boldsymbol{k}(\boldsymbol{R_s} - \boldsymbol{R_t})} \sum_L e^{-i\boldsymbol{k}\boldsymbol{R_L}} t_{Lst}. \tag{1.23} $$

In Eq. (1.23) we have expressed the compound site index i by the lattice index L and an atomic index s within the unit cell, such that

$$ \boldsymbol{R_i} = \boldsymbol{R_L} + \boldsymbol{R_s}. \tag{1.24} $$

From this we may calculate the effective medium Green's function according to

$$ \Gamma_{ss}(\omega) = \int_{1.\mathrm{BZ}} \mathrm{d}^3k \, \Gamma_{ss}(\boldsymbol{k}, \omega) = \int_{1.\mathrm{BZ}} \mathrm{d}^3k \, \left[\omega - t(\boldsymbol{k}) - \Sigma \right]^{-1} \Big|_{ss} , \tag{1.25} $$

where only the onsite elements Γ_{ss} are needed in the CPA cycle.
With Eqs. (1.20), (1.21), and (1.25) we have thus found a set of self-consistent equations for the CPA formalism. They may be solved according to the following iterative scheme:

1. For iteration n, compute the effective medium Green's function ${}^{(n-1)}\Gamma$ according to Eq. (1.25) with the hopping matrix elements and self-energy from the previous iteration $n-1$. In the first iteration the initial self-energy must be guessed.

2. Calculate the impurity Green's function according to Eq. (1.20) for every species q.

3. Using the CPA condition (Eq. (1.21)), calculate the current effective medium Green's function ${}^{n}\Gamma$.

4. Calculate the change in self-energy via $\mathrm{d}\Sigma_i = \left({}^{(n-1)}\Gamma\right)^{-1}\Big|_{ii} - \left({}^{(n)}\Gamma\right)^{-1}\Big|_{ii}$.

5. If $\mathrm{d}\Sigma < \delta$ for a user defined threshold δ the scheme is finished, else continue with iteration $n+1$ at step 1.

As we have mentioned in the beginning of this section, the CPA presented here is of single-site nature. Consequently, it neglects environmental disorder effects. Nonetheless, it provides a computationally feasible approach to arbitrarily disordered systems in an *ab-initio* framework and has been applied successfully. Most commonly within the KKR method that relies on a multi-scattering Greens function formalism [34]. A number of extensions have emerged in the past seeking to incorporate environmental disorder, such as the molecular coherent potential approximation (MCPA) [43] and the nonlocal coherent potential approximation (NLCPA) [44]. Both these methods go beyond embedding single impurities into the effective medium by rather embedding impurity "clusters". Although successful in their own right, most of these methods suffer from symmetry violation or nonanalyticity [40]. We shall now present a powerful formalism free of these shortcomings: the BEB-CPA.

1.2.3 The Blackman, Esterling and Berk formalism

As we have discussed, the CPA as introduced in Sec. 1.2.2 lacks the ability to capture off-diagonal disorder. A description which allows to incorporate off-diagonal disorder by accounting for disordered hopping elements was introduced by Blackman, Esterling and Berk (BEB) [3]. Not only was this approach proven to be analytic [45] but it also preserves all symmetries of the parent compound. Furthermore, as was shown by Koepernik *et al.* [37] that it is applicable in the context of nonorthogonal, overlapping basis sets, as employed within this work.
In order to incorporate off-diagonal disorder, BEB introduced a set of binary occupation variables

$$\eta_i^P = \begin{cases} 1 & \text{if site } i \text{ is occupied with species } P \\ 0 & \text{otherwise.} \end{cases} \tag{1.26}$$

that are subject to a number of rules to ensure physical plausibility:

1. Avoid occupation of the same site by multiple species

$$\eta_i^P \eta_i^Q = \delta_{PQ} \eta_i^P \tag{1.27}$$

2. Ensure that a site is occupied by a species

$$\sum_P \eta_i^P = 1 \tag{1.28}$$

3. Relate the random occupation variables to an atomic concentration

$$\langle \eta_i^P \rangle = c_i^P \tag{1.29}$$

4. Assume statistical independence of the occupations of different sites

$$\langle \eta_i^P \eta_j^Q \rangle = c_i^P c_j^Q \tag{1.30}$$

Formally, the BEB-CPA deals with a non stochastic extended Hilbert space containing *all* configurations from which we can project a *single specific* configuration via these η:

$$\hat{H} = \sum_{ijPQ} \eta_i^P \underline{H}_{ij}^{PQ} \eta_j^Q c_i^\dagger c_j = \sum_{ijPQ} \eta_i^P \underline{t}_{ij}^{PQ} \eta_j^Q c_i^\dagger c_j + \sum_{iP} \eta_i^P \underline{\epsilon}_i^P c_i^\dagger c_j. \tag{1.31}$$

Here and in the following, underlined symbols denote quantities in extended Hilbert space. In Eq. (1.31), the Hamiltonian $\hat{H}$ describes a *specific* configuration that is acquired from the more general $\underline{H}$ by specificying the η. Being non stochastic, all quantities in extended Hilbert space (such as $\underline{H}$ and $\underline{S}$) retain the full translational and point group symmetries of the parent compound. Only via the η do we introduce randomness into a configuration. As was highlighted in the beginning of this section, the BEB-CPA accommodates disorder not only via the random onsite energies ϵ_i but also via the random distribution of hopping elements $t_{ij} = \eta_i^P \underline{t}_{ij}^{PQ} \eta_j^Q$. In this way, the η encode the disordered environment of a site in the crystal for a specific random configuration.
In deriving the self-consistency equations for the BEB formalism, we closely follow the route chosen in Ref. [6] which leans on Ref. [45] and provided the basis for the presented thesis. It may be understood as a generalization to the derivation presented in Sec. 1.2.2. Instead of complex numbers (as in Sec. 1.2.2) the site matrix elements take the form of matrices in species space due to the BEB-transformation in Eq. (1.31). Thus for the Green's function and locator we find

$$\underline{G}_{ij}^{PQ} = \eta_i^P G_{ij} \eta_j^Q \qquad \underline{g}_i^P = \eta_i^P g_i. \tag{1.32}$$

Special care must be taken in considering the locator $\underline{g}_i^P$: having been defined as a site-diagonal quantity, BEB-rule Eq. (1.26) additionally enforces species diagonality. Within the BEB-formalism, the equations of motion of the real physical system and the effective medium

$$\underline{G}_{ii} = \left(\underline{g}_i^{-1} - \underline{\Delta}_i\right)^{-1} \qquad \underline{\Gamma}_{ii} = \left(\underline{\gamma}_i^{-1} - \underline{\bar{\Delta}}_i\right)^{-1} \tag{1.33}$$

take on the same form in site indices of extended Hilbert space as in the conventional CPA. However, they become matrix equations in species space. We may now define a self-energy $\underline{\Sigma}$, analogous to the conventional case, via

$$\underline{\gamma}_i = \left(\omega - \underline{\Sigma}_i\right)^{-1}. \tag{1.34}$$

In contrast to the Green's function, the locator and the Hamiltonian, the self-energy is not related to its conventional counterpart via a BEB-transformation. The impurity locator in which we replace the self-energy with an onsite energy of a particular species q at site i then follows as

$${}^q\underline{g}_i^P = \left[\omega - \epsilon_i^q \delta_{Pq} - (1 - \delta_{Pq}) \Sigma_i^{PP}\right]^{-1}. \tag{1.35}$$

Analogous to Sec. 1.2.2, we find the impurity Green's function

$${}^q\underline{G}_{ii}^{PQ} = \left[\left(\underline{\Gamma}^{-1}\right)_{ii}^{PQ} + \left(\underline{\Sigma}_i^{PQ} - \underline{\epsilon}_i^q\right) \delta_{PQ} \delta_{Pq}\right]^{-1} \tag{1.36}$$

and the CPA condition to be

$$\underline{\Gamma}_{ii}^{PQ} = \sum_q c_i^q \, {}^q\underline{G}_{ii}^{PQ}. \tag{1.37}$$

Given the preserved translational symmetry in extended Hilbert space, we can define

$$\underline{\Gamma}_{ii}^{PQ} = \int_{1.\mathrm{BZ}} \mathrm{d}^3k \ \left[\omega\mathbb{1} - \underline{t}(\boldsymbol{k}) - \underline{\Sigma}_i\right]^{-1}\Big|^{PQ} \tag{1.38}$$

in analogy to Eq. (1.25) to complete our set of self-consistent equations. These equations are the BEB-analog to those of the conventional CPA defined in Eqs. (1.20), (1.21) and (1.25). The only formal difference lies in the underlined quantities, which now represent complex matrices in species indices instead of complex numbers. They are solved in the same iterative scheme as described in Sec. 1.2.2.

1.2.4 *Ab-initio* implementation of the pseudopotential framework in an orbital basis

In the last section we have introduced the BEB-CPA formalism as a tool for the description of substitutionally disordered systems. This theory grants access not only to arbitrary impurity concentrations but also to the treatment of off-diagonal environmental disorder. The physics of such a system is governed by its Hamiltonian, whose matrix elements $\underline{H}_{ij}^{PQ}$ enter the self-consistent equations via the onsite terms and the hopping matrix elements. Thus, we are task with extracting these matrix elements from a first-principles DFT calculation following the work of Koepernik *et al.* [37].
For this purpose, we generalize the site- and species dependent matrix elements to include an orbital degree of freedom, i.e., an orbital momentum quantum number l and the corresponding magnetic quantum number $m \in \{-l, l\}$. With this we may define the CPA Hamiltonian matrix elements as the result of evaluating our DFT Hamiltonian operator $\hat{H}_{\mathrm{DFT}}$ between LCAO orbitals

$$\underline{H}_{ilm,jl'm'}^{PQ} = \left\langle iPlm \middle| \hat{H}_{\mathrm{DFT}} \middle| jQl'm' \right\rangle \tag{1.39}$$

where i and j are site indices, and P and Q denote species. From this we may identify the onsite matrix elements $\dot{\underline{H}}$ as the onsite energies ϵ_i and the offsite elements $\breve{\underline{H}}$ as the hopping matrix elements t. As the LCAO basis is not restricted to be orthonormal, the overlap

$$\underline{S}_{ilm,jl'm'}^{PQ} = \left\langle iPlm \middle| jQl'm' \right\rangle \tag{1.40}$$

may take a nontrivial form. Within this work, such a nonorthonormal basis is employed (see App. B for a detailed discussion) for which the unit operator takes the form

$$\mathbb{1} = \sum_{\substack{iPlm \\ jQl'm'}} |iPlm\rangle \left(S^{-1}\right)_{ilm,jl'm'}^{PQ} \langle jQl'm'| \,. \tag{1.41}$$

As we have discussed in Sec. 1.1.3, in the MBPP code a basis set comprised of localized functions and plane waves was chosen in order to efficiently cover a wide range of elements. However, the latter are not well suited in the framework of a local, site dependent theory such as the BEB-CPA.
To gain purely atom centered LCAO basis functions that can describe its local nature, some post processing of the Kohn-Sham orbitals in the mixed-basis representation is necessary within the MBPP. This transformation is performed by a number of subroutines initially intended for local chemical analysis [31]. These routines employ the same atomic functions as in the mixed basis, but modified by cut-off functions. The parameters describing these cut-off functions are then optimized according to the so-called spillage function [46, 47] to best reproduce a converged band structure as obtained from the mixed-basis approach.

The focus of this optimization lies on the region below the Fermi level and thus generally gives a poor reproduction of the unoccupied DFT bands. However, being a ground state theory, DFT itself is not supposed to be reliable with respect to these unoccupied bands and they usually are not important. In order to gain a good representation of the Kohn-Sham orbitals in terms of a local basis, a large overlap of the involved functions is required. From the LCAO-scheme we find the basis functions ϕ_{lm} of the local orbitals expressed in terms of radial functions f_l and cubic Harmonics K_{lm}:

$$\left\langle \boldsymbol{r} \middle| iPlm \right\rangle = \phi^P_{ilm}(\boldsymbol{r}) = \phi^P_{lm}(\boldsymbol{r} - \boldsymbol{R_i}) \qquad \phi^P_{lm}(\boldsymbol{r}) = i^l f^P_l(r) K_{lm}(\hat{r}). \tag{1.42}$$

Here, $r = |\boldsymbol{r}|$ and $\hat{\boldsymbol{r}} = \boldsymbol{r}/r$ is the unit vector along $\boldsymbol{r}$. The basis functions themselves are normalized within this thesis, such that the onsite overlap

$$\dot{S}^P_{ilm,l'm'} = \underline{S}^{PP}_{ilm,il'm'} = \left\langle iPlm \middle| iPl'm' \right\rangle = \delta_{ll'}\delta_{mm'} \tag{1.43}$$

is always unity. In order to evaluate the Hamiltonian matrix elements, we must first assume a local decomposition of the electronic density according to

$$n(\boldsymbol{r}) = \sum_{iP} \eta^P_i n^P_i(\boldsymbol{r}). \tag{1.44}$$

Taking the fundamental Kohn-Sham equation for the electronic density

$$n(\boldsymbol{r}) = \sum_{n=1}^{N} |\varphi_n(\boldsymbol{r})|^2, \tag{1.45}$$

where n is a band index, and expanding the Kohn-Sham orbitals in terms of the local orbitals ϕ yields

$$n(\boldsymbol{r}) = \sum_{iPlm} \phi^P_{ilm}(\boldsymbol{r}) \sum_{jQl'm'} C^{PQ}_{ilm,jl'm'} \left[\phi^Q_{jl'm'}(\boldsymbol{r})\right]^*. \tag{1.46}$$

Here, the expansion coefficients C are given by

$$C^{PQ}_{ilm,jl'm'} = \sum_{i'P'l_1m_1} \sum_{j'Q'l_2m_2} \left(S^{-1}\right)^{PP'}_{ilm,i'l_1m_1} \left\langle i'P'l_1m_1 \middle| n \right\rangle \left\langle n \middle| j'Q'l_2m_2 \right\rangle \left(S^{-1}\right)^{Q'Q}_{j'l_2m_2,jl'm'}. \tag{1.47}$$

They are provided in by the LCAO routine in the MBPP in a slightly different form in $\boldsymbol{k}$-space. For a more detailed discussion of these local decomposition we refer to App. D.
With the local decomposition of the electronic density we can now in turn locally decompose the potential

$$V(\boldsymbol{r}) = \sum_{iP} \eta^P_i V^P_i(\boldsymbol{r}) = V_{\text{pseudo}}(\boldsymbol{r}) + V_{\text{Hartree}}(\boldsymbol{r}) + V_{\text{XC}}(\boldsymbol{r}). \tag{1.48}$$

To this end, we must locally decompose all three contributing terms. For the first term this is trivial, as the pseudopotential is already decomposed in terms of species and angular momentum by construction. As the Hartree potential depends linearly on the electronic density, its decomposition can be found directly from Eq. (1.44). The most difficult contribution to decompose is the XC potential which in fact is a non-linear functional of the electronic density and, consequently, a multipole expansion cannot be carried out analytically.
A simple treatment can be achieved via the atomic sphere approximation (ASA), as used by Ref. [37].

Within a sphere of radius $\boldsymbol{r}$, V_{XC} is calculated from the total electronic density of the disordered system and a constant value is postulated in the interstitial region between spheres. A major limitation to this scheme is the fact that it only works under isotropic considerations, neglecting all angular momentum contributions beyond $l = 0$.
For the BEB-CPA implementation used within this work, a more sophisticated approach was chosen: instead of non-overlapping atomic spheres, spherically symmetric shape functions S were introduced to deal with the decomposition of V_{XC}. They are characterized by a site-dependent cutoff radius R_i such that

$$S_i(\boldsymbol{r}) = S_i(|\boldsymbol{r}|) = S\left(\frac{r}{R_i}\right) \qquad S(1) = 0. \tag{1.49}$$

In contrast to the ASA, these shape functions are not only allowed but even required to overlap. In order to circumvent double-counting and guarantee a well-defined result we define the local decomposition according to

$${}^{\mathrm{XC}}V_i^P(\boldsymbol{r} - \boldsymbol{R_i}) = V_{\mathrm{XC}}[n(\boldsymbol{r})]\frac{S_i(\boldsymbol{r} - \boldsymbol{R_i})}{\mathcal{N}(\boldsymbol{r})}, \tag{1.50}$$

where

$$\mathcal{N}(\boldsymbol{r}) = \sum_i S_i(\boldsymbol{r} - \boldsymbol{R_i}) \tag{1.51}$$

ensures proper normalization. This decomposition can be shown to be exact and consistent in the special case of a clean compound for which

$$\begin{aligned} V_{\mathrm{XC}}[n(\boldsymbol{r})] &\overset{!}{=} \sum_i {}^{\mathrm{XC}}V_i(\boldsymbol{r} - \boldsymbol{R_i}) = \sum_i V_{\mathrm{XC}}[n(\boldsymbol{r})]\frac{S_i(\boldsymbol{r} - \boldsymbol{R_i})}{\mathcal{N}(\boldsymbol{r})} \\ &= V_{\mathrm{XC}}[n(\boldsymbol{r})]\frac{\mathcal{N}(\boldsymbol{r})}{\mathcal{N}(\boldsymbol{r})}. \end{aligned} \tag{1.52}$$

In case of a disordered system the decomposition is obviously no longer exact, but is only approximately valid.
In order to acquire the decomposed XC-potential, we begin from the full XC-potential which is calculated from the total electronic density. We then proceed by locally decomposing it via the shape functions for each species and additionally an angular momentum decomposition is performed numerically via a Gauß-Legendre integration [48–50]. For a more detailed discussion of the shape function approach and the XC-potential decomposition see App. D.1.4.
For a random configuration the Hamiltonian matrix elements are calculated according to

$$H_{ilm,jl'm'} = \eta_i^P \underline{H}^{PQ}_{ilm,jl'm'} \eta_j^Q = \eta_i^P \left\langle iPlm \middle| \hat{T} + \sum_{kR} \eta_k^R \hat{V}_k^R(\boldsymbol{r}) \middle| jQl'm' \right\rangle \eta_j^Q, \tag{1.53}$$

with the kinetic energy operator $\hat{T}$. Strictly speaking, due to the contributions of the decomposed potentials to $\underline{H}^{PQ}_{ilm,jl'm'}$ and their dependence on η (Eq. (1.48)), the above equation is no longer non-stochastic. Consequently, the Hamiltonian matrix elements defined in extended Hilbert space would no longer retain the full translational symmetry of the crystal. However, we can overcome this obstacle by only treating the potentials located at the terminal sites exactly and considering the rest of the sum as a conditional average over the whole crystal [37]. This procedure restores the full translational symmetry of $\underline{H}$, which is a prerequisite of the BEB formalism. Thus, we find the Hamiltonian matrix elements to be

$$\underline{H}^{PQ}_{ilm,jl'm'} = \left\langle iPlm \middle| \hat{T} + \hat{V}_i^P + \hat{V}_j^Q + \sum_{k\neq(i,j),R} c_k^R V_k^R \middle| jQl'm' \right\rangle. \tag{1.54}$$

It is then straight forward to decompose Eq. (1.54) into its onsite

$$\underline{\dot{H}}^{PQ}_{ilm,jl'm'} = \delta_{ij}\delta_{PQ}\left\langle iPlm\middle|\hat{T} + \hat{V}_i^P + \sum_{k\neq i,R} c_k^R \hat{V}_k^R\middle|iPl'm'\right\rangle \tag{1.55}$$

and offsite contribution

$$\underline{\breve{H}}^{PQ}_{ilm,jl'm'} = (1-\delta_{ij})\left\langle iPlm\middle|\hat{T} + \hat{V}_i^P + \hat{V}_j^Q + \sum_{k\neq(i,j),R} c_k^R \hat{V}_k^R\middle|jQl'm'\right\rangle. \tag{1.56}$$

Once again, BEB rule Eq. (1.26) manifests itself in the onsite term via δ_{PQ}. The computation of the Hamiltonian matrix elements requires the solution of multi-center integrals between wavefunctions expressed in cubic Harmonics (see Eq. (1.42)), which is computationally demanding. To simplify these calculations, a multipole expansion of the potentials is implemented in the CPA code, reducing the workload to the solution of one-dimensional radial integrals (a detailed discussion can be found in App. D). An exemption to this is V_{XC}, as discussed above.
We shall now turn to the discussion of the central self-consistent equations of the BEB-CPA formalism. As the CPA implementation works with a non-orthogonal basis we will briefly summarize some of the most important properties of Green's functions in this context. Once again, we will closely follow the derivation given in Ref. [6], which is based on Refs. [51] and [52]. Further details can be found in App. G. We will drop species indices and underscores denoting quantities in extended Hilbert space for the time being. Given a non-orthogonal basis set we are faced with two sets of Green's functions

$$G_{ilm,jl'm'}(t) = -i\theta(t)\left\langle\{a_{ilm}(t), a^\dagger_{jl'm'}\}\right\rangle \tag{1.57}$$

$$\mathcal{G}_{ilm,jl'm'}(t) = -i\theta(t)\left\langle\{c_{ilm}(t), c^\dagger_{jl'm'}\}\right\rangle \tag{1.58}$$

where $\{\cdot,\cdot\}$ once again denotes the anticommutator. These Green's functions are defined via two distinct types of creation and annihilation operators. For Eq. (1.57), $a^\dagger_{i\mu}$ ($a_{i\mu}$) creates (annihilates) an electron in orbital $\varphi_\mu(\boldsymbol{r}-\boldsymbol{R}_i)$ with commutation relations given as

$$\{a_{ilm}, a^\dagger_{jl'm'}\} = S_{ilm,jl'm'}. \tag{1.59}$$

The second case corresponds to an operator $c_{i\mu}$ defined via the field operators $\Psi(\boldsymbol{r}) = \sum_{i\mu} c_{i\mu}\varphi_\mu(\boldsymbol{r}-\boldsymbol{R}_i)$. Here, the commutation relations can be shown to be given by

$$\{c_{ilm}, c^\dagger_{jl'm'}\} = S^{-1}_{ilm,jl'm'}. \tag{1.60}$$

Considering a system of non-interacting electrons, we follow the standard procedure [53, 54] inserting a complete set of eigenstates $\sum_n |n\rangle\langle n| = \mathbb{1}$ and Fourier transforming into frequency domain, where the Green's functions are given by

$$\mathcal{G}(\omega) = \left(\omega^+ S - H\right)^{-1} \tag{1.61}$$

$$G(\omega) = S\mathcal{G}(\omega)S = S(\omega^+ S - H)^{-1}S. \tag{1.62}$$

Here, H is the LCAO-Hamiltonian and $\omega^+ = \omega + i\delta$. The infinitesimal complex part δ ensures analyticity of the retarded Green's functions in the upper complex half plane. Similar to Sec. 1.2.3, we

will introduce the locator concept, which can be done most conveniently from the equation of motion for $\mathcal{G}$:

$$\underbrace{\left(\omega\dot{S}-\dot{H}\right)}_{\equiv g^{-1}}\mathcal{G}+\left(\omega\breve{S}-\breve{H}\right)\mathcal{G}=\mathbb{1}. \tag{1.63}$$

In Eq. (1.63) we have already decomposed the Hamiltonian and overlap matrices into their onsite and offsite contributions. Comparing this to Eq. (1.15) we can identify the inverse of the locator g and transform the equation into the corresponding locator equation of motion

$$\mathcal{G}=g+g\left(\breve{H}-\omega\breve{S}\right)\mathcal{G}\qquad g=\left(\omega\dot{S}-\dot{H}\right)^{-1}\overset{\dot{S}=\mathbb{1}}{=}\left(\omega-\dot{H}\right)^{-1}, \tag{1.64}$$

where we have made use of $\dot{S}=\mathbb{1}$ for the LCAO basis. In this context, we can consider the term $\breve{H}-\omega\breve{S}$ in Eq. (1.64) as a generalized hopping matrix t. This allows us to generalize the BEB-CPA self-consistency Eqs. (1.36)-(1.38) to the non-orthogonal basis via the substitution $t\to\breve{H}-\omega\breve{S}$ in the effective medium Green's function Γ. We then arrive at our new set of self-consistent equations:

$$\underline{\Gamma}_{ii}^{PQ}=\int_{1.\mathrm{BZ}}\mathrm{d}^3k\,\left[\omega\left(\mathbb{1}+\underline{\breve{S}}\right)-\underline{\breve{H}}(\boldsymbol{k})-\underline{\Sigma}_i\right]^{-1}\Bigg|^{PQ} \tag{1.65}$$

$${}^{q}\underline{G}_{ii}^{PQ}=\left[\left(\underline{\Gamma}^{-1}\right)_{ii}^{PQ}+\left(\underline{\Sigma}_i^{PQ}-\underline{\dot{H}}_{ii}^{PQ}\right)\delta_{PQ}\delta_{Pq}\right]^{-1} \tag{1.66}$$

$$\underline{\Gamma}_{ii}^{PQ}=\sum_q c_i^q\,{}^{q}\underline{G}_{ii}^{PQ}. \tag{1.67}$$

In analogy to the conventional CPA introduced in Sec. 1.2.2, we may now define an iterative scheme for the solution of our set of self-consistent equations. This yields an update formula for the effective medium self-energy:

$$\mathrm{d}\underline{\Sigma}_{ilm,jl'm'}^{PQ}=\left(\underline{\Gamma}_i^{-1}\right)_{lm,l'm'}^{PQ}+\sum_q\frac{1}{c_i^q}\left[\underline{\dot{H}}_i-\underline{\Sigma}_i-\underline{\Gamma}_i^{-1}\right]_{lm,l'm'}^{qq}\delta_{PQ}\delta_{Pq}. \tag{1.68}$$

Most physical quantities are evaluated from the effective medium Green's function $\underline{\Gamma}$, which is defined analogously to $\mathcal{G}$ in Eq. (1.58). However, an exception is the density of states which is connected to the creation and annihilation of electrons and, thus, is defined over the second Green's function $\underline{G}$. The connection between the two can be made via $\underline{G}=\underline{S}\underline{\Gamma}\underline{S}$. From this the density of states is found to be

$$\nu(\omega)=-\frac{2}{\pi}\,\mathrm{Im}\,\mathrm{Tr}\left[\underline{S}\underline{\Gamma}(\omega^+)\right], \tag{1.69}$$

where an additional factor $\underline{S}^{-1}$ arises from taking the trace of an operator in a non-orthogonal basis. In Eq. (1.69), the factor two accounts for spin degeneracy (which is of course dropped for spin polarized calculations). In practical calculations, some care must be taken with respect to the argument of $\underline{\Gamma}(\omega^+)$. The infinitesimal imaginary part δ in $\omega^+=\omega+i\delta$ determined the level of fine structure to the density of states. The lower δ, the higher the resolution. However, this entails amplified numerical noise and consequently one must always balance resolution versus noise.
Finally, we come to another important quantity: the Bloch spectral function:

$$A(\boldsymbol{k},\omega)=-\frac{1}{\pi}\,\mathrm{Im}\,\mathrm{Tr}\left[\sum_{L\in\mathrm{lattice}}e^{i\boldsymbol{k}\boldsymbol{R_L}}\int_{\mathrm{u.c.}}\mathrm{d}^3r\,\underline{\Gamma}(\boldsymbol{r}-\boldsymbol{R_L},\boldsymbol{r},\omega^+)\right]. \tag{1.70}$$

It is defined as a discrete Fourier transformation of the Green's function in real space on the crystal lattice and an integration over one unit cell. This can be shown to be equivalent to

$$A(\boldsymbol{k},\omega) = -\frac{1}{\pi}\,\mathrm{Im}\,\mathrm{Tr}\left[\underline{S}(\boldsymbol{k})\underline{\Gamma}(\boldsymbol{k},\omega^+)\right] \tag{1.71}$$

with $\Gamma(\boldsymbol{k},\omega^+)$ being the kernel of the integral in Eq. (1.65). The spectral function contains all information relevant to the band structure of a disordered crystal and thus is the most important quantity to study momentum resolved disorder effects in more detail.

1.3 CPA work flow and charge self-consistency

With the BEB-CPA formalism outlined in the last section we have developed all necessary tools for *ab-inito* electronic structure calculations of arbitrarily substituted crystals. Before we can carry out a CPA calculation a few preparations must be made: we begin with a MBPP-DFT calculation of the parent compound from which we gain the pseudopotentials of the involved atomic species, the local basis functions obtained via the LCAO-fit and relevant information concerning the crystal lattice such as crystal symmetries. An equivalent calculation must then follow for each substitutional end member, instead of performing a DFT calculation for the bare atomic substituent. While in principle possible, the latter approach would have the major disadvantage of not taking into account the environmental influence on the local electronic densities of the end member constituents. By considering the substituent atomic species in the substitutional end member configuration, we achieve faster convergence in the CPA calculations. All MBPP-DFT calculations must be performed for the same crystal structure to be compatible with the CPA program.
From the local basis functions of all involved species the CPA program then calculates the overlap matrix and the locally decomposed electronic density according to Eq. (1.44), which is needed for the local decomposition of the Hartree potential and the computation of the XC potential. The local decomposition of the latter is then performed using the shape function approach discussed in Sec. 1.2.4. At this point, the matrix elements of the Hamiltonian are evaluated and fed into the self-consistency Eqs. (1.65)-(1.67), yielding a change in self-energy via Eq. (1.68).
The newly found self-energy is then reinserted into the self-consistency equations until $\mathrm{d}\underline{\Sigma}$ falls below a user-defined threshold and the CPA-cycle delivers an effective medium Green's function $\underline{\Gamma}(\omega)$. The Green's function and the spectral function contain all relevant information and one could therefore naively stop the procedure at this point. However, our starting point were several independent DFT calculations which contain no knowledge of the presence of respective substituted species. Consequently, the initial densities could only be calculated from the mutually isolated end members and the only coupling between the isolated calculations would come about through the off-diagonal terms of the Hamiltonian. Even so, the Hartree- and XC-potential explicitly depend on the density which, up to this point, contains no disorder effects.

1.3.1 Charge self-consistency

This short-coming was recognized and resolved by Koepernik *et al.* [37] by the implementation of a charge self-consistency condition: for each converged CPA calculation a new charge density is calculated from the respective Green's function via

$$n(\boldsymbol{r}) = -\frac{1}{\pi}\int_0^{E_F} \mathrm{d}\omega\,\mathrm{Im}\,G(\boldsymbol{r},\boldsymbol{r},\omega^+) \tag{1.72}$$

with the Fermi energy E_F being the upper integration limit. This ensures that only occupied states are taken into account. The new density is then reinserted into the computation of the Hamiltonian. A repetition of this procedure gradually improves the Hamiltonian until the difference in densities of two successive iteration drops below a threshold, i.e., convergence is reached.
The real space Green's function of the disordered system may be connected to the matrix $\mathcal{G}$ (see App. G) using the basis functions $\varphi^P_{ilm}(\boldsymbol{r})$ of the LCAO framework. From this connection, using the BEB transformation, we may express the electronic density of a random configuration as

$$n(\boldsymbol{r}) = -\frac{1}{\pi} \sum_{\substack{iPlm \\ jQl'm'}} \varphi^P_{ilm}(\boldsymbol{r}) \int_0^{E_F} \mathrm{d}\omega \, \mathrm{Im} \left[\eta^P_i \mathcal{G}_{ilm,jl'm'}(\omega^+) \eta^Q_j \right] \left(\varphi^Q_{jl'm'} \right)^* . \tag{1.73}$$

A meaningful comparison with experiment is only possible for configurationally averaged quantities and so Eq. (1.73) must be averaged leading to

$$\langle n \rangle (\boldsymbol{r}) = -\frac{1}{\pi} \sum_{\substack{iPlm \\ jQl'm'}} \varphi^P_{ilm}(\boldsymbol{r}) \int_0^{E_F} \mathrm{d}\omega \, \mathrm{Im} \underbrace{\left\langle \eta^P_i \mathcal{G}_{ilm,jl'm'}(\omega^+) \eta^Q_j \right\rangle}_{\overset{\text{CPA}}{=} \Gamma^{PQ}_{ilm,jl'm'}} \left(\varphi^Q_{jl'm'} \right)^* . \tag{1.74}$$

Additionally, for the computation of Hamiltonian matrix elements in extended Hilbert space (which are *not* configurationally averaged) we need the species and site decomposition not only of the potential but also of the electronic density. Thus, we must derive expressions for the local components n^P_i which yield the respective decomposition of Eq. (1.73) according to

$$n(\boldsymbol{r}) = \sum_{iP} \eta^P_i n^P_i(\boldsymbol{r}). \tag{1.75}$$

At this point we must resort to another approximation - the so-called terminal point approximation described in Ref. [37] which we shall briefly discuss in the following. The main idea behind this approximation is to replace the Green's function in extended Hilbert space by its twofold conditional average

$$\underline{\mathcal{G}}^{PQ}_{ilm,jl'm'} = \eta^P_i \mathcal{G}_{ilm,jl'm'} \eta^Q_j \qquad \rightarrow \qquad \eta^P_i \left\langle \underline{\mathcal{G}}^{PQ}_{ilm,jl'm'} \right\rangle_{P_i Q_j} \eta^Q_j . \tag{1.76}$$

Here, the average $\langle \ldots \rangle_{P_i,Q_j}$ is to be understood as an average over all members of the ensemble of configurations that contain fixed occupations at the two terminal points, i.e., $\eta^P_i = \eta^Q_j = 1$. Thus, we are averaging over all sites, except i and j. As Eq. (1.75) demands the full charge density be additively decomposed into single-site components, we must perform another average: this time only over the right index of the overlap elements in Eq. (1.76), such that only η^P_i remains and Eq. (1.73) takes the form of a sum over single-site expressions:

$$n^P_i(\boldsymbol{r}) = -\frac{1}{\pi} \sum_{\substack{jQ \\ lml'm'}} \varphi^P_{ilm}(\boldsymbol{r}) \int_0^{E_F} \mathrm{d}\omega \, \mathrm{Im} \left\langle \underline{\mathcal{G}}^{PQ}_{ilm,jl'm'}(\omega^+) \right\rangle_{P_i Q_j} \left(\varphi^Q_{jlm}(\boldsymbol{r}) \right)^* \left[\delta_{ij} + (1-\delta_{ij}) c^Q_j \right] . \tag{1.77}$$

The expression $\left[\delta_{ij} + (1-\delta_{ij}) c^Q_j \right]$ is a consequence of Eq. (1.30) (BEB-rule four), which postulates statistical independence of the occupation of different sites. The required conditionally averaged

Green's functions may be obtained via

$$\left\langle \underline{\mathcal{G}}^{PP}_{ilm,il'm'} \right\rangle_{P_i} = \frac{\underline{\Gamma}^{PP}_{ilm,il'm'}}{c_i^P} \qquad \left\langle \underline{\mathcal{G}}^{PQ}_{ilm,jl'm'} \right\rangle_{P_iQ_j} = \frac{\underline{\Gamma}^{PQ}_{ilm,jl'm'}}{c_i^P c_j^Q} \tag{1.78}$$

from the effective medium Green's function (see Ref. [37]). Finally, we may express the local species-decomposed electronic densities as

$$n_i^P(\boldsymbol{r}) = -\frac{1}{\pi}\frac{1}{c_i^P} \sum_{\substack{jQ \\ lml'm'}} \varphi^P_{ilm}(\boldsymbol{r}) \int_0^{E_F} \mathrm{d}\omega \, \mathrm{Im}\, \underline{\Gamma}^{PQ}_{ilm,jl'm'}(\omega^+) \left(\varphi^Q_{jl'm'}(\boldsymbol{r})\right)^* . \tag{1.79}$$

A brief remark on the actual implementation of the charge self-consistency in the CPA code is in order: were we to use the newly calculated density for the computation of the Hamiltonian matrix elements we would encounter numerical instabilities. This is a common problem found with self-consistency methods and may typically be resolved by employing a density that is a mixture of the current and previous density. To this end, a modified Broyden mixing scheme after Ref. [55] was implemented in the CPA program by A. Herbig [6].
As was mentioned above, for the evaluation of Eq. (1.73) in the self-consistency cycle we need the Fermi level of our disordered system. Similar to the density components, it may (indirectly) be calculated from the effective medium Green's function: we make use of the fact that the number of valence electrons $\mathcal{N}$ in the pseudopotential framework must be conserved and in a generic disordered compound is given by

$$\mathcal{N} = \sum_{iP} c_i^P \mathcal{N}_i^P \tag{1.80}$$

to fulfill the constraint of charge neutrality ($\mathcal{N}_i^P$ is the number of valence electrons for individual atomic types). We can then calculate $\mathcal{N}$ from the density of states via

$$\mathcal{N} = \int_0^{E_F} \mathrm{d}\omega \nu(\omega) = -\frac{2}{\pi} \int_0^{E_F} \mathrm{Im}\, \mathrm{Tr} \left[\underline{S\Gamma}(\omega^+)\right] . \tag{1.81}$$

The upper integration limit in Eq. (1.81) is successively shifted until we recover the actual number of valence electrons $\mathcal{N}$. The implementation uses a bisection method that cuts the energy interval in which E_F is searched for in half in each iteration step. The schematic workflow of the implementation of the *ab-initio* charge self-consistent CPA method outlined above is depicted in Fig. 1.2.

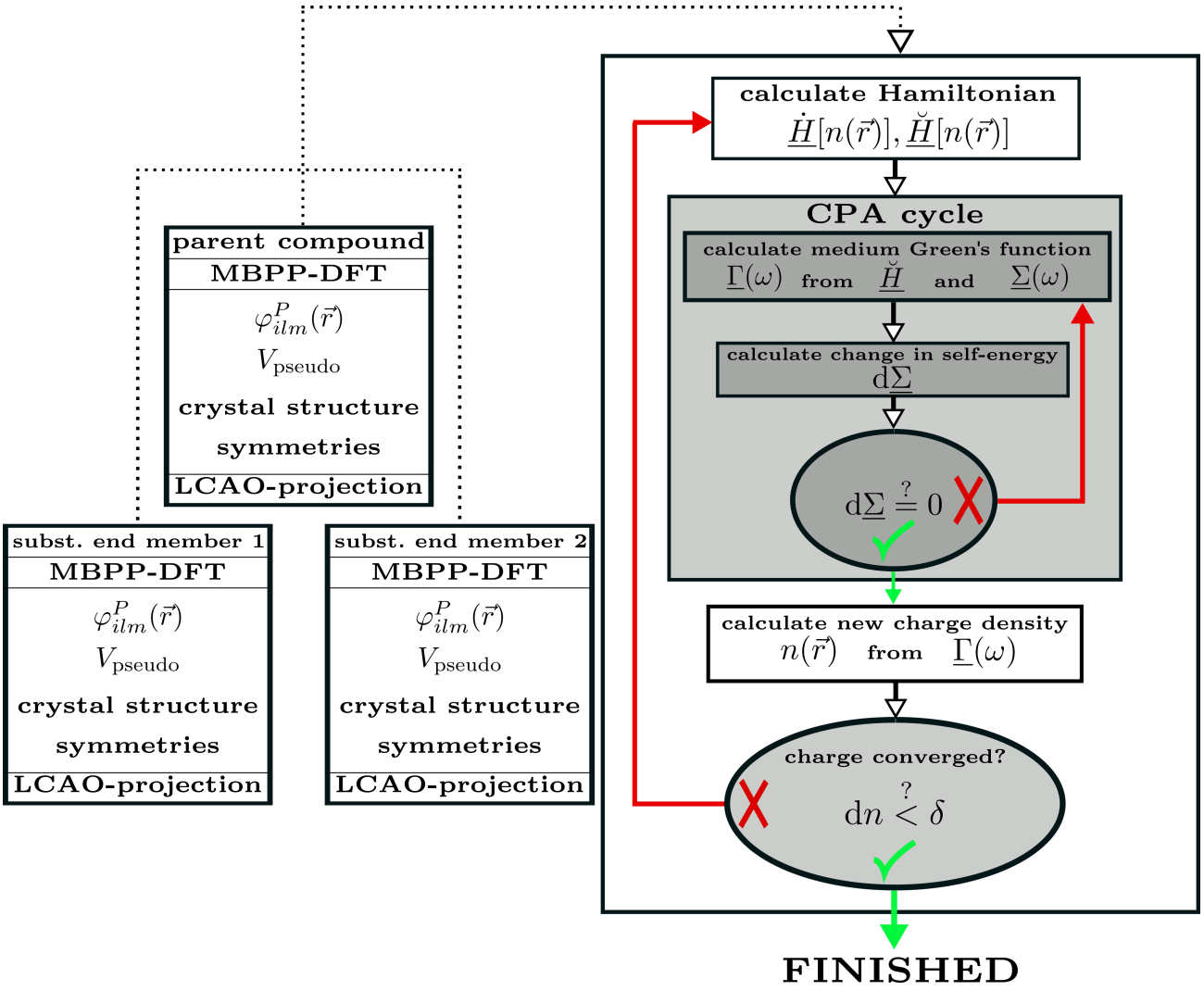

Figure 1.2: Exemplary work flow of the *ab-initio* CPA program for a doubly substituted system: Input preparation for parent compound and substitutional end members. Inner self-consistency CPA-cycle to determine the effective medium and outer loop for charge self-consistent calculation of the Hamiltonian matrix. Schematic drawing in the style of Fig. 2.2 in Ref. [6].

Chapter 2

2 Extensions to the original CPA formalism - Proof of concept

This chapter serves as an overview of the main extensions to the original CPA formalism [6] developed within this work. Aside from a number of minor alterations to the underlying idea, four major extensions have been implemented to increase the functionality and thus provide an even more powerful and versatile tool for the study of disordered solid state systems.

2.1 Fermi sheets and surfaces extension

The simplest definition of a metal is that of a solid with a Fermi surface, separating the occupied from the unoccupied states [56]. Intricate knowledge of a metal's Fermi surface is of great importance for its physical properties: phenomena like Fermi surface nesting are essential ingredients to the formation of charge-density waves (CDWs) [57], or the potential enhancement of the superconducting pairing mechanism in the iron-based superconductors [58, 59].

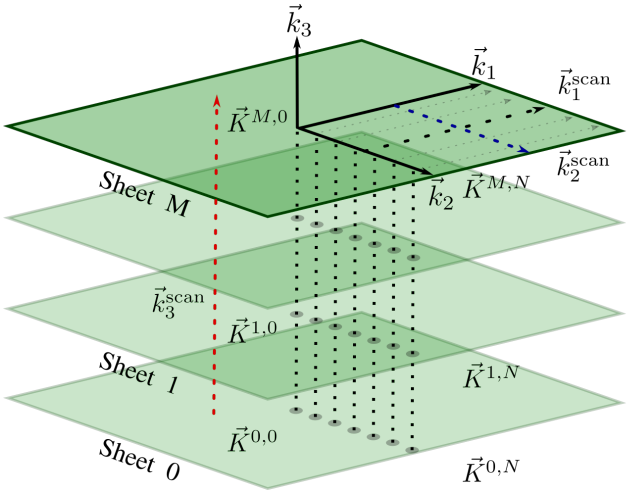

Figure 2.1: Schematics of the Fermi surface scan extension for a square BZ.

Thus, it is vital to have access to its shape and geometry, especially in the context of substituted

crystals. In order to calculate cross sections of the Fermi surface, we have adapted the preexisting method for band structure calculations to scan a user defined plane in the first Brillouin zone (1. BZ). The Bloch spectral function $A(\boldsymbol{k}, \omega = E_F) = -\frac{1}{\pi} \operatorname{Im} \operatorname{Tr} \left[\underline{S}\underline{\Gamma}(\boldsymbol{k}, \omega^+) \right]$ is calculated from the effective medium Green's function in extended Hilbert space $\underline{\Gamma}$ at the Fermi energy E_F (for details see App. G.4). Here, $\underline{S}$ is the orbital overlap. The spectral function yields quasi particle weight where bands intersect the scanned plane. This is used to map out the Fermi surface within each sheet (see, e.g., Fig. 2.12). In order to construct the 3-dimensional Fermi surface, we compute multiple parallel sheets. For the visualization, spectral weight below a user defined threshold $A(\boldsymbol{k}, E_F) < \delta$ must be discarded so as to only plot regions with considerable contributions (see, e.g., Fig. 2.2 (b)). The sampling scheme is as follows: for each sheet $i \in \{0, M\}$, we fix an initial starting point $\boldsymbol{K}^{i,0}$ from which we evaluate $A(\boldsymbol{k}, E_F)$ along a user defined direction $\boldsymbol{k}_1^{\text{scan}}$.
Subsequently, the starting point is shifted along a second predefined direction $\boldsymbol{k}_2^{\text{scan}}$ according to

$$\boldsymbol{K}^{i,j+1} = \boldsymbol{K}^{i,j} + \frac{\boldsymbol{k}_2^{\text{scan}}}{N}, \tag{2.1}$$

with N being the number of sampling points along $\boldsymbol{k}_2^{\text{scan}}$ and $j \in \{0, N\}$. From each new starting point in sheet i, we perform another scan along $\boldsymbol{k}_1^{\text{scan}}$, thus, sampling the plane spanned by $\boldsymbol{k}_1^{\text{scan}}$ and $\boldsymbol{k}_2^{\text{scan}}$. This procedure is repeated for each sheet, reached by shifting the initial starting point according to

$$\boldsymbol{K}^{i+1,0} = \boldsymbol{K}^{i,0} + \frac{\boldsymbol{k}_3^{\text{scan}}}{M} \tag{2.2}$$

along a third direction $\boldsymbol{k}_3^{\text{scan}}$. A schematic drawing of this procedure can be found in Fig. 2.1.

2.1.1 Proof of principle - Fermi surface of copper

As a proof of principle for our Fermi surface extension, we turn to one of the historically most prominent Fermi surfaces - that of face centered cubic (fcc) Cu - the first sharp Fermi surface to be measured via anomalous skin resistance [60]. These measurements revealed a roughly spherical "belly" and eight "necks" intersecting the hexagonal faces of the Brillouin zone - in contrast to the ideal free-electron sphere.

$\times\boldsymbol{k}_1$	$\times\boldsymbol{k}_2$	$\times\boldsymbol{k}_3$		$\times\boldsymbol{k}_1$	$\times\boldsymbol{k}_2$	$\times\boldsymbol{k}_3$	
0	0	0	**Γ**	5/8	1/4	5/8	**U**
3/8	3/8	3/4	**K**	1/2	1/4	3/4	**W**
1/2	1/2	1/2	**L**	1/2	0	1/2	**X**

Table 2.1: Symmetry $\boldsymbol{k}$-points of the fcc lattice. In style of Tab. 3 in Ref. [61].

In Fig. 2.2 (a) we present a schematic drawing of the BZ of the fcc lattice, along with some high symmetry $\boldsymbol{k}$-points (see Tab. 2.1). A comprehensive overview on Brillouin zones and high symmetry $\boldsymbol{k}$-points for different crystal lattices can be found in Ref. [61]. As can be seen in Fig. 2.2 (b), the belly deviating from the perfect sphere and the necks, intersecting the hexagonal zone faces, are well reproduced by our CPA calculation.

This deviation from the perfect free-electron sphere is attributed to the interaction of d bands and the conduction bands [62]. Here, we have constructed the Fermi surface from Fermi sheets calculated on 100×100 $\boldsymbol{k}$-mesh grids at 50 discrete sampling points along $\boldsymbol{k}_3^{\text{scan}}$.

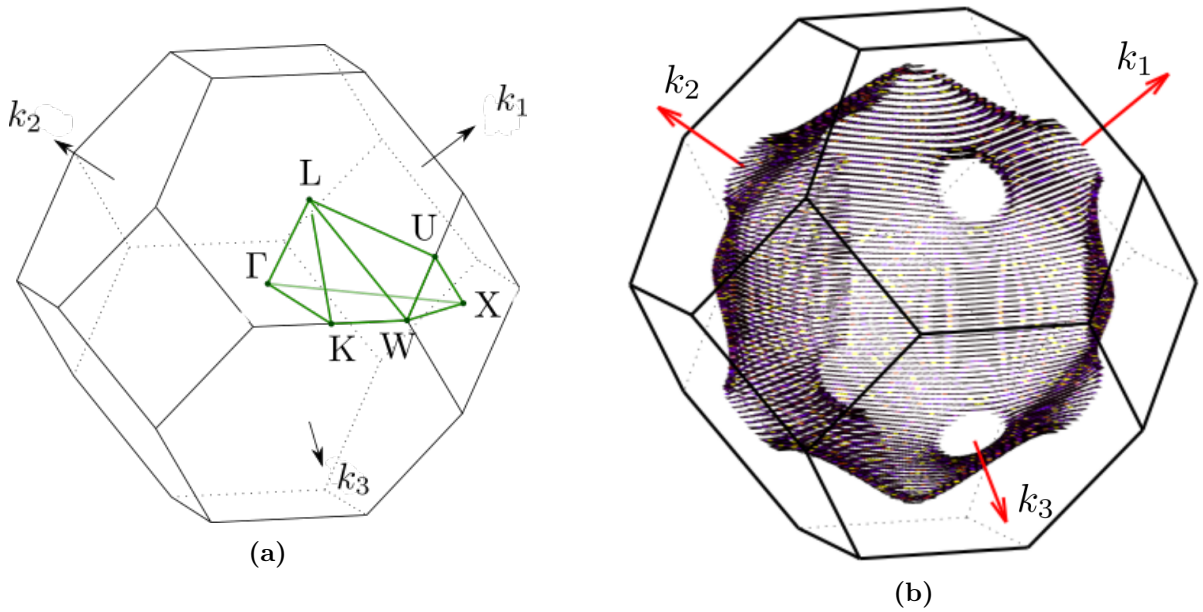

Figure 2.2: (a) Brillouin zone of the fcc lattice with symmetry $\boldsymbol{k}$-points (figure in style of Fig. 2 Ref. [61]). (b) Fermi surface of fcc Cu generated from 50 sheets calculated on 100×100 $\boldsymbol{k}$-mesh grids. The polyhedron represents the 1. Brillouin zone.

In the notation presented above, the choices for the Fermi sheet scans were made to be $\boldsymbol{k}_1^{\text{scan}} = (\frac{3}{8}, \frac{3}{8}, \frac{3}{4})$, $\boldsymbol{k}_2^{\text{scan}} = (\frac{3}{8}, -\frac{3}{8}, 0)$, $\boldsymbol{k}_3^{\text{scan}} = (\frac{1}{2}, \frac{1}{2}, 0)$. In the practical calculation, only the upper right quadrant of the Fermi surface in Fig. 2.2 (b) was computed and the crystal symmetry exploited to gain the full Fermi surface. Calculational details can be found in App. J.1.

2.1.2 Fermi surface of a disordered alloy

Having applied our Fermi surface computation scheme to a pure crystal, we shall now apply it to a disordered alloy: $\text{Cu}_{1-x}\text{Ni}_x$.
We can expect the Fermi surface to be changed drastically with increasing Ni content: new Fermi surfaces may appear, while others disappear or get reshaped. In order to investigate the effect of Ni substitution on the Fermi surface, we have performed multiple CPA calculations with varying content $x = \{0.1, 0.25, 0.5, 0.75\}$. The Fermi surfaces were constructed from individual Fermi sheets computed on regular 100×100 $\boldsymbol{k}$-mesh grids at 50 discrete sampling points along k_3^{scan} as described above.
We begin by first considering pure Ni, in order to have access to the Fermi surfaces of both clean systems. This will allow us to interpret the Fermi surfaces of the intermediate compounds $\text{Cu}_{1-x}\text{Ni}_x$. Here, some remarks are in order: firstly, the Fermi surface of fcc Ni consists of two parts - an inner and an outer part. Accordingly, we have depicted both parts separately in Fig. 2.3. Secondly, the color coding and perspective for all subsequent Fermi surfaces have been chosen appropriately to best emphasize the most relevant features of the inner and outer Fermi surfaces, respectively. Finally, for better visibility, some of the rear segments have been neglected in all depictions.

The inner part of the Ni Fermi surface (see Fig. 2.3 (a)) exhibits two main features: firstly, a central body (similar to Cu) with neck-like deformations towards the hexagonal faces. In contrast to Cu, these necks do not penetrate the hexagonal faces.

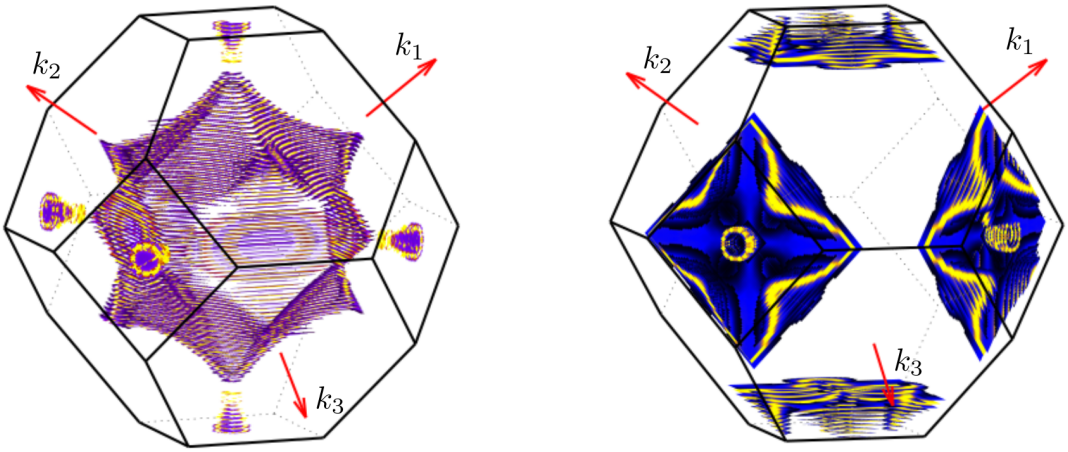

(a) **(b)**

Figure 2.3: (a) Inner, and (b) outer part of the Fermi surface of Ni.

Furthermore, we find Fermi surfaces disconnected from the central body in the shape of paraboloids which intersect the square faces. Secondly, the outer part (see Fig. 2.3 (b)) consists of petal-shaped Fermi surfaces at the square faces. At their center, we can observe the paraboloids mentioned above.

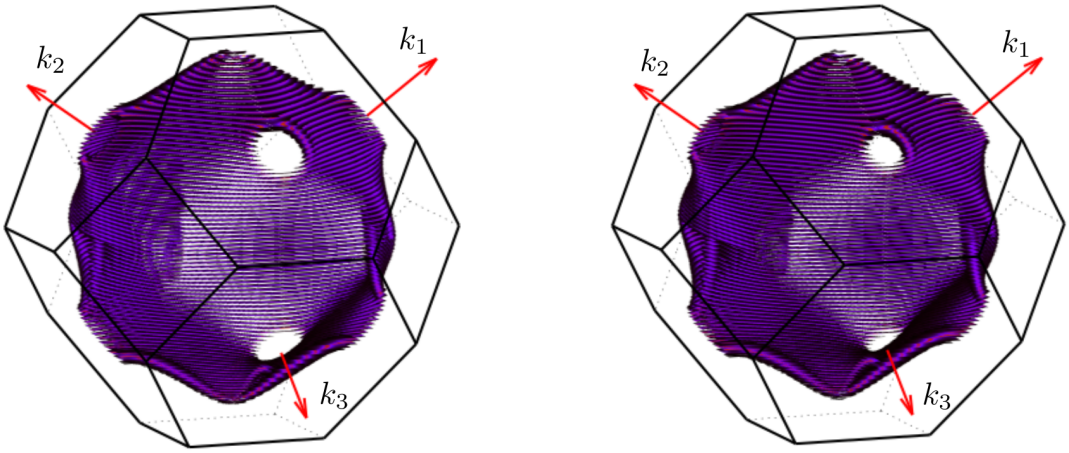

(a) **(b)**

Figure 2.4: Fermi surfaces of $Cu_{1-x}Ni_x$ for (a) $x = 0.1$, and (b) $x = 0.25$.

With knowledge of the Fermi surfaces of both clean systems, we can assume the substituted compounds $Cu_{1-x}Ni_x$ to gradually morph from one into the other, as Ni content is increased.
While for low Ni content ($x = 0.1$ and $x = 0.25$) the Fermi surface still closely resembles that of pure Cu, the diameter of the necks passing through the hexagonal faces has decreased (see Fig. 2.4). Half way from Cu to Ni, i.e., $x = 0.5$, we can already identify clear features of Ni in the Fermi surface (see

Fig. 2.5). The central body, along with the Cu necks, has shrunk considerably and already closely resembles that of pure Ni.

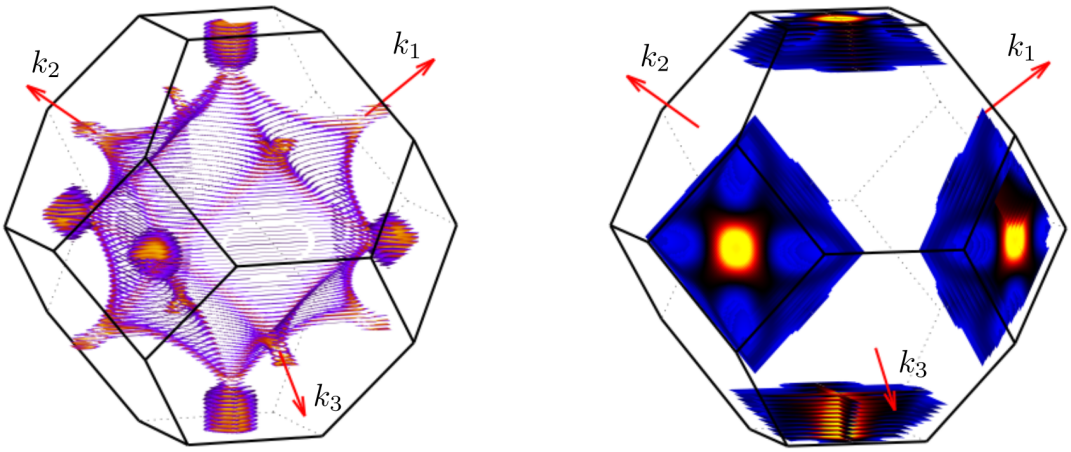

(a) **(b)**

Figure 2.5: (a) Inner, and (b) outer part of the Fermi surface of $Cu_{1-x}Ni_x$ for $x = 0.5$.

Additionally, paraboloid necks have appeared, penetrating the zone boundary at the square faces. In contrast to low Ni content, $Cu_{0.5}Ni_{0.5}$ posses additional well defined (although strongly broadened) Fermi surfaces close to the BZ boundary (see Fig. 2.5 (b)) with the recognizable petal-shape known from Ni.

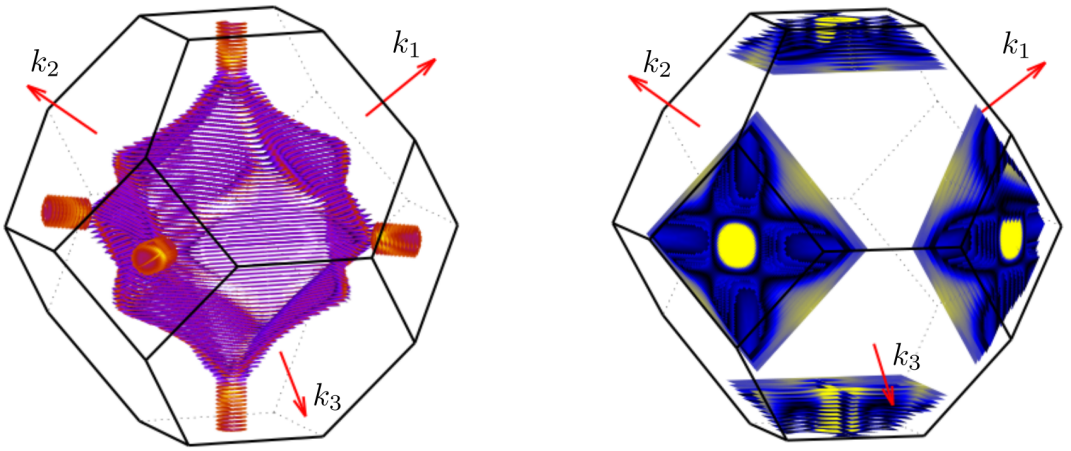

(a) **(b)**

Figure 2.6: (a) Inner, and (b) outer part of the Fermi surface of $Cu_{1-x}Ni_x$ for $x = 0.75$.

As we further approach pure Ni, these features are enhanced. For $x = 0.75$ the central body has shrunk even further, and the necks through the hexagonal faces have disappeared entirely - while the petal-shaped Fermi surfaces are clearly visible.
Thus, we have shown the Fermi surface of $Cu_{1-x}Ni_x$ to gradually transition from one clean end member to the other. Together with the qualitative reproduction of the measured Cu Fermi surface [60], we

conclude our method to be applicable in both clean and substituted systems.

2.2 Vacancy extension

The ability to treat vacancies in the context of substitutional disorder has a wide range of applicability in a number of interesting solid state systems: be it the crystallographic interstitial iron site present in $Fe_{1+y}Te$ and $Fe_{1+y}(Se,Te)$ crystals and its impact on magnetic and superconducting properties [63–65] (for further details see Chap. 4) or electron doping via oxygen deficiencies in $ReFeAsO_{1-\delta}$ [66] (*Re* - rare-earth metals) and $NdFeAsO_{1-\delta}$ [67].
All of these can, in principle, be treated within the LCAO-CPA given a physically meaningful treatment of vacancies as a substituent species. As the MBPP is not capable of dealing with vacancies, a number of quantities that are usually provided by the DFT calculation must be determined independently. An important question is that of the choice of basis functions: while Koepernik *et al* [37] treat such impurities by considering a smooth Gaussian for at least one basis orbital per vacancy site, here, we have chosen a more sophisticated approach. Instead of assuming a somewhat arbitrary basis functions, we adopt the basis functions of the to be substituted species for all angular momenta. In this fashion, we hope to employ basis functions which best suit the underlying environment.
Furthermore, we must deal with other quantities usually provided by the MBPP - the initial angular momentum resolved real space density and pseudopotentials. The former are initially set to zero, however, we allow for charge transfer to these vacancy-occupied sites during the CPA process. This will lead to the generation of Hartree potential contributions from vacancy sites. Trivially, the pseudopotentials and also the partial core potential are set to zero for all vacancies and remain so during the charge self-consistency cycle.

2.2.1 Proof of principle - turning body centered cubic Fe into simple cubic Fe

In order to benchmark the vacancy extension outline above, we compare two systems: we consider body centered cubic (bcc) Fe and compare it to hypothetical simple cubic (sc) Fe with one atoms per unit cell (see Fig. 2.7). The former can also be considered as a sc structure with two atoms per unit cell.

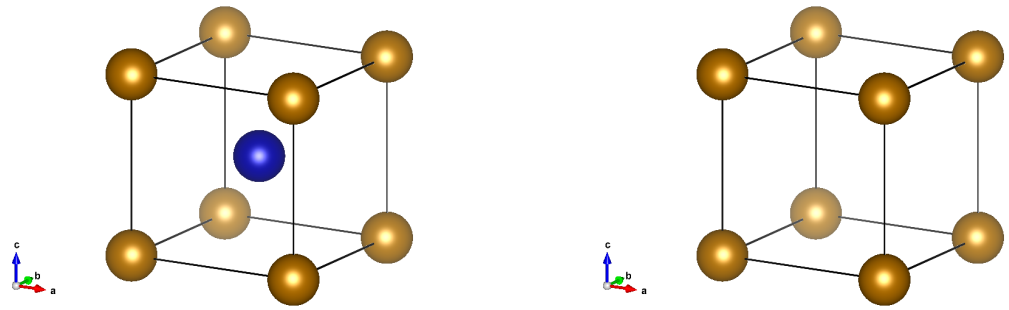

(a) **(b)**

Figure 2.7: Unit cell for (a) bcc Fe, and (b) sc Fe. Blue atom indicates site to be substituted in the following. For both structures the lattice parameter $a = 5.4\,a_0$ was chosen.

The idea now is to perform a substitution of the central atomic site of bcc Fe. In the limit of a complete substitution, i.e., an impurity concentration of $c_{\text{vacancy}} = 1$, we would expect to recover the band structure of sc Fe. For practical reasons, we consider a substituted crystal with a very small but finite iron concentration at the central site, i.e., a vacancy concentration of $c = 0.999$. Further calculational details can be found in App. J.2.

2.2.2 Band structure and density of states

We begin our discussion by first considering the respective clean cases and a comparison of their electronic properties. The resulting band structures along high symmetry lines of the simple cubic Brillouin zone may be found in Figs. 2.8 (a) and 2.8 (b).

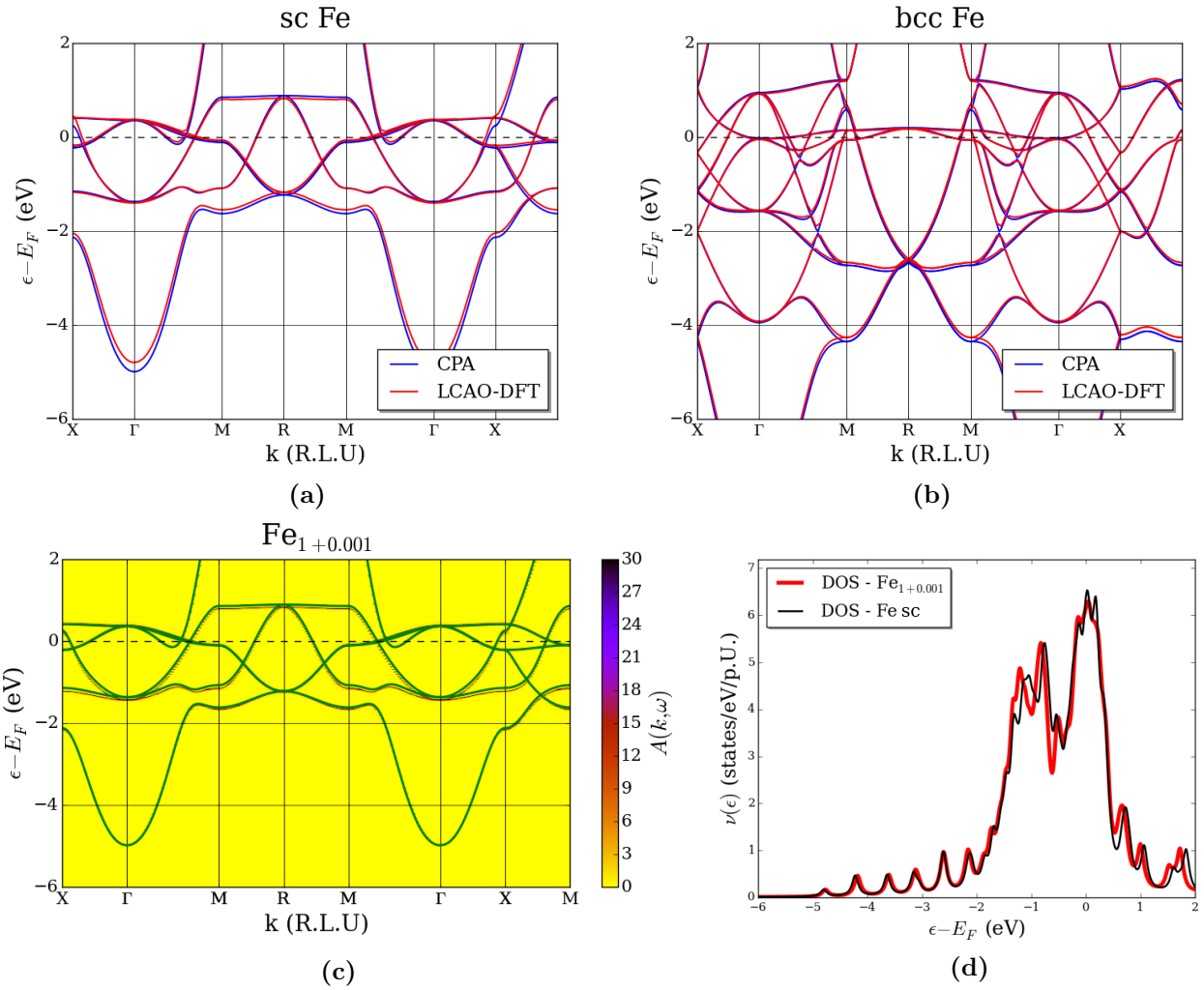

Figure 2.8: Comparison of the clean DFT-LCAO and CPA band structure for (a) sc Fe, and (b) bcc Fe. (c) CPA clean band structure (green) of sc Fe vs. Bloch spectral function (false color) of $Fe_{1+0.001}$. (d) DOS $Fe_{1+0.001}$ vs. sc Fe.

Clearly, these band structures differ substantially from one another. As outlined above, the idea

now is to replace the central atomic site in bcc Fe, which should result in the band structure and DOS of sc Fe. The results of the aforementioned substitution with a concentration of $c_{\text{vacancy}} = 0.999$ are presented in Figs. 2.8 (c) and 2.8 (d).

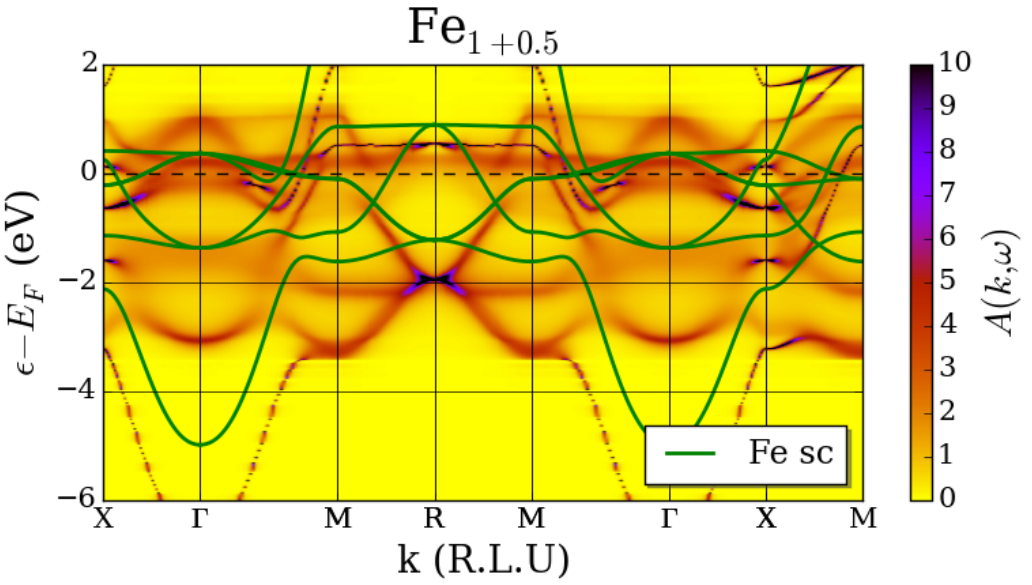

(a)

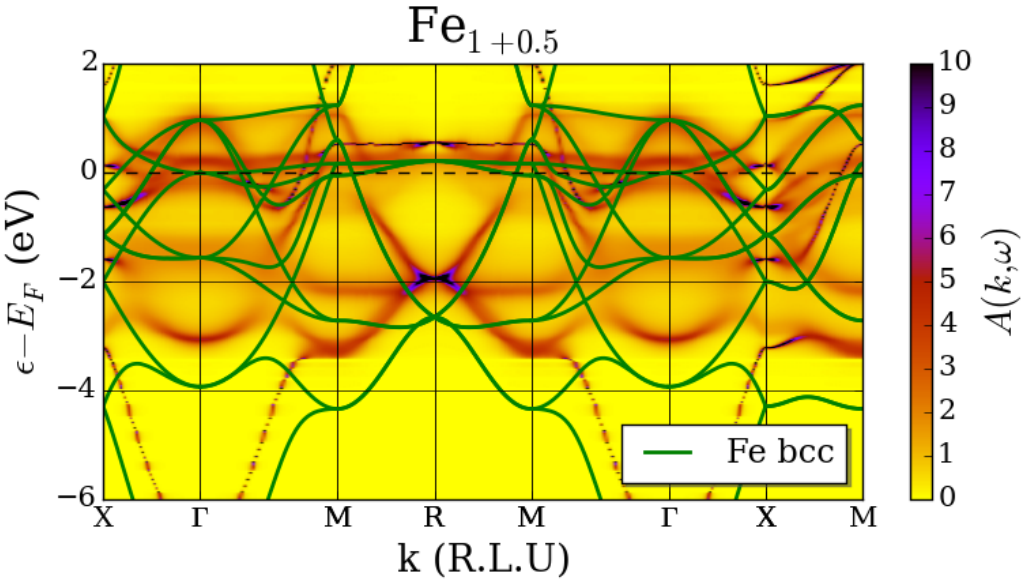

(b)

Figure 2.9: Comparison of the Bloch spectral function of $Fe_{1+0.5}$ and the clean band structures (green lines) of (a) sc Fe, and (b) bcc Fe.

As can be seen in, the vacancy substitution on the second atomic site leads to a band structure almost identical to that of the crystal with one atom per unit cell. Minor discrepancies may be attributed to

the remaining iron on the second atomic site and mainly occur well above and below the Fermi level and may thus be deemed irrelevant.
Similar observations can be made about the DOS presented in Fig. 2.8 (d), which closely coincides with that of the simple cubic structure with only one atom per unit cell. Though there are minor discrepancies, the prominent features are well replicated. From these results we may conclude our approach to the inclusion of vacancies to be not only justified but also successful.
Having shown that our formalism extension works for the extreme limit of a (near) full substitution, we shall now consider an intermediate configuration to validate our approach: a 50% substitution of the second atom in the unit cell. Naively, one could expect a band structure somewhere in between the two clean cases, albeit with a more complex composition. A comparison of the Bloch spectral function of $Fe_{1+0.5}$ to the clean band structures of sc Fe and bcc Fe is given in Fig. 2.9.

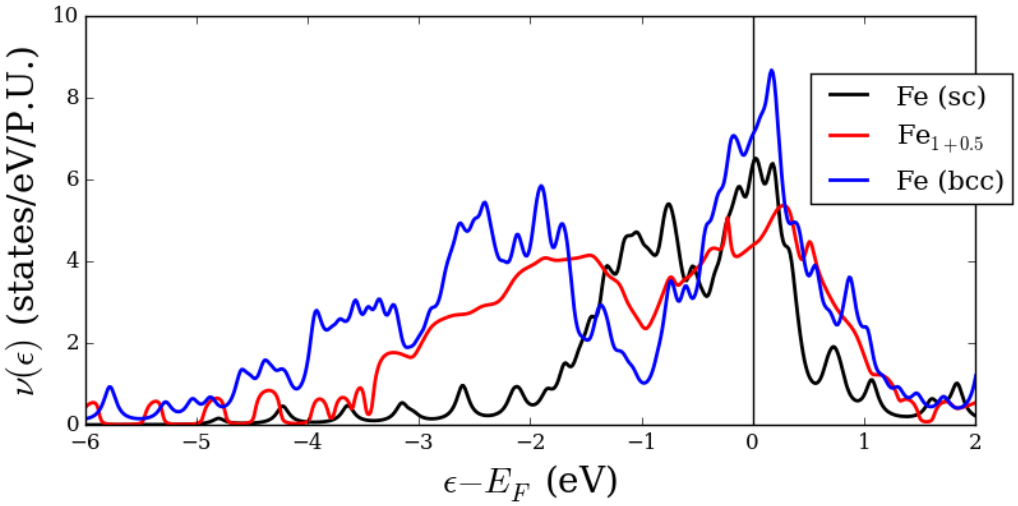

Figure 2.10: Comparison of the DOS of $Fe_{1+0.5}$ (red), and clean sc Fe (black), and clean bcc Fe (blue).

Although the resulting band structure is highly complex for the intermediate system, and shows significant band broadening due to disorder, it appears to fit the naive expectation. This becomes most clear along M-R-M, where the band structure exhibits features of both subsystems.
For our purposes it is more convenient to consider the DOSs for our three systems. A comparison of the three can be found in Fig. 2.10. Here, it is more evident that $F_{1+0.5}$ lies in between sc Fe and bcc Fe. Both sc Fe and bcc Fe exhibit two high-density regions: one around E_F and the other below E_F. However, the latter regions are well separated in energy, and our intermediate system exhibits a "mixed" behavior. The lower high-density region appears to be shifted between the lower regions of the clean cases. Additionally, around E_F, the high-density region of $Fe_{1+0.5}$ shows a peak structure similar to that of bcc Fe, due to the additional states introduced by the second iron atom.
In conclusion, we find our vacancy extension to the CPA formalism to work both in the extreme limit of a (near) complete substitution and the intermediate regime. We shall apply the vacancy substitution in a more complex scenario in Chap. 4, when we study the effect of interstitial iron on the iron chalcogenide $FeSe_{0.5}Te_{0.5}$.

2.3 Spin polarization extension

Magnetism is an interesting quantum mechanical phenomenon in many respects, especially in the context of substitutional disorder in the iron superconductors. In many of the iron-pnictide and iron-chalcogenides superconductivity exists close to antiferromagnetic order [68] and the pairing mechanisms are believed to be closely related to the strong spin fluctuations. Another phenomenon believed to be connected to the magnetic phase is the nematic phase transition commonly encountered in the Fe superconductors [69]. It is essential to have a tool which can treat substitutional disorder in combination with spin polarization, in order to gain greater insight into the nature and origin of superconductivity and nematicity in the iron superconductors. This extension to the basic CPA formalism lends such a tool.
We shall only briefly discuss the theoretical and implementational details of the spin polarization extension here, and refer the interested reader to App. D for a more comprehensive discussion. Including spin introduces an additional degree of freedom and we must discern between quantities which explicitly depend on spin and those who don't. It is common practice to use the pseudopotentials of the unpolarized atoms, i.e., to assume them equal for both spin channels. Additionally, the Hartree potential only depends on the total density $n = n_\uparrow + n_\downarrow$ (Sec. D.1.3). As most quantities are spin-independent, their computation runs analogously to the unpolarized case and we need only account for spin by doubling the dimensionality of said quantities as

$$\hat{\mathcal{O}} = \begin{pmatrix} \hat{\mathcal{O}}_0 & 0 \\ 0 & \hat{\mathcal{O}}_0 \end{pmatrix} \tag{2.3}$$

where $\hat{\mathcal{O}}$ denotes the operator in spin space and $\hat{\mathcal{O}}_0$ is that of the unpolarized case. The only potential explicitly spin-dependent is the XC potential, being a nonlinear functional of the density components $n_\uparrow$ and $n_\downarrow$. As such, it must be calculated separately for each spin component.

2.3.1 $Fe_{1-x}Co_x$ as benchmark

In order to test the inclusion of spin polarization in the CPA, we will investigate the evolution of the magnetic moment of bcc $Fe_{1-x}Co_x$ alloys with substitutional degree x. Details on the crystal structure used for our calculations can be found in Sec. J.3, along with relevant calculational parameters.

2.3.2 Band structure of spin polarized clean Fe and Co

We begin our inquiry into spin polarized $Fe_{1-x}Co_x$ by first studying the pure parent compounds. A comparison of the MBPP-DFT and CPA band structures can be found in Fig. 2.11.

Atomic type P	μ (μ_B) from DFT	μ (μ_B) from CPA
Fe	2.223	2.183
Co	1.709	1.700

Table 2.2: Magnetic moments of Fe and Co calculated by DFT and CPA.

We find that, for Fe, there is good agreement for both spin up and spin down components (see Figs. 2.11 (a) and 2.11 (b)), while there is a minor shift in the spin up component of Co compared to

the MBPP-calculation (see Fig. 2.11 (c)). However, this shift is only relevant well below the Fermi level and should thus not be important in our further calculations.
In Tab. 2.2, a comparison of the magnetic moments μ for Fe and Co as calculated by our MBPP-DFT and CPA method can be found. For both atomic types, the resulting magnetic moments of our CPA calculations are in good agreement, differing only by $0.04\,\mu_B$ and $0.009\,\mu_B$ for Fe and Co, respectively.

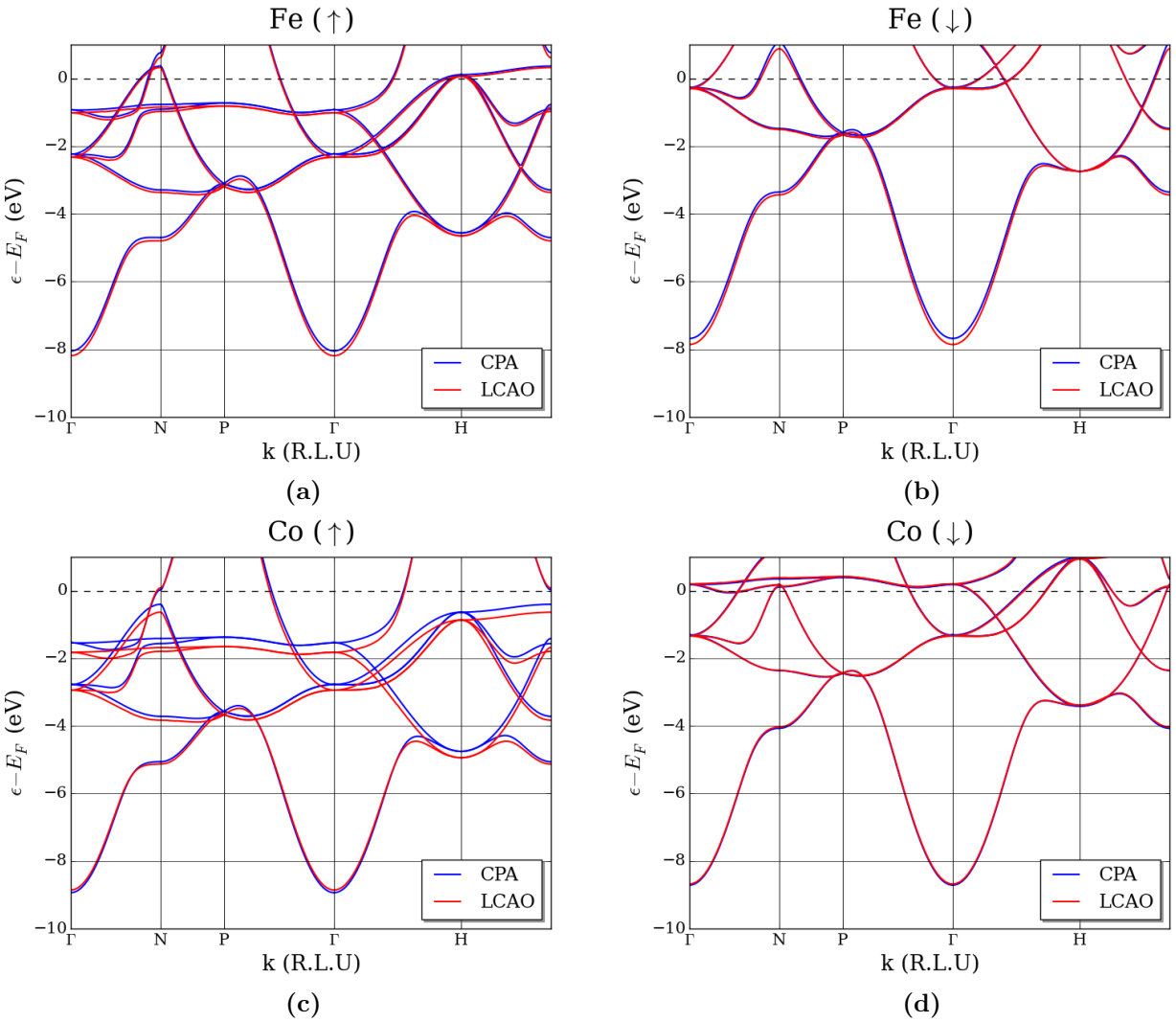

Figure 2.11: Comparison of DFT-LCAO and CPA band structure for (a) Fe spin up (↑), (b) Fe spin down (↓), (c) Co spin up (↑) and (d) Co spin down (↓).

In Fig. 2.12 we present the cross sections of the Fermi surface of bcc Fe for both spin components in the $(\bar{1}10)$ plane. Here, we have marked distinct sections of the Fermi surface with roman numerals to indicate electron and hole surfaces for both majority and minority spins (see Tab. 2.3 for details). For the majority spin (↑) we find a large electron surface (I) around Γ and a major hole surface around H (II). Additionally, around H we find an intermediate (III) and minor (IV) hole pocket. The minority spin (↓) contributes a large hole surface (V) around H and a large electron surface around Γ.

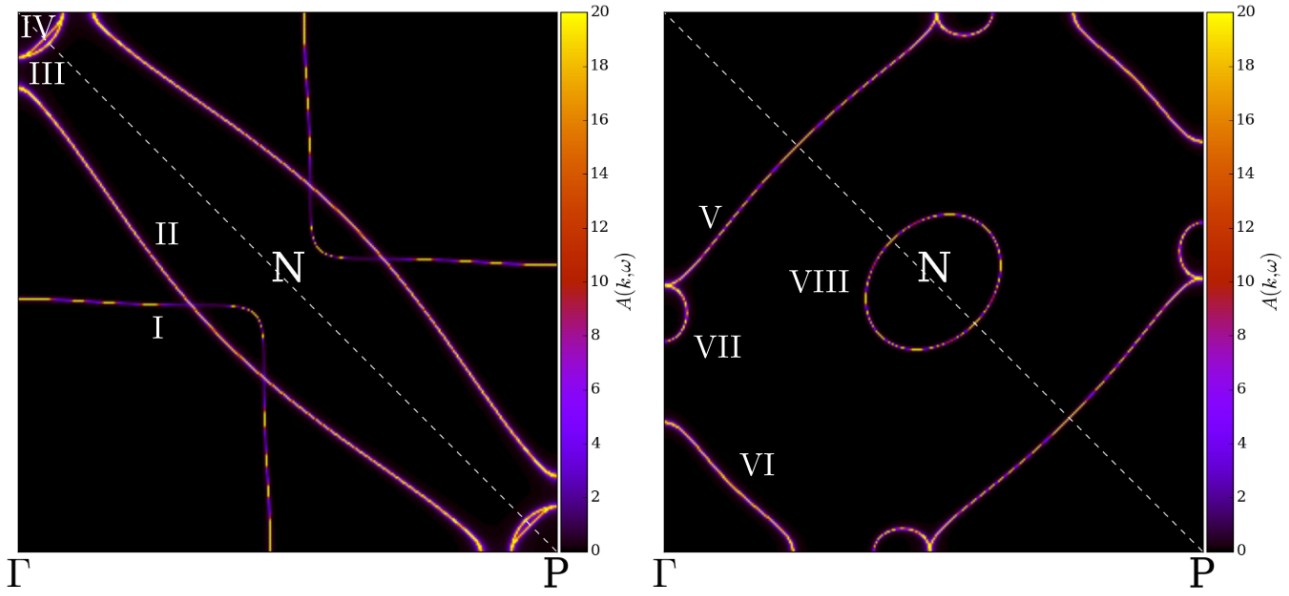

(a) **(b)**

Figure 2.12: Fermi sheet of bcc Fe for (a) spin up, and (b) spin down in the (001) plane. Different Fermi surfaces are marked with roman numerals (see Tab. 2.3). Calculation performed on a 300×300 $\boldsymbol{k}$-mesh.

Centered at N, we find a large hole pocket (VII) and along $\overline{\mathrm{H\Gamma}}$ the Fermi surface shows a ball shaped electron pocket. These results are in good agreement with other calculations on bcc Fe with spin polarization (see Ref. [70]).

	Majority (↑)		Minority (↓)
I.	Large electron surface around Γ	V.	Large hole surface around H
II.	Major hole surface around H	VI.	Large electron surface around Γ
III.	Intermediate hole pocket around H	VII.	Electron pocket along $\overline{\mathrm{H\Gamma}}$
IV.	Minor hole pocket around H	VIII.	Hole pocket around N

Table 2.3: Classification of majority and minority Fermi surfaces of bcc Fe with spin polarization. Table in style of Tab. IV in Ref. [70].

2.3.3 Evolution of the magnetic moment in $Fe_{1-x}Co_x$

Having examined the parent compounds in the last section, we will now turn to spin polarization in the context of chemical substitution: we will study the evolution of the magnetic moment of $Fe_{1-x}Co_x$ with Co-content x. A comparison of our results to those obtained via LCAO-CPA by Koerpernik *et al* [37], via TB-LMTO-CPA by Turek *et al* [71], and experiment can be found in Fig. 2.13. Our calculations were performed with the local-spin-density approximation (LSDA). Clearly, our implementation of

the LCAO-CPA qualitatively reproduces the overall trend, i.e., an initial monotonous increase of the averaged magnetic moment $\langle\mu\rangle_{\mathrm{CPA}}$ with increasing Co content x, followed by a decrease towards pure Co.

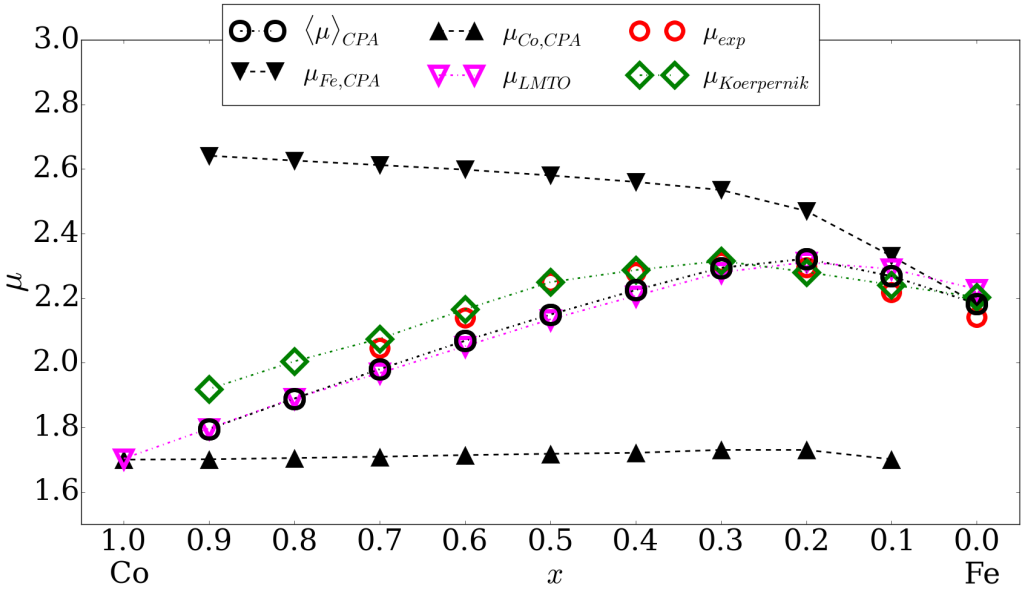

Figure 2.13: Evolution of magnetic moment of $Fe_{1-x}Co_x$ with cobalt content x. Comparison of results from our LCAO-CPA (black), LMTO taken from Ref. [71] (fuchsia), LCAO-CPA from Ref. [37] (green) and experimental values (red, extracted from Ref. [37] Fig. 2).

The averaged magnetic moment is calculated from the local magnetic moments μ_P of the constituent atomic types P according to $\langle\mu\rangle_{\mathrm{CPA}} = \sum_P c_P \mu_P$, where c_P are the respective concentrations.

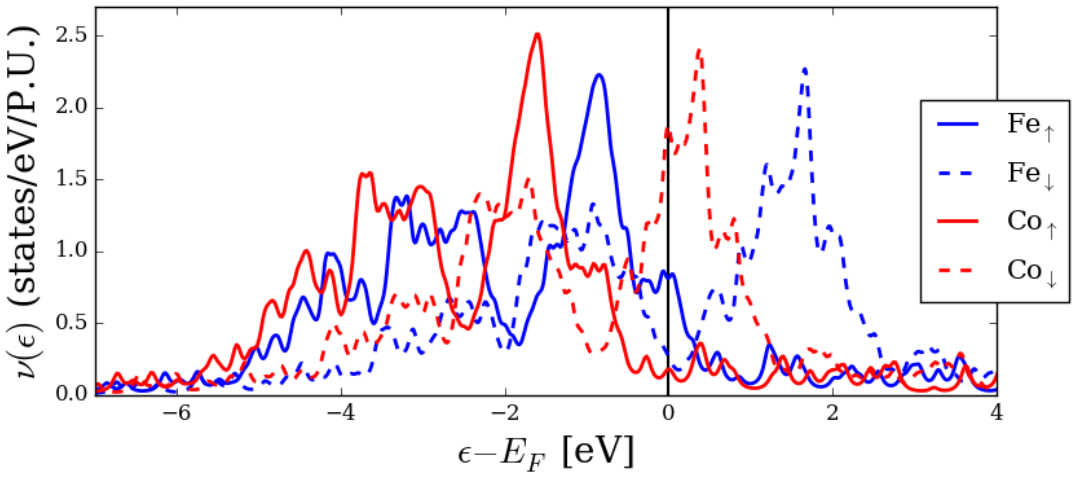

Figure 2.14: Density of states for bcc Fe (blue) and hypothetical bcc Co (red). Solid lines indicate spin up, dashed lines indicate spin down component.

From the local magnetic moments for each atomic species (delivered by the CPA) we observe that while the cobalt moment remains relatively constant, the iron moment is strongly affected by the cobalt content. Cobalt substitution leads to an initial strong enhancement of μ_{Fe}, resulting in a maximum of $\langle\mu\rangle$ around $x = 0.2 - 0.3$, followed by a saturation to $\mu_{\mathrm{Fe}} \sim 2.6\,\mu_B$. While our results are in good agreement with those obtained via TB-LMTO-CPA, they overestimate the averaged magnetic moment on the Fe side ($\mathcal{O}(\Delta\mu) \sim 2\%$) and underestimate it on the Co side ($\mathcal{O}(\Delta\mu) \sim 5\%$) compared to the experimental results and the LCAO-CPA by Ref. [37].

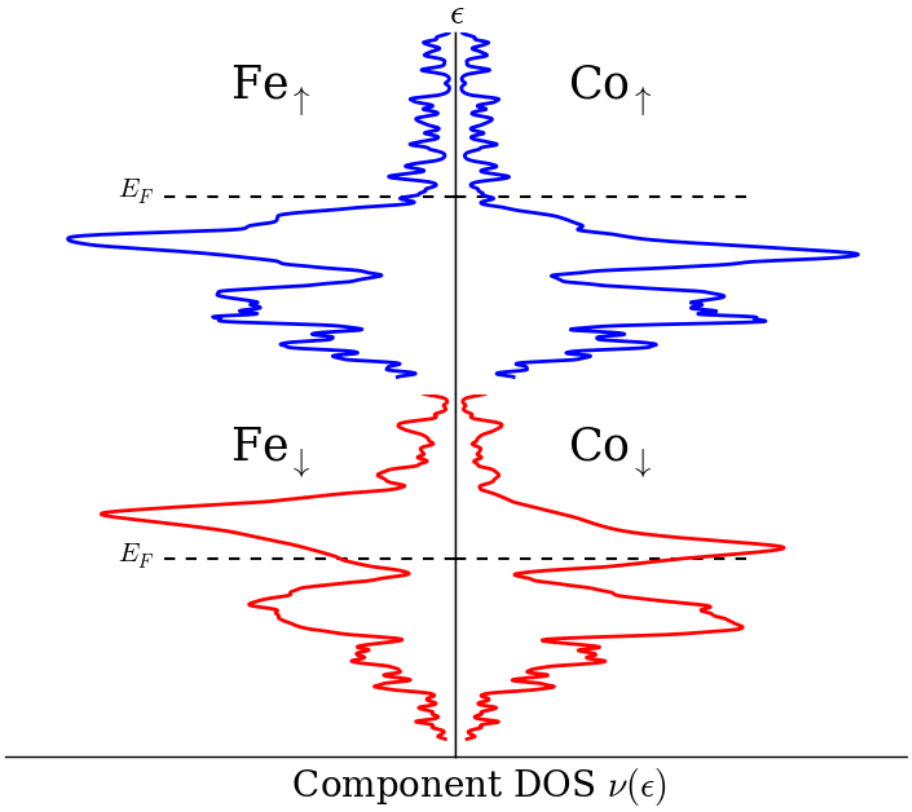

Figure 2.15: Component DOS of $Fe_{0.5}Co_{0.5}$ for Fe spin up (upper left), Co spin up (upper right), Fe spin down (lower left), and Co spin down (lower right).

While charge transfer often influences the local magnetic moments in substituted systems, for $Fe_{1-x}Co_x$ no noticeable net charge transfer between the constituents occurs - due to almost identical electronegativities [72]. This observation is supported by our CPA calculations, in which no perceptible transfer between Fe and Co is found for any concentration x.
From Fig. 2.14 we can tell that the $d_\uparrow$-band in hypothetical bcc Co is fully occupied. Consequently, Co is already a saturated ferromagnet [72], and no considerable increase in majority spin electrons ($\uparrow$) is possible. This is why the Co local magnetic moment in the alloy is largely independent of substitutional content. In contrast, the $d_\uparrow$-band in pure bcc Fe (see Fig. 2.14) is not fully occupied and in principle, majority spin states could be filled with minority spin electrons. These observations are in agreement

with results presented in the literature [72].
While the majority spin states of Fe and Co are fully occupied in the fully polarized alloy (see Fig. 2.15), those of the minority spin are not. According to Ref. [72], this results in a redistribution of minority spin electrons from Fe to Co and a subsequent back donation of Co-↓ electrons to the Fe $d_{\uparrow}$-band due to local charge neutrality conservation. As a result, a net redistribution of electrons from Fe-↓ to Fe-↑ states occurs and the local magnetic moment of Fe is increased.
Overall, we have shown our spin polarization extension to capture the dominant phenomena in clean compounds as well as in a substituted spin polarized system (as reported in the literature).

2.4 Full *ab-initio* spin-orbit coupling extension

Spin-orbit coupling (SOC) arises in solid state systems due to the relativistic interaction of a particles spin with its orbital motion. There are numerous systems which exhibit fascinating physical phenomena due to spin-orbit coupling, such as the quantum spin hall effect (QSHE) [73], surface Dirac cones [19], and Majorana zero modes [20, 74], to name a few. All of these are a consequence of the material's topology and SOC is often a necessary ingredient in the realization of topologically nontrivial systems. Consequently, if we wish to study such systems (as we will in Chap. 3), we must extend our CPA formalism to include SOC.
The full *ab-initio* treatment of spin-orbit coupling is one of the major formalism extensions to the CPA that have been developed in this work. A detailed derivation of the SOC Hamiltonian matrix elements can be found in App. E.

2.4.1 Band structure and Fermi surface of bcc Fe with spin-orbit coupling

We once again turn to bcc Fe as a benchmark for our formalism extensions, this time: spin-orbit coupling.

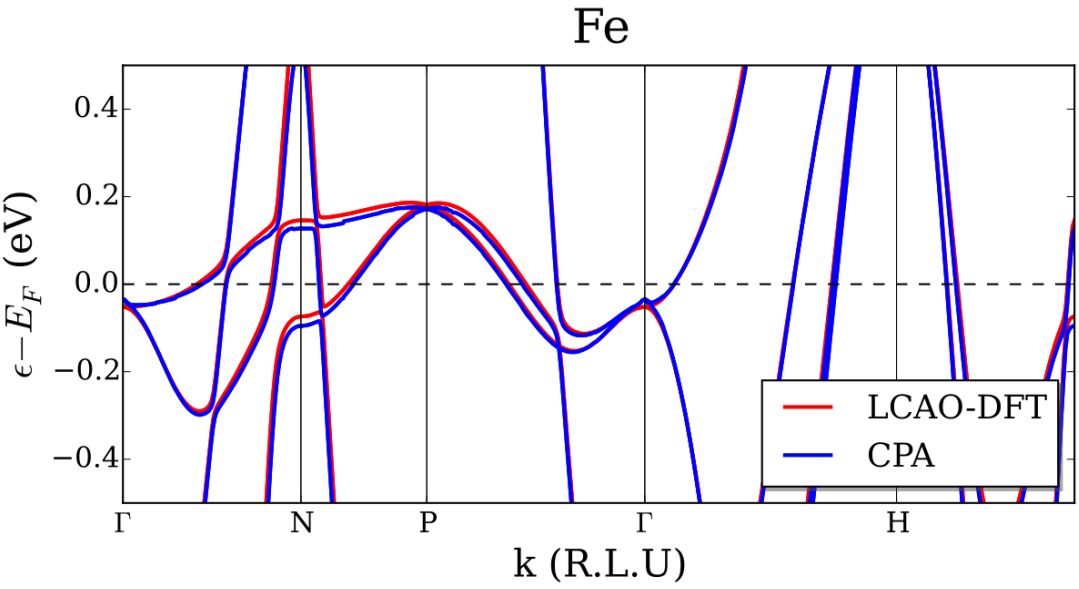

Figure 2.16: Comparison of DFT-LCAO and CPA band structure of Fe with spin orbit coupling.

As a first benchmark we compare the band structures resulting from the CPA and MBPP calculations with SOC in Fig. 2.16, before discussing the effects of SOC in detail.

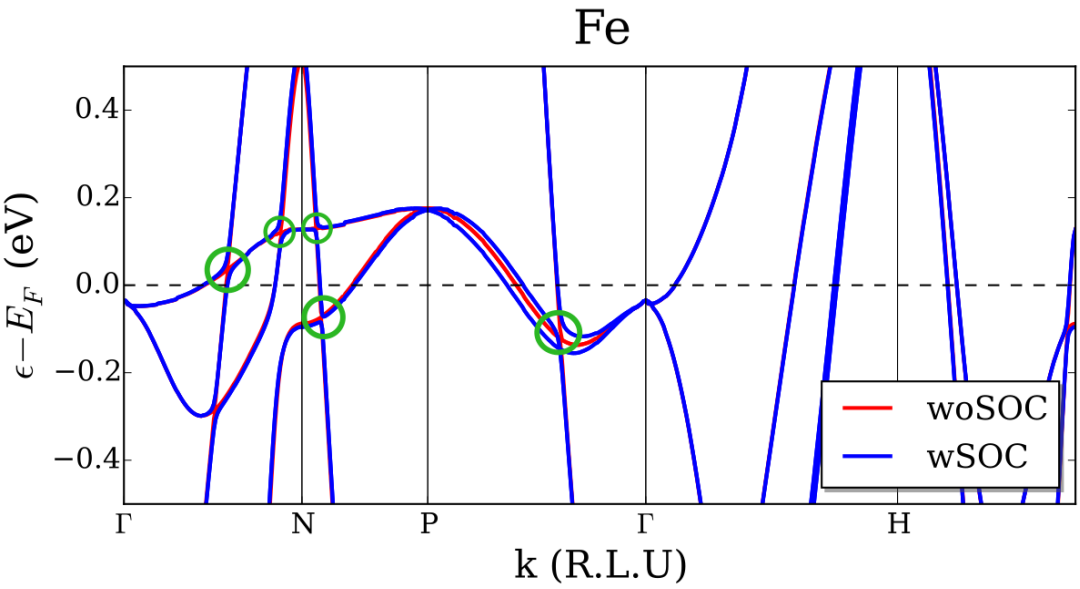

Figure 2.17: Comparison of CPA band structure of bcc Fe with and without SOC. Green circles indicate lifted degeneracies due to SOC.

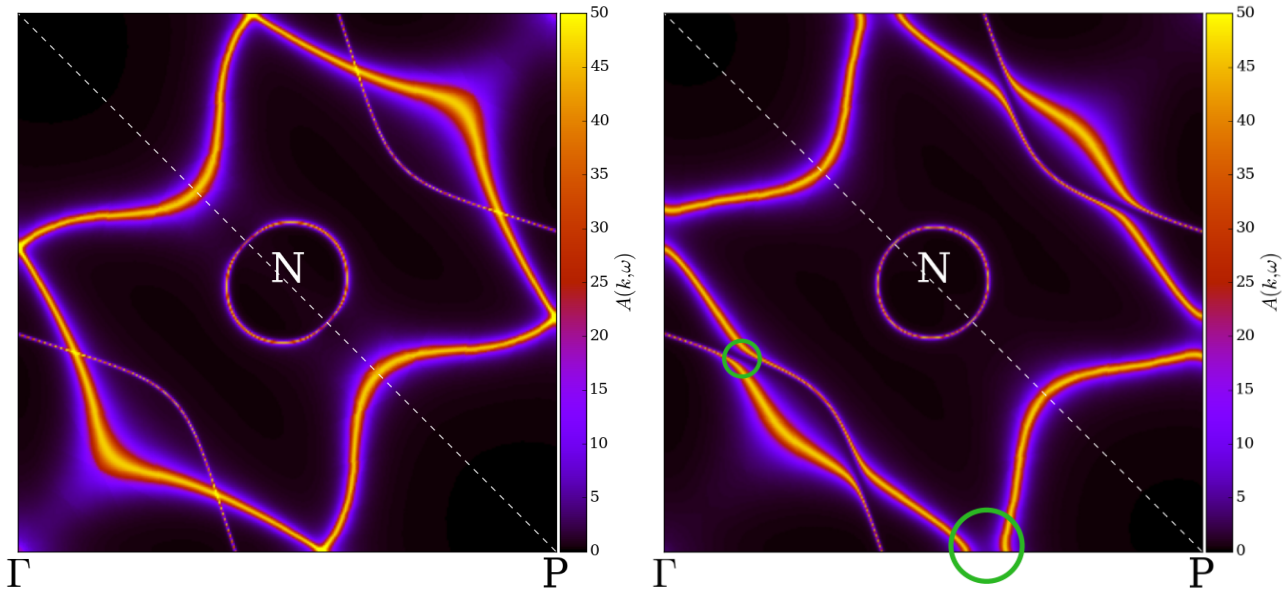

(a) **(b)**

Figure 2.18: Fermi surface cross section in the $(\bar{1}10)$ plane of bcc Fe (a) without, and (b) with spin-orbit coupling calculated on a 300×300 $\boldsymbol{k}$-mesh. Green circles indicate splitting due to SOC

Apart from some minor shifts, the two band structures are qualitatively in good agreement. In order to visualize the effects of SOC, we next compare the CPA band structures with and without SOC. From Fig. 2.17, we can identify a number of effects on the band structure of bcc Fe: along ΓN and NP, we find multiple lifted degeneracies in form of avoided crossings (indicated by green circles). Additionally, along PΓ another lifted degeneracy presents itself where a formerly degenerate band clearly splits into two separate bands.
Although SOC is only a weak effect in bcc Fe, we clearly see the induced band splitting in the comparison of the Fermi surface cross section in the $(\bar{1}10)$ plane of Fe without SOC and with SOC in Figs. 2.18 (a) and 2.18 (b). The band splitting along PΓ (see large green circle in Fig. 2.17) is clearly reproduced in the Fermi surface cross section which shows additional splitting occurs between further Fermi surfaces (see small green circle).
Thus, we have shown our SOC extension to the CPA to work reasonably well for clean systems, reproducing all relevant effects, and we shall apply it in a more complex scenario in Sec. 3.5 when we study the effect of SOC in substituted iron chalcogenides.

3 Chapter 3
Band engineering of Dirac cones in iron chalcogenides

The search for solid state systems hosting topologically protected surface states has drawn significant attention in recent years. Next to topological insulators, another group of interesting systems has emerged in this context: topological superconductors. Due to the fascinating properties of their associated surface states, the Majorana zero modes, they hold great promise for the realization of scalable quantum computers [20, 21, 74–76]. Recent attempts to fabricate such superconductors have concentrated on layered hetero-structures of semi-conductors and conventional superconductors. Aside from the complicated manufacturing process, the relatively low superconducting transition temperature typically found in these compounds is a major drawback. Thus, access to a material with a high T_c, in addition to intrinsic topological superconductivity, is highly desirable.

A promising platform for the single crystal, high-T_c realization of Majorana zero modes is the Fe-based superconductor $FeSe_{1-x}Te_x$: it exhibits superconductivity over a wide range of composition x [77–79], while its transition temperature can be brought up to 30 K via application of external pressure [80] and even above 40 K in monolayer thin films [81]. It exhibits a high tunability of its internal parameters via chemical substitution [82–84], while possessing a simple crystalline structure (see Fig. 3.2). Most notably, $FeSe_{0.5}Te_{0.5}$ was argued to possess a nontrivial band topology characterized by a non zero $\mathbb{Z}_2$ topological invariant [19]. As a consequence, it hosts a surface Dirac cone (SDC) [85] that could lead to the emergence of Majorana zero modes in vortices [19, 83, 86, 87] due to the proximity to bulk superconductivity [88].

Here, we are however presented with a significant obstacle: the aforementioned Dirac cone is located well above the Fermi level, thus rendering it irrelevant with respect to experiments such as surface transport. Furthermore, as suggested by Ref. [22], topological superconductivity is only realized if the SDC crosses E_F. Recently, attempts to circumvent this problem via surface deposition have shown promising results [19]. However, such a strategy inevitably disrupts surface transport, a quantity of great interest in the context of topologically protected surface states. The main goal of this work is to provide an alternative, non-disruptive strategy to lower the SDC towards the Fermi level, all the while preserving the pristine surface and allowing access to undisturbed surface transport: intrinsic doping. The main findings of this chapter were published in Ref. [89].

3.1 A brief introduction to iron-based superconductors

¸ The age of superconductivity began in the year 1911 with a startling observation made by dutch physicist Heike Kamerlingh Onnes: upon cooling mercury below 4.2K its electrical resistivity appeared to have dropped to zero. Although he received the Nobel Prize for his discovery, it took almost 60 years for scientists to explain this phenomenon. In 1957 Bardeen, Cooper and Schrieffer published their famed "Microscopic Theory of Superconductivity" [90], now widely known as *BCS* theory. They were able to ascribe superconductivity to the formation of so called *Cooper-pairs*, a bound state formed by two electrons with opposing momentum and spin, due to an attractive force mediated by the positively-charged ionic lattice. In the presence of an arbitrarily small attractive interaction, the Fermi sea becomes unstable against the formation of these bound states and the system undergoes a phase transition to the energetically favorable BCS ground state, below a transition temperature T_c. Aside from a vanishing resistivity, superconductors exhibit a second unique phenomenon: the Meissner effect. A superconductor presents itself with perfect diamagnetism, expelling an external magnetic field (up to a critical strength) from its bulk.

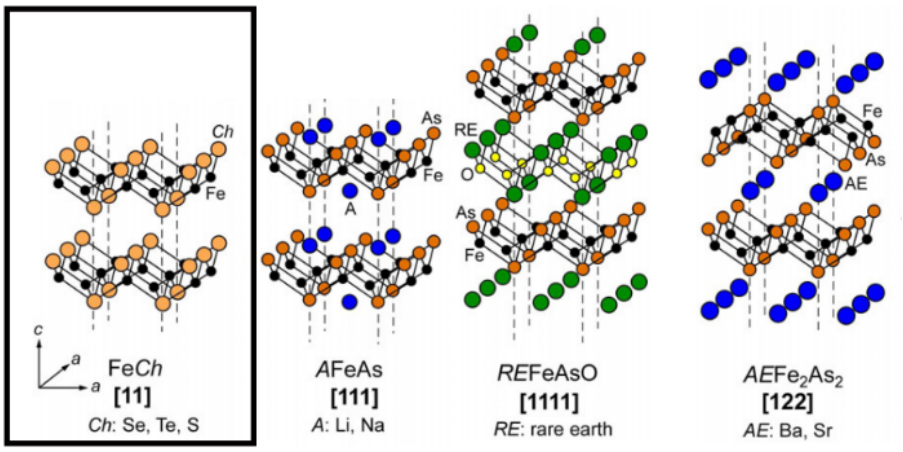

Figure 3.1: Schematic drawing of crystal structures of the Fe-based superconductors (figure reproduced from Ref. [91] in style of Fig. 5.1. in Ref. [6]).

At the time it seemed that superconductivity as a whole had been understood and only occurred at very low transition temperatures until the high-T_c cuprates were discovered by Bednorz and Müller [12] in 1986. The BCS theory failed in describing this new type of superconductor and hence began the search for *unconventional* superconductors with pairing-mechanisms distinct from *conventional* ones. More and more examples of such superconductors have since been found, most notably the cuprates and iron-based superconductors (FeSCs). As local magnetic moments can induce spin flips, they have a Cooper-pair-breaking effect on conventional superconductors [92], and so it was widely assumed that superconductivity could not be realized in a solid containing magnetic elements such as iron, which made it all the more astonishing when superconductivity was discovered in LaOFeP below $\sim$ 4 K [93]. Shortly after, the first high-T_c candidates were identified: $LaFeAsO_{1-x}F_x$ (T_c = 26 K) [7] and $SmO_{1-x}F_xFeAs$ (T_c = 55 K) [94]. Since then, the iron-based superconductors (FeSCs) have attracted enormous attention with strong evidence pointing towards unconventional pairing mechanisms via electron correlation [95, 96], such as spin fluctuations [97, 98] and orbital ordering [99, 100]. Superconductivity has been realized in a wide variety of solid state systems, both bulk and thin films

[83, 101, 102].
In general, the FeSCs may be classified in terms of families according to their composition. For this brief introduction to the topic, we will focus on the four prominent families depicted in Fig. 3.1 (reproduced from Ref. [91]). All of these families have one trait in common: a layered structure composed of iron atoms that form a planar square lattice surrounded by either chalcogen (Ch) or pnictogen (Pn) atoms [103]. What they differ on is the existence and composition of an additional spacer layer in between the FeCh/Pn planes. In the 111-family this layer is made up of a single atom of either Li or Na, while the 122-family exhibits one alkali or alkaline earth atom per two Fe atoms. A more complicated structure is presented by the 1111-family, which exhibits an alternating pattern of rare earth and oxygen planes. The only family not to exhibit such a spacer layer is the 11-family. In this chapter, we shall concentrate on three of its members - FeSe, FeTe, and the substituted compound $FeSe_{1-x}Te_x$.

3.2 The iron chalcogenides - FeSe, FeTe, Fe(Se,Te)

The iron chalcogenides are part of the 11-family, consisting of an iron layer forming a planar square lattice surrounded by chalcogens, which site alternately above and below the plane (see Fig. 3.2 (a)). These layers periodically extend along the c-axis as in Fig. 3.2 (b), primarily bound by van der Waals forces. Here, we will mainly focus on FeSe, FeTe, and Fe(Se,Te) - the main goal of our inquiries. An extensive and comprehensive review of FeSe can be found in Ref. [104].

FeSe

Although FeSe possesses the simplest structure of the FeSCs, it exhibits rich physics and allows for high tunability of superconductivity. Application of high external pressure can raise the transition temperature from $T_c \sim 8.7$ K up to 36.7 K [15], and even $T_c > 65$ K can be reach in single layer FeSe deposited onto $SrTiO_3$ [13, 14].

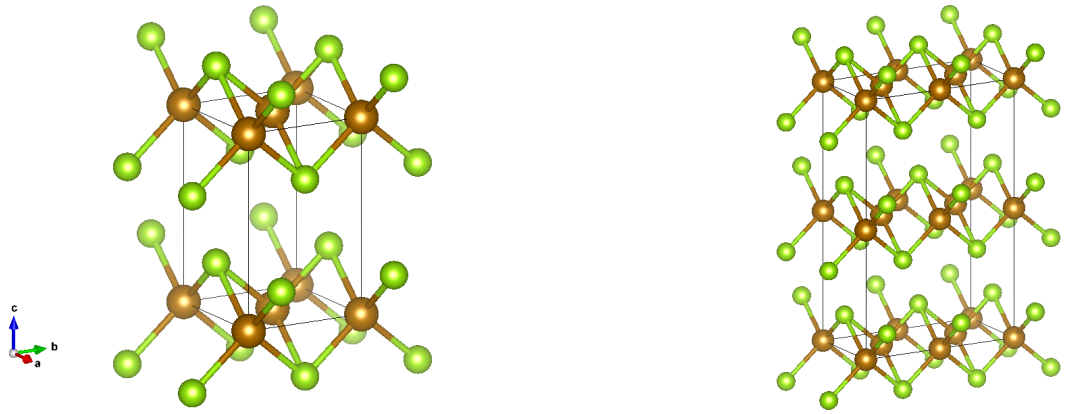

(a) **(b)**

Figure 3.2: Crystal structure of FeSe/FeTe for (a) a single unit cell (b) layered unit cells. Green balls denote Fe-sites and brown balls symbolize Se/Te-sites.

While spin fluctuations and the suppression of spin-density wave (SDW) order is considered to be the dominant superconducting pairing mechanism in the FeSCs, this cannot be the case for FeSe which

lacks long-range magnetic order. Rather, it has been suggested that superconductivity is linked both to the nematic phase transition from tetragonal $P4/nmm$ to orthorombic $Cmma$ close to $T_s = 90$K, and orbitally selective pairing [105, 106]. As high quality single crystals can easily be grown via chemical vapor transport [107, 108], it is an ideal candidate for detailed experimental analysis.

FeTe

In contrast to FeSe, our second end member FeTe exhibits no superconducting phase [109] but a a stripe magnetic phase [110]. Among the iron-chalcogenides it was shown to have the strongest correlations [111]. Some additional remarks on FeTe are in order for our CPA calculations: firstly, grown samples always exhibit an interstitial Fe-site, i.e., have stoichiometric composition $\mathrm{Fe}_{1+y}\mathrm{Te}$ with occupational degree y. This iron interstitial might play an important role in the first-order structural phase transitions from tetragonal to orthorombic at $\mathrm{T}_s \sim 80$ K, and the associated magnetic phase transitions [112, 113]. In our calculations we ignore this excess Fe and assume a tetragonal crystal structure without magnetism.

Fe(Se,Te)

Our target system in this chapter will be $\mathrm{FeSe}_{1-x}\mathrm{Te}_x$, for which similar observations as in FeSe have been made: the moderate $\mathrm{T}_c \sim 14.5$ K can be brought up 30 K under pressure [114], and even 40 K [81] in thin films. Most interestingly, however, for $x = 0.5$ Fe(Se,Te) is proposed to belong to a rare class of materials: the intrinsic topological superconductors. In this context, topological superconductivity refers to the superconducting surface states, while in the bulk it remains trivial. The nontrivial topology of its band structure manifests itself in the emergence of a spin-helical surface Dirac cone (SDC) inside a spin-orbit-induced gap and centered around Γ of the BZ on (001) surfaces. [19, 85]. Due to proximity to the bulk superconducting electrons, the Dirac cone can host Majorana zero modes at the core of superconducting vortices [83, 86, 87, 115]. These exotic states are characterized by non-Abelian quantum statistics and constitute their own antiparticles [116–118]. They are promising candidates for the realization of fault-tolerant and scalable quantum computers [20, 21, 74].
It should be noted that grown Fe(Se,Te) samples exhibit an interstitial site occupied by excess iron atoms which has significant effects on the superconducting and magnetic properties of the system [63–65]. Although superconductivity is suppressed for higher occupational content, it may persist at lower concentrations [64] and excess iron can even be removed via annealing [119]. This is vital to our search for Majorana zero modes, as superconductivity is a mandatory prerequisite. In this chapter, we shall neglect the interstitial iron site and shall study its effects in detail in Chap. 4. So far, experimental evidence of these states in solid state systems has been found in spin-orbit coupling semiconductor nanowires [120, 121], ferromagnetic atomic chains [122], and topological insulators [123]. All these systems, however, come with major drawbacks: proximity to conventional s-wave superconductors is required, and they must be operated at very low temperatures. Here, Fe(Se,Te) could present us with the first realization of Majorana zero modes with a high T_c.
However, the position of the SDC well above the Fermi level in Fe(Se,Te) is an obstacle to experiments such as transport measurements - which are of great interest in the context of nontrivial surface states. It will be the main goal of this work to establish a strategy to make the SDC accessible to such experiments by theoretically designing a crystal of either the form $\mathrm{Fe}_{1-y}TM_y\mathrm{Se}_{0.5}\mathrm{Te}_{0.5}$ or $\mathrm{FeSe}_{1-x-y}\mathrm{Te}_x Ha_y$, where TM and Ha denote a generic substitution of concentration y with transition metals and halogens, respectively.

3.3 The origin of the surface Dirac cone in Fe(Se,Te)

We begin our discussion of the emergence of a surface Dirac cone by first postulating the necessary ingredients for its realization:

1. A band inversion in the ΓZ line.
2. A spin-orbit coupling gap.
3. A nonzero topological invariant $\mathbb{Z}_2$.

In the following discussion we will show these conditions to be fulfilled in Fe(Se,Te), where we closely follow the argumentation presented in Ref. [19]. As a starting point for our discussion of the emergence of a SDC in $FeSe_{1-x}Te_x$ we choose to first study the system under consideration without spin-orbit coupling (SOC).
For a substitutional degree of $x = 0.5$, we are presented with a band structure along ΓZ as schematically depicted in the left half of Fig. 3.3. Close to the Fermi level, we find three distinct bands: a highly dispersive nondegenerate band D (blue line) with p_z- and d_{xy}-character, a "flat" nondegenerate band F_1 (green line) with d_{xy}-character and a two-fold degenerate band F_2 (red line) with d_{yz}/d_{xz}-character. We will restrict ourselves to a qualitative discussion here and focus on the effect of Te substitution and the source of the band structure characteristics in greater detail in Sec. 3.5.

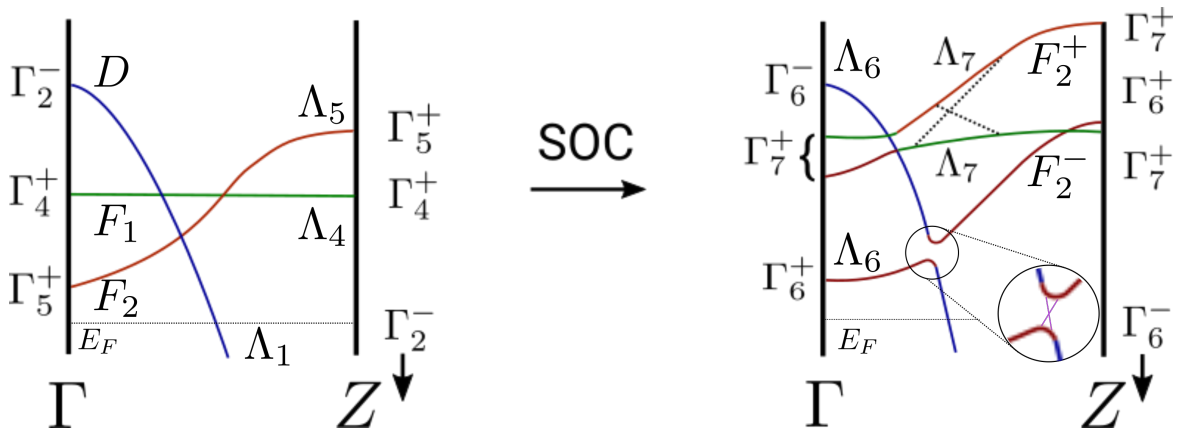

Figure 3.3: Schematic band structure of $FeSe_{0.5}Te_{0.5}$ without SOC (left), and with SOC (right). Figurative states at Γ and Z are labeled according to their irreducible representations $\Gamma_n^{\pm}$, and Λ_n denote small representations along ΓZ. Dashed line indicates Fermi level.

Without spin-orbit coupling (SOC), tetragonal Fe(Se,Te) has point group symmetry D_{4h}. In general, an arbitrary $\boldsymbol{k}$-point will have a lower symmetry, transforming as the *small group* of $\boldsymbol{k}$. However, certain high symmetry points retain the full D_{4h} symmetry. This is the case for both Γ and Z, and we can label the states of the aforementioned bands at these special points according to the irreducible representations (IRs) of D_{4h}, which we denote as $\Gamma_n^{\pm}$, following Ref. [19]. Even and odd parity are indicated by $+$ and $-$, respectively. For a comprehensive introduction to group and representation theory in the context of condensed matter physics, we refer the interested reader to Ref. [124].
Here, we only present the character table for symmetry point group D_4 (see Tab. 3.1) along with the

corresponding IRs and basis functions. The $C_n^{(\prime/\prime\prime)}$ signify n-fold rotational axes. The character table for D_{4h} is obtained via the direct product $D_4 \otimes (E, i)$, where E is the unit and i the inversion element. The inclusion of inversion symmetry will double the number of IRs, due to parity.

basis functions		IR	E	$C_2 = C_4^2$	$2C_4$	$2C_2'$	$2C_2''$
x^2+y^2, z^2		Γ_1	1	1	1	1	1
	R_z, z^2	Γ_2	1	1	1	-1	-1
x^2-y^2		Γ_3	1	1	-1	1	-1
xy		Γ_4	1	1	-1	-1	1
(xz, yz)	(x, y), (R_x, R_y)	Γ_5	2	-2	0	0	0

Table 3.1: Character table for symmetry point group D_4. Character table for D_{4h} can be obtained from the direct product $D_4 \otimes (E, i)$ with unit element E and inversion element i.

According to Ref. [19], with inversion symmetry present in Fe(Se,Te), we can combine orbitals into bonding and anti bonding states with well defined parity. Since Fe only contributes via d-orbitals to the aforementioned bands, and the chalcogens Se and Te only via p-orbitals, we can confine ourselves to states

$$\left|D_\alpha^\pm\right\rangle = \frac{1}{\sqrt{2}}\left(\left|\mathrm{Fe}_\alpha\right\rangle \pm \left|\mathrm{Fe'}_\alpha\right\rangle\right) \qquad \alpha \in \{z^2, xz, yz, xy, x^2-y^2\} \tag{3.1}$$

$$\left|P_\beta^\pm\right\rangle = \frac{1}{\sqrt{2}}\left(\left|\mathrm{X}_\beta\right\rangle \mp \left|\mathrm{X'}_\beta\right\rangle\right) \qquad \beta \in \{x, y, z\}, \tag{3.2}$$

where X $\in$ {Se,Te}. Following the convention chosen in Ref. [19], the (x, y) axes are rotated 45° with respect to the crystallographic axes. The difference in sign of Eq. (3.2) stems from the odd parity of p-states. In Tab. 3.2 we present the IRs connected to these combined states both at Γ and Z, respectively, and along the high symmetry line ΓZ. From this we can tell that the states of band D at Γ and Z transform as Γ_2^-, since it is comprised of anti bonding P_z and D_{xy}. In general, as we move from one high symmetry point to another, the symmetry of the involved $\boldsymbol{k}$-points is reduced.

$\left\|D_\alpha\right\rangle$	parity	z^2	xz/yz	xy	x^2-y^2	$\left\|P_\beta\right\rangle$	parity	x/y	z
D_{4h}	+	Γ_1^+	Γ_5^+	Γ_4^+	Γ_3^+	D_{4h}	+	Γ_5^+	Γ_1^+
	-	Γ_3^-	Γ_5^-	Γ_2^-	Γ_1^-		-	Γ_5^-	Γ_2^-
C_{4v}	+	Λ_1	Λ_5	Λ_4	Λ_3	C_{4v}	+	Λ_5	Λ_1
	-	Λ_4	Λ_5	Λ_1	Λ_2		-	Λ_5	Λ_1

Table 3.2: Combined states $\left|D_\alpha\right\rangle$ (left) and $\left|P_\beta\right\rangle$ (right) with corresponding irreducible representations $\Gamma_n^\pm$ at Γ/Z, and Λ_n along the ΓZ line. Table in style of Tab. II in Ref. [19].

In our case, we start from the Γ point with symmetry group D_{4h}, move along a path Λ with symmetry group C_{4v}, and end up at Z - which again has D_{4h}. Due to the reduced symmetry along Λ, the states

which make up the bands transform according to different IRs - the *small* representations Λ_n - as opposed to those at the high symmetry points. Clearly, all relevant bands transform as distinct small representations ($D \to \Lambda_1$, $F_1 \to \Lambda_4$, and $F_2 \to \Lambda_5$) and, consequently, no mixing and no avoided crossings occur.
A comparison of the schematic band structure in Fig. 3.3 and the band structure of FeSe in Fig. 3.4 (a) (which we shall discuss in greater detail in the following section) mainly yields a shift of D towards lower energies due to Te-substitution (see Sec. 3.5). As a result, the SOC gap will open closer to E_F, as we shall explain below. For both FeSe and $FeSe_{0.5}Te_{0.5}$ we can identify a band inversion, i.e., an inversion of the order of the odd parity state of D and the even parity state of F_2 as we move from Γ to Z. Thus, one of the postulated conditions for a SDC is fulfilled.
Up to now, we have neglected the considerable SOC in Fe(Se,Te) introduced mainly via the chalcogens. If we now include SOC, we will need to consider spin degrees of freedom which leads us to the *double group* of D_{4h} (see Ref. [124]). In addition to the IRs of D_{4h} the double group contains additional IRs due to the rotational properties of half-integer angular momenta. These new representations are at least two-fold degenerate (Kramer's Theorem [125]). We shall not present the character table for the double group or the concrete IRs here, but will only comment qualitatively on the impact of SOC on the IRs of the relevant states and bands.
Without SOC, the highest state at the Γ point (belonging to band D) transformed according to the irreducible representation Γ_2^-, while the states connected to band F_1 and the doubly degenerate F_2 transformed according to Γ_4^+ and Γ_5^+, respectively. The inclusion of SOC has a significant effect on the bands in question (see right panel of Fig. 3.3): first and foremost, the twofold degeneracy of Γ_5^+ states is lifted, now transforming as the IRs Γ_6^+ and Γ_7^+ of the double group. Due to the lifted degeneracy, we label these new bands as F_2^+ and F_2^-. Secondly, band F_1 (with IR Γ_4^+ in D_{4h}) now transforms as Γ_7^+ at Γ (and Z), and due to the identical small representation Λ_7 of bands F_1 and F_2^-, we can expect strong mixing along the high symmetry line (see Fig. 3.3).
Finally, the odd parity state Γ_2^- of band D now transforms as Γ_6^-. Thus, at the former crossing point we find states associated with the same small representation Λ_6, the consequence of which is an avoided crossing, i.e., a direct SOC gap as required for our surface Dirac cone.
As argued in Ref. [19], given the SOC gap, a nonzero topological $\mathbb{Z}_2$ invariant [126, 127] can be defined via a "curved chemical potential" and calculated from the parity criterion: from the product of parities of the occupied states at the time-reversal-invariant momenta (TRIM) $\mathbb{Z}_2$ is found to be 1. Such a nonzero invariant implies a topological phase for $FeSe_{0.5}Te_{0.5}$, which is necessary for the possibility to host nontrivial surface states. The generation of these topological surface states is similar to that in 3D strong topological insulators [126], however, for metallic Fe(Se,Te), the surface states necessarily overlap with bulk states.
According to the arguments and model calculations presented in Ref. [22], in order to realize a topological superconducting phase in which Majorana zero modes can be trapped at the ends of magnetic vortex lines, the Fermi level is required to cross the surface Dirac cone. This is in general not the case for Fe(Se,Te) and we shall address this issue in Sec. 3.7. It should be noted here, that there is some debate as to the position of band D, which is not seen in angle-resolved photoemission spectroscopy (ARPES) measurements [128] and, consequently, the band inversion needed for the SDC is in question. These measurements suggest band D to be situated well above F_2, an issue that might be resolved by our inquiries in Sec. 3.7.2.
Having *qualitatively* reasoned for the emergence of a SDC in Fe(Se,Te), we will now take a step back and have a closer look at the parent compound FeSe and its band structure, in order to gain a more *quantitative* understanding of the effects of Te substitution.

3.4 Band structure and Fermi surface of FeSe

The band structure of FeSe has been studied in great detail by ARPES measurements and we shall give a brief overview of its main features here, closely relating to Ref. [19]. In the DFT and CPA band structure calculations presented below, we have neglected SOC for the time being, but will include it in our CPA calculations presented in Sec. 3.7.2. Looking at Figs. 3.4 (a) and 3.4 (b), we find three hole like bands at the Γ point, where all three valance band tops are unoccupied. These bands are formed from Fe-d_{xz}, -d_{yz} (labeled α, β in Fig. 3.4 (b)), and -d_{xy} orbitals (labelled γ), respectively. They form the well known hole pockets of the Fermi surface around Γ, as determined from our CPA calculation in Fig. 3.5 (b). Experimentally, only two of these are detected by ARPES measurements [129–132].

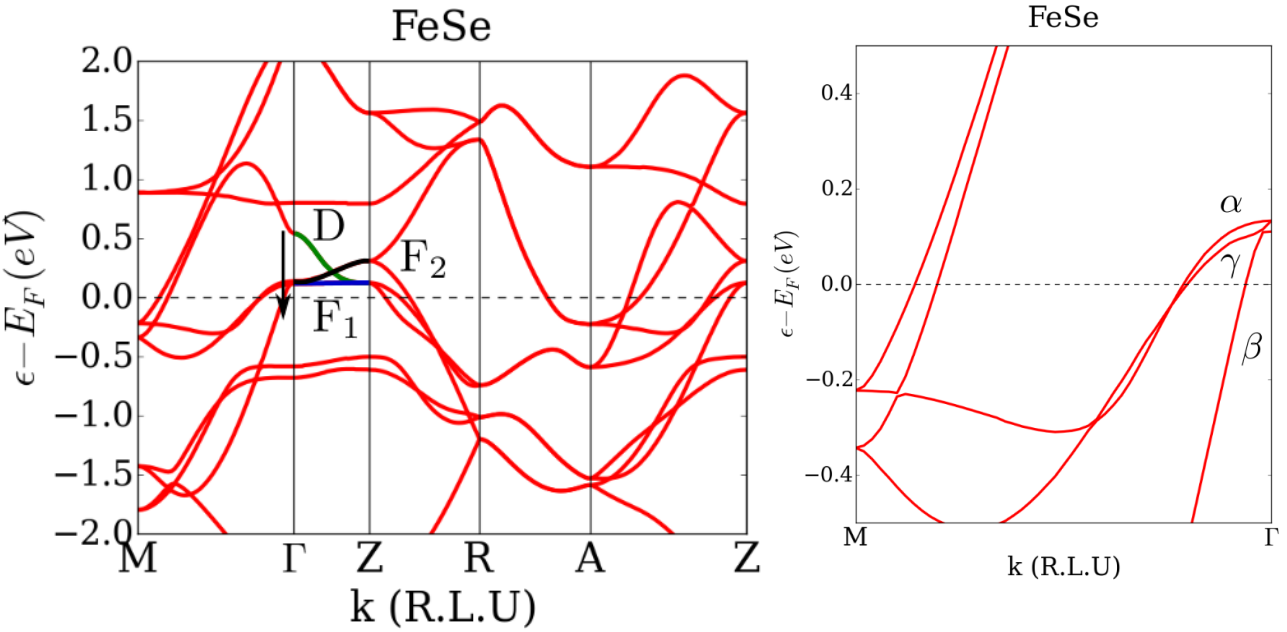

Figure 3.4: (a) DFT band structure (red lines) of FeSe with lattice parameters $a = 3.7688$Å, $c = 5.520$Å and $z = 0.2668$. Green line highlights band D, blue line highlights nondegenerate band F_1, and black line highlights twofold degenerate band F_2. Arrow indicates effect of Te-substitution. (b) The band structure along MΓ with hole-like bands α, β, and γ.

This is a common short coming of most electronic structure calculations when it comes to FeSe and can be attributed to strong electron-electron correlations [133–135] which are insufficiently captured by these methods. These correlations typically lead to relatively large renormalization factors of ~ 3.5 for α and β and even ~ 9 for γ, and band-dependent energy shifts (see Ref. [132]). Most notably, γ is situated ~ 50 meV below the Fermi level in experiments and consequently does not contribute to the Fermi surface. Here, it is crucial to note that this short-coming of the electronic structure methods here applied has no negative influence on the emergence of the SDC and our inquiry. As is clear from our discussion in Sec. 3.3, the hole band γ is not involved in the formation of the SOC gap and hence irrelevant to the SDC.

Apart from the three hole pockets, the Fermi surface exhibits two electron pockets around M which take on the form of crossed ellipses. These can clearly be observed in the cross section of the Fermi surface at $k_z = 0$ in Fig. 3.5 (b). Additionally, we have depicted the atomic type and angular momentum decomposed contributions to the Fermi surface in Fig. 3.6. Clearly, the largest contributions stem from Fe $3d$-orbitals with only minor contributions by Se p_z.

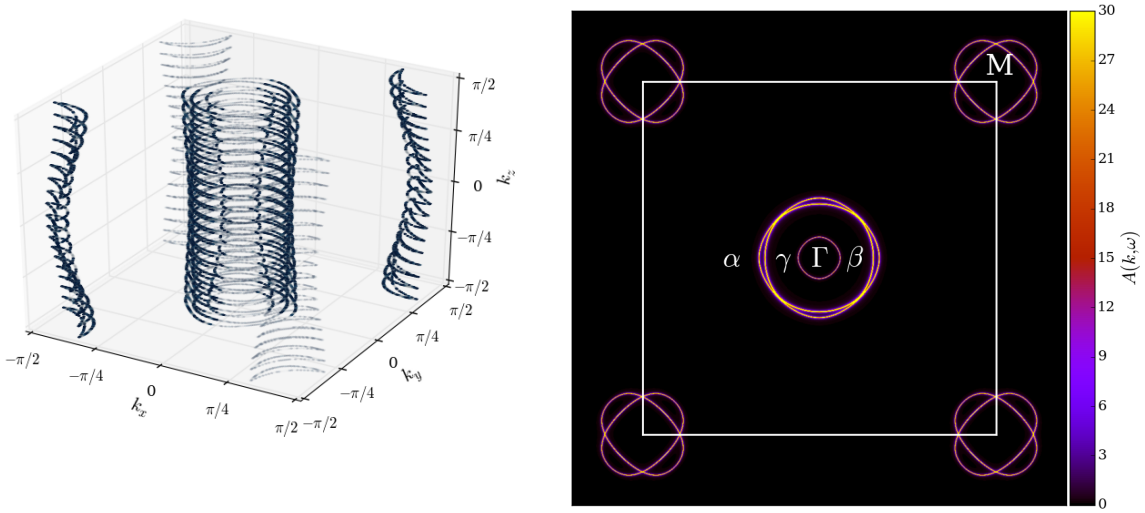

(a) **(b)**

Figure 3.5: (a) Fermi surface of FeSe ($100 \times 100 \times 10$ $\boldsymbol{k}$-mesh grid), where transparency for certain sections has been increased for better visibility. (b) Fermi surface sheet in the (k_x, k_y)-plane at $k_z = 0$ (300×300 $\boldsymbol{k}$-mesh grid) where white lines indicate boundaries of 1. BZ and high symmetry points Γ and M and hole bands α, β, and γ are labeled.

Above the valence band top we find a gap of $\sim$ 0.5eV to the next state belonging to the Γ_2^- representation, a mixture of Fe-d_{xy} and chalcogen p_z-orbitals. As we are interested in the possible realization of a SDC within the SOC gap, we will now restrict ourselves to the discussion of the ΓZ-line which contains the participating bands (see Sec. 3.3). Similar to the situation in Fe(Se,Te), along the ΓZ line, the band connected to Γ_2^- (labeled D in Fig. 3.4 (a)) exhibits the strongest dispersion of the three bands closest to the Fermi level. Compared to Fe(Se,Te), however, it is situated even further above E_F. The relatively small dispersivity of bands F_1 and F_2 close to the Fermi level along ΓZ reflects the predominant *intra*layer hopping, while *inter*layer hopping is strongly reduced. This makes FeSe rather two- than three-dimensional, most commonly attributed to the limited spatial orbital extent of the Se-p_z-orbitals, giving rise to small orbital overlap and interlayer hybridization [19].
As we have discussed in Sec. 3.3, the SOC gap will open at the crossing point of D and F_2 which for FeSe resides well above the Fermi level. However, for a topological superconducting phase, the SDC must cross E_F ([22]), and so we must lower the crossing point. In Sec. 3.5, we will use our CPA method to show how this can be achieved via chalcogen, i.e., Te-substitution. We will then include SOC in our calculations in Sec. 3.6 to show the formation of the SOC gap.
Before we turn to applying our CPA method in this context of substitutional disorder, we will first study the dependence of the band structure of FeSe, especially of the bands deemed relevant, on the specific lattice parameters of our system.

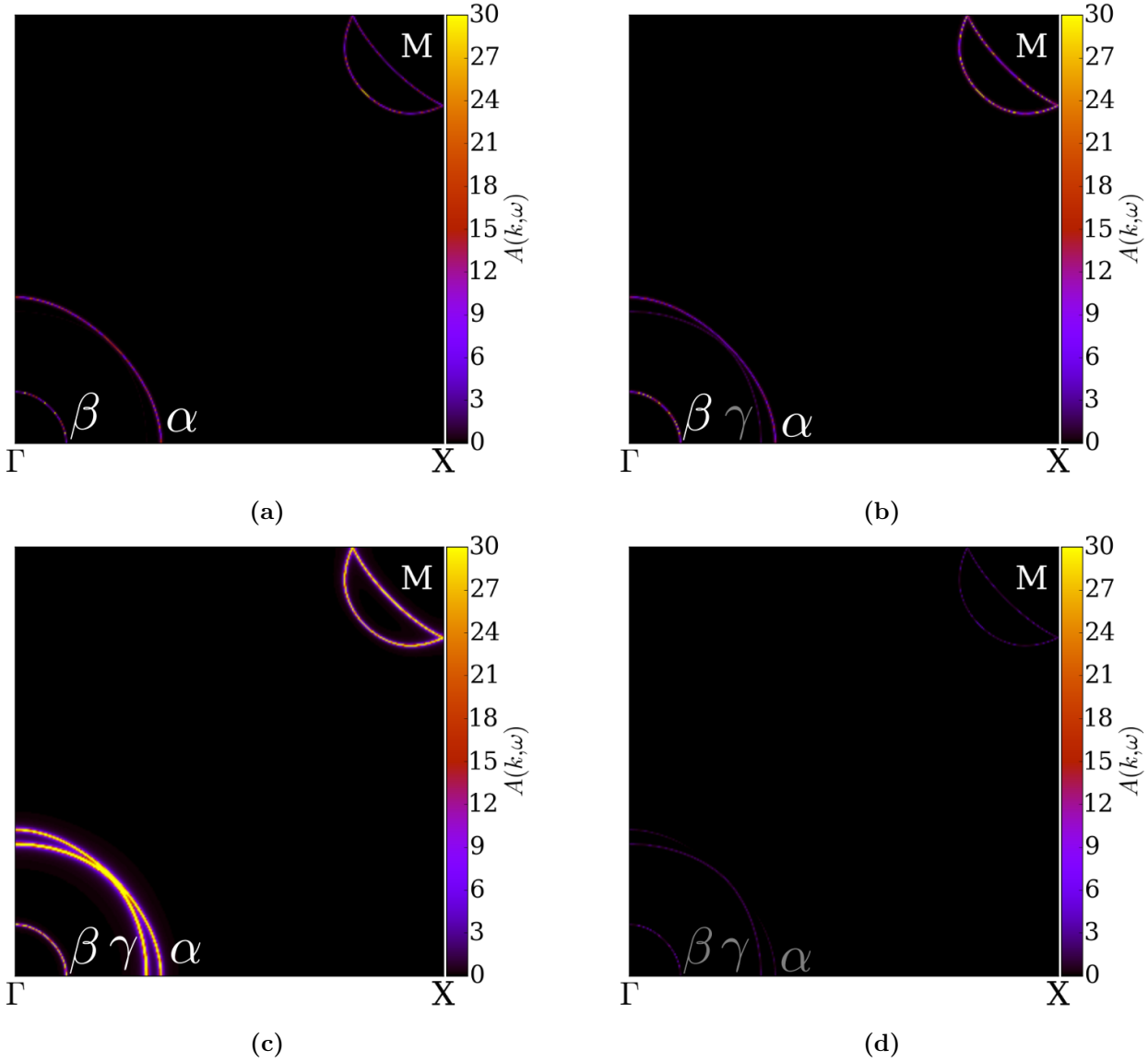

Figure 3.6: Fermi surface cross section of FeSe from atomic type and angular momentum decomposed Bloch spectral function $A(\omega, \boldsymbol{k})$. (a) Fe $l = 1$, (b) Se $l = 1$, (c) Fe $l = 2$, and (d) Se $l = 2$. Hole pockets indicated by α, β and γ (for very low contributions, labels have been dimmed).

3.4.1 The influence of the lattice parameters on the band structure of FeSe

We now turn to a key characteristic of the band structure of FeSe: its sensitivity towards the specific lattice parameters - especially with respect to bands D and F_2 which are relevant to the formation of the surface Dirac cone (see Sec. 3.3). In order to gain insight into the dependence of these bands, we have performed a study concentrating on two key parameters: the chalcogen-height z and the interlayer distance c. Since both are relevant for the overlap of the chalcogen p_z-orbitals between the iron planes, i.e., the pp-hybridization, we may suspect them to have a crucial impact especially on band D.

Variation of the chalcogen-height z

The results for a variation of the chalcogen-height z can be found in Fig. 3.7, where we compare the states of the relevant bands a both Γ and Z. Increasing z shortens the distance between the Se atoms in between the Fe layers and consequently, their orbital overlap increases.
Clearly, the chalcogen-height has only a minor impact on F_1, which gets shifted in energy and crosses the Fermi level, as z is increased. However, its dispersion remains unaltered, indicating that the p_z orbital overlap has barely an influence on this $3d$ iron band. For our second iron band F_2 we find the opposite situation: while the dispersion is slightly but steadily increased, the center of F_2 remains unshifted. The greatest effect can be found in band D, where we see a minor decrease in dispersion but an extensive shift downward in energy.

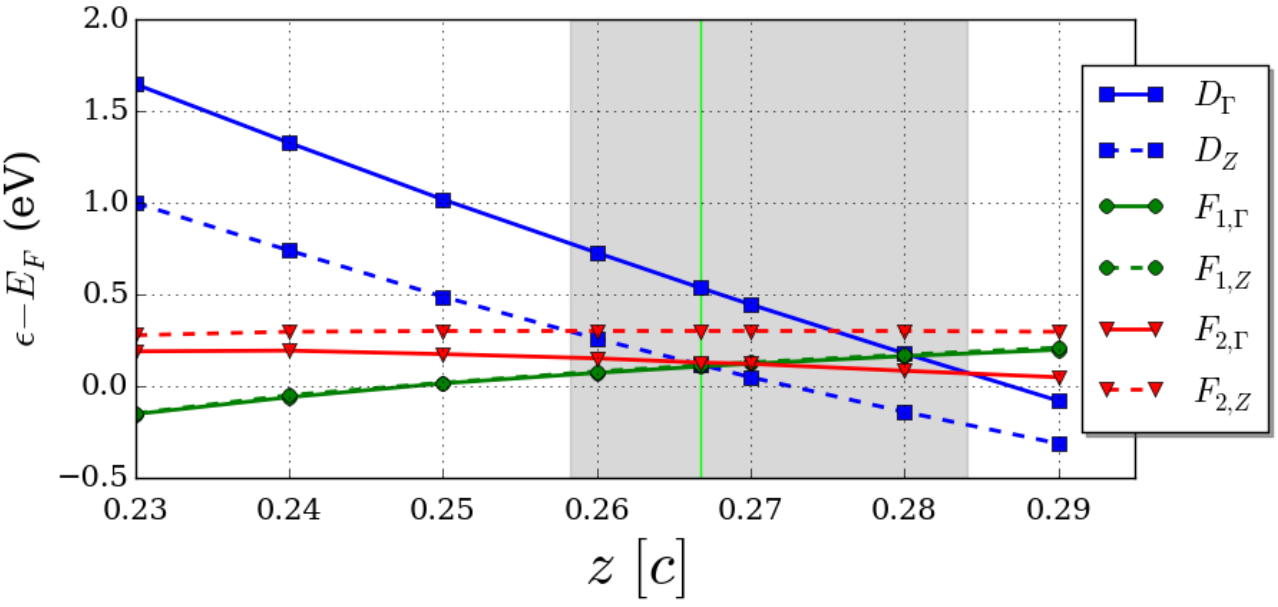

Figure 3.7: Evolution of the position of the states connected to band D, F_1, and F_2 at the Γ and Z point with respect to the chalcogen-height z in units of c. Grey region marks subspace in which a band crossing of D and F_2 occurs. Vertical green line indicates the experimentally measured parameter.

Most notably, only in a small region of the parameter space do we find a crossing point between D and F_2, which we have highlighted in gray in Fig. 3.7. Thus, the specific value of z strongly influences

the outset of our search for a SDC: without a crossing point between D and F_2, no SOC gap can emerge.

Variation of the interlayer distance c

The results for our parameter study with respect to the intralayer distance c are presented in Fig. 3.8. Similar to a variation of z, the intralayer distance has an impact on the magnitude of the orbital overlap of the p_z orbitals. Shortening this distance brings the Se atoms closer together - increasing the overlap.

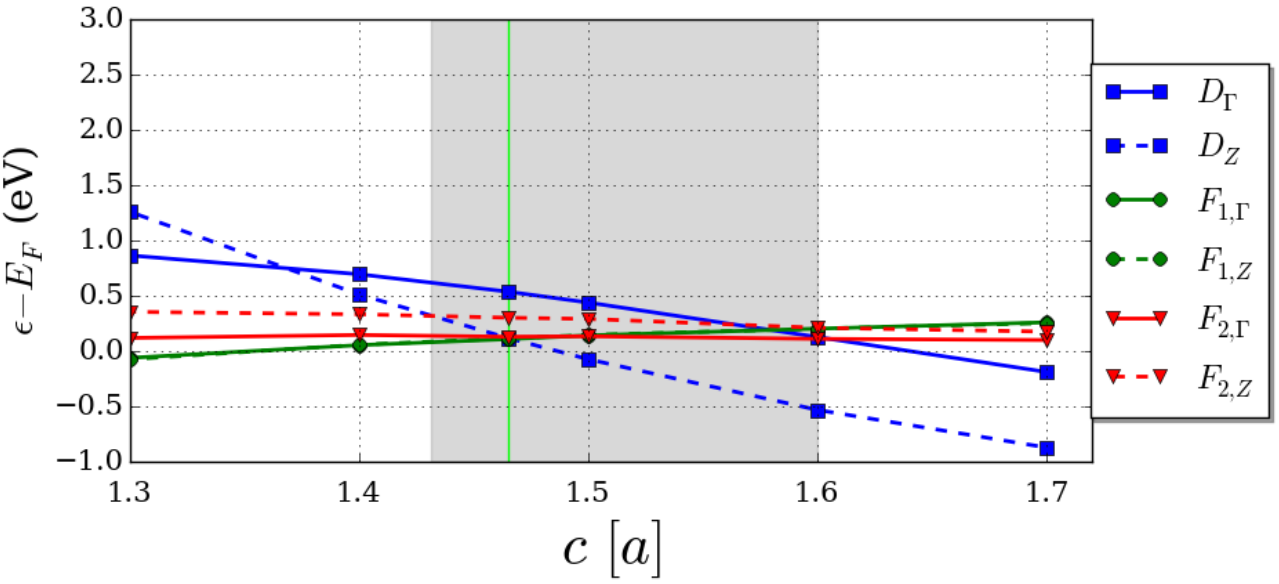

Figure 3.8: Evolution of the position of the states connected to band D, F_1, and F_2 at the Γ and Z point with respect to the interlayer distance c in units of a. Grey region marks subspace in which a band crossing of D and F_2 occurs. Vertical green line indicates the experimentally measured parameter.

For band F_1 we find a behavior similar to that found above: while the band is shifted upward in energy (and across the Fermi level) no change in dispersion occurs. While we now find a minor decrease in dispersion for F_2, the band center still remains unshifted. Once again, we find the strongest effect in D, which is not only shifted downward in energy, but shows an inversion of its slope between $c = 1.3$ and $c = 1.4$ along with an increase in dispersion. Similar to before, only within a small region of the parameter space do we find a crossing point between D and F_2.
As we have shown here, the specific lattice configuration plays a vital role in realizing the SDC cone and it is thus of paramount importance for our following CPA calculations to use sensible parameters as input. Given the strong dependence on lattice parameters, it is most reasonable to resort to the real lattice parameters as measured by experiment. To his end, we have determined the lattice parameters used within our subsequent CPA calculations by averaging over two $FeSe_{1-x}Te_x$ samples close to $x = 0.5$. Details of the calculations performed in the remainder of this chapter can be found in App. J.5.

3.5 The effect of Te-substitution

We have already qualitatively discussed the band structure of Fe(Se,Te) in Sec. 3.3 and shall now take a closer and more quantitative look at the effects of Te-substitution on the band structure of FeSe. On our route to realize the SDC, we seek to lower band D sufficiently to bring the crossing point with F_2 closer to the Fermi level. This can be achieved via Te-substitution - an effect most commonly attributed to the greater spatial extent of Te p_z-orbitals compared to their Se counterparts [19] (a schematic drawing of the orbital overlap of FeSe and FeTe can be found in Fig. 3.9).

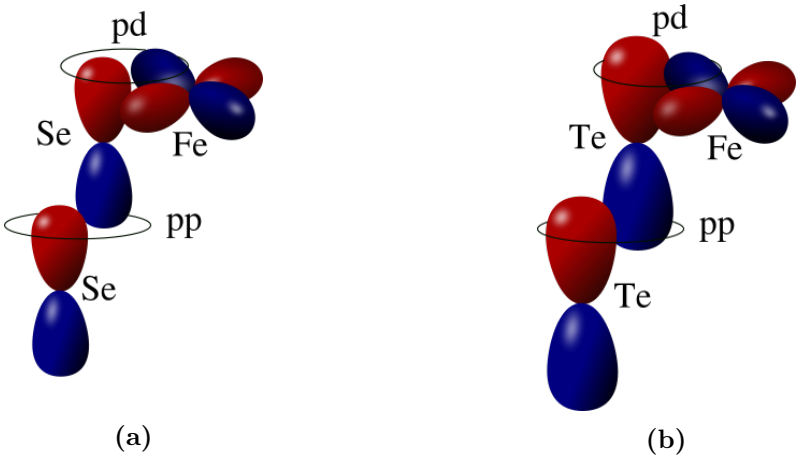

Figure 3.9: Schematic drawing of orbital overlap for (a) FeSe and (b) FeTe. Figures in style of Fig. 1 (c) in Ref. [19].

The increased pp-hybridization leads to increased interlayer hopping, resulting in band D being shifted closer to the Fermi level. This effect of Te-substitution on band D becomes evident from the comparison of the FeSe band structure in Fig. 3.4 (a) and the Bloch spectral function $A(\boldsymbol{k}, \omega)$ of $FeSe_{0.5}Te_{0.5}$ in Fig. 3.10 (b), which is calculated according to

$$A(\boldsymbol{k}, \omega) = -\frac{1}{\pi} \operatorname{Im} \operatorname{Tr} \left[\underline{S\Gamma}(\boldsymbol{k}, \omega^+) \right], \tag{3.3}$$

where $\underline{S}$ and $\underline{\Gamma}$ are the orbital overlap and effective medium Green's function in extended Hilbert space, respectively. Here, $\omega^+ = \omega + i\delta$ with infinitesimal δ. A detailed derivation and discussion of the Bloch spectral function is given in App. G.4.
From Fig. 3.10 (b) it is evident that Te-substitution affects the highly dispersive D band in the desired way: it has been lowered significantly in energy compared to the band structure of real FeSe (Fig. 3.4 (a)), now crossing the Fermi level and the $3d$-bands F_1 and F_2. In Fig. 3.10 we compare the band structures of our parent compounds FeSe and FeTe to that of substitutionally disordered $FeSe_{0.5}Te_{0.5}$. Here, the lattice parameters for the substituted compound were used in all three CPA calculations, as the CPA formalism demands equal crystal structures for all substitutional end members (see App. A.3 for details). This is the reason behind the discrepancy between the band structures of FeSe in Fig. 3.4 (a) and Fig. 3.10 (a). While the D band lies well above the Fermi level and crosses the F_2 band for real lattice parameters, in the hypothetical crystal it crosses the Fermi level and lies beneath both $3d$-bands, F_1 and F_2 at Z.
For the second end member FeTe, we find that band D crosses both flat bands. As we have mentioned

in Sec. 3.2, we have ignored the structural and magnetic phase transitions, and the interstitial iron in this system. Considering these hypothetical crystals, we can clearly observe that the substituted compound is intermediate to the two end members with respect to the location of band D.

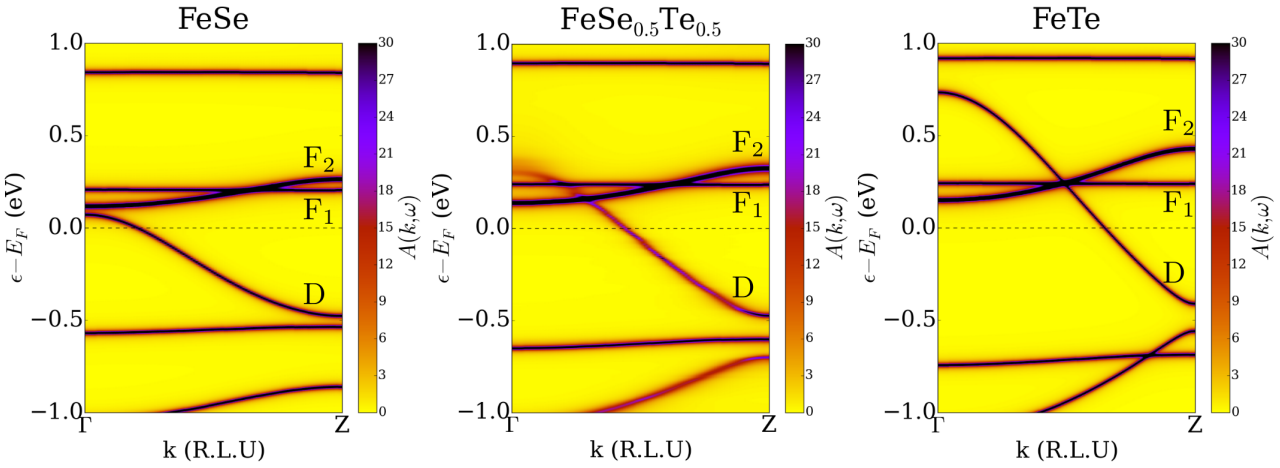

Figure 3.10: Bloch spectral function $A(\boldsymbol{k}, \omega)$ of (a) FeSe, (b) $FeSe_{0.5}Te_{0.5}$, and (c) FeTe for lattice parameters of substituted compound ($a = 3.793$Å, $c = 5.9656$Å, $z = 0.27885$). Relevant bands are labeled D, F_1 and F_2.

Now that we have shown the possibility of affecting the location of p_z-character band D through Te-substitution, we have most of the ingredients necessary for the formation of the SDC. The last missing building block is spin-orbit coupling, which we will include in our calculations in the next section.

3.6 Inclusion of Spin-orbit coupling

Having discussed the theoretical effects of SOC on the band structure of $FeSe_{0.5}Te_{0.5}$ and the origin of the SDC in Sec. 3.3, we can now extend our prior investigation: we will include the considerable SOC introduced by the chalcogens - especially the heavier Te - in our calculations.
The results presented in this section were obtained by a full *ab-initio* treatment of SOC within the CPA (see App. E for details). From Fig. 3.11 (c), we can confirm the predicted effects of SOC on the bands of interest: for one, the degeneracy of band F_2 is lifted, splitting into bands F_2^+ and F_2^- and a SOC gap is opened at the crossing point of D and F_2^-.
We can clearly identify this SOC gap from the comparison of the project Bloch spectral functions of $FeSe_{0.5}Te_{0.5}$ without and with SOC in Figs. 3.11 (b) and 3.11 (d). This approach allows us to directly map disorder effects to individual bands of the parent compound by projecting the $\boldsymbol{k}$-dependent Green's function $S(\boldsymbol{k})\Gamma(\boldsymbol{k})S(\boldsymbol{k})$ onto the eigenvectors of the parent compound. We can define this as

$$G_n(\boldsymbol{k}, \omega) = \sum_{i,j \in \text{parent}} c^*_{n,i}(\boldsymbol{k}) \left[S(\boldsymbol{k})\Gamma(\boldsymbol{k})S(\boldsymbol{k})\right]_{i,j} c_{n,j}(\boldsymbol{k}) \tag{3.4}$$

where $c_{n,i}$ is the ith orbital component of the eigenvector of band n. A detailed discussion of the projection technique can be found in App. G.

Another direct consequence of the lifted degeneracy is a shift of the crossing point not only in energy but also in $\boldsymbol{k}$-space. As F_2^- is shifted below the original F_2 band, the crossing point shifts from $\boldsymbol{k}_\otimes = 0.285\overline{\Gamma Z}$ and $\epsilon_\otimes \simeq 0.1587$eV to $\boldsymbol{k}_\otimes = 0.310\overline{\Gamma Z}$ and $\epsilon_\otimes \simeq 0.109$eV. At this new crossing point we can identify the SOC hybridization gap with a magnitude of $\Delta_{\mathrm{SOC}} \simeq 30$ meV. Clearly, each spectral peak splits into two, transferring spectral weight across the gap.

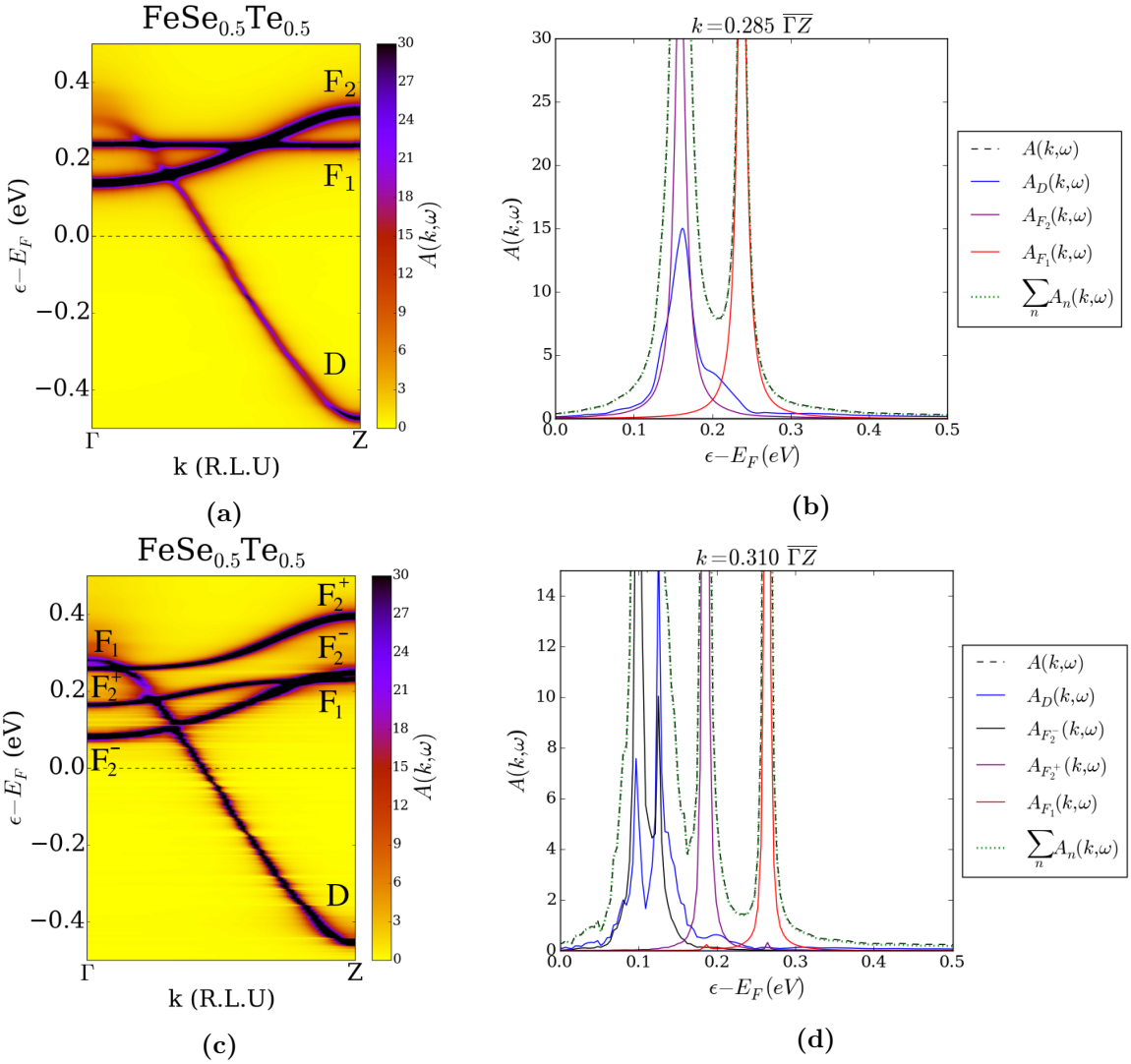

Figure 3.11: Bloch spectral function $A(\boldsymbol{k}, \omega)$ along ΓZ for $FeSe_{0.5}Te_{0.5}$ (a) without SOC, and (c) with SOC. Comparison of the projected spectral function at the band crossing point (b) without SOC, and (d) with SOC.

It is within this gap that a SDC occurs on the surface of the system, that is theoretically predicted to host topologically nontrivial surface states - the Majorana zero modes - in the superconducting phase [19, 22, 85]. However, there is one major obstacle to overcome in realizing the SDC and topological surface states: the crossing point, and consequently the SOC gap, lies well above the Fermi level. Thus, a possible SDC would be irrelevant with respect to experiments such as transport measurements, and

following Ref. [22] the resulting superconducting phase would be topologically trivial. We are thus tasked with raising the Fermi level into the vicinity of the SOC gap. In the course of this attempt, we must also investigate the additional spectral broadening induced by the cosubstitution - it must not conceal the SOC gap. A major advantage of the CPA, which we will employ for our line of inquiry, is that it readily supplies us with this information.

3.7 Electron doping via chemical substitution - shifting the Fermi level

In order to bring the band crossing point in Fig. 3.10 (b) closer to the Fermi level, we consider cosubstitution, thus bringing additional electrons into the bulk crystal. This allows us to circumvent the disruption of surface transport due to surface deposition, as proposed in Ref. [19]. In the search for topologically nontrivial surface states it is paramount to have access to an unperturbed surface and surface transport measurements. Here, we follow two distinct strategies: firstly, we consider cosubstitution of $3d$ transition metals, namely Ni, Cu, and Co, at the Fe site. Secondly, we consider cosubstitution at the Se site with the halogens bromine and iodine. The reasons for our specific choices are two-fold: firstly, introduction of additional electrons. Secondly, without grown and fully characterized crystals, we must resort to the lattice parameters of $FeSe_{0.5}Te_{0.5}$. A cosubstitution, however, will inevitably change the crystal structure and thus our candidates are chosen due to their close similarity in ionic radii to those atomic types we wish to substitute. Consequently, we can expect them not to alter the lattice to severely.

3.7.1 $3d$ transition metal substitution at the Fe site

One possibility to bring additional electrons into the system is a cosubstitution with $3d$ transition metals at the Fe site.

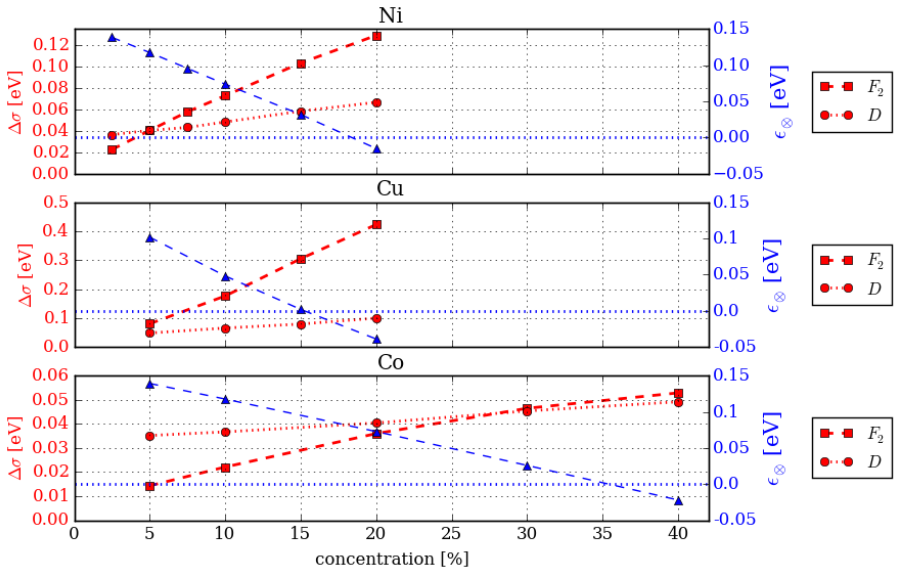

Figure 3.12: Half-widths (red) and energy position of the band crossing point relative to E_F (blue) of D and F_2 for Ni , Cu, and Co for various substitutional degrees. Dotted blue line indicates Fermi level.

Accordingly, we consider compounds of the form $Fe_{1-y}TM_ySe_{0.5}Te_{0.5}$ with TM={Ni, Cu, Co} and substitutional degree y. Due to the enormous computational cost, we have performed the subsequent CPA calculations without SOC, concentrating on the doping effect. Only for those compounds which we identify as promising, will we include SOC for further investigation.
In Fig. 3.12 we present the spectral half-widths $\Delta\sigma$ of bands D and F_2 at their crossing point, along with the energetic and $\boldsymbol{k}$-space positions $\epsilon_\otimes$ and $\boldsymbol{k}_\otimes$, respectively, for all substituents at different concentrations. The respective values are summarized in Tab. 3.3.

	$\boldsymbol{k}_\otimes$ [$\overline{\Gamma Z}$]	$\epsilon_\otimes$ [eV]	$\Delta\sigma_D$ [eV]	$\Delta\sigma_{F_2}$ [eV]
$FeSe_{0.5}Te_{0.5}$	0.285	0.1586	0.0156	0.0057
Co concentration				
5%	0.30	0.1394	0.0352	0.0143
10%	0.31	0.1178	0.0367	0.0221
20%	0.33	0.0728	0.0404	0.0360
30%	0.35	0.0259	0.0454	0.0465
40%	0.37	-0.0220	0.0492	0.0529
Ni concentration				
2.5%	0.30	0.1387	0.0365	0.0225
5.0%	0.31	0.1177	0.0404	0.0404
7.5%	0.32	0.0958	0.0432	0.0578
10%	0.33	0.0739	0.0483	0.0729
15%	0.35	0.0319	0.0584	0.1034
20%	0.38	-0.0152	0.0667	0.1292
Cu concentration				
5%	0.31	0.1010	0.0482	0.0802
10%	0.33	0.0483	0.0654	0.1764
15%	0.36	0.0020	0.0792	0.3053
20%	0.39	-0.0390	0.0998	0.4236

Table 3.3: Table containing the $\boldsymbol{k}_\otimes$-point and energy $\epsilon_\otimes$ of the crossing point between bands D and F_2 and the corresponding half-widths for $FeSe_{0.5}Te_{0.5}$, and substituents Co, Ni, and Cu at different concentrations.

We find the desired effect for all three candidates, i.e., the band crossing point is lowered towards the Fermi level by introducing additional charges into the bulk. As could have naively been expected, this is most efficiently achieved with Cu, which possesses the most valence electrons of the substituents. For $y_{\mathrm{Cu}} = 20\%$, we find $\epsilon_\otimes = -0.039$ eV to be below E_F, which would make the corresponding SDC accessible to transport measurements. This is closely followed by Ni-substitution, which posses one valence electron less ($\epsilon_\otimes = -0.0152$ eV at $y_{\mathrm{Ni}} = 20\%$). However, the major drawback of Cu in comparison to Ni is the spectral half-width $\Delta\sigma$ of the relevant bands. Here, we find much larger band broadening due to disorder with $\Delta\sigma$ more than an order of magnitude above that of Ni. The least pronounced broadening is found for Co-substitution. However, as can be seen from the bottom panel in Fig. 3.12, a high substitutional degree of $y_{\mathrm{Co}} = 40\%$ is necessary to cross the Fermi level.

From Fig. 3.12 we can clearly identify a common trend in the band broadening with increased transition metal content: while the spectral width of band D is only increased by a factor of ~ 2, that of F_2 is increased by a factor of $\sim 4-6$. This can be attributed to the orbital composition of the respective bands. As F_2 mainly stems from Fe $3d$ orbitals, it seems natural that substitution with $3d$ transition metals would have a greater effect here that on the p_z character band D. Both the band broadening effect and the raised Fermi level can qualitatively be observed in the band structure plots presented in Fig. 3.13 for the "optimal" doping contents. While the respective bands are still well discernible in Ni and Co, for Cu the band broadening effect is clearly too large to yield well defined bands - especially considering F_2.

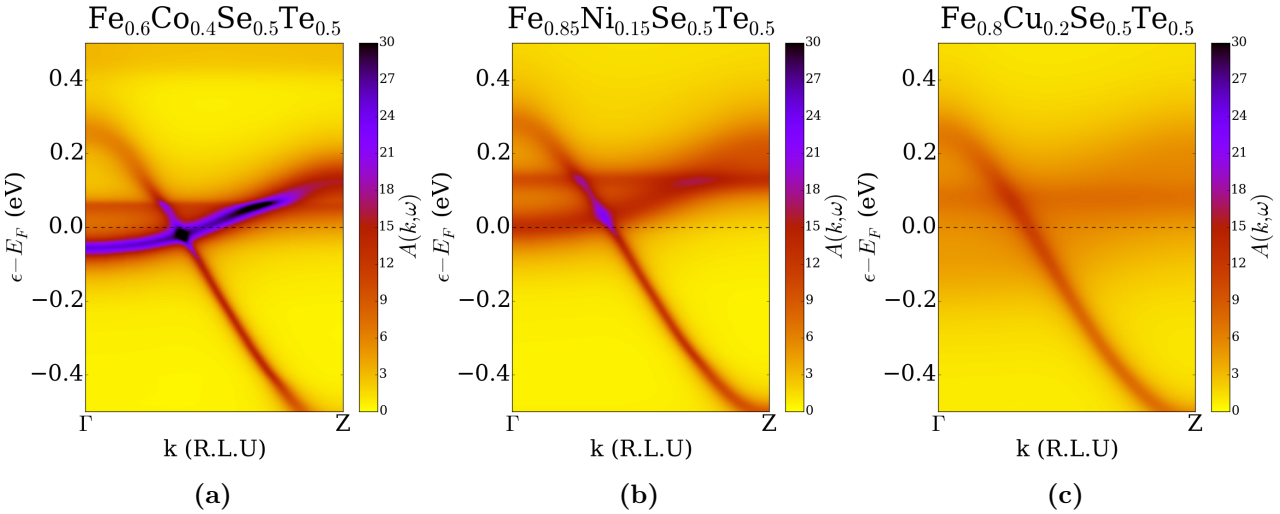

Figure 3.13: Comparison of the Bloch spectral function $A(\boldsymbol{k},\omega)$ along ΓZ of (a) $Fe_{0.6}Co_{0.4}Se_{0.5}Te_{0.5}$, (b) $Fe_{0.85}Ni_{0.15}Se_{0.5}Te_{0.5}$, and (c) $Fe_{0.8}Cu_{0.2}Se_{0.5}Te_{0.5}$.

As we have discussed previously, band broadening is a limiting factor for the realization of the SDC: as the SOC gap is relatively small, the additional disorder could conceal it and prevent a SDC from emerging. It is to be expected that the $3d$ transition metal cosubstitution could violate the necessity for small band broadenings, considering the results obtained from our CPA calculation.
Apart from this complication, there is a second circumstance which renders the suggested strategy useless in the search for a SDC and possible realization of Majorana zero modes: due to the strong scattering properties of Ni, Cu and Co, superconductivity is suppressed at lower concentrations ($y_{\mathrm{Co}} \sim 20\%$, $y_{\mathrm{Ni}} \sim 10\%$, $y_{\mathrm{Cu}} \sim 1.5\%$) [136–139] than those proposed by us. Thus, for concentrations which bring the crossing point to E_F, superconductivity no longer exists. This is the main drawback of *TM* substitution, as the lack of superconductivity inevitably prohibits Majorana zero modes. In conclusion, $3d$ transition metal cosubstitution in Fe(Se,Te) can be excluded from the search for Majorana zero modes.

3.7.2 Halogen substitution at the Se site

The second strategy we employ is a cosubstitution at the Se site with halogens, namely bromine and iodine. Thus, we seek to virtually design an appropriate crystal of the form $FeSe_{1-x-y}Te_xHa_y$ ($Ha = \{Br, I\}$). We shall, once again, begin our inquiries by neglecting SOC in order to concentrate on the doping effects and shall include when discussing our most promising candidate.

Cosubstitution with bromine

As a first candidate for cosubstitution at the Se site we consider bromine for different substitutional degrees. The results of the corresponding CPA calculations with respect to the shift and band broadening effects can be found in Tab. 3.4.

	$\boldsymbol{k}_{\otimes}$ [$\overline{\Gamma Z}$]	$\epsilon_{\otimes}$ [eV]	$\Delta\sigma_D$ [eV]	$\Delta\sigma_{F_2}$ [eV]
$\mathbf{FeSe_{0.5}Te_{0.5}}$	0.285	0.1586	0.0156	0.0057
Br concentration				
5%	0.20	0.1155	0.1152	0.0150
10%	0.05	0.0796	0.1281	0.0214
15%	-	-	-	-

Table 3.4: Table containing the $\boldsymbol{k}_{\otimes}$-point and energy $\epsilon_{\otimes}$ of the crossing point between bands D and F_2 and the corresponding half-widths of $FeSe_{0.5}Te_{0.5}$ and bromine cosubstitution. For $y = 0.15$ no crossing point is found and no specification can be made.

From these results we can identify the desired effect of lowering the crossing point of bands D and F_2 closer to the Fermi level. Due to the p-orbital contributions of Br we find a strong broadening of band D, which is an order of magnitude larger than that for band F_2 which stems mainly from Fe $3d$-orbitals.

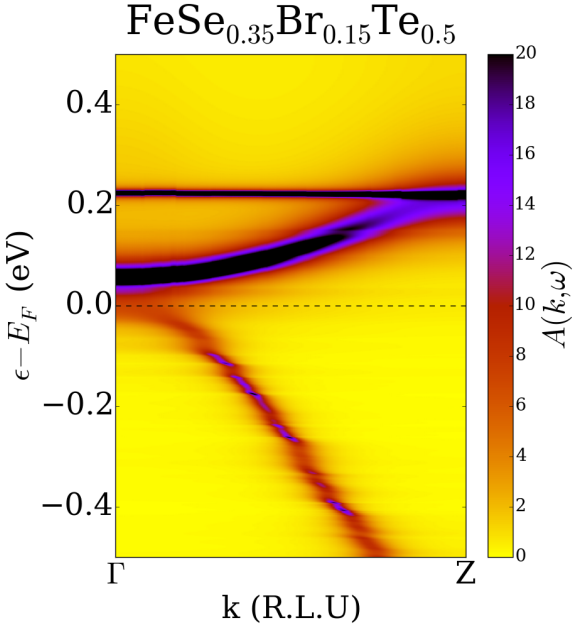

Figure 3.14: Bloch spectral function $A(\boldsymbol{k}, \omega)$ of $FeSe_{0.35}Br_{0.15}Te_{0.5}$ along ΓZ.

However, with increasing Br content band D is shifted down in energy too excessively, thus falling below F_2 before reaching E_F. Consequently, the substituted compound no longer exhibits the band

crossing point necessary for the SOC gap. This can clearly be seen from Fig. 3.14, in which we present the band structure along ΓZ for $y = 15\%$. Without a crossing point we must exclude Br substitution from our attempt to realize a SDC close to the Fermi level. We should, however, keep in mind that these results strongly depend on the lattice parameters, which might differ in a real sample. Consequently, this strategy should be reexamined with real parameters obtained from a grown sample. We shall now turn to the most promising candidate our CPA has identified: iodine.

Cosubstitution with iodine

We finally turn to our last candidate in the Se site substitution: iodine. We have performed multiple CPA calculations for varying substitutional degree y and summarized the results with respect to the band crossing point in Tab. 3.5.

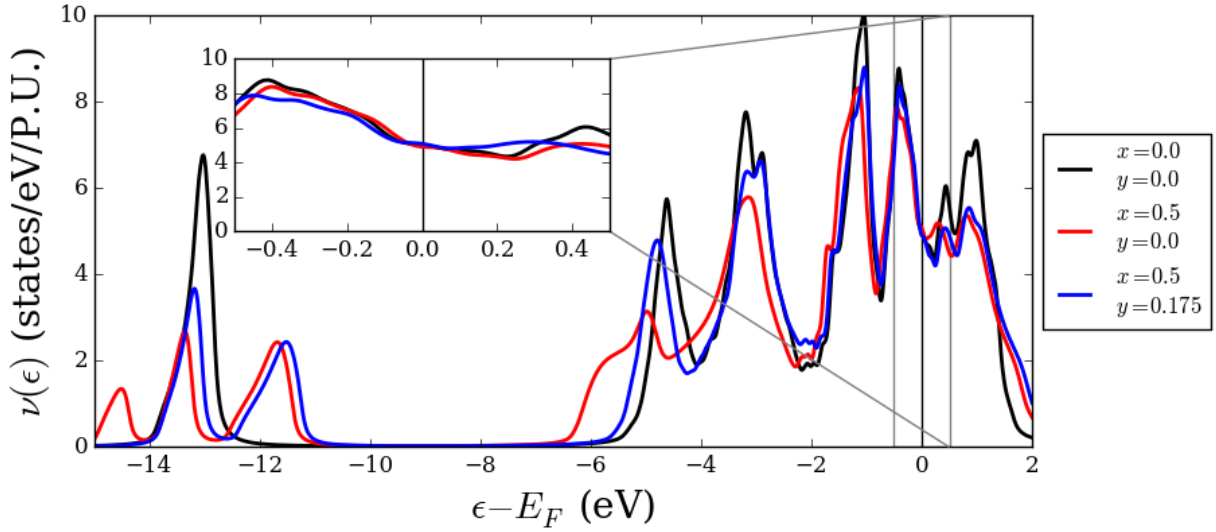

Figure 3.15: Comparision of the DOS of FeSe, $FeSe_{0.5}Te_{0.5}$ and $FeSe_{0.325}I_{0.175}Te_{0.5}$ without SOC.

In the preliminary calculations we have neglected SOC, due to the immense computational effort connected to the full ab-initio calculations containing multiple atomic types and substituents.

	$\boldsymbol{k}_\otimes$ [$\overline{\Gamma Z}$]	$\epsilon_\otimes$ [eV]	$\Delta\sigma_D$ [eV]	$\Delta\sigma_{F_2}$ [eV]
$FeSe_{0.5}Te_{0.5}$	0.285	0.1586	0.0156	0.0057
I concentration				
5%	0.25	0.1272	0.0226	0.0064
10%	0.21	0.0973	0.0253	0.0089
15%	0.16	0.0686	0.0261	0.0098
17.5%	0.13	0.0541	0.0263	0.0100

Table 3.5: Table containing the $\boldsymbol{k}_\otimes$-point and energy $\epsilon_\otimes$ of the crossing point between bands D and F_2 and the corresponding half-widths for $FeSe_{0.5}Te_{0.5}$, and iodine cosubstitution.

We shall, however, include it for the substitutional degree we deem optimal. Before going into detail on the band broadening effects, we first turn to the intended effect of raising the Fermi level. This effect can clearly be observed in the DOS. In Fig. 3.15, we compare the DOS of FeSe, $FeSe_{0.5}Te_{0.5}$ and our cosubstitution with the highest iodine content - $FeSe_{0.325}I_{0.175}Te_{0.5}$. The inset in Fig. 3.15 shows a small region about the Fermi level for all three systems. For the isoelectronic substitution of Se with Te, no shift in the DOS states is found. In contrast, the DOS for Fe(Se,I,Te) appears shifted to lower energies. This clearly indicates that more charges have the be accommodated for.

Substituent	optimal conc.	$\Delta\sigma_D$ [eV]	$\Delta\sigma_{F_2}$ [eV]	$\epsilon_\otimes$ [eV]
Ni	20%	0.0667	0.1292	-0.0152
Cu	20%	0.0998	0.4236	-0.0390
Co	40%	0.0492	0.0529	-0.0220
Br	10%	0.1281	0.0214	0.0796
I	17.5%	0.0263	0.0100	0.0541

Table 3.6: Comparison of half-widths for all cosubstitution candidates at their optimal doping without SOC.

We can now turn to the discussion of the results presented in Tab. 3.5 where we give the position of the crossing point in both $\boldsymbol{k}$-space ($\boldsymbol{k}_\otimes$) and energy ($\epsilon_\otimes$), together with the half-widths of bands D and F_2 for multiple substitutional degrees y.

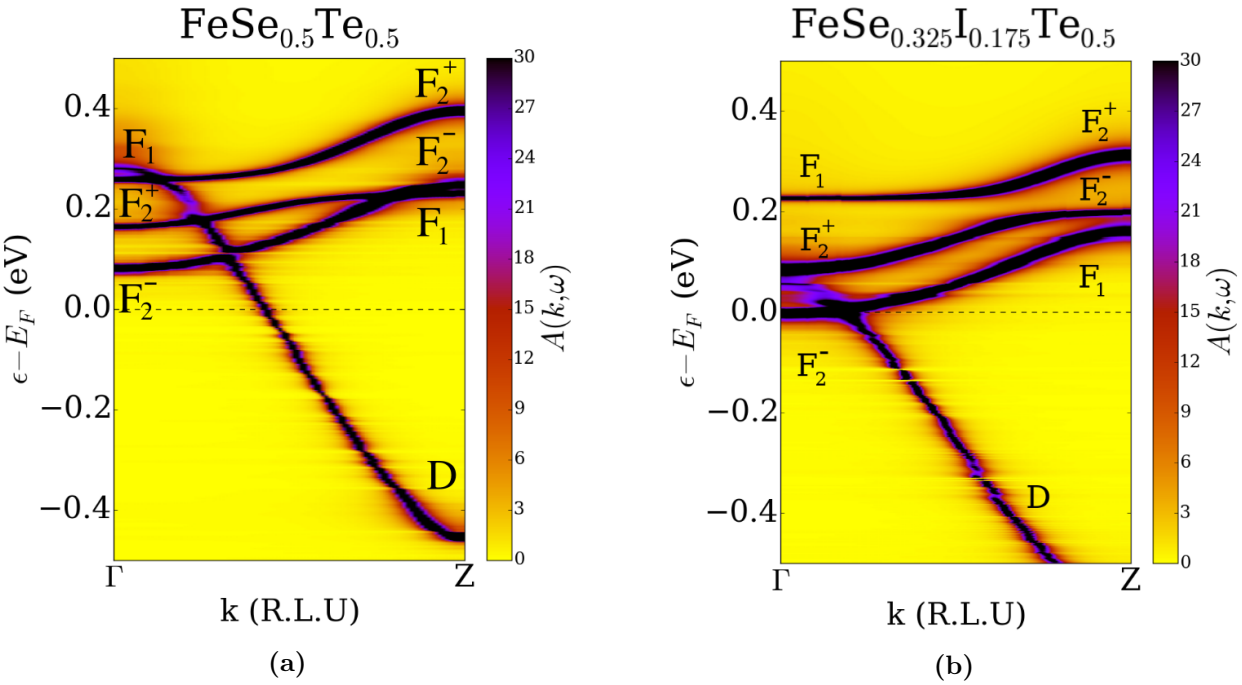

Figure 3.16: Bloch spectral function $A(\boldsymbol{k},\omega)$ of (a) $FeSe_{0.5}Te_{0.5}$, and (b) $FeSe_{0.325}I_{0.175}Te_{0.5}$ along high symmetry line ΓZ with SOC.

From Tab. 3.5, we clearly find the desired effect of the band crossing point being shifted downward closer to the Fermi level. Overall the band broadening effects to both band F_2 and D are minimal, leading only to a small increase of $\Delta\sigma$ with increasing iodine content.
As the magnitude of the spectral broadening is vital to the survival of the SOC gap, we compare the spectral half-widths of all candidates considered for cosubstitution in this work at their optimal concentrations in Tab. 3.6. These results verify that iodine cosubstitution induces the least broadening to the relevant bands and provides the best chances of not concealing the SOC gap.
With the lowest $\Delta\sigma$ (for both D and F_2) among our candidates we can expect iodine cosubstitution to be the least likely to conceal the SOC gap. Although the crossing point resides just above the Fermi level ($\epsilon_\otimes = 0.0524$ eV) for the proclaimed optimal concentration $y = 17.5\%$, we can expect it to be shifted downward in energy upon including SOC. As we have discussed in Sec. 3.3, SOC will lift the degeneracy of F_2 and the resulting bands F_2^+ and F_2^- will be pushed above and below the former band position, respectively. This obviously leads to a lowered crossing point between D and F_2^- (at which the SOC gap opens). From the comparison of $FeSe_{0.5}Te_{0.5}$ with and without SOC, we can estimate the magnitude of the energy shift connected to bands F_2^+ and F_2^-. The latter band is shifted by $\Delta\epsilon \simeq 0.055$ eV compared to the position of F_2 without SOC. Thus, it is reasonable to assume that $y = 17.5\%$ suffices to bring the crossing point below E_F ($\epsilon_\otimes < \Delta\epsilon$).

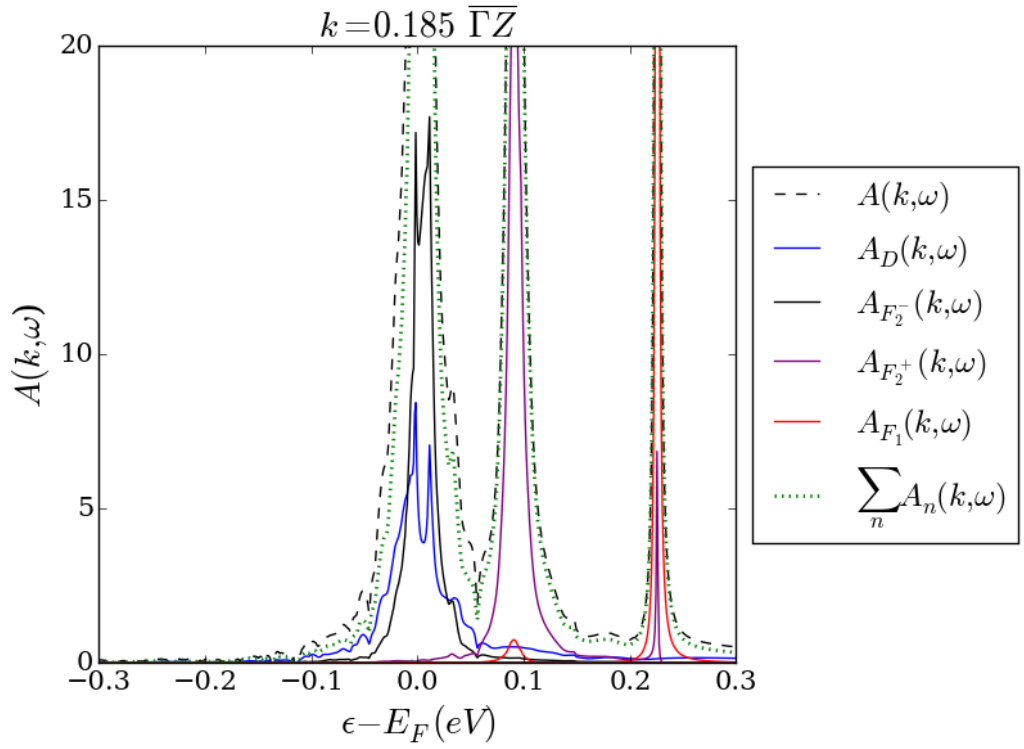

Figure 3.17: Projected Bloch spectral function $A(\boldsymbol{k},\omega)$ of $FeSe_{0.375}I_{0.175}Te_{0.5}$ at the crossing point of D and F_2^- at $\boldsymbol{k}_\otimes = 0.185\overline{\Gamma Z}$.

Now that we have identified our most promising candidate and an optimal substitutional degree we can turn to the inclusion of spin-orbit coupling. In Fig. 3.16, we compare the Bloch spectral function of $FeSe_{0.5}Te_{0.5}$ to that of $FeSe_{0.325}I_{0.175}Te_{0.5}$ with SOC.

As we have discussed above, the shift of the crossing point closer to the Fermi level can clearly be observed. We are thus left with answering the question whether the SOC gap has survived the enhanced disorder due to the additional iodine. While indiscernible in Fig. 3.16 (b), we can clearly identify the gap in Fig. 3.17. At the crossing point ($\boldsymbol{k}_{\otimes} = 0.185\overline{\Gamma Z}$) of band D and F_2^-, the respective projected spectral functions show two well discernible peaks each. The gap is now centered at $\epsilon \simeq 5$ meV with a magnitude of $\Delta_{\mathrm{SOC}} \simeq 10$ meV, such that the Fermi level would now cross a SDC arising within the SOC gap. Additionally, we can observe strong mixing of bands F_1 and F_2^+ in Fig. 3.17, as theoretically predicted in Sec. 3.3. Both peaks exhibit contributions from the respective other band.
In conclusion, we have shown that iodine is the most promising candidate for chemical substitution with the goal of raising the Fermi level and making the surface Dirac cone accessible to experiment. We have furthermore virtually designed a specific hypothetical crystal with the optimal iodine content in which the SOC gap survives the enhanced disorder. Thus, $\mathrm{FeSe_{0.325}I_{0.175}Te_{0.5}}$ is a highly promising candidate for the solid state realization of Majorana zero modes.

3.8 Conclusion and outlook

In this chapter we have applied the coherent potential approximation (CPA) in the context of materials design by band engineering the iron-chalcogenide Fe(Se,Te) via chemical substitution with the goal of providing a strategy to bring the surface Dirac cone closer to the Fermi level, and thus making it accessible to surface transport measurements without disrupting the pristineness of the crystal's surface. As theory predicts the SDC to host topologically nontrivial Majorana surface states inside vortices in the superconducting phase [19], such experiments can yield vital information about these exotic states.
In our inquiry we have considered multiple routes, such as transition metal substitution on the Fe site as well as cosubstitution at the Se site with halogens. Using the CPA, we were able to exclude the former strategy due to the substantial disorder scattering introduced by the considered candidates. Not only would their introduction to the system lead to substantial band broadening, which could conceal the spin-orbit coupling gap necessary for the emergence of the SDC, but superconductivity would even be suppressed. All in all, this exempts the approach from realizing a platform in which to find Majorana zero modes.
More promising results are yielded by our second strategy: we have shown that among the two contenders explored within this work, bromine and iodine, the latter is a highly promising candidate. Not only does iodine substitution introduce the necessary additional charges into our bulk system to raise the Fermi level to the SDC cone, but the induced band broadening in the relevant bands is sufficiently small to allow for the SOC gap to survive the increased disorder. We thus conclude, that this substitutional strategy provides a viable foundation for the single crystal realization of Majorana zero modes and lends a valuable tool for their study.
As we have discussed in Sec. 3.7.2, the choice of iodine as a substituent was in part motivated by its close similarity to Te with respect to ionic radii. We had argued it to be a reasonable assumption that this similarity might result in only minor alteration of the lattice parameters. Given the fact that our CPA calculations pertaining to the substituted crystal are based on the experimentally determined lattice parameters of the parent compound $\mathrm{FeSe_{0.5}Te_{0.5}}$, and that the effect of minor variations can be substantial (see Sec. 3.4.1), the reliability of our results is strongly coupled to the *de facto* structure of the theoretically predicted compound. Consequently, the crystal growth of a sample of the proposed compound is not only indispensable to the experimental search of Majorana zero modes but is indeed

an inevitable step in the refinement of our method and model. The full characterization of such a sample would yield the true lattice parameters on which the next iteration of calculations must be based. Only by taking into account these parameters can we confirm - or refute - our predictions.
It should be noted here, that due to the substitutional effects on the lattice parameters we should not fully exclude bromine from further investigations. Rather, the growth and characterization of such a sample could yield lattice parameters which might allow a band crossing point close to the Fermi level. This calls for further collaboration between theory and experiment in the endeavor towards the solid state realization of Majorana zero modes.

Chapter 4

4 Interstitial iron in $Fe_{1+y}Se_{0.5}Te_{0.5}$ and its possible impact on superconductivity

In this chapter we will investigate the effect of interstitial iron on the band structure and Fermi surface of $Fe_{1+y}Se_{0.5}Te_{0.5}$ and possible connections to the suppression of superconductivity with increasing interstitial content y.

4.1 Superconductivity in FeSe and Fe(Se,Te)

Among the iron-based superconductors, FeSe is unique in that it does not exhibit a magnetically ordered phase in close proximity to superconductivity, providing us with a highly fascinating platform to study the underlying unconventional pairing mechanism.
While FeSe shows a modest transition temperature of $T_c = 8 - 9K$, it can be tuned in numerous ways: via external pressure [15], chemical substitution, and even monolayer FeSe on $SrTiO_3$ bringing T_c above 60 K[13, 14]. Although no magnetic long-range order has been found down to low temperatures, strong magnetic fluctuations with complex temperature and momentum dependence have been observed [140–142].
The specific origin of superconductivity in FeSe is still subject to debate with numerous scenarios being considered. Some experimental finding point toward spin-fluctuation-mediated pairing with a gap that changes sign between electron and hole Fermi surfaces [142, 143], while strong electron-phonon interactions could also be of importance [144]. Furthermore, due to the relatively small magnitude of the superconducting gap $\Delta \sim 2 - 3$ meV and the resulting large ratio $\Delta/E_F \sim 0.1 - 1$ it could even fall into the regime of a BCS-BEC crossover [145, 146].
The same holds for Fe(Se,Te)[147, 148], for which spectroscopic-imaging scanning tunneling microscopy (SI-STM) measurements suggest unconventional $s^{\pm}$-wave superconductivity [149], i.e., the superconducting gap function undergoes a relative sign change between the hole and electron Fermi surface pockets . Inter-band nesting between these disconnected pockets is proposed to generate spin fluctuations responsible for the pairing mechanism [149]. It should be noted that different paring symmetries, such as d-wave and nodal $s^{\pm}$-wave (sign change within a single electron-like Fermi surface) have been suggested for the Fe-pnictides [150, 151].
Superconductivity in this system, however, strongly depends on the occurrence of interstitial iron.

4.2 Iron interstitial in Fe(Se,Te)

As we have briefly discussed in Sec. 3.2, grown samples of $FeSe_{1-x}Te_x$ almost always host an interstitial site between the iron planes that is occupied by excess iron to varying degree. The unit cell of the corresponding crystal structure can be seen in Fig. 4.1. The interstitial iron site is depicted by semi filled brown balls, where the colored wedges indicate the low occupational degree. It is situated above and below the chalcogen site and strong hybridization with both the chalcogens and the in-plane iron can be expected.

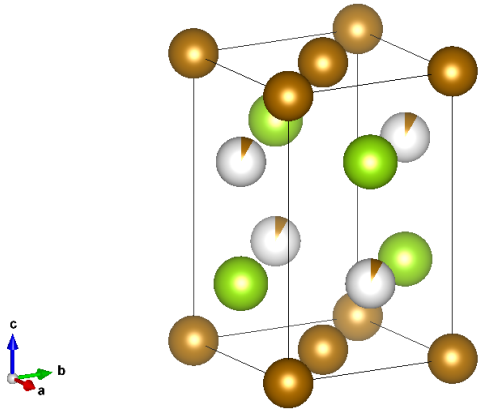

Figure 4.1: Unit cell of $Fe_{1+y}Se_{1-x}Te_x$. Filled brown balls indicate Fe, semi filled brown balls indicate interstitial Fe, and filled green balls indicate Se and Te.

This interstitial site, and the degree to which it is occupied by excess iron, has significant effect on the magnetic and superconducting properties of the system [63–65].
We shall here concentrate on superconductivity in light of our inquiry presented in the previous chapter. While at low interstitial content superconductivity can persist [64], for higher concentrations no transition temperature is found. This would be a hindrance to the strategy proposed in Chap. 3 to realize a platform for the search for Majorana zero modes. However, annealing strategies have been suggested [119] to reduce excess iron from as-grown samples - enhancing superconductivity and allowing for Majorana zero modes. Nevertheless, a thorough study of the effects on the band structure and Fermi surface of Fe(Se,Te) might shed light onto the intricate connection between interstitial iron and superconductivity - which is still a topic of ongoing debate.
With our CPA method, making use of the vacancy extension described in Sec. 2.2, we are able to treat the partial occupation of the interstitial site and study the disorder effects induced on both band structure and Fermi surface.
The crystal structure of $Fe_{1+y}Se_{0.5}Te_{0.5}$ was obtained via x-ray diffraction (XRD)[1] from a sample with $y \simeq 0.084$. The measured lattice parameters were used in all subsequent calculations irrespective of interstitial iron content (for details on XRD measurements and calculations, see App. J.6). This will certainly lead to some inaccuracy of the obtained results, as excess iron has significant effects on the real lattice parameters of the compound. Yet for the qualitative discussion presented here it suffices.

[1] Private communication with Michael Merz

4.3 Impact of excess iron on DOS, band structure, and Fermi surface

We begin our investigation into interstitial iron in Fe(Se,Te) by considering its effects on the DOS and the band structure, before focusing on their implications on superconductivity. We can naively expect two distinct effects: on the one hand, interstitial iron introduces additional electrons into the system, thus raising the Fermi level with respect to Fe(Se,Te). On the other hand, we can expect bands close to the Fermi level to be subject to strong alterations. This is due to the fact that the main contributions to these bands stem from the $3d$-orbitals of the in-plane iron atoms. Due to their close proximity to the interstitial site we can expect strong hybridization with d-orbitals of the excess iron.
From the comparison of the DOS in Fig. 4.2, we can clearly identify the doping effect which manifests itself in the shift of the low lying peaks towards lower energies with increasing content $y = \{0.01, 0.04, 0.084\}$. This is a clear indication of E_F being shifted to accommodate the additional electrons.

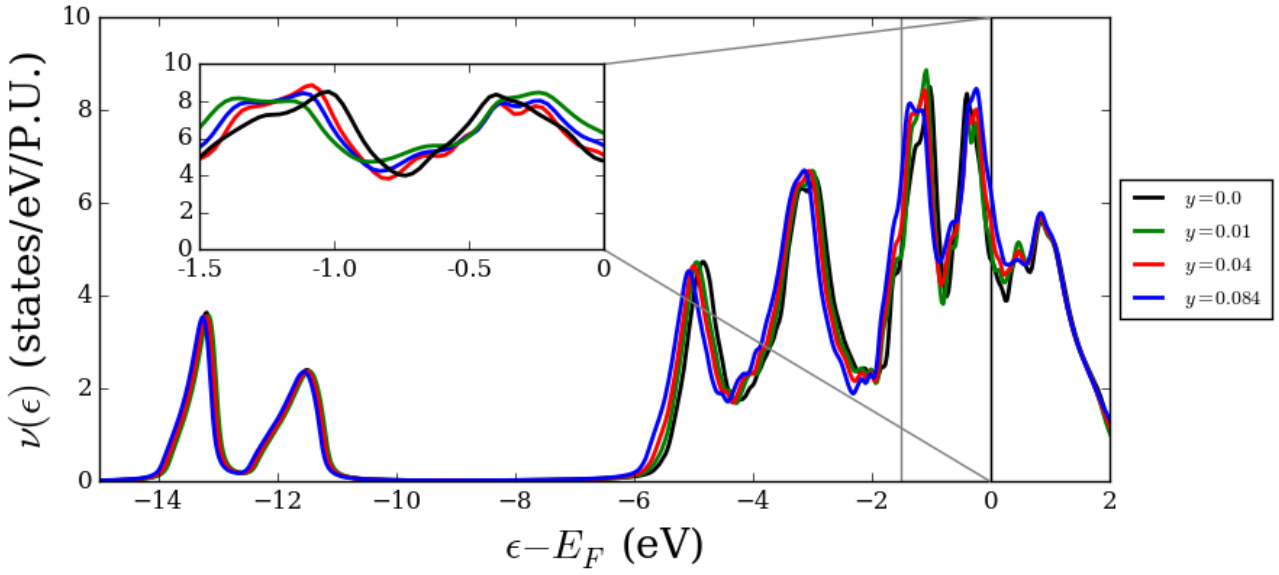

Figure 4.2: Comparision of the DOS of $Fe_{1+y}Se_{0.5}Te_{0.5}$ for different degrees y of interstitial iron occupation. Inset highlights region around E_F.

However, the most significant changes to the DOS occur close to the Fermi level. As can be seen in the inset of Fig. 4.2, compared to "pure" $FeSe_{0.5}Te_{0.5}$, the DOS acquires additional structure as the interstitial content is increased. This is especially prominent in the first two large peaks below E_F: as the occupation of the interstitial site is increased, a clear double peak structure evolves. This indicates additional states emerging close to the Fermi level.
This observation is reflected in the corresponding band structures presented in Figs. 4.3, 4.4, and 4.5. Apart from the expected band broadening induced by the additional disorder, some remarkable effects on the band structure can be observed around Γ, and along ΓZ and ΓM. Firstly, hole band β appears to separate and is pushed below E_F. For $y = 0.084$, there is only little spectral weight associated with this band close to the Fermi level, which will be reflected in the corresponding hole pocket of the Fermi surface.
This can be observed in Fig. 4.6, where we have plotted the respective Fermi surfaces for all y considered. While the hole pocket corresponding to band β can still clearly be observed for $y = 0.01$,

for higher concentrations it is smeared out severely.

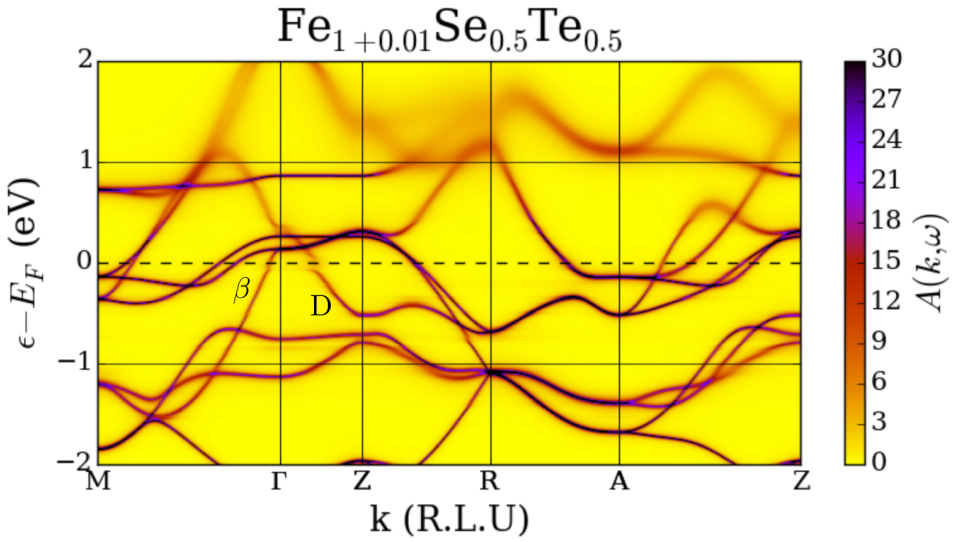

Figure 4.3: Band structure of $Fe_{1+0.01}Se_{0.5}Te_{0.5}$ along high symmetry lines.

The second change to the band structure could have severe implications on the proposal made in the previous chapter. The highly dispersive p_z-character band D in the ΓZ line also separates and is strongly shifted down in energy. This drastically affects the crossing point between D and F_2, which was a necessary condition for the emergence of the SDC discussed in Chap. 3.
For high excess iron content ($y = 0.084$), it is impossible to identify this crossing point, which would clearly hinder our attempts to make the SDC accessible to transport measurements in the topologically nontrivial superconducting phase and prevent the realization of Majorana zero modes.

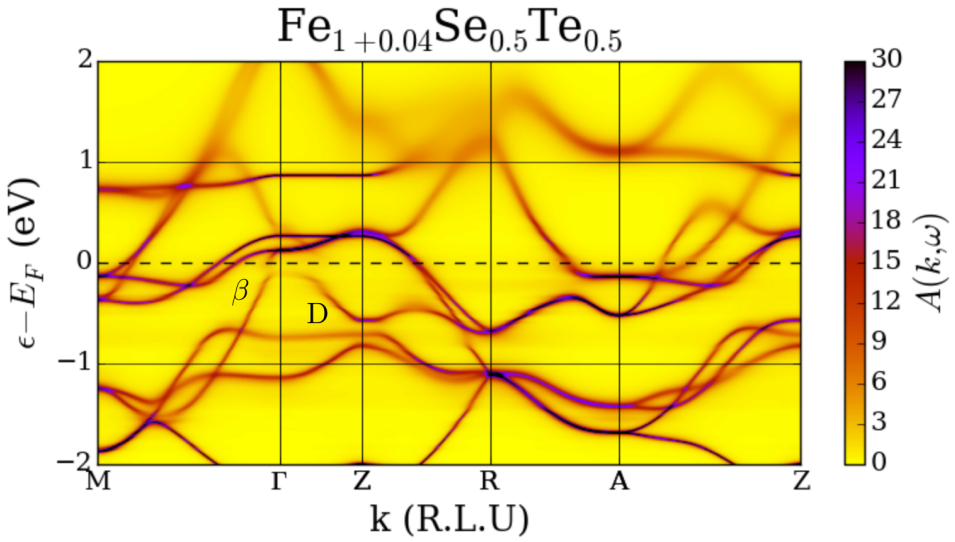

Figure 4.4: Band structure of $Fe_{1+0.04}Se_{0.5}Te_{0.5}$ along high symmetry lines.

Thus, it is vital to the realization of these exotic surface states to grow crystals with an interstitial content as low as possible, or to reduce the excess iron from as-grown samples via annealing techniques described in Ref. [119].

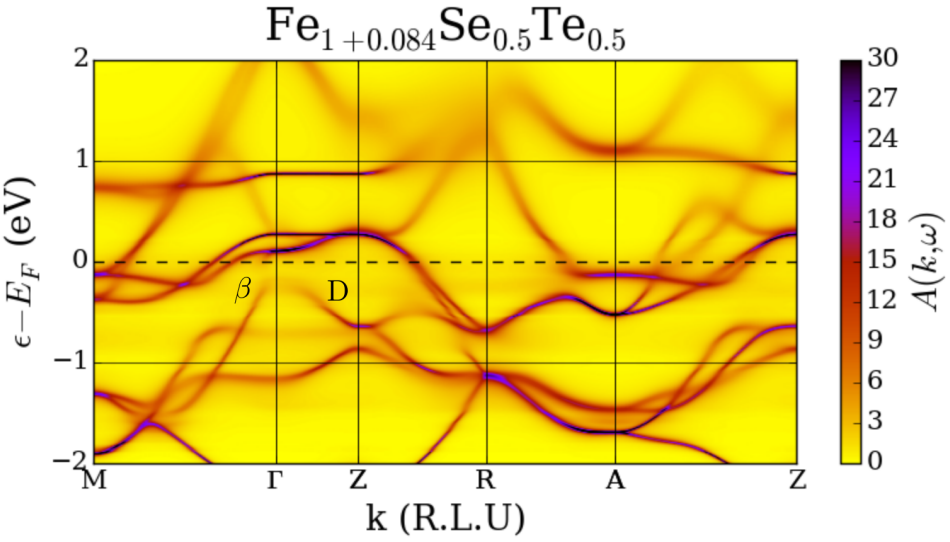

Figure 4.5: Band structure of $Fe_{1+0.084}Se_{0.5}Te_{0.5}$ along high symmetry lines.

The last significant effect on the band structure, and subsequently on the Fermi surface, can be observed along ΓM. Here, one the of the electron-like bands crossing the Fermi level close to M is strongly broadened due to the excess iron. This effect can be observed most clearly in the corresponding electron pocket of the Fermi surface cross sections at $k_z = 0$ in Fig. 4.7. While both electron pockets are well discernible for $y = 0.01$, for higher content they are significantly broadened. This effect is most pronounced for the outer electron pocket, which is gradually suppressed with increasing y, and barely visible for the highest concentration considered here.

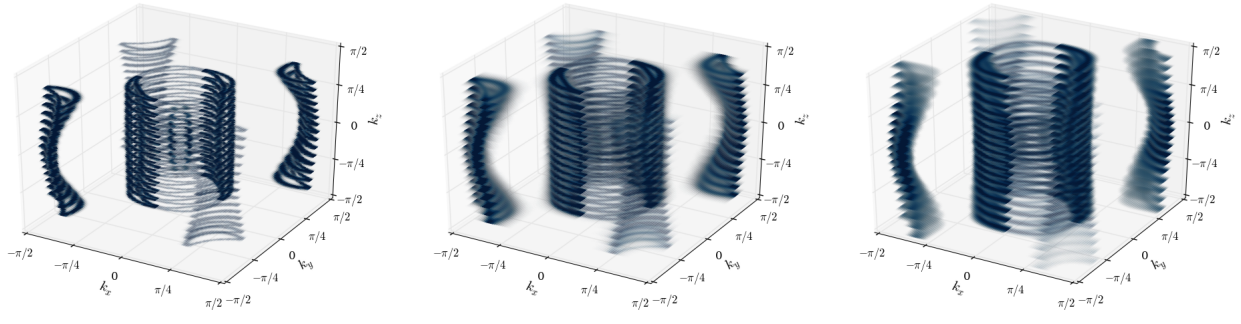

(a) **(b)** **(c)**

Figure 4.6: Fermi surfaces of $Fe_{1+y}Se_{0.5}Te_{0.5}$ for (a) $y = 0.01$, (b) $y = 0.04$, and (c) $y = 0.084$. Transparency for certain sections has been increased for better visibility.

4.4 Impurity scattering and the suppression of superconductivity

Without a comprehensive theory of the pairing mechanism in Fe(Se,Te) it is difficult to establish a connection between these disorder effects and superconductivity. However, we have already encountered a class of compounds related to $FeSe_{0.5}Te_{0.5}$ in Chap. 3 for which superconductivity is suppressed due to impurity scattering: $3d$ transition metal substituted $FeSe_{0.5}Te_{0.5}$, i.e., $Fe_{1-y}TM_ySe_{0.5}Te_{0.5}$ with $TM = \{\mathrm{Co}, \mathrm{Ni}, \mathrm{Cu}\}$.

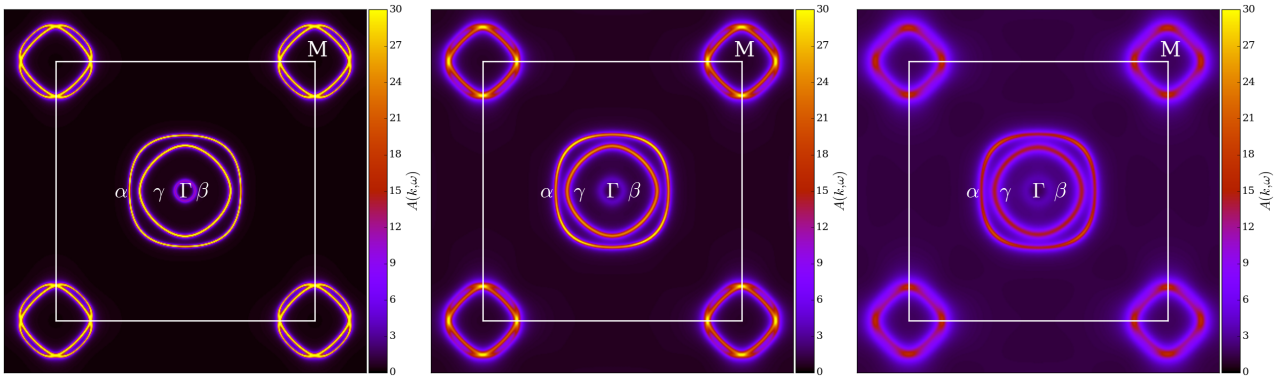

(a) **(b)** **(c)**

Figure 4.7: Fermi surface cross sections at $k_z = 0$ of $Fe_{1+y}Se_{0.5}Te_{0.5}$ for (a) $y = 0.01$, (b) $y = 0.04$, and (c) $y = 0.084$. Boundaries of first Brillouin zone indicated by white lines.

Thus, we resort to a qualitative comparison of interstitial iron to these system for TM concentrations for which superconductivity is known to have vanished [136–139]. To this end, we have performed CPA calculations for Co ($y = 0.2$), Ni ($y = 0.1$), and Cu ($= 0.05$) substitutions.

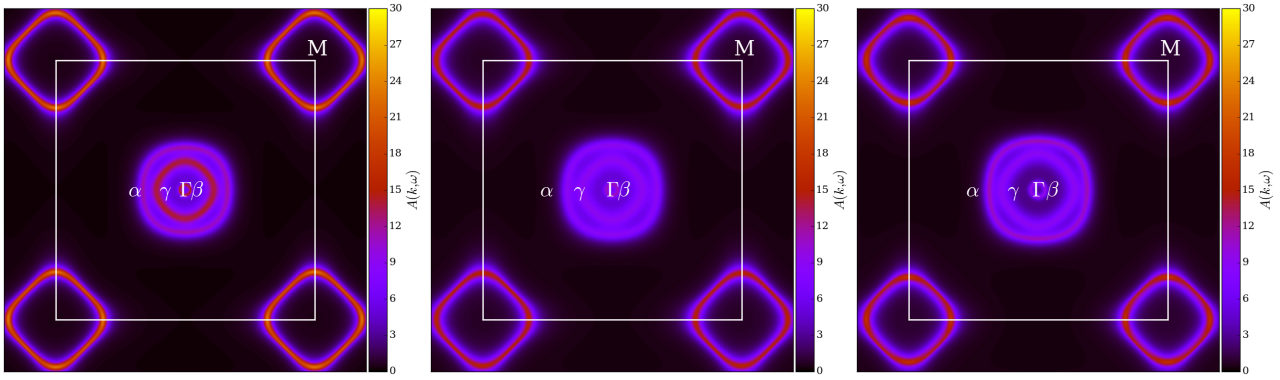

(a) **(b)** **(c)**

Figure 4.8: Fermi surface cross sections at $k_z = 0$ for (a) $Fe_{0.8}Co_{0.2}Se_{0.5}Te_{0.5}$, (b) $Fe_{0.9}Ni_{0.1}Se_{0.5}Te_{0.5}$, and (c) $Fe_{0.95}Cu_{0.05}Se_{0.5}Te_{0.5}$. Boundaries of first Brillouin zone indicated by white lines.

From the resulting Fermi surface cross sections in Fig. 4.8, we can identify similar effects on the respective Fermi surfaces compared to a high interstitial content (see Fig. 4.7 (c)). On the one hand,

we find substantial broadening of the hole pockets centered around Γ, although the broadening is more pronounced for transition metal substitution.
On the other hand, while the outer electron pocket at M is strongly suppressed for interstitial iron, for all three transition metal candidates it has disappeared entirely. Additionally, the remaining electron pocket exhibits enhanced broadening as we found for excess iron. The pronounced broadening in all compounds considered implies strong impurity scattering - which is the cause of suppressed superconductivity for Co, Ni, and Cu.
In order to compare the strength of impurity scattering for the transition metal compounds to that of high interstitial iron content ($y = 0.084$), we present cuts through the diagonal of the Fermi surface cross sections, i.e., along ΓM, in Fig. 4.9. Apart from differing locations of the individual Fermi surfaces, we can clearly identify the broadening of the respective electron pockets to be of comparable magnitude.
Consequently, we can estimate conjecture the excess iron to posses scattering strength similar to $3d$ transition metal substitution. Thus, it is reasonable to assume that the suppression of superconductivity in $Fe_{1+y}Se_{0.5}Te_{0.5}$ is closely linked to impurity scattering.

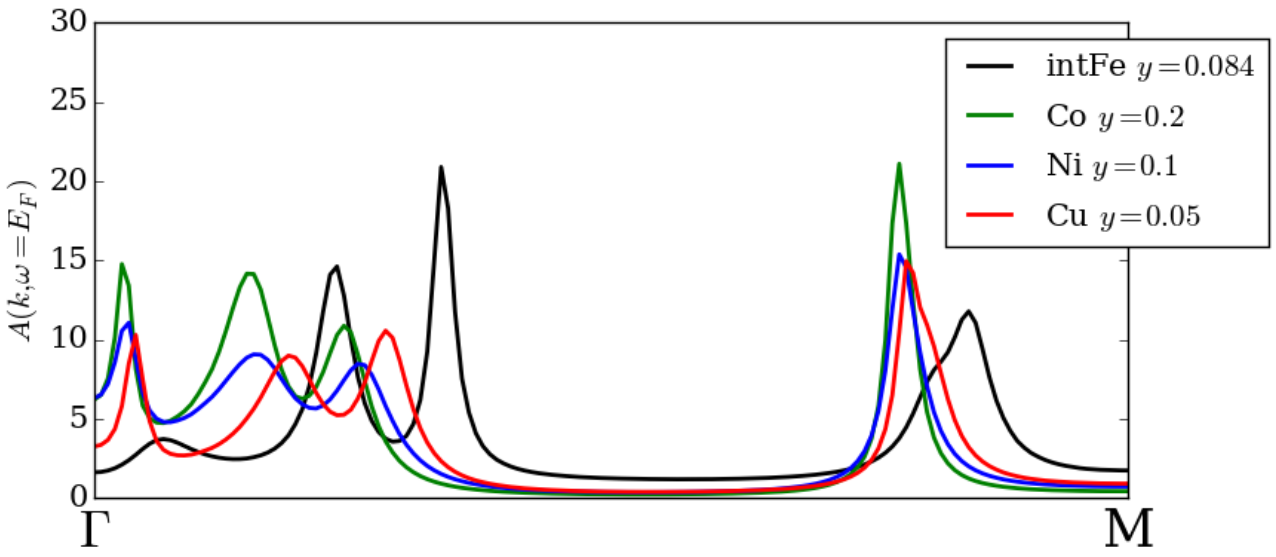

Figure 4.9: Comparison of diagonal cut of Fermi surface cross sections along ΓM for $Fe_{1+0.084}Se_{0.5}Te_{0.5}$ (black), $Fe_{0.8}Co_{0.2}Se_{0.5}Te_{0.5}$ (green), $Fe_{0.9}Ni_{0.1}Se_{0.5}Te_{0.5}$ (blue), and $Fe_{0.95}Cu_{0.05}Se_{0.5}Te_{0.5}$ (red).

The results presented in this chapter allow for another - although highly speculative - conjecture concerning the suppression of superconductivity due to interstitial iron. As we have mentioned above, a possible candidate for superconductivity in Fe(Se,Te) is an $s^{\pm}$ gap function where the pairing mechanism is induced by spin fluctuations due to nesting between hole and electron pockets [149]. Thus, the gradual disappearance of the outer electron pocket could strongly reduce the phase space for such nesting.
However, we must emphasize the highly speculative nature of this proposal. In order to investigate this possibility, a comprehensive theory is needed to determine the influence of the broadening effects on the nesting properties.

4.5 Conclusion and outlook

This chapter has served as a preliminary investigation into the connection between interstitial iron in Fe(Se,Te) and the suppression of superconductivity. To this end, we have applied the coherent potential approximation in combination with the vacancy extension presented in Sec. 2.2 for various interstitial concentrations. We were able to identify two main effects: a minor doping effect, due to the additional electrons introduced by the excess iron, and significant changes to the band structure - and hence the Fermi surfaces.
Our calculations showed two bands to be most prominently affected: on the one hand, the p_z-character band D in the ΓZ line separates and is shifted below the Fermi level. This would severely hinder the strategy presented in Chap. 3 to bring the surface Dirac cone in $FeSe_{0.5}Te_{0.5}$ towards the Fermi level and consequently realize Majorana zero modes. Consequently, it is of paramount importance to grow samples with low interstitial content or reduce excess iron via annealing techniques as described in Ref. [119]. On the other hand, hole band β exhibits a similar behavior, reflected in the gradual disappearance of the corresponding hole pocket of the Fermi surface with increasing interstitial iron content.
In order to make a connection between interstitial iron and the suppression of superconductivity, we have used $3d$ transition metal substitution in $Fe_{1-y}TM_ySe_{0.5}Te_{0.5}$ ($TM = \{Co, Ni, Cu\}$) as a comparison. By examining these compounds for TM concentrations for which superconductivity is known to be suppressed [136–139], we have established a qualitative link to impurity scattering induced by interstitial iron. This was achieved by identifying multiple similarities with respect to Fermi surfaces. For all systems considered, significant broadening of the hole pockets centered around Γ was observed. Most notably, however, are the effects on the electron pockets around M. While the outer electron pocket is already absent in all transition metal compounds, it seems to gradually disappear with increasing interstitial content.
From the broadening of the respective Fermi surfaces we find interstitial iron to result in impurity scattering of comparable strength as in the transition metal compounds for which it leads to a suppression of superconductivity. We thus conclude that the impurity scattering potential is responsible for the suppression of superconductivity with increasing interstitial iron content.
We have further hinted at the possibility of connecting the gradual disappearance of the outer electron pocket to the nesting induced, spin fluctuation driven pairing mechanism proposed by Ref. [149]. However, at this point a possible connection remains highly speculative and further investigation would require a comprehensive theory of the pairing mechanism in Fe(Se,Te). This presents a possible subject for future works to gain further insight into the superconducting mechanism in Fe(Se,Te).
As we have mentioned in the beginning of this chapter, all CPA calculations pertaining to interstitial iron were performed using lattice parameters determined from a sample with $y = 0.084$. Given the strong influence of the actual crystal structure on the electronic properties of Fe(Se,Te) (see Sec. 3.4.1), further investigations into the nature of interstitial iron should make use of the correct lattice parameters determined experimentally from respective samples.

Summary and Conclusion

In this thesis we have analyzed the effects of chemical substitution in the iron-based superconductors with special emphasis on the iron chalcogenide Fe(Se,Te). This chapter serves to summarize the main results and discuss possible future research projects in the context of substitutional disorder and materials design.

The first part of this thesis was concerned with the extension of the coherent potential approximation (CPA) formalism in a pseudopotential density functional theory (DFT) framework derived in earlier work Ref. [6], to include the description of vacancies, spin polarization, and spin-orbit coupling (SOC). Chap. 2 served to establish these extensions and test our theoretical approaches. Furthermore, a method for the computation of the Fermi surface and individual Fermi surface cross sections was devised and implemented. Each of the aforementioned extensions was validated with an appropriate study.
We were able to reproduce the experimentally measured Fermi surface of fcc Cu [60]. Additionally, we have shown our Fermi surface method to work in a substitutional context by demonstrating a gradual transformation of the Fermi surface from fcc Cu to the fcc Ni by studying $Cu_{1-x}Ni_x$ for increasing substitutional degree x.

The vacancy extension was tested by almost completely removing the central atom in body centered cubic Fe, thus resulting in a hypothetical simple cubic structure. A substitution of this atomic site with a vacancy of concentration 99.9% reproduced the band structure and DOS of hypothetical simple cubic Fe to a high degree of accordance. Furthermore, the vacancy extension was shown to be well behaved in the intermediate substitutional regime. Here, both band structure and DOS of bcc Fe with a 50% vacancy at the central site were shown to exhibits features of both bcc and sc Fe - indicating a gradual transition from one system to the other.

The spin polarization extension was shown to reproduce the magnetic moments of bcc Fe and Co to a reasonable degree and yield Fermi surfaces in accordance with the literature [70]. To verify its applicability in a substitutional context, the well established evolution of the magnetic moment in $Fe_{1-x}Co_x$ [37, 71, 72] was studied. Our spin polarized calculations were able to reproduce the overall trend of the averaged magnetic moment with increasing Co content with reasonable accuracy. We were able to replicate the initial increase of the averaged magnetic moment, followed by a gradual decrease towards that of pure Co. Hereby, our results coincided well with TB-LMTO-CPA calculations of Ref. [71], but slightly underestimated experimental results presented in Ref. [37]. Furthermore, charge transfer data and the DOS supplied by our CPA were in good agreement with theoretical explanations of the aforementioned phenomenon [72]. In future works the spin polarized CPA, in combination with the vacancy extension, could be applied to the study of layered magnetic materials which deviate from stoichiometry. A possible system of interest is the 2-dimensional ferromagnet $Fe_{3-x}GeTe_2$, in which the magnetic properties strongly depend on the exact Fe composition [152].

Finally, our SOC extension was benchmarked against MBPP-DFT calculations of bcc Fe. We were able to achieve overall good agreement with respect to the effects of SOC on the band structure - replicating avoided band crossings and lifted degeneracies. The same holds for the calculated Fermi

surface cross section in the $(\bar{1}10)$ plane.

In the second part of this thesis we have applied the CPA to members of the iron-based superconductors. The central topic of this thesis was concerned with band engineering the surface Dirac cone (SDC) in the iron chalcogenide $FeSe_{0.5}Te_{0.5}$ (Chap. 3) so as to bring it into the vicinity of the Fermi level via chemical substitution. This is believed to realize a topological superconducting phase [22] in which Majorana zero modes emerge in vortex cores [19, 85] and furthermore allows access of the SDC to experimental techniques such as transport measurements. These exotic surface states have drawn immense scientific attention over the last two decades, as they constitute promising candidates for the fault-tolerant realization of scalable quantum computers [21, 74–76]

We have first considered the band structure and Fermi surface of FeSe, one of the substitutional end members. Via MBPP-DFT study we have shown the significant impact of the underlying crystal structure on the prerequisites for the formation of a SDC. By varying the interlayer distance c and the chalcogen height z, independently, we have determined a lattice parameter subspace in which these requirements are fulfilled - emphasizing the importance of experimentally determined lattice parameters for our CPA calculations. We have further applied the CPA to study the effect of Te substitution on the band structure and revealing the existence of the SOC gap.

The main goal was to devise a substitutional strategy which lowers the SDC towards the Fermi level while sustaining the SOC gap, despite additional disorder broadening. To this end, we have considered two distinct strategies: $3d$ transition metal substitution at the Fe site, and halogen substitution at the Se site. Both strategies rely on two effects: primarily, an electron doping effect aimed at raising of Fermi level, and secondly a downward shift in energy of the bands connected to the SOC gap. All substitution candidates were chosen taking into account the impact of the lattice parameters on the electronic band structure. Consequently, elements were selected that possess more valence electrons and exhibit similar ionic radii compared to the to-be-substituted types.

The main results are the following: we have shown the transition metal strategy (doping with Co, Ni, and Cu) to be effective in terms of electron doping, i.e., raising the Fermi level in the desired way (see Sec. 3.7.1). However, this strategy was discarded due to strong impurity scattering of the considered candidates. On the one hand, all candidates introduce substantial disorder band broadening potentially concealing the SOC gap and consequently preventing a SDC cone. One the other hand, for the necessary substitutional degrees superconductivity is suppressed [136–139], due to strong impurity scattering, preventing the emergence of Majorana zero modes.

For the second strategy we considered substitution with bromine and iodine at the Se site (see Sec. 3.7.2). For the former candidate an electron doping effect was observed. However, our CPA calculations revealed an excessive relative shift of the relevant bands such that the crossing point vanished before reaching the Fermi level. While these preliminary results exclude Br from our pursuit further investigations employing more realistic lattice parameters might be fruitful, as we have shown the actual lattice parameters to have significant impact on the electronic structure (see Sec. 3.4.1). To this end, attempts to grow an appropriately substituted crystal should be undertaken and calculations repeated with lattice parameters gained from a full characterization.

Our last candidate, iodine, shows great promise in the attempt to realize a single-crystal platform for the emergence of Majorana zero modes. Not only does iodine substitution introduce the additional electrons necessary to raise the Fermi level appropriately, but also the induced disorder band broadening is the smallest among all candidates considered. Our CPA calculations clearly show the SOC gap to survive the additional disorder and to be aligned with the Fermi level. In conclusion, we have theoretically designed a crystal of the form $FeSe_{0.325}I_{0.175}Te_{0.5}$ which exhibits a spin-orbit coupling gap at the Fermi level, thus possessing a topologically nontrivial superconducting phase. The effort

presented in this work has laid the groundwork for a promising route to the realization of a single-crystal platform for the emergence and study of Majorana zero modes.
Future work along this route should be aimed at the growth and full characterization of the proposed compound. Not only is this indispensable for further experimental investigations, but would serve to validate - or refute - the predictions made. Here, the preceding calculations should be repeated with the true lattice parameters to further refine our method and model.

The last chapter of this thesis serves to conclude our investigations into $FeSe_{0.5}Te_{0.5}$. In Chap. 4, we explored the suppression of superconductivity due to interstitial iron content y in $Fe_{1+y}Se_{0.5}Te_{0.5}$ [63–65]. Aside from being of great interest in its own right, the suppression of superconductivity has great baring on the success of the substitution strategy devised in the central part of this work. A loss of superconductivity would exclude the emergence of Majorana zero modes.
The description of excess iron was made possible by the vacancy extension outlined above which allows the treatment of partial occupation. Our CPA calculations revealed two main effects on the electronic properties of the system: a minor electron doping effect due to the occupation of the interstitial site, and significant alterations to the band structure. Of the latter, the effects on the p_z character band along the ΓZ line (connected to the formation of the SDC) were the most relevant to our main goal. A high interstitial content proved detrimental to the existence of the band crossing point at which the SOC gap opens.
The second prominent alteration of the band structure is connected to the electron bands forming the two electron Fermi surface pockets around the high symmetry point M. We were able to show that increasing interstitial content entails significant broadening of the outer electron pocket, culminating in its disappearance.
In order to gain a qualitative estimate of the impurity scattering strength and to draw a possible connection to the suppression of superconductivity, we have compared the Fermi surfaces for varying interstitial content in $Fe_{1+y}Se_{0.5}Te_{0.5}$ to that of transition metal substituted $FeSe_{0.5}Te_{0.5}$. As mentioned above, Co, Ni and Cu are known to destroy the superconducting state, due to their impurity scattering strength. We were able to identify close similarities between the doping effects on the respective Fermi surfaces. Aside from substantial broadening of the hole pockets centered at Γ, the most dominant effects were observed for the outer electron pocket. For all three transition metal candidates, at concentrations for which the superconducting state is known to be destroyed [136–139], only the inner electron pocket at M could be observed. This closely resembles the situation observed for high interstitial content. The comparable extent of Fermi surface broadening in these systems supports the assumption that impurity scattering, due to interstitial iron, plays an important role in the suppression of superconductivity. The results outlined above emphasize the importance of growing crystals with minimal interstitial iron content, so as to preserve superconductivity [64] and not destroy the SDC.
The intricate connection between interstitial iron in Fe(Se,Te) and the suppression of superconductivity warrant further systematic investigations. Future works should focus on the gradual disappearance of the outer Fermi surface electron pocket and strive for a more quantitative description of the observed phenomena. One possible field of research in this context could be the proclaimed $s^{\pm}$ superconducting state and underlying nesting induced pairing mechanism [149] in Fe(Se,Te). In order to estimate the impact of the vanishing electron pocket on the nesting properties, a comprehensive theory of the pairing mechanism is needed. Furthermore, the spin polarized CPA could be applied to study the effects of excess iron on the magnetic properties of $Fe_{1+y}Se_{1-x}Te_x$ [63, 64].

Beyond its relevance for fundamental research, we have seen that a first-principles based theory for chemical substitution in electronic materials can serve as a helping hand in guiding experiment in the search for new and fascinating materials.

On a more general level, this thesis has accomplished the following central achievements. This thesis has extensively increased the versatility of the CPA formalism and its implementation in a pseudopotential density functional theory framework. The developed functionalities grant access to the study of a multitude of fascinating physical phenomena, such as magnetic order and systems with relevant spin-orbit interactions. Conceptually, this thesis has shown the applicability of the CPA in the context of virtual materials design. It has employed design principles to tailor specific electronic properties of solid states systems. However, the hallmark of science is its aspiration to scrutinize its predictions, and the same holds for the results presented in this work. It is of paramount importance to validate the statements made in close cooperation with experiment and to further refine the underlying models and methods. In conclusion, this thesis shows that an *ab-initio* treatment of substitutional disorder can provide an efficient and versatile tool in the search for new and exotic states of matter.

Bibliography

[1] P. Soven, *Coherent-Potential Model of Substitutional Disordered Alloys*, Phys. Rev. **156**, 809 (1967).

[2] D. W. Taylor, *Vibrational Properties of Imperfect Crystals with Large Defect Concentrations*, Phys. Rev. **156**, 1017 (1967).

[3] J. A. Blackman, D. M. Esterling, and N. F. Berk, *Generalized Locator-Coherent-Potential Approach to Binary Alloys*, Phys. Rev. B **4**, 2412 (1971).

[4] J. Korringa, *On the calculation of the energy of a Bloch wave in a metal*, Physica **13**, 392 (1947).

[5] W. Kohn and N. Rostoker, *Solution of the Schrödinger Equation in Periodic Lattices with an Application to Metallic Lithium*, Phys. Rev. **94**, 1111 (1954).

[6] A. Herbig, *Ab-initio Electronic Structure Method for Substitutional Disorder Applied to Iron-Based Superconductors*, Ph.D. thesis, Karlsruher Institut für Technologie (KIT) (2016).

[7] Y. Kamihara, T. Watanabe, M. Hirano, and H. Hosono, *Iron-Based Layered Superconductor $La[O_{1-x}F_x]FeAs$ ($x = 0.05-0.12$) with $T_c = 26$ K*, Journal of the American Chemical Society **130**, 3296 (2008).

[8] A. Martinelli, F. Bernardini, and S. Massidda, *The phase diagrams of iron-based superconductors: Theory and experiments*, Comptes Rendus Physique **17**, 5 (2016).

[9] F. Hardy, P. Burger, T. Wolf, R. A. Fisher, P. Schweiss, P. Adelmann, R. Heid, R. Fromknecht, R. Eder, D. Ernst, H. v. Löhneysen, and C. Meingast, *Doping evolution of superconducting gaps and electronic densities of states in $Ba(Fe_{1-x}Co_x)_2As_2$ iron pnictides*, EPL (Europhysics Letters) **91**, 47008 (2010).

[10] A. E. Böhmer, P. Burger, F. Hardy, T. Wolf, P. Schweiss, R. Fromknecht, H. v. Löhneysen, C. Meingast, H. K. Mak, R. Lortz, S. Kasahara, T. Terashima, T. Shibauchi, and Y. Matsuda, *Thermodynamic phase diagram, phase competition, and uniaxial pressure effects in $BaFe_2(As_{1-x}P_x)_2$ studied by thermal expansion*, Phys. Rev. B **86**, 094521 (2012).

[11] K. Matsuura, Y. Mizukami, Y. Arai, Y. Sugimura, N. Maejima, A. Machida, T. Watanuki, T. Fukuda, T. Yajima, Z. Hiroi, K. Y. Yip, Y. C. Chan, Q. Niu, S. Hosoi, K. Ishida, K. Mukasa, S. Kasahara, J.-G. Cheng, S. K. Goh, Y. Matsuda, Y. Uwatoko, and T. Shibauchi, *Maximizing T_c by tuning nematicity and magnetism in $FeSe_{1-x}S_x$ superconductors*, Nature Communications **8**, 1143 (2017).

[12] J. G. Bednorz and K. A. Müller, *Possible highT_c superconductivity in the Ba-La-Cu-O system*, Zeitschrift für Physik B Condensed Matter **64**, 189 (1986).

[13] Q.-Y. Wang, Z. Li, W.-H. Zhang, Z.-C. Zhang, J.-S. Zhang, W. Li, H. Ding, Y.-B. Ou, P. Deng, K. Chang, J. Wen, C.-L. Song, K. He, J.-F. Jia, S.-H. Ji, Y.-Y. Wang, L.-L. Wang, X. Chen, X.-C. Ma, and Q.-K. Xue, *Interface-Induced High-Temperature Superconductivity in Single Unit-Cell FeSe Films on $SrTiO_3$*, Chinese Physics Letters **29**, 037402 (2012).

[14] Z. Wang, C. Liu, Y. Liu, and J. Wang, *High-temperature superconductivity in one-unit-cell FeSe films*, Journal of Physics: Condensed Matter **29**, 153001 (2017).

[15] S. Medvedev, T. M. McQueen, I. A. Troyan, T. Palasyk, M. I. Eremets, R. J. Cava, S. Naghavi, F. Casper, V. Ksenofontov, G. Wortmann, and C. Felser, *Electronic and magnetic phase diagram of β-$Fe_{1.01}Se$ with superconductivity at 36.7 K under pressure*, Nature Materials **8**, 630 (2009).

[16] L. Landau, *The Theory of Phase Transitions*, Nature **138**, 840 (1936).

[17] K. v. Klitzing, G. Dorda, and M. Pepper, *New Method for High-Accuracy Determination of the Fine-Structure Constant Based on Quantized Hall Resistance*, Phys. Rev. Lett. **45**, 494 (1980).

[18] D. J. Thouless, M. Kohmoto, M. P. Nightingale, and M. den Nijs, *Quantized Hall Conductance in a Two-Dimensional Periodic Potential*, Phys. Rev. Lett. **49**, 405 (1982).

[19] Z. Wang, P. Zhang, G. Xu, L. K. Zeng, H. Miao, X. Xu, T. Qian, H. Weng, P. Richard, A. V. Fedorov, H. Ding, X. Dai, and Z. Fang, *Topological nature of the $FeSe_{0.5}Te_{0.5}$ superconductor*, Phys. Rev. B **92**, 115119 (2015).

[20] A. Y. Kitaev, *Unpaired Majorana fermions in quantum wires*, Physics-Uspekhi **44**, 131 (2001).

[21] A. Kitaev, *Fault-tolerant quantum computation by anyons*, Annals of Physics **303**, 2 (2003).

[22] G. Xu, B. Lian, P. Tang, X.-L. Qi, and S.-C. Zhang, *Topological Superconductivity on the Surface of Fe-Based Superconductors*, Phys. Rev. Lett. **117**, 047001 (2016).

[23] R. Car and M. Parrinello, *Unified Approach for Molecular Dynamics and Density-Functional Theory*, Phys. Rev. Lett. **55**, 2471 (1985).

[24] S. D. Wong, M. Srnec, M. L. Matthews, L. V. Liu, Y. Kwak, K. Park, C. B. Bell III, E. E. Alp, J. Zhao, Y. Yoda, S. Kitao, M. Seto, C. Krebs, J. M. Bollinger, and E. I. Solomon, *Elucidation of the Fe(IV)=O intermediate in the catalytic cycle of the halogenase SyrB2*, Nature **499**, 320 (2013).

[25] E. Fermi, *Eine statistische Methode zur Bestimmung einiger Eigenschaften des Atoms und ihre Anwendung auf die Theorie des periodischen Systems der Elemente*, Zeitschrift für Physik **48**, 73 (1928).

[26] L. H. Thomas, *The calculation of atomic fields*, Mathematical Proceedings of the Cambridge Philosophical Society **23**, 542–548 (1927).

[27] P. A. M. Dirac, *Note on Exchange Phenomena in the Thomas Atom*, Mathematical Proceedings of the Cambridge Philosophical Society **26**, 376–385 (1930).

[28] P. Hohenberg and W. Kohn, *Inhomogeneous Electron Gas*, Phys. Rev. **136**, B864 (1964).

[29] W. Kohn and L. J. Sham, *Self-Consistent Equations Including Exchange and Correlation Effects*, Phys. Rev. **140**, A1133 (1965).

[30] B. Meyer, F. Lechermann, C. Elsässer, and M. Fähnle, *Fortran90 Program for Mixed-Basis Pseudopotential Calculations for Crystals*, Max-Planck-Institute für Metallforschung, Stuttgart (1998).

[31] B. Meyer, *Entwicklung eines neuen ab-initio "mixed-basis"-Pseudopotentialprogrammes und Untersuchung atomarer Fehlstellen in Molybdän und intermetallischen Verbindungen*, Dissertation (Cuvillier Verlag, Göttingen, 1999).

[32] D. Vanderbilt, *Optimally smooth norm-conserving pseudopotentials*, Phys. Rev. B **32**, 8412 (1985).

[33] S. G. Louie, K.-M. Ho, and M. L. Cohen, *Self-consistent mixed-basis approach to the electronic structure of solids*, Phys. Rev. B **19**, 1774 (1979).

[34] H. Ebert, D. Ködderitzsch, and J. Minar, *Calculating condensed matter properties using the KKR-Green's function method - Recent developments and applications*, Reports on Progress in Physics **74**, 096501 (2011).

[35] G. M. Stocks, W. M. Temmerman, and B. L. Gyorffy, *Complete Solution of the Korringa-Kohn-Rostoker Coherent-Potential-Approximation Equations: Cu-Ni Alloys*, Phys. Rev. Lett. **41**, 339 (1978).

[36] J. Kudrnovský, V. Drchal, and J. Maek, *Canonical description of electron states in random alloys*, Phys. Rev. B **35**, 2487 (1987).

[37] K. Koepernik, B. Velický, R. Hayn, and H. Eschrig, *Self-consistent LCAO-CPA Method for Disordered Alloys*, Phys. Rev. B **55**, 5717 (1997).

[38] R. Richter, H. Eschrig, and B. Velicky, *LCAO approach to the coherent potential approximation: electronic structure of substitutionally disordered CuNi alloys*, Journal of Physics F: Metal Physics **17**, 351 (1987).

[39] H. Shiba, *A Reformulation of the Coherent Potential Approximation and Its Applications*, Progress of Theoretical Physics **46**, 77 (1971).

[40] D. A. Rowlands, *Short-range correlations in disordered systems: nonlocal coherent-potential approximation*, Reports on Progress in Physics **72**, 086501 (2009).

[41] T. Matsubara and Y. Toyozawa, *Theory of Impurity Band Conduction in Semiconductors: An Approach to Random Lattice Problem*, Progress of Theoretical Physics **26**, 739 (1961).

[42] F. Brouers, M. Cyrot, and F. Cyrot-Lackman, *Bethe-Peierls Approximation in the Electronic Theory of Disordered Materials*, Phys. Rev. B **7**, 4370 (1973).

[43] M. Tsukada, *Contribution to the Many Site Theory of the Disordered System*, Journal of the Physical Society of Japan **32**, 1475 (1972).

[44] M. Jarrell and H. R. Krishnamurthy, *Systematic and causal corrections to the coherent potential approximation*, Phys. Rev. B **63**, 125102 (2001).

[45] A. Gonis and J. W. Garland, *Rederivation and proof of analyticity of the Blackman-Esterling-Berk approximation*, Phys. Rev. B **16**, 1495 (1977).

[46] D. Sanchez-Portal, E. Artacho, and J. M. Soler, *Projection of plane-wave calculations into atomic orbitals*, Solid State Communications **95**, 685 (1995).

[47] D. Sánchez-Portal, E. Artacho, and J. M. Soler, *Analysis of atomic orbital basis sets from the projection of plane-wave results*, Journal of Physics: Condensed Matter **8**, 3859 (1996).

[48] C. G. J. Jacobi, *Ueber Gauß neue Methode, die Werthe der Integrale näherungsweise zu finden*, Journal für die reine und angewandte Mathematik **1** (1826).

[49] J. Stoer, *Numerische Mathematik 1*, Springer-Verlag Berlin Heidelberg, 9th ed. (2005).

[50] J. B. Scarborough, *Numerical Mathematical Analysis*, The John Hopkins Press, Baltimore (1966).

[51] P. Horsch and P. Fulde, *On the theory of electronic correlations in solids*, Zeitschrift für Physik B Condensed Matter **36**, 23 (1979).

[52] G. Stollhoff and A. Heiligbrunner, *Coupled-cluster-equations for the local ansatz*, Zeitschrift für Physik B Condensed Matter **83**, 85 (1991).

[53] A. A. Abrikosov, G. L. P., and I. E. Dzyaloshinski, *Methods of quantum field theory in statistical physics*, Dover Publications Inc. (1975).

[54] G. D. Mahan, *Many-particle Physics*, Springer (1990).

[55] D. D. Johnson, *Modified Broyden's method for accelerating convergence in self-consistent calculations*, Phys. Rev. B **38**, 12807 (1988).

[56] A. R. Mackintosh, *The Fermi Surface of Metals*, Scientific American **209**, 110 (1963).

[57] R. Peierls, *Zur Theorie der elektrischen und thermischen Leitfähigkeit von Metallen*, Annalen der Physik **396**, 121 (1930).

[58] K. Terashima, Y. Sekiba, J. H. Bowen, K. Nakayama, T. Kawahara, T. Sato, P. Richard, Y.-M. Xu, L. J. Li, G. H. Cao, Z.-A. Xu, H. Ding, and T. Takahashi, *Fermi surface nesting induced strong pairing in iron-based superconductors*, Proceedings of the National Academy of Sciences **106**, 7330 (2009).

[59] M. Sunagawa, T. Ishiga, K. Tsubota, T. Jabuchi, J. Sonoyama, K. Iba, K. Kudo, M. Nohara, K. Ono, H. Kumigashira, T. Matsushita, M. Arita, K. Shimada, H. Namatame, M. Taniguchi, T. Wakita, Y. Muraoka, and T. Yokoya, *Characteristic two-dimensional Fermi surface topology of high-T_c iron-based superconductors*, Scientific Reports **4**, 4381 (2014).

[60] A. B. Pippard, *An experimental determination of the Fermi surface in copper*, Philosophical Transactions of the Royal Society of London. Series A, Mathematical and Physical Sciences **250**, 325 (1957).

[61] W. Setyawan and S. Curtarolo, *High-throughput electronic band structure calculations: Challenges and tools*, Computational Materials Science **49**, 299 (2010).

[62] B. Segall, *Fermi Surface and Energy Bands of Copper*, Phys. Rev. **125**, 109 (1962).

[63] M. Bendele, P. Babkevich, S. Katrych, S. N. Gvasaliya, E. Pomjakushina, K. Conder, B. Roessli, A. T. Boothroyd, R. Khasanov, and H. Keller, *Tuning the superconducting and magnetic properties of* $Fe_ySe_{0.25}Te_{0.75}$ *by varying the iron content*, Phys. Rev. B **82**, 212504 (2010).

[64] R. Viennois, E. Giannini, D. van der Marel, and R. Černý, *Effect of Fe excess on structural, magnetic and superconducting properties of single-crystalline* $Fe_{1+x}Te_{1-y}Se_y$, Journal of Solid State Chemistry **183**, 769 (2010).

[65] E. E. Rodriguez, C. Stock, P.-Y. Hsieh, N. P. Butch, J. Paglione, and M. A. Green, *Chemical control of interstitial iron leading to superconductivity in* $Fe_{1+x}Te_{0.7}Se_{0.3}$, Chem. Sci. **2**, 1782 (2011).

[66] Z.-A. Ren, G.-C. Che, X.-L. Dong, J. Yang, W. Lu, W. Yi, X.-L. Shen, Z.-C. Li, L.-L. Sun, F. Zhou, and Z.-X. Zhao, *Superconductivity and phase diagram in iron-based arsenic-oxides* $ReFeAsO_{1-\delta}$ *(Re = rare-earth metal) without fluorine doping*, EPL (Europhysics Letters) **83**, 17002 (2008).

[67] H. Kito, H. Eisaki, and A. Iyo, *Superconductivity at 54 K in F-free* $NdFeAsO_{1-y}$, Journal of the Physical Society of Japan **77** (2008).

[68] C. de la Cruz, Q. Huang, J. W. Lynn, J. Li, W. R. II, J. L. Zarestky, H. A. Mook, G. F. Chen, J. L. Luo, N. L. Wang, and P. Dai, *Magnetic order close to superconductivity in the iron-based layered* $LaO_{1-x}F_x$ *FeAs systems*, Nature **453**, 899 (2008).

[69] P. Dai, *Antiferromagnetic order and spin dynamics in iron-based superconductors*, Rev. Mod. Phys. **87**, 855 (2015).

[70] R. A. Tawil and J. Callaway, *Energy Bands in Ferromagnetic Iron*, Phys. Rev. B **7**, 4242 (1973).

[71] I. Turek, J. Kudrnovský, V. Drchal, and P. Weinberger, *Itinerant magnetism of disordered Fe-Co and Ni-Cu alloys in two and three dimensions*, Phys. Rev. B **49**, 3352 (1994).

[72] R. Richter and H. Eschrig, *LCAO-CPA for disordered ferromagnetic 3d transition metal alloys. magnetic moment formation in NiCu and FeCo*, Physica Scripta **37**, 948 (1988).

[73] C. L. Kane and E. J. Mele, *Quantum Spin Hall Effect in Graphene*, Phys. Rev. Lett. **95**, 226801 (2005).

[74] J. Alicea, *New directions in the pursuit of Majorana fermions in solid state systems*, Reports on Progress in Physics **75**, 076501 (2012).

[75] C. Nayak, S. H. Simon, A. Stern, M. Freedman, and S. Das Sarma, *Non-Abelian anyons and topological quantum computation*, Rev. Mod. Phys. **80**, 1083 (2008).

[76] M. Sato and Y. Ando, *Topological superconductors: a review*, Reports on Progress in Physics **80**, 076501 (2017).

[77] M. H. Fang, H. M. Pham, B. Qian, T. J. Liu, E. K. Vehstedt, Y. Liu, L. Spinu, and Z. Q. Mao, *Superconductivity close to magnetic instability in* $Fe(Se_{1-x}Te_x)_{0.82}$, Phys. Rev. B **78**, 224503 (2008).

[78] B. C. Sales, A. S. Sefat, M. A. McGuire, R. Y. Jin, D. Mandrus, and Y. Mozharivskyj, *Bulk superconductivity at 14 K in single crystals of $Fe_{1+y}Te_xSe_{1-x}$*, Phys. Rev. B **79**, 094521 (2009).

[79] K.-W. Yeh, T.-W. Huang, Y. lin Huang, T.-K. Chen, F.-C. Hsu, P. M. Wu, Y.-C. Lee, Y.-Y. Chu, C.-L. Chen, J.-Y. Luo, D.-C. Yan, and M.-K. Wu, *Tellurium substitution effect on superconductivity of the α-phase iron selenide*, EPL (Europhysics Letters) **84**, 37002 (2008).

[80] K. Horigane, N. Takeshita, C.-H. Lee, H. Hiraka, and K. Yamada, *First Investigation of Pressure Effects on Transition from Superconductive to Metallic Phase in $FeSe_{0.5}Te_{0.5}$*, Journal of the Physical Society of Japan **78**, 063705 (2009).

[81] F. Li, H. Ding, C. Tang, J. Peng, Q. Zhang, W. Zhang, G. Zhou, D. Zhang, C.-L. Song, K. He, S. Ji, X. Chen, L. Gu, L. Wang, X.-C. Ma, and Q.-K. Xue, *Interface-enhanced high-temperature superconductivity in single-unit-cell $FeTe_{1-x}Se_x$ films on $SrTiO_3$*, Phys. Rev. B **91**, 220503 (2015).

[82] S. Li, C. de la Cruz, Q. Huang, Y. Chen, J. W. Lynn, J. Hu, Y.-L. Huang, F.-C. Hsu, K.-W. Yeh, M.-K. Wu, and P. Dai, *First-order magnetic and structural phase transitions in $Fe_{1+y}Se_xTe_{1-x}$*, Phys. Rev. B **79**, 054503 (2009).

[83] X. Wu, S. Qin, Y. Liang, H. Fan, and J. Hu, *Topological characters in $FeTe_{1-x}Se_x$) thin films*, Phys. Rev. B **93**, 115129 (2016).

[84] L. C. C. Ambolode, K. Okazaki, M. Horio, H. Suzuki, L. Liu, S. Ideta, T. Yoshida, T. Mikami, T. Kakeshita, S. Uchida, K. Ono, H. Kumigashira, M. Hashimoto, D.-H. Lu, Z.-X. Shen, and A. Fujimori, *Dependence of electron correlation strength in $Fe_{1+y}Te_{1-x}Se_x$ on Se content*, Phys. Rev. B **92**, 035104 (2015).

[85] P. Zhang, K. Yaji, T. Hashimoto, Y. Ota, T. Kondo, K. Okazaki, Z. Wang, J. Wen, G. D. Gu, H. Ding, and S. Shin, *Observation of topological superconductivity on the surface of an iron-based superconductor*, Science (2018).

[86] D. Wang, L. Kong, P. Fan, H. Chen, S. Zhu, W. Liu, L. Cao, Y. Sun, S. Du, J. Schneeloch, R. Zhong, G. Gu, L. Fu, H. Ding, and H.-J. Gao, *Evidence for Majorana bound states in an iron-based superconductor*, Science **362**, 333 (2018).

[87] T. Machida, Y. Sun, S. Pyon, S. Takeda, Y. Kohsaka, T. Hanaguri, T. Sasagawa, and T. Tamegai, *Zero-energy vortex bound state in the superconducting topological surface state of Fe(Se,Te)*, Nature Materials **18**, 811 (2019).

[88] L. Fu and C. L. Kane, *Superconducting Proximity Effect and Majorana Fermions at the Surface of a Topological Insulator*, Phys. Rev. Lett. **100**, 096407 (2008).

[89] L. Lauke, R. Heid, M. Merz, T. Wolf, A.-A. Haghighirad, and J. Schmalian, *Band engineering of Dirac cones in iron chalcogenides*, Phys. Rev. B **102**, 054209 (2020).

[90] J. Bardeen, L. N. Cooper, and J. R. Schrieffer, *Microscopic Theory of Superconductivity*, Phys. Rev. **106**, 162 (1957).

[91] S. J., *Potentials of iron-based superconductors for practical future materials*, Superconductor Science and Technology **27**, 044002 (2014).

[92] P. Anderson, *Theory of dirty superconductors*, Journal of Physics and Chemistry of Solids **11**, 26 (1959).

[93] Y. Kamihara, H. Hiramatsu, M. Hirano, R. Kawamura, H. Yanagi, T. Kamiya, and H. Hosono, *Iron-based layered superconductor: LaOFeP*, Journal of the American Chemical Society **128**, 10012 (2006).

[94] R. Zhi-An, L. Wei, Y. Jie, Y. Wei, S. Xiao-Li, Zheng-Cai, C. Guang-Can, D. Xiao-Li, S. Li-Ling, Z. Fang, and Z. Zhong-Xian, *Superconductivity at 55 K in Iron-Based F-Doped Layered Quaternary Compound Sm[$O_{1-x}F_x$]FeAs*, Chinese Physics Letters **25**, 2215 (2008).

[95] K. Kuroki, S. Onari, R. Arita, H. Usui, Y. Tanaka, H. Kontani, and H. Aoki, *Unconventional Pairing Originating from the Disconnected Fermi Surfaces of Superconducting $LaFeAsO_{1-x}F_x$*, Phys. Rev. Lett. **101**, 087004 (2008).

[96] I. I. Mazin, D. J. Singh, M. D. Johannes, and M. H. Du, *Unconventional Superconductivity with a Sign Reversal in the Order Parameter of $LaFeAsO_{1-x}F_x$*, Phys. Rev. Lett. **101**, 057003 (2008).

[97] I. Mazin and J. Schmalian, *Pairing symmetry and pairing state in ferropnictides: Theoretical overview*, Physica C: Superconductivity **469**, 614 (2009).

[98] M. D. Lumsden, A. D. Christianson, D. Parshall, M. B. Stone, S. E. Nagler, G. J. MacDougall, H. A. Mook, K. Lokshin, T. Egami, D. L. Abernathy, E. A. Goremychkin, R. Osborn, M. A. McGuire, A. S. Sefat, R. Jin, B. C. Sales, and D. Mandrus, *Two-dimensional resonant magnetic excitation in $BaFe_{1.84}Co_{0.16}As_2$*, Phys. Rev. Lett. **102**, 107005 (2009).

[99] H. Kontani and S. Onari, *Orbital-Fluctuation-Mediated Superconductivity in Iron Pnictides: Analysis of the Five-Orbital Hubbard-Holstein Model*, Phys. Rev. Lett. **104**, 157001 (2010).

[100] Y. Yanagi, Y. Yamakawa, and Y. Ōno, *Two types of s-wave pairing due to magnetic and orbital fluctuations in the two-dimensional 16-band $d-p$ model for iron-based superconductors*, Phys. Rev. B **81**, 054518 (2010).

[101] E.-M. Choi, S.-G. Jung, N. H. Lee, Y.-S. Kwon, W. N. Kang, D. H. Kim, M.-H. Jung, S.-I. Lee, and L. Sun, *In situ fabrication of cobalt-doped SrFe2As2 thin films by using pulsed laser deposition with excimer laser*, Applied Physics Letters **95**, 062507 (2009).

[102] J. Hänisch, K. Iida, R. Hühne, and C. Tarantini, *Fe-based superconducting thin films—preparation and tuning of superconducting properties*, Superconductor Science and Technology **32**, 093001 (2019).

[103] H. Hosono and K. Kuroki, *Iron-based superconductors: Current status of materials and pairing mechanism*, Physica C: Superconductivity and its Applications **514**, 399 (2015).

[104] A. I. Coldea and M. D. Watson, *The Key Ingredients of the Electronic Structure of FeSe*, Annual Review of Condensed Matter Physics **9**, 125 (2018).

[105] P. O. Sprau, A. Kostin, A. Kreisel, A. E. Böhmer, V. Taufour, P. C. Canfield, S. Mukherjee, P. J. Hirschfeld, B. M. Andersen, and J. C. S. Davis, *Discovery of orbital-selective Cooper pairing in FeSe*, Science **357**, 75 (2017).

[106] M. A. Tanatar, A. E. Böhmer, E. I. Timmons, M. Schütt, G. Drachuck, V. Taufour, K. Kothapalli, A. Kreyssig, S. L. Bud'ko, P. C. Canfield, R. M. Fernandes, and R. Prozorov, *Origin of the Resistivity Anisotropy in the Nematic Phase of FeSe*, Phys. Rev. Lett. **117**, 127001 (2016).

[107] A. E. Böhmer, F. Hardy, F. Eilers, D. Ernst, P. Adelmann, P. Schweiss, T. Wolf, and C. Meingast, *Lack of coupling between superconductivity and orthorhombic distortion in stoichiometric single-crystalline FeSe*, Phys. Rev. B **87**, 180505 (2013).

[108] A. E. Böhmer, V. Taufour, W. E. Straszheim, T. Wolf, and P. C. Canfield, *Variation of transition temperatures and residual resistivity ratio in vapor-grown FeSe*, Phys. Rev. B **94**, 024526 (2016).

[109] Y. Mizuguchi, F. Tomioka, S. Tsuda, T. Yamaguchi, and Y. Takano, *Superconductivity in S-substituted FeTe*, Applied Physics Letters **94**, 012503 (2009).

[110] W. Bao, Y. Qiu, Q. Huang, M. A. Green, P. Zajdel, M. R. Fitzsimmons, M. Zhernenkov, S. Chang, M. Fang, B. Qian, E. K. Vehstedt, J. Yang, H. M. Pham, L. Spinu, and Z. Q. Mao, *Tunable ($\delta\pi$, $\delta\pi$)-Type Antiferromagnetic Order in α-Fe(Te,Se) Superconductors*, Phys. Rev. Lett. **102**, 247001 (2009).

[111] Z. Yin, K. Haule, and G. Kotliar, *Kinetic frustration and the nature of the magnetic and paramagnetic states in iron pnictides and iron chalcogenides*, Nature materials **10**, 932 (2011).

[112] M. K. Frampton, J. Crocker, D. A. Gilbert, N. Curro, K. Liu, J. A. Schneeloch, G. D. Gu, and R. J. Zieve, *First-order reversal curve of the magnetostructural phase transition in FeTe*, Phys. Rev. B **95**, 214402 (2017).

[113] L. Zhang, D. J. Singh, and M. H. Du, *Density functional study of excess Fe in $Fe_{1+x}Te$: Magnetism and doping*, Phys. Rev. B **79**, 012506 (2009).

[114] K. Horigane, N. Takeshita, C.-H. Lee, H. Hiraka, and K. Yamada, *First Investigation of Pressure Effects on Transition from Superconductive to Metallic Phase in $FeSe_{0.5}Te_{0.5}$*, Journal of the Physical Society of Japan **78**, 063705 (2009).

[115] J. Yin, Z. Wu, J. Wang, Z. Ye, J. Gong, X. Hou, L. Shan, A. Li, X. Liang, X. Wu, J. Li, C. Ting, Z.-Q. Wang, J. Hu, P. Hor, H. Ding, and S. Pan, *Observation of a Robust Zero-energy Bound State in Iron-based Superconductor Fe(Te,Se)*, Nature Physics **11** (2014).

[116] E. Majorana, *Teoria simmetrica dell'elettrone e del positrone*, Il Nuovo Cimento (1924-1942) **14**, 171 (2008).

[117] F. Wilczek, *Majorana returns*, Nature Physics **5**, 614 (2009).

[118] S. R. Elliott and M. Franz, *Colloquium: Majorana fermions in nuclear, particle, and solid-state physics*, Rev. Mod. Phys. **87**, 137 (2015).

[119] Y. Sun, Z. Shi, and T. Tamegai, *Review of annealing effects and superconductivity in $Fe_{1+y}Te_{1-x}Se_x$ superconductors*, Superconductor Science and Technology **32**, 103001 (2019).

[120] V. Mourik, K. Zuo, S. M. Frolov, S. R. Plissard, E. P. A. M. Bakkers, and L. P. Kouwenhoven, *Signatures of Majorana Fermions in Hybrid Superconductor-Semiconductor Nanowire Devices*, Science **336**, 1003 (2012).

[121] M. T. Deng, S. Vaitiekenas, E. B. Hansen, J. Danon, M. Leijnse, K. Flensberg, J. Nygård, P. Krogstrup, and C. M. Marcus, *Majorana bound state in a coupled quantum-dot hybrid-nanowire system*, Science **354**, 1557 (2016).

[122] S. Nadj-Perge, I. K. Drozdov, J. Li, H. Chen, S. Jeon, J. Seo, A. H. MacDonald, B. A. Bernevig, and A. Yazdani, *Observation of Majorana fermions in ferromagnetic atomic chains on a superconductor*, Science **346**, 602 (2014).

[123] H.-H. Sun, K.-W. Zhang, L.-H. Hu, C. Li, G.-Y. Wang, H.-Y. Ma, Z.-A. Xu, C.-L. Gao, D.-D. Guan, Y.-Y. Li, C. Liu, D. Qian, Y. Zhou, L. Fu, S.-C. Li, F.-C. Zhang, and J.-F. Jia, *Majorana Zero Mode Detected with Spin Selective Andreev Reflection in the Vortex of a Topological Superconductor*, Phys. Rev. Lett. **116**, 257003 (2016).

[124] M. S. Dresselhaus, G. Dresselhaus, and A. Jorio, *Group Theory*, Springer-Verlag Berlin Heidelberg, 1st ed. (2008).

[125] *Théorie générale de la rotation paramagnétique dans les cristaux*, vol. 33, Proceedings of the Royal Netherlands Academy of Arts and Sciences (1930).

[126] L. Fu and C. L. Kane, *Topological insulators with inversion symmetry*, Phys. Rev. B **76**, 045302 (2007).

[127] L. Fu, C. L. Kane, and E. J. Mele, *Topological insulators in three dimensions*, Phys. Rev. Lett. **98**, 106803 (2007).

[128] H. Lohani, T. Hazra, A. Ribak, Y. Nitzav, H. Fu, B. Yan, M. Randeria, and A. Kanigel, *Band inversion and topology of the bulk electronic structure in* $FeSe_{0.45}Te_{0.55}$, Phys. Rev. B **101**, 245146 (2020).

[129] M. D. Watson, A. A. Haghighirad, L. C. Rhodes, M. Hoesch, and T. K. Kim, *Electronic anisotropies revealed by detwinned angle-resolved photo-emission spectroscopy measurements of FeSe*, New Journal of Physics **19**, 103021 (2017).

[130] M. D. Watson, S. Backes, A. A. Haghighirad, M. Hoesch, T. K. Kim, A. I. Coldea, and R. Valentí, *Formation of Hubbard-like bands as a fingerprint of strong electron-electron interactions in FeSe*, Phys. Rev. B **95**, 081106 (2017).

[131] M. D. Watson, T. K. Kim, A. A. Haghighirad, N. R. Davies, A. McCollam, A. Narayanan, S. F. Blake, Y. L. Chen, S. Ghannadzadeh, A. J. Schofield, M. Hoesch, C. Meingast, T. Wolf, and A. I. Coldea, *Emergence of the nematic electronic state in FeSe*, Phys. Rev. B **91**, 155106 (2015).

[132] J. Maletz, V. B. Zabolotnyy, D. V. Evtushinsky, S. Thirupathaiah, A. U. B. Wolter, L. Harnagea, A. N. Yaresko, A. N. Vasiliev, D. A. Chareev, A. E. Böhmer, F. Hardy, T. Wolf, C. Meingast, E. D. L. Rienks, B. Büchner, and S. V. Borisenko, *Unusual band renormalization in the simplest iron-based superconductor* $FeSe_{1-x}$, Phys. Rev. B **89**, 220506 (2014).

[133] M. D. Watson, T. K. Kim, A. A. Haghighirad, N. R. Davies, A. McCollam, A. Narayanan, S. F. Blake, Y. L. Chen, S. Ghannadzadeh, A. J. Schofield, M. Hoesch, C. Meingast, T. Wolf, and A. I. Coldea, *Emergence of the nematic electronic state in FeSe*, Phys. Rev. B **91**, 155106 (2015).

[134] T. Shimojima, Y. Suzuki, T. Sonobe, A. Nakamura, M. Sakano, J. Omachi, K. Yoshioka, M. Kuwata-Gonokami, K. Ono, H. Kumigashira, A. E. Böhmer, F. Hardy, T. Wolf, C. Meingast, H. v. Löhneysen, H. Ikeda, and K. Ishizaka, *Lifting of xz/yz orbital degeneracy at the structural transition in detwinned FeSe*, Phys. Rev. B **90**, 121111 (2014).

[135] M. D. Watson, T. Yamashita, S. Kasahara, W. Knafo, M. Nardone, J. Béard, F. Hardy, A. McCollam, A. Narayanan, S. F. Blake, T. Wolf, A. A. Haghighirad, C. Meingast, A. J. Schofield, H. v. Löhneysen, Y. Matsuda, A. I. Coldea, and T. Shibauchi, *Dichotomy between the Hole and Electron Behavior in Multiband Superconductor FeSe Probed by Ultrahigh Magnetic Fields*, Phys. Rev. Lett. **115**, 027006 (2015).

[136] E. L. Thomas, W. Wong-Ng, D. Phelan, and J. N. Millican, *Thermopower of Co-doped FeSe*, Journal of Applied Physics **105**, 073906 (2009).

[137] T. Urata, Y. Tanabe, K. K. Huynh, Y. Yamakawa, H. Kontani, and K. Tanigaki, *Superconductivity pairing mechanism from cobalt impurity doping in FeSe: Spin ($s_{\pm}$) or orbital (s_{++}) fluctuation*, Phys. Rev. B **93**, 014507 (2016).

[138] Y. Mizuguchi, F. Tomioka, S. Tsuda, T. Yamaguchi, and Y. Takano, *Substitution Effects on FeSe Superconductor*, Journal of the Physical Society of Japan **78**, 074712 (2009).

[139] A. J. Williams, T. M. McQueen, V. Ksenofontov, C. Felser, and R. J. Cava, *The metal-insulator transition in $Fe_{1.01-x}Cu_xSe$*, Journal of Physics: Condensed Matter **21**, 305701 (2009).

[140] M. C. Rahn, R. A. Ewings, S. J. Sedlmaier, S. J. Clarke, and A. T. Boothroyd, *Strong* $(\pi, 0)$ *spin fluctuations in* $\beta -$ FeSe *observed by neutron spectroscopy*, Phys. Rev. B **91**, 180501 (2015).

[141] Q. Wang, Y. Shen, B. Pan, X. Zhang, K. Ikeuchi, K. Iida, A. D. Christianson, H. C. Walker, D. T. Adroja, M. Abdel-Hafiez, X. Chen, D. A. Chareev, A. N. Vasiliev, and J. Zhao, *Magnetic ground state of FeSe*, Nature Communications **7**, 12182 (2016).

[142] Q. Wang, Y. Shen, B. Pan, Y. Hao, M. Ma, F. Zhou, P. Steffens, K. Schmalzl, T. R. Forrest, M. Abdel-Hafiez, X. Chen, D. A. Chareev, A. N. Vasiliev, P. Bourges, Y. Sidis, H. Cao, and J. Zhao, *Strong interplay between stripe spin fluctuations, nematicity and superconductivity in FeSe*, Nature Materials **15**, 159 (2016).

[143] P. O. Sprau, A. Kostin, A. Kreisel, A. E. Böhmer, V. Taufour, P. C. Canfield, S. Mukherjee, P. J. Hirschfeld, B. M. Andersen, and J. C. S. Davis, *Discovery of orbital-selective Cooper pairing in FeSe*, Science **357**, 75 (2017).

[144] S. Gerber, S.-L. Yang, D. Zhu, H. Soifer, J. A. Sobota, S. Rebec, J. J. Lee, T. Jia, B. Moritz, C. Jia, A. Gauthier, Y. Li, D. Leuenberger, Y. Zhang, L. Chaix, W. Li, H. Jang, J.-S. Lee, M. Yi, G. L. Dakovski, S. Song, J. M. Glownia, S. Nelson, K. W. Kim, Y.-D. Chuang, Z. Hussain, R. G. Moore, T. P. Devereaux, W.-S. Lee, P. S. Kirchmann, and Z.-X. Shen, *Femtosecond electron-phonon lock-in by photoemission and x-ray free-electron laser*, Science **357**, 71 (2017).

[145] S. Kasahara, T. Yamashita, A. Shi, R. Kobayashi, Y. Shimoyama, T. Watashige, K. Ishida, T. Terashima, T. Wolf, F. Hardy, C. Meingast, H. v. Löhneysen, A. Levchenko, T. Shibauchi, and Y. Matsuda, *Giant superconducting fluctuations in the compensated semimetal FeSe at the BCS–BEC crossover*, Nature Communications **7**, 12843 (2016).

[146] T. Watashige, S. Arsenijević, T. Yamashita, D. Terazawa, T. Onishi, L. Opherden, S. Kasahara, Y. Tokiwa, Y. Kasahara, T. Shibauchi, H. von Löhneysen, J. Wosnitza, and Y. Matsuda, *Quasiparticle Excitations in the Superconducting State of FeSe Probed by Thermal Hall Conductivity in the Vicinity of the BCS–BEC Crossover*, Journal of the Physical Society of Japan **86**, 014707 (2017).

[147] Y. Lubashevsky, E. Lahoud, K. Chashka, D. Podolsky, and A. Kanigel, *Shallow pockets and very strong coupling superconductivity in* $FeSe_xTe_{1-x}$, Nature Physics **8**, 309 (2012).

[148] K. Okazaki, Y. Ito, Y. Ota, Y. Kotani, T. Shimojima, T. Kiss, S. Watanabe, C.-T. Chen, S. Niitaka, T. Hanaguri, H. Takagi, A. Chainani, and S. Shin, *Superconductivity in an electron band just above the fermi level: possible route to bcs-bec superconductivity*, Scientific Reports **4**, 4109 (2014).

[149] T. Hanaguri, S. Niitaka, K. Kuroki, and H. Takagi, *Unconventional s-Wave Superconductivity in Fe(Se,Te)*, Science **328**, 474 (2010).

[150] S. Graser, T. A. Maier, P. J. Hirschfeld, and D. J. Scalapino, *Near-degeneracy of several pairing channels in multiorbital models for the Fe pnictides*, New Journal of Physics **11**, 025016 (2009).

[151] K. Kuroki, H. Usui, S. Onari, R. Arita, and H. Aoki, *Pnictogen height as a possible switch between high-*T_c *nodeless and low-*T_c *nodal pairings in the iron-based superconductors*, Phys. Rev. B **79**, 224511 (2009).

[152] A. F. May, S. Calder, C. Cantoni, H. Cao, and M. A. McGuire, *Magnetic structure and phase stability of the van der Waals bonded ferromagnet* $Fe_{3-x}GeTe_2$, Phys. Rev. B **93**, 014411 (2016).

[153] L. S. Blackford, A. Petitet, R. Pozo, K. Remington, R. C. Whaley, J. Demmel, J. Dongarra, I. Duff, S. Hammarling, G. Henry *et al.*, *An updated set of Basic Linear Algebra Subprograms (BLAS)*, ACM Transactions on Mathematical Software **28**, 135 (2002).

[154] E. Anderson, Z. Bai, C. Bischof, S. Blackford, J. Demmel, J. Dongarra, J. Du Croz, A. Greenbaum, S. Hammarling, A. McKenney, and D. Sorensen, *LAPACK Users' Guide*, Society for Industrial and Applied Mathematics, Philadelphia, PA, 3rd ed. (1999).

[155] M. Kamermans, *Gaussian Quadrature Weights and Abscissae*, https://pomax.github.io/bezierinfo/legendre-gauss.html.

[156] R. Heid, K.-P. Bohnen, I. Y. Sklyadneva, and E. V. Chulkov, *Effect of spin-orbit coupling on the electron-phonon interaction of the superconductors Pb and Tl*, Phys. Rev. B **81**, 174527 (2010).

[157] L. Kleinman, *Relativistic norm-conserving pseudopotential*, Phys. Rev. B **21**, 2630 (1980).

[158] G. B. Bachelet and M. Schlüter, *Relativistic norm-conserving pseudopotentials*, Phys. Rev. B **25**, 2103 (1982).

[159] G. Rickayzen, *Green's functions and Condensed Matter*, Dover Publications Inc. (2013).

[160] T. Weddle, *A new, simple, and general method of solving numerical equations of all orders*, Palala Press (2016).

[161] H. R. Schwarz and N. Köckler, *Numerische Mathematik*, Vieweg+Teubner Verlag, 5th ed. (2004).

[162] H. J. Monkhorst and J. D. Pack, *Special points for Brillouin-zone integrations*, Phys. Rev. B **13**, 5188 (1976).

[163] J. P. Perdew and Y. Wang, *Accurate and simple analytic representation of the electron-gas correlation energy*, Phys. Rev. B **45**, 13244 (1992).

[164] G. M. Sheldrick, *A short history of SHELX*, Acta Crystallographica Section A **64**, 112 (2008).

[165] V. Petříček, M. Dušek, and L. Palatinus, *Crystallographic Computing System JANA2006: General features*, Zeitschrift für Kristallographie - Crystalline Materials **229**, 345 (2014).

List of Figures

1.1 Illustration of the CPA scheme after Ref. [6] taken from Ref. [39] . . . 7
1.2 CPA program workflow in style of Ref. [6] . . . 19

2.1 Schematics of the Fermi surface scan extension for a square BZ . . . 21
2.2 Brillouin zone of the fcc lattice and Fermi surface of fcc Cu . . . 23
2.3 Fermi surfaces of fcc Ni . . . 24
2.4 Fermi surfaces of $Cu_{1-x}Ni_x$ for $x = \{0.1, 0.25\}$ . . . 24
2.5 Fermi surfaces of $Cu_{1-x}Ni_x$ for $x = 0.5$ . . . 25
2.6 Fermi surfaces of $Cu_{1-x}Ni_x$ for $x = 0.75$ . . . 25
2.7 Unit cell of bcc Fe and sc Fe . . . 26
2.8 Comparison of DFT vs. CPA band structure for sc Fe and bcc Fe, and DOS for $Fe_{1+0.001}$ vs. sc Fe . . . 27
2.9 Comparison of the Bloch spectral function of $Fe_{1+0.5}$ to clean sc Fe, and bcc Fe . . . 28
2.10 Comparison of the DOS of $Fe_{1+0.5}$ to clean sc Fe and bcc Fe . . . 29
2.11 Comparison of DFT vs. CPA for Fe, and Co with spin polarization . . . 31
2.12 Fermi sheet for bcc Fe with spin polarization in $(\bar{1}10)$ plane . . . 32
2.13 Evolution of the magnetic moment in $Fe_{1-x}Co_x$ . . . 33
2.14 DOS for spin polarized bcc Fe and bcc Co . . . 33
2.15 Component DOS of spin polarized $Fe_{0.5}Co_{0.5}$ . . . 34
2.16 Comparison DFT vs. CPA for Fe with SOC . . . 35
2.17 Comparison CPA band structure of Fe without vs with SOC . . . 36
2.18 Comparison of the Fermi surface cross section in bcc Fe with and without SOC . . . 36

3.1 Schematic crystal structures of Fe-based superconductors . . . 40
3.2 Crystal structure and unit cell of FeSe/FeTe/Fe(Se,Te) . . . 41
3.3 Schematics of the effect of SOC on the band structure in Fe(Se,Te) . . . 43
3.4 DFT band structure of FeSe . . . 46
3.5 Fermi surface and cross section at $k_z = 0$ of FeSe . . . 47
3.6 Angular and atomic type resolved contributions to Fermi surface cross section at $k_z = 0$ for FeSe . . . 48
3.7 Evolution of electronic states in FeSe with chalcogen height z . . . 49
3.8 Evolution of electronic states in FeSe with interlayer distance c . . . 50
3.9 Schematic drawing of orbital overlap in FeSe and FeTe . . . 51
3.10 Comparison of CPA band structures for FeSe, $FeSe_{0.5}Te_{0.5}$ and FeTe . . . 52
3.11 Comparison of CPA band structure and projected spectral function for $FeSe_{0.5}Te_{0.5}$ without and with SOC . . . 53
3.12 Half-widths and band crossing points of Ni, Cu, and Co substitutions in $FeSe_{0.5}Te_{0.5}$ . . . 54
3.13 Comparison of CPA band structure for transition metal substitution in Fe(Se,Te) . . . 56
3.14 Bloch spectral function of $FeSe_{0.35}Br_{0.15}Te_{0.5}$ along ΓZ . . . 57

3.15 Comparison of the DOS of FeSe, $FeSe_{0.5}Te_{0.5}$ and $FeSe_{0.325}I_{0.175}Te_{0.5}$ 58
3.16 Comparison of CPA band structure of Fe(Se,Te) and Fe(Se,Te,I) with SOC 59
3.17 Projected Bloch spectral function of $FeSe_{0.375}I_{0.175}Te_{0.5}$ at the band crossing point . . . 60

4.1 Unit cell of $Fe_{1+y}Se_{1-x}Te_x$ 64
4.2 Comparison of the DOS of $Fe_{1+y}Se_{0.5}Te_{0.5}$ for different degrees y of interstitial iron occupation 65
4.3 Band structure of $Fe_{1+0.01}Se_{0.5}Te_{0.5}$ along high symmetry lines 66
4.4 Band structure of $Fe_{1+0.04}Se_{0.5}Te_{0.5}$ along high symmetry lines 66
4.5 Band structure of $Fe_{1+0.084}Se_{0.5}Te_{0.5}$ along high symmetry lines 67
4.6 Fermi surfaces of $Fe_{1+y}Se_{0.5}Te_{0.5}$ for varying y 67
4.7 Fermi surface cross sections at $k_z = 0$ of $Fe_{1+y}Se_{0.5}Te_{0.5}$ for varying y 68
4.8 Fermi surface cross sections at $k_z = 0$ for $Fe_{0.8}Co_{0.2}Se_{0.5}Te_{0.5}$, $Fe_{0.9}Ni_{0.1}Se_{0.5}Te_{0.5}$, and $Fe_{0.95}Cu_{0.05}Se_{0.5}Te_{0.5}$ 68
4.9 Comparison of diagonal cut of Fermi surface cross sections along ΓM for interstitial iron and transition metal substitutions 69

I.1 Main window of the CPA GUI 153

J.1 Radial basis functions $f_l^P(r)$ for Cu and Ni 156
J.2 Radial basis functions $f_l^P(r)$ for sc Fe and bcc Fe 157
J.3 Radial basis functions $f_l^P(r)$ for Fe and Co with spin polarization 158
J.4 Radial basis functions $f_l^P(r)$ for Fe without and with spin-orbit coupling 159
J.5 Radial basis functions $f_l^P(r)$ for NiSe, CuSe, CoSe, and FeBr without SOC 162
J.6 Radial basis functions $f_l^P(r)$ for FeSe, FeTe, and FeI with and without SOC 163
J.7 Radial basis functions $f_l^P(r)$ for FeFeSe and FeFeTe 164

Acronyms

1. BZ first Brillouin zone

3D three-dimensional

ARPES angle-resolved photoemission spectroscopy

ASA atomic sphere approximation

bcc body centered cubic

BLAS Basic Linear Algebra subprograms

CDWs charge-density waves

CPA Coherent potential approximation

DFT density functional theory

fcc face centered cubic

FeSCs iron-based superconductors

GGA generalized gradient approximation

GUI graphical user interface

IRs irreducible representations

KKR-CPA Korringa-Kohn-Rostoker CPA

LAPACK Linear Algebra Package

LCAO linear combination of atomic orbitals

LCAO-CPA linear-combination-of-atomic-orbitals CPA

LDA local-density approximation

LSDA local-spin-density approximation

MCPA molecular coherent potential approximation

NLCPA nonlocal coherent potential approximation

QSHE quantum spin hall effect

rFT radial Fourier transformation

sc simple cubic

SDC surface Dirac cone

SDW spin-density wave

SI-STM spectroscopic-imaging scanning tunneling microscopy

SOC spin-orbit coupling

TB-LMTO-CPA tight-binding-linear-muffin-tin-orbital CPA

TRIM time-reversal-invariant momenta

VCA virtual crystal approximation

XC exchange and correlation

XRD x-ray diffraction

Danksagung

Die vorgelegte Arbeit hätte ohne die Hilfe und Unterstützung zahlreicher Menschen niemals in dieser Form verwirklicht werden können und an dieser Stelle möchte ich die Möglichkeit nutzen ihnen in ein paar Zeilen für ihren Beitrag zu danken.
Zuallererst gilt mein Dank Jörg Schmalian, für das Vertrauen und die Möglichkeit diese Arbeit am Institut für Festkörperphysik (später Institut für QuantenMaterialien und Technologien) anzufertigen und die Übernahme des Referats. Für seine Geduld und Nachsicht und ganz besonders dafür, dass ich mich ausschließlich meiner Dissertation widmen konnte. Neben allen fachlichen Kompetenzen die er mir vermittelt hat möchte ich mich noch dafür bedanken, dass er mir beigebracht hat unsere wissenschatliche Arbeit als Geschichte zu erzählt.
Dann möchte ich mich bei Matthieu Le Tacon für die Übernahme des Korreferats bedanken. Für die ruhige und stets hilfsbereite Art, wie er das Institut geleitet hat.
Mein ganz besonderer Dank gilt meinem Betreuer, Rolf Heid. Danke, dass du dir immer die Zeit genommen hast mit mir zu diskutieren, neue Ideen zu entwickeln und es auch nicht müde geworden bist mir Dinge mehr als einmal zu erklären. Ohne deine tägliche Hilfe und deine Unterstützung wäre diese Arbeit nicht zustande gekommen. Danke, dass ich zwar selbstständig meinen Weg gehen durfte, aber immer auf deine Unterstützung und Erfahrung zählen konnte. Und nicht zuletzt für das Korrekturlesen dieses Manuskripts. Ich hätte mir keinen besseren Betreuer für diese Arbeit wünschen können.
Da die theoretische Physik ohne das Experiment nur eitles Gekritzel ist, gilt mein nächster Dank Michael Merz und Amir-Abbas Haghighirad. Ohne euren Beitrag wäre das Projekt nicht möglich gewesen. Vielen Dank für die tollen Diskussionen, eure fachliche Kompetenz und die Zeit, die ihr immer wieder für mich gefunden habt. Die Hauptidee dieser Arbeit wäre ohne eure Mithilfe niemals entwickelt und umgesetzt worden.
Für die angenehme Arbeitsatmosphäre und die schönen Institutsfeste möchte ich allen Mitarbeitern und Mitarbeiterinnen am IFP (später IQMT) danken. Besonders Frédéric Hardy, Robert Eder, Roland Hott, Roland Schäfer, Anna Böhmer, Dirch Fuchs, Frank Weber und Kai Grube.
Nicht zuletzt besonders Frau Dörflinger, die mir bei organisatorischen und bürokratischen Hürden immer geholfen hat. Den Doktoranden und Post-Docs (und Ehemaligen) am IFP/IQMT und am TKM: Daniel Arnold, Matthias Hecker, Markus Klug, Roland Willa, Matthias Keßler, Mareike Hoyer, Julia Link, Yi Yao und Fatemeh Ghorbani. Für die schöne Zeit zusammen und unterhaltsame DPG Konferenzen. Ein besonderer Dank gilt Daniel Arnold, der mir im Dickicht der Promotionsvorbereitung immer wieder den Weg gewiesen hat.
Mein Dank gebührt außerdem der Dekanastsekretärin Regina Hühn für ihre Geduld und Hilfe mit allen Formalitäten der Prüfung.
Der vielleicht größte Dank gilt meinen Eltern Harald und Brita Lauke. Für die Erziehung die meinen Weg erst ermöglicht hat. Für ihren unerschütterlichen Glauben an mich. Dafür, dass sie nie an mir gezweifelt haben. Nicht zuletzt dafür, dass ich ihnen ein finanziell sorgloses Studium zu verdanken haben.
Vielen Dank auch meinen Geschwistern Lara, Sven und Lennart. Für die gemeinsame Kindheit und

dafür, dass sie mich in all diesen Jahren ertragen haben.
Und auch dir, Patrick, für die wöchentlichen Ablenkungen am Wasser.
Zu guter Letzt möchte ich mich noch bei dir bedanken, Sophie. Für deine unerschütterliche Liebe und Unterstützung. Dafür, dass du mich in den letzten Monaten ertragen und vor dem Wahnsinn bewahrt hast. Ohne dich und deinen Glauben an mich hätte ich diese Arbeit nicht beenden können.

Appendix A

Ab-initio CPA program

This chapter serves as an introduction to the *ab-inito* LCAO-CPA program which implements the scheme outlined in Sec. 1.2.3. The original code was implemented by Dr. Alexander Herbig (see Ref. [6]) and further developed in this work.

A.1 Code extensions

We begin with a brief overview of the major extensions added to the pre-existing code:

1. **Fermi sheet and surface extension** to calculate single or multiple cross sections of the Fermi surface Sec. 2.1.

2. **Vacancy extension** allowing for the treatment of vacancies and interstitial site occupation. Herein, a vacancy is treated as an independent 'species' with the basis functions of the type to be substituted and zero initial density. For a detailed description see Sec. 2.2.

3. **Non-relativistic spin polarization** for the treatment of magnetic phases and properties. For a detailed description see Sec. 2.3

4. **Full *ab-initio* spin-orbit coupling** according to the spin-orbit potentials calculated from the MBBP for each species (App. E). For a detailed description see Sec. 2.4.

It should be noted, that here spin polarization and spin-orbit coupling are mutually exclusive and can only be applied separately. Apart from these extensions, a number of optimizations were implemented to further increase the code stability and reduce computational and memory cost. Consequently, systems with unit cells containing multiple atomic species and substitutions can be treated with feasible effort.

A.2 Program file structure

The program code was implemented in Fortran90 (apart from the Broyden mixing scheme implemented in Fortran77) and currently contains ca. 23000 lines of code, among which roughly 10000 lines were written in this work. The rest is made up of pre-existing CPA code and routine libraries taken over from MBPP. A summary of the source code files and the respective authors is given in Tab. A.1 below. The

CPA program code		
File	Developed	Description
broyd.f77	H. Winter	Broyden mixing for charge self-consistency
excorr.f90	MBPP	Routines for exchange-correlation (XC) potential
funkt.f90	MBPP	Mathematical functions, in particular cubic harmonics, Gaunt coefficients, Legendre polynomials, Wigner matrices
geo.f90	MBPP	Characterization of bonds between neighboring sites
specialpar.f90	MBPP	Parameters and fundamental constants
cpa.f90	A. Herbig & this work	Main program
cpaSolver.f90	A. Herbig & this work	BEB-CPA impurity solver, band structure calculations, Fermi level, DOS and charge self-consistency
density.f90	A. Herbig & this work	Calculations concerning electronic density
hamilton.f90	A. Herbig & this work	Hamilton matrix elements
hloc.f90	R. Heid & this work	Calculation of mixing potential and spin-orbit potential
hmatloc.f90	R. Heid & this work	Calculates Hamilton and overlap matrix elements via local and nonlocal parts of the basis functions
locmat.f90	R. Heid & this work	see above
hsomat.f90	R. Heid & this work	Main calculation of SOC matrix elements
input.f90	A. Herbig & this work	Processing input from MBPP
overlap.f90	A. Herbig & this work	Overlap matrix elements
potential.f90	A. Herbig & this work	Local potentials including V_{XC} decomposition
symmetry.f90	A. Herbig & this work	Symmetrization routines
tools.f90	A. Herbig	Useful routines such as scalar product, Fourier transformations, etc.

Table A.1: Source code files of the CPA-program. Table taken from Ref. [6] and by contributions from this thesis.

analytic expressions of the matrix elements implemented in the code are derived in Apps. D and E and references to the subroutines performing the calculations are made in the respective texts. Demanding calculations were parellelized using `OpenMP`, which allows for multi-core calculations on a *single* node of a cluster machine. Furthermore, the open-source libraries Basic Linear Algebra subprograms (BLAS) [153] and Linear Algebra Package (LAPACK) [154] need to be linked in the compilation of the CPA-program that mainly deal with matrix operations such as diagonalization and inversion. In order to make the CPA program accessible to a broader scientific audience, a graphical user interface (GUI) was implemented using the `Tkinter` package of `phyton`. A detailed introduction thereof is presented in App. I.

A.3 Mode of operation

All CPA calculations require input files generated by the MBPP program for each substitutional end member. Furthermore, the CPA formalism demands each substitutional end member to have the same crystal structure and lattice parameters. Aside from the radial basis functions delivered by the LCAO fit a number of relevant quantities is output to ASCII files with the prefix `CPA_*`, containing information on crystal structure and symmetry, pseudopotentials and expansion coefficients. Internally, the parent compound is called "master", while all corresponding substituents are called "slaves". The CPA program expects a symbolic link to the directory in which the respective MBPP calculations were performed for all end members. The symbolic link to the master must be named `CM`, while the substituents are labeled as `CS`i ($i \in [1, \ldots, $`#slaves`$]$ being the substituent index). The only exception to the use of symbolic links are substituents of vacancy type: here, all relevant information is copied from the atomic type which is to be substituted (for a detailed discussion of the vacancy extension see Sec. 2.2). Aside from this input, the CPA program relies on a number of additional parameters, such as the number of overall types, substituents, cutoff radii and numerical parameters for integration methods and intervals. This mandatory information is encoded in a formatted input file named `CPA_INP` of which a generic example is provided in Listing A.1. While the MBPP makes use of identifiers, rendering the order of calculation parameters irrelevant, the CPA program does not come with this feature and as such the order of lines and placement of newline characters are important.

```
1  outdebug
2  calcRestart
3  calcOvlp
4  calcHamiltonian
5  readOldRadDen
6  chargeConverged
7  plotDenR
8  allocPot
9  symm
10 calcFS
11 nTypes
12 nSlaveCalc
13 kmax qcutar lcutpw lmcutExt lmcutInt
14 shpFuncType shpFuncPar
15 coincTol
16 nameHostAtom1 hostTypeIndex1 nameImpurityAtom1 impurityTypeIndex1
17 .                          .                    .
18 .                          .                    .
19 .                          .                    .
20 nameHostAtomN hostTypeIndexN nameImpurityAtomN impurityTypeIndexN
21 concType1Atom1 ... concType1AtomN shpFuncCutOffRadius Type1ValQ
22 .                          .                    .                 .
23 .                          .                    .                 .
24 .                          .                    .                 .
25 concTypeNAtom1 ... concTypeNAtomN shpFuncCutOffRadius TypeNValQ
26 leften numLeft fermileften numFermi fermirighten numRight righten numImag topen
27 maxCpaIter cpaTol numFermiIter fermiTol cpaNtemp csItemp
28 cpaTemp1 cpaTemp2
29 dosleft dosright numDos dosSmear
30 csStartIter csMaxIter linMix denUpdtBound chargeScfLim
31 nDir
32 bandSmear
33 FSk_start
```

```
34  k_scandir1
35  k_scandir2 nkmesh
36  k_scandir3 nkz_scan
37  start_dir1 end_dir1 nk Dir1Name
38       .         .      .      .
39       .         .      .      .
40       .         .      .      .
41  start_dirN end_dirN nk DirNName
42  ibandProjMin ibandProjMax psf1 psf2 bandIntLeft bandIntRight bandnum
```

Listing A.1: Generic example of a CPA input file CPA_INP

The parameters presented above have the following meaning:

L1-L10. Logical flags to set calculation status:

- `outdebug` (**logical**): If `True` produces a huge amount of debugging output, otherwise it is suppressed.
- `calcRestart` (**logical**): If `False` calculation is started from scratch, otherwise an old calculation is restarted.
- `calcOvlp` (**logical**): If `True` overlap is calculated, otherwise it is read from file (must have been calculated in previous calculation).
- `calcHamiltonian` (**logical**): If `True` Hamiltonian is calculated, otherwise it is read from file (must have been calculated in previous calculation).
- `readOldRadDen` (**logical**): If `True` radial densities are calculated, otherwise they are read from file (must have been calculated in previous calculation).
- `chargeConverged` (**logical**): If `False` CPA calculation is performed completely, otherwise only subroutines are run once which are needed for post processing (e.g. bandstructure calculation).
- `plotDenR` (**logical**): If `True` calculate full real-space densities.
- `allocPot` (**logical**): Logical variable that determines, whether potential arrays must be allocated. Must be set depending on mode of operation [new/old calculation].
- `symm` (**logical**): If `True` calculation makes use of symmetrization routines. Must be consistent with MBPP calculations.
- `calcFS` (**logical**): If `True` Fermi sheets or surface will be calculated. Additional scan parameters needed below.

L11. `nTypes` (**integer**): Total number of atomic types, including substituents.

L12. `nSlaveCalc` (**integer**): Number of slave calculations, i.e. number of substitutions.

L13. Cutoff for summations and Fourier transformations:

- `kmax` (**float**): Cutoff radius in atomic units up to which the radial Fourier transformation of wave functions will be calculated. Additionally, used for evaluation of matrix elements (two times this cutoff is used for the local pseudopotentials).
- `qcutar`(**float**): Cutoff for plane wave expansion of delocalized wave functions.

- `lcutpw` (**integer**): Cuttoff for angular expansion of plane waves.
- `lmCutExtern` (**integer**): Cutoff for internal summations over orbital quantum numbers l, m. Individual quantum numbers can be found from this combined lm index via $l(lm) = 0, 1, 1, 1, 2, 2, 2, 2, 2, ... = (l+1)^2$ and $m(lm) = 0, 0, 1, -1, 0, 1, -1, 2, -2, ...$ These fields are defined in `specialpar.f90`. For a maximum angular momentum $l = 2$ and $lm = 9$ would be required.
- `lmCutIntern` (**integer**): A separated cutoff for internal summations over l, m quantum numbers in the calculation of B-coefficients Eq. (C.6). This is a historical remnant that no longer serves a purpose and `lmCutExtern=lmCutIntern` should be used.

L14. Shape function specifications :

- `shpFuncType` (**integer**): Functional type of shape functions used according to (D.23). Is the same for all types and sites.
- `shpFuncPar` (**float**): Parameter γ of shape functions in (D.23).

L15. `coincTol` (**float**): Threshold used in consistency check of atomic coordinated for all types involved (usually set to 10^{-6}).

L16-L20. This line is read `nSlaveCalc` times (i = 1,...,`nSlaveCalc`):

- `nameHostAtom<i>` (**char[2]**): Name of atomic type of the host that is to be replaced for i-th substitution.
- `hostTypeIndex<i>` (**integer**): Index of atomic type of the host atom in the parent compound (equivalent to the order of types chosen in MBPP) for i-th substitution.
- `nameImpurityAtom<i>` (**char[2]**): Name of atomic type of the substituent species for i-th substitution.
- `impurityTypeIndex<i>` (**integer**): Index of atomic type of the impurity atom in the substitutional end-member (equivalent to the order of types chosen in MBPP) for i-th substitution. Typically `impurityTypeIndex<i>`=`hostTypeIndex` and must never exceed the number of types in either parent compound or substitutional end member.

L21-L25. This line will be read `nTypes` times:

- `concType<i>Atom<j>` (**float**): Atomic concentration of type i at atomic position j. With $i = 1, ...,$ `nTypes` and $j = 1,$ `natomax`. `natomax` (used in MBPP and CPA) is the maximum number of sites occupied by a single type in the unit cell. For each type, concentrations must be specified for `natomax` sites, even if considered type occurs less often in the unit cell. In this case, the concentration must be set to 0 for all superfluous sites.
- `shpFuncCutOffRadius` (**float**): Cutoff radius of the shape function associated with the considered type.
- `Type<i>ValQ` (**float**): Number of valence electrons for type i (may be fractional).

L26. Specification of the closed curve integration (see Sec. 1.3) involved in the calculation of the Fermi level and the charge self-consistency. A finer sampling is needed for the region around the estimated Fermi level. Due to the special integration method applied, the number of sampling points must fulfill mod(`#sampling points`, 6) $\stackrel{!}{=} 1$.

- `leften` (**float**): Lower energy bound (Ry) of the box on the real axis far from Fermi level.
- `numLeft` (**integer**): Number of sampling points below Fermi region.
- `fermileften` (**float**): Lower energy bound (Ry) of the region the Fermi level is assumed to lie in.
- `numFermi` (**integer**): Number of sampling points in Fermi region.
- `fermirighten` (**float**): Upper energy bound (Ry) of the region the Fermi level is assumed to lie in.
- `numRight` (**integer**): Number of sampling points above Fermi region.
- `righten` (**float**): Upper energy bound (Ry) of the box on the real axis.
- `numImag` (**integer**): Number of sampling points on the positive imaginary axis.
- `topen` (**float**): Upper energy bound (Ry) of the box on the imaginary axis.

L27. Parameters for the CPA cycle:

- `maxCpaIter` (**integer**): Maximum number of iterations for the inner loop of the CPA cycle (see Fig. 1.2). Implemented to avoid infinite loops due to bad convergence.
- `cpaTol` (**float**): Convergence criterion (Ry) for the change in self-energyin the CPA cycle. The
- `numFermiIter` (**integer**): Maximum number of iterations for the bisection method used to determine the Fermi level from the number of valence electrons.
- `fermiTol` (**float**): Threshold (Ry) for the determination of the Fermi level by the bisection method.
- `cpaNtemp` (**integer**): The number of temperatures the chemical potential is calculated for. Used to extrapolate to $T = 0$ for the Fermi level. Currently, `cpaNtemp` $= \{1, 2\}$ is implemented.
- `csItemp` (**integer**): Index of the temperature for which the charge self-consistency should be calculated at. So far no extrapolation to $T = 0$ is implemented.

L28. `cpaTemp` (**float**): The `cpaNtemp` temperatures used in the Fermi level and charge self-consistency calculation. Specifically, $k_{\mathrm{B}}T$ in Ry must be supplied.

L29. Specification for DOS calculation:

- `dosleft` (**float**): Lower energy bound (Ry) of the interval on which the DOS is calculated on. Here, an absolute scale is used and only for the output file `CPA_TOTDOS` is the energy zero shifted to the Fermi level in addition to a conversion to eV.
- `dosright` (**float**): Upper energy bound (Ry) of the interval on which the DOS is calculated on.
- `numDos` (**int**): Number of sampling points in the energy interval.
- `dosSmear` (**float**): Imaginary part δ of the complex frequency for which the retarded Green's function is evaluated in the DOS calculation.

L30. Parameters for the charge self-consistency:

- `csStartIter` (**integer**): Iteration from which to start calculation. If a calculation is set up from scratch, this will need to be set to 1. This parameter allows to restart a calculation from a later iteration if the densities have been calculated for said iteration and can be read from file.
- `csMaxIter` (**integer**): Maximum number of charge iterations to avoid endless calculations in case of bad convergence. Due to the file name structure the constraint `csMaxIter`≤ 99 must be considered.
- `linMix` (**float**): In the first iteration a linear mixing is performed by the Broyden scheme in order to set up the Jacobi matrix. For parameter values > 0.05 the algorithm becomes unstable.
- `denUpdtBound` (**float**): Threshold below which an orbital density component is considered to vanish due to symmetry. In the first charge iteration an analysis is performed in order to determine relevant and vanishing orbital indices. They are stored in the files `CPA_UPDATE_DEN` and `CPA_ZERO_DEN`, respectively. This protects the program against numerical errors which violate symmetry and leads to a more robust convergence.
- `chargeScfLim` (**float**): Threshold below which the charge self-consistent cycle is assumed to have converged. Must be fulfilled for the difference of all orbital contributions between two consecutive iterations.

L31. `nDir` (**integer**): Number of directions in $\boldsymbol{k}$-space along which the band structure is calculated.

L32. `bandSmear` (**float**): Imaginary part δ of the complex frequency for the evaluation of the Bloch spectral function. In order to resolve all bands it must typically be chosen smaller than `dosSmear`.

L33-L36. Specifications for Fermi sheet or -surface calculation:

- `Fsk_start` (**float[3]**): Starting point in BZ for Fermi sheet or - surface scan in reciprocal lattice coordinates.
- `k_scandir1` (**float[3]**): First scan direction of Fermi sheet.First and second direction define plane in which Fermi scan is performed.
- `k_scandir2`, `nkmesh` (**float[3]**, **integer**): Second scan direction of Fermi sheet and number of sampling points for $\boldsymbol{k}$-mesh.
- `k_scandir3`, `nkz_scan` (**float[3]**, **integer**): Third scan direction and number of Fermi sheets to sample along that direction. If `nkz_scan = 1` only one sheet will be calculated.

L37-L41. Specification of the direction $i = 1, ..., $`nDir` in $\boldsymbol{k}$-space for the band structure calculation:

- `start_dir<i>` (**float[3]**): Starting point of line i in reciprocal lattice coordinates.
- `end_dir<i>` (**float[3]**): End point of line i in reciprocal lattice coordinates.
- `nk` (**integer**): Number of sampling points along line.
- `Dir<i>Name` (**char[2]**): Name of line. Usually letters for starting and end point (e.g. high symmetry points in BZ).

L42. Parameters for the projection of the Bloch spectral function on the eigenstates of the parent compound:

- `ibandProjMin` (**integer**): Lower band index for projection.
- `ibandProjMax` (**integer**): Upper band index for projection.
- `psf1` (**float**): Lower energy limit (Ry) of the energy interval in which the projection shall be performed. Here, an absolute scale is used in the calculation and the chemical potential is not included. This must be considered in setting the energy interval. For the output file `CPA_PROJSPECFUNC_<iband>_<dirName>` the energy zero is shifted to the Fermi level.
- `psf2` (**float**): Upper energy limit (Ry) of the energy interval in which the projection shall be performed.
- `bandIntLeft` (**float**): Lower energy integration limit (Ry) for the normalization of the projected spectral function.
- `bandIntRight` (**float**): Upper energy integration limit (Ry) for the normalization of the projected spectral function.
- `bandnum` (**integer**): Number of energy sampling points in the energy interval [`psf1`,`psf2`].

In Listing A.2, we provide an exemplary C shell script for a CPA calculation of $FeSe_{1-x}Te_x$ with $x = 0.5$.

```
#!/bin/csh
# c-shell script for the execution of a CPA calculation of Fe(Se,Te)
setenv OMP_NUM_THREADS 16

# Logical flags
set outdebug = false
set calcRestart = true
set calcOvlp = false
set calcHamiltonian = false
set readOldRadDen = true
set chargeConverged = true
set plotDenR = false
set allocPot = true
set symm = true

# Calculation parameters
set nType = 3                       #total number of atomic types
set nSlaveCalc = 1                  #number of substitutions

set kmax = 20.0                     #k-cutoff
set qcutar = 8.0                    #q-cutoff for plane waves
set lcutpw = 4                      #l-cutoff for plane waves
set lmcutExt = 49                   #lm-cutoff
set lmcutInt = 49                   #lm-cutoff

set coincTol = 0.000001             #threshold to discern atomic positions
# Concentrations and valence electrons for all atomic types
set fe1conc = 1.0
set fe2conc = 1.0
set feq = 8.0
set se1conc = 0.5
set se2conc = 0.5
set seq = 6.0
set te1conc = 0.5
```

```
set te2conc = 0.5
set teq = 6.0

# Shape function parameter
set shpFuncType = 6                  #shape function type
set shpFuncPar = 90                  #shape function parameter
set feShpCutoff = 5.9                #shape function cutoff
set seShpCutoff = 5.9
set teShpCutoff = 5.9
set coShpCutoff = 5.9

# Substituent
set itypeHostSlave1  = 2             #type index of to be substituted type in parent
    compound
set nameatHostSlave1 = Se            #name of to be substituted type
set itypeImpSlave1   = 2             #type index of substituent in end member
set nameatImpSlave1  = Te            #name of substituent

# Specify the box in upper complex half plane for Green's function integration
set leften = -5.0                    #left lower boundary
set numLeft = 61                     #number of sampling points in lower region
set fermileften = -0.9               #left boundary of fermi region
set numFermi = 121                   #number of sampling points in fermi region
set fermirighten = 0.0               #right boundary of fermi region
set numRight = 61                    #number of sampling points above fermi region
set righten = 10.0                   #right upper boundary
set numImag = 121                    #number of sampling points on imaginary axis
set topen = 3.0                      #top energy on imaginary axis

# Specify parameters for CPA solver
set maxCpaIter = 1000                #maximum number of iterations in inner CPA loop
set cpaTol = 0.00000001              #convergence criterion for CPA self-energy (Ry)
set numFermiIter = 40                #maximum number of biscetional search steps for
    chemical potential
set fermiTol = 0.000000001           #convergence criterion for chemical potential (Ry)
set set cpaNtemp = 2                 #number of temperatures for chemical potential
set csItemp = 2                      #temperature index for charge self-consistency

# Specify the temperatures (k_B*T in Ry)
set cpaTemp1 = 0.005
set cpaTemp2 = 0.02

# Parameters for densities of states
set dosleft = -1.4                   #left energy (Ry)
set dosright = 0.5                   #right energy (Ry)
set numDos = 2000                    #number of sampling points
set dosSmear = 0.005                 #Smearing of density of states

# Parameters for charge self-consistency loop
set csStartIter = 1                  #Iteration from which to start
set csMaxIter = 60                   #Maximal number of charge iterations
set linMix = 0.005                   #Linear mixing for broyden scheme in first
    iteration
set denUpdtBound = 0.00000001        #Program assumes orbital density component to
    vanish for symmetry reasons below this limit
set chargeScfLim = 0.00000001        #Maximal density change for convergence of charge
```

```
    self-consistency

# For the band structures evaluate Bloch-Spectral function
set nDir = 9                          #number of directions
set bandSmear = 0.0001                #energy smearing for the spectral function (Ry)

#For the projection on clean bands
set ibandProjMin = 8                  #lowest band index to project on
set ibandProjMax = 15                 #highest band index to project on
set bandIntLeft = -0.2                #lower integration limit for normalization (Ry)
set bandIntRight = 0.2                #upper integration limit for normalization (Ry)
set psf1 = -1.4                       #lower energy boundary for projection (Ry)
set psf2 = 0.5                        #upper energy boundary for projection (Ry)

set dummy = 0                         # unused relic

# Set directories
set cpaMaster = $HOME/cpaprep_FeSe #path to parent compound MBPP folder
set cpaSlave1 = $HOME/cpaprep_FeTe #path to substituent end member MBPP folder
set cpaProg = $HOME/cpa_v36_SO/cpa #path to CPA program
set pdir = $HOME/project/          #path to parent directory
set wd = $HOME/projects/FeSeTe     #path to calculation folder

if ( ! -d $wd) then
  mkdir -p $wd
endif

cd $wd

\rm -f CPA_TIME

# Symbolic links to MBPP folder of end members
ln -sf $cpaMaster CM
ln -sf $cpaSlave1 CS1

cat > CPA_INP << END
$outdebug
$calcRestart
$calcOvlp
$calcHamiltonian
$readOldRadDen
$chargeConverged
$plotDenR
$allocPot
$symm
$nType
$nSlaveCalc
$kmax $qcutar $lcutpw  $lmcutExt $lmcutInt
$shpFuncType $shpFuncPar
$coincTol $coincTol $coincTol
$itypeHostSlave1 $nameatHostSlave1 $itypeImpSlave1 $nameatImpSlave1
$fe1conc  $fe2conc $feShpCutoff $feq
$se1conc  $se2conc $seShpCutoff $seq
$te1conc  $te2conc $teShpCutoff $teq
$leften $numLeft $fermileften $numFermi $fermirighten $numRight $righten $numImag
    $topen
```

```
$maxCpaIter $cpaTol $numFermiIter $fermiTol $cpaNtemp $csItemp
$cpaTemp1 $cpaTemp2
$dosleft $dosright $numDos $dosSmear
$csStartIter   $csMaxIter  $linMix  $denUpdtBound $chargeScfLim
$nDir
$bandSmear
0.5  0.5  0.0   0.5  0.5  0.5   50  MA
0.5  0.5  0.5   0.0  0.0  0.0   50  AG
0.0  0.0  0.0   0.5  0.0  0.0   50  GX
0.5  0.0  0.0   0.5  0.5  0.0   50  XM
0.5  0.5  0.0   0.0  0.0  0.0   50  MG
0.0  0.0  0.0   0.0  0.0  0.5   50  GZ
0.0  0.0  0.5   0.5  0.0  0.5   50  ZR
0.5  0.0  0.5   0.5  0.5  0.5   50  RA
0.5  0.5  0.5   0.0  0.0  0.5   50  AZ
$ibandProjMin $ibandProjMax $psf1 $psf2 $bandIntLeft $bandIntRight
$dummy $dummy
END
time $cpaProg > DUMP
```

Listing A.2: Exemplary C shell script for CPA calculation of Fe(Se,Te).

A.4 Output file structure

Given the enormous amount of data produced by the CPA program, we shall give a brief overview over the most important output files below. Apart from these, a number of formatted files are provided for debugging purposes, which can be muted via the `output=false` flag introduced above. This greatly reduces the number of files output by the program and therefore the amount of memory consumed by a calculation. Some of the quantities computed within an iteration of the charge self-consistent cycle (such as Hamilton matrix elements, densities and overlap matrix elements) are written to file. This allows for a preexisting calculation to be restarted at an arbitrary iteration, given the respective files exist. In the following listing we mark these files by an asterisk (*).

Progress files

- `Progress`: Provides a progress log-file containing information on the calculation status, computational time of each subroutine and further relevant data.
- `CPA_OUT`: Provides information on geometry, Fermi level calculation, integrals of the orbital charge densities calculated during the self-consistency cycle, electron numbers and much more.
- `DUMP`: File to which the output of the program is piped (see end of shell script above). Contains intermediate results, important data and warning and error messages.

Density files

- `CPA_DEN_<type>_`l`_`m`_<chargeIter>` (*): Species and atom resolved radial components of the electronic density in real space for angular quantum numbers l and m.
- `CPA_UPDATE_DEN`: Relevant density components larger than user defined threshold.
- `CPA_ZERO_DEN`: Density components below threshold, considered symmetry-forbidden.

Hamiltonian files

- `CPA_HTOT_<chargeIter>`: Full $\boldsymbol{k}$-dependent Hamiltonian.
- `CPA_HOFFSITE_<chargeIter>` (*): Full $\boldsymbol{k}$-dependent offsite Hamiltonian.
- `CPA_HOFFSITE_REAL_<chargeIter>`: Respective real part.
- `CPA_HOFFSITE_IMAG_<chargeIter>`: Respective imaginary part.
- `CPA_HONSITE_<chargeIter>` (*): Full $\boldsymbol{k}$-independent onsite Hamiltonian.
- `CPA_HONSITE_REAL_<chargeIter>`: Respective real part.
- `CPA_HONSITE_IMAG_<chargeIter>`: Respective imaginary part.
- `CPA_MIX_REAL_<chargeIter>`: Real part of $\boldsymbol{k}$ dependent mixing Hamiltonian ${}^{\mathrm{mix}}H(\boldsymbol{k}) + {}^{\mathrm{mix,nl}}H(\boldsymbol{k}) + T(\boldsymbol{k})$ according to Eqs. (D.39) and (D.42) plus kinetic term. This reduces to the crystal Hamiltonian for a clean compound.
- `CPA_HMIX_IMAG_<chargeIter>`: Respective imaginary part.
- `CPA_TOFFSITE_<chargeIter>` (*): $\boldsymbol{k}$-dependent kinetic energy according to Eq. (D.50) without onsite corrections.
- `CPA_TOFFSITE_REAL_<chargeIter>`: Respective real part.
- `CPA_TOFFSITE_IMAG_<chargeIter>`: Respective imaginary part.
- `CPA_VOFFSITE_<chargeIter>` (*): Full $\boldsymbol{k}$-dependent potential according to Eq. (D.54) without onsite corrections.
- `CPA_VOFFSITE_REAL_<chargeIter>`: Respective real part.
- `CPA_VOFFSITE_IMAG_<chargeIter>`: Respective imaginary part.
- `CPA_VONSITE_<chargeIter>`: Full $\boldsymbol{k}$-independent onsite Hamiltonian.
- `CPA_VXC_<type>_<atomNumber>_`l_m`_<chargeIter>`: Species and atom resolved radial component of the exchange and correlation potential in real space for angular quantum numbers l and m.
- `CPA_VXCK_<type>_<atomNumber>_`l_m`_<chargeIter>`: Respective reciprocal space representation.
- `CPA_VMIXK_<chargeIter>`: Full $\boldsymbol{k}$-dependent mixing potential ${}^{\mathrm{mix}}H(\boldsymbol{k}) + {}^{\mathrm{mix,nl}}H(\boldsymbol{k})$.
- `CPA_VMIXK_REAL_<chargeIter>`: Respective real part.
- `CPA_VMIXK_IMAG_<chargeIter>`: Respective imaginary part.
- `CPA_VMIX_ONSITE_<chargeIter>` (*): $\boldsymbol{k}$-independent onsite mixing potential.
- `CPA_VSO_TOT` (*): Full $\boldsymbol{k}$-dependent spin-orbit Hamiltonian according to Eq. (E.31).
- `CPA_VSO_OFFSITE` (*): Respective $\boldsymbol{k}$-dependent offsite part.
- `CPA_VSO_ONSITE` (*): Respective $\boldsymbol{k}$-independent onsite part.

Band structure files

- `CPA_TOTDOS_<chargeIter>`: Total density of states, energy in eV with respect to the Fermi level, DOS in 1/(eV unit cell).
- `CPA_TYPEDOS_<chargeIter>`: Total density of states decomposed according to atomic type, energy in eV with respect to the Fermi level, DOS in 1/(eV unit cell).
- `CPA_BDOS_<bandIndex>_<chargeIter>`: Density of states of a given band. Similar to a band projected spectral function, but summed over a regular $\boldsymbol{k}$-mesh.
- `CPA_ORBDOS_<type><atomNumber>_`l_m`_<chargeIter>`: Orbital decomposition of density of states. Units equal to `CPA_TOTDOS`.
- `CPA_CLEANDBSTRUC_<bandIndex>_<direction>`: Band structure of the parent compound, i.e. eigenvalues of the mixing Hamiltonian. This is only calculated if `nSlaveCalc`$= 0$.
- `CPA_CLEANEIGEN_<direction>`: All eigenvectors of the crystal Hamiltonian of the parent compound. This is only calculated if `nSlaveCalc`$= 0$. Needed as input for the projection onto clean bands.
- `CPA_CLEANEIGEN_REG`: Respective eigenvectors on a regular $\boldsymbol{k}$-mesh.
- `CPA_KDOS_<direction>`: Total Bloch spectral function. First column: $\boldsymbol{k}$, second column: energy with respect to the Fermi level in eV, third column: spectral function in 1/(eV unit cell). For the length of the path in $\boldsymbol{k}$-space the same conventions as in the MBPP are chosen: length of first direction is normalized to unity and all further direction lengths are rescaled accordingly.
- `CPA_KDOS_<direction>_<type>_`l: Respective species and l-decomposition.
- `CPA_PROJSPECFUNC_<bandIndex>_<direction>`: Bloch spectral function projected onto clean band of parent compound.
- `CPA_SPROJSPEC_<bandIndex>_<direction>`: Respective quantity for perturbative spin-orbit coupling calculation.
- `CPA_PSFFWHM2_<bandIndex>_<direction>`: Properties of band-projected spectral function: first column: $\boldsymbol{k}$, second column: energy of peak, third column: spectral half width, fourth column: spectral broadening (half width minus band smearing), fifth column: norm (integration over energy).

Spin polarization

For spin polarized calculations the following files are appended by a spin index:

- `CPA_CLEANBDSTRUC_<bandIndex>_<direction>_<spin>`:

Fermi-sheets and surfaces

Some additional output files are produced if `calcFS=true`.

- `CPA_FERMISURFACE_<sheetindex>`: Bloch spectral function at Fermi level for sheet=`sheetindex`. First column $\boldsymbol{k}_x$, second column $\boldsymbol{k}_y$, third column $\boldsymbol{k}_z$, forth column $A(\boldsymbol{k}, E_F)$.
- `CPA_FERMISURFACE_<spinprojection>_<sheetindex>`: Bloch spectral function at Fermi level for `spinprojection`=UP, DOWN and sheet=`sheetindex`. First column $\boldsymbol{k}_x$, second column $\boldsymbol{k}_y$, third column $\boldsymbol{k}_z$, forth column $A(\boldsymbol{k}, E_F)$.
- `CPA_FERMISURFACE_<typename>_<typeindex>_<l>`: Bloch spectral function at Fermi level decomposed according to `typename`, `typeindex`, and angular momentum `l`. First column $\boldsymbol{k}_x$, second column $\boldsymbol{k}_y$, third column $\boldsymbol{k}_z$, forth column $A(\boldsymbol{k}, E_F)$.
- `CPA_FERMISURFACE_<typename>_<typeindex>_<l>_<sheetindex>`: Same as above for multiple sheets (`sheetindex`).
- `CPA_FERMISURFACE_<typename>_<typeindex>_<l>_<spinprojection>`: Same as above for `spinprojection` in spin polarized calculations.
- `CPA_FERMISURFACE_<typename>_<typeindex>_<l>_<spinprojection>_<sheetindex>`: Same as above for `spinprojection` in spin polarized calculations and multiple sheets (`sheetindex`).

B Appendix B

Basis set and overlap matrix elements

This chapter is devoted to the linear combination of atomic orbitals (LCAO) basis set employed in this work for the calculation of matrix elements. Such an LCAO basis is not necessarily orthonormal and may exhibit a non-trivial overlap matrix S. In the description of the basis set and the derivation of the overlap matrix elements we closely lean on Ref. [6] in which the base CPA-code was implemented.

B.1 Orbital representations

B.1.1 Localized orbitals in real space

We define the basis functions in three dimensional real space for a given set of quantum numbers in the following form

$$\phi^{Qs}_{Lslm}(\boldsymbol{r}) = \langle \boldsymbol{r} | LsPlm \rangle = \phi^{Qs}_{lm}(\boldsymbol{r} - \boldsymbol{R_L} - \boldsymbol{R_s}) \tag{B.1}$$

with the quantum numbers:

- L : index of unit cell in Bravais lattice
- s: index of atomic site within the unit cell
- Q : index of atomic species, which is connected to an atomic index in the unit cell via BEB-variables η^Q_s
- l: orbital angular momentum
- m: magnetic quantum number $m = \{-l, ..., +l\}$

Within the pseudopotential framework, following the MBPP, a single orbital per orbital momentum suffices to accurately describe the valence electrons, for which reason we omit a principal quantum number n. We can make use of the cubic harmonics $K_{lm}(\hat{r})$ to express the angular momentum dependence of our basis functions:

$$\phi^{Q}_{lm}(\boldsymbol{r}) = i^l f^Q_l(r) K_{lm}(\hat{r}) \tag{B.2}$$

where $\hat{r} = \boldsymbol{r}/r$ is the unit vector pointing along $\boldsymbol{r}$ and $r = |\boldsymbol{r}|$ is the magnitude of $\boldsymbol{r}$. The radial functions $f^Q_l(r)$ are the only quantities relevant for the treatment of disorder. They are generated by the LCAO-fit numerically on an equidistant radial grid with a finite cutoff radius R_c. This cutoff has

to be chosen by the user in the LCAO-fit of the MBPP so as to best suit the problem at hand.
The use of cubic harmonics over spherical harmonics stems from a computational advantage. Cubic harmonics are real functions in contrast to the complex spherical harmonics. The lack of an imaginary part reduces computational effort in summations, multiplications and matrix operations as well as memory consumption.

B.1.2 Localized orbitals in reciprocal space

The connection between the real space representation introduced above and the reciprocal representation is given by a Fourier transformation

$$\phi^Q_{lm}(\boldsymbol{k}) = \frac{1}{\sqrt{\Omega_C}} \int \mathrm{d}^3 r \, \phi^Q_{lm}(\boldsymbol{r}) e^{-i\boldsymbol{kr}} \tag{B.3a}$$

$$\phi^Q_{lm}(\boldsymbol{r}) = \frac{\sqrt{\Omega_C}}{(2\pi)^3} \int \mathrm{d}^3 k \, \phi^Q_{lm}(\boldsymbol{k}) e^{i\boldsymbol{kr}} \tag{B.3b}$$

where Ω_C denotes the unit cell volume and we have made use of $\int d^3 r e^{-i\boldsymbol{kr}} = (2\pi)^3 \delta(\boldsymbol{r})$. Furthermore, we introduce a radial Fourier transformation (rFT)

$$f^Q_l(k) \equiv 4\pi \int \mathrm{d}r \, r^2 f^Q_l(r) \, j_l(kr) \tag{B.4a}$$

$$f^Q_l(r) \equiv \frac{1}{2\pi^2} \int \mathrm{d}k \, k^2 f^Q_l(k) \, j_l(kr) \tag{B.4b}$$

where j_l are spherical Bessel functions. The radial Fourier transformations in Eqs. (B.4a) and (B.4b) are implemented in `subroutine rft_rToK` and `subroutine rft_kToR` in the module `tools.f90`. Some care has to be taken, as the historically chosen conventions here do not match those in the MBPP. With the rFT we may express the angular dependence of the basis functions in reciprocal space in a similar fashion as in real space. We thus find

$$\phi^Q_{lm}(\boldsymbol{r}) = i^l f^Q_l(r) K_{lm}(\hat{r}) \tag{B.5}$$

and

$$\phi^Q_{lm}(\boldsymbol{k}) = \frac{1}{\sqrt{\Omega_C}} f^Q_l(k) K_{lm}(\hat{k}) \tag{B.6}$$

for the two representations. In contrast to $\phi^Q_{lm}(\boldsymbol{r})$, $\phi^Q_{lm}(\boldsymbol{k})$ is a real quantity.

B.1.3 Translation of localized orbitals

In order to calculate matrix elements that involve multi-center integrals, we must gain knowledge about the transformation properties of the basis functions in Eqs. (B.5) and (B.6) under a translation in real space. With the definitions given above we may write

$$\phi^Q_{Lslm}(\boldsymbol{r}) = \frac{\sqrt{\Omega_C}}{(2\pi)^3} \int \mathrm{d}^3 k \, e^{-i\boldsymbol{k}(\boldsymbol{R_L}+\boldsymbol{R_s})} \, e^{i\boldsymbol{kr}} \, \phi^Q_{lm}(\boldsymbol{k}) \tag{B.7}$$

$$= \frac{1}{(2\pi)^3} \int \mathrm{d}^3 k \, e^{-i\boldsymbol{k}(\boldsymbol{R_L}+\boldsymbol{R_s})} \, e^{i\boldsymbol{kr}} \, f^Q_l(k) K_{lm}(\hat{k}) \tag{B.8}$$

$$= \frac{1}{(2\pi)^3} \int \mathrm{d}^3 k \, \mathrm{d}^3 r' \, e^{-i\boldsymbol{k}(\boldsymbol{R_L}+\boldsymbol{R_s})} \, e^{i\boldsymbol{kr}} \, \phi^Q_{lm}(\boldsymbol{r'}) e^{-i\boldsymbol{kr'}} \tag{B.9}$$

where we always pay the price of additional integrations for the advantage of evaluating K_{lm} and f_l^Q only with respect to an unshifted origin.

B.2 Useful properties of cubic harmonics and other relations

We shall briefly discuss some properties of the cubic harmonics, which will come in useful in the evaluation of matrix elements. For one, they fulfill an orthonormality relation

$$\int \mathrm{d}\Omega \, K_{lm}(\hat{r}) K_{l'm'}(\hat{r}) = \delta_{ll'}\delta_{mm'} \tag{B.10}$$

where the integration runs over an element of solid angle $\mathrm{d}\Omega$. Similarly, the so-called Gaunt coefficients (calculated by the `subroutine clgd` in file `tools.f90`) are given by the integral of three distinct cubic harmonics

$$C(lm, l'm', l''m'') = \int \mathrm{d}\Omega K_{lm}(\hat{r}) K_{l'm'}(\hat{r}) K_{l''m''}(\hat{r}). \tag{B.11}$$

Below, we list a number of further relations that we will make use of regularly in deriving the matrix elements in App. D:

1. The expansion of the phase factor in cubic harmonics K_{lm} and spherical Bessel functions j_l

$$e^{i\boldsymbol{kr}} = \sum_{l,m} 4\pi \, i^l \, j_l(kr) K_{lm}(\hat{r}) K_{lm}(\hat{k}). \tag{B.12}$$

2. We will often encounter multi-center integrals which are most efficiently evaluated in reciprocal space according to the discrete Fourier transformation

$$A_{s,t}(\boldsymbol{k}) = e^{-i\boldsymbol{k}(\boldsymbol{R_s}-\boldsymbol{R_t})} \sum_L e^{-i\boldsymbol{kR_L}} A_{Ls,0t} \tag{B.13}$$

   of an arbitrary quantity A. This transformation is justified as long as the system exhibits translational symmetry.

3. In this context we will often use the relation

$$\sum_L e^{-i\boldsymbol{kR_L}} = N_{\boldsymbol{k}} \sum_{\boldsymbol{G}} \delta_{\boldsymbol{kG}} = \frac{(2\pi)^3}{\Omega_C} \sum_{\boldsymbol{G}} \delta(\boldsymbol{G}-\boldsymbol{k}) \tag{B.14}$$

   with $\boldsymbol{R_L} \in$ Bravais-lattice, $\boldsymbol{G} \in$ reciprocal lattice and $N_{\boldsymbol{k}}$ the number of $\boldsymbol{k}$-points in the first Brillouin zone.

B.3 Overlap matrix elements

As the LCAO basis set that we have chosen is a non-orthonormal one, the overlap between different orbitals is non-trivial and will consist of onsite and offsite terms. Here, we will restrict our discussion to the spinless case, i.e. neglecting spin indices that would formally appear if we consider spin-orbit coupling or spin polarization. This is justified, as the overlap matrix is diagonal in spin-space and therefore only an increase in matrix dimensionality must be taken into account for these special cases.

B.3.1 Onsite overlap

The onsite terms of the overlap matrix may well serve as an illustrative example of how to apply some of the relations introduced in the last section. Within the BEB-formalism they can be expressed as

$$\dot{S}^{PQ}_{slm,l'm'} = \left\langle sPlm \middle| sPl'm' \right\rangle \delta_{PQ} = \int \mathrm{d}^3 r \left[\phi^P_{lm}(\boldsymbol{r}-\boldsymbol{R_s})\right]^* \phi^P_{l'm'}(\boldsymbol{r}-\boldsymbol{R_s})\delta_{PQ} \tag{B.15}$$

where δ_{PQ} is a consequence of the BEB-rule Eq. (1.27). Shifting $\boldsymbol{r} \to \boldsymbol{r}+\boldsymbol{R_s}$ we find

$$\dot{S}^{PQ}_{slm,l'm'} = i^{(l'-l)} \int \mathrm{d}\Omega \mathrm{d}r\, r^2 f^P_l(r) f^Q_{l'}(r) K_{lm}(\hat{r}) K_{l'm'}(\hat{r}) \delta_{PQ} \tag{B.16}$$

$$= \delta_{ll'}\delta_{mm'} \int \mathrm{d}r\, r^2 \left(f^P_l(\boldsymbol{r})\right)^2 \delta_{PQ} \tag{B.17}$$

where we have used the angular momentum decomposition of ϕ^P_{lm} and the orthonormality of the cubic harmonics. As the orbitals of the same species are normalized in our basis set the onsite overlap becomes unity

$$\dot{S} = \mathbb{1}, \tag{B.18}$$

For the given basis, the unit operator takes the form

$$\mathbb{1} = \sum_{iPlm,jl'm'} |iPlm\rangle \left(S^{-1}\right)^{PQ}_{ilm,jl'm'} \langle jQl'm'| \tag{B.19}$$

where $i(j)$ denotes a site index, species are labelled by $P(Q)$, and $l^{(\prime)}$ and $m^{(\prime)}$ are angular momentum and magnetic quantum numbers, respectively. As a consistency check, Eq. (B.17) has been implemented in `subroutine calcOverlapOnsite` in the file `overlap.f90`.

B.3.2 Offsite overlap

To receive the offsite terms of the overlap matrix it is more convenient to compute the total overlap in reciprocal space and then subtract the onsite terms, accordingly. Due to the translational invariance of the underlined quantities in extended Hilbert space of the BEB-formalism we can write

$$S^{PQ}_{slm,tl'm'} = \sum_L e^{-i\boldsymbol{k}\boldsymbol{R_L}} e^{-i\boldsymbol{k}(\boldsymbol{R_s}-\boldsymbol{R_t})} \int \mathrm{d}^3 r \left[\phi^P_{lm}(\boldsymbol{r}-\boldsymbol{R_L}-\boldsymbol{R_s})\right]^* \phi^Q_{l'm'}(\boldsymbol{r}-\boldsymbol{R_t}) \tag{B.20}$$

Inserting the Fourier transform of the basis functions yields

$$S^{PQ}_{slm,tl'm'} = \frac{\Omega_C}{(2\pi)^6} \sum_L e^{-i\boldsymbol{k}\boldsymbol{R_L}} e^{-i\boldsymbol{k}(\boldsymbol{R_s}-\boldsymbol{R_t})} \int \mathrm{d}^3k' \mathrm{d}^3k'' \phi^{P*}_{lm}(\boldsymbol{k'}) \phi^Q_{l'm'}(\boldsymbol{k''}) \underbrace{\left(\int \mathrm{d}^3 r e^{-i(\boldsymbol{k'}-\boldsymbol{k''})r}\right)}_{=(2\pi)^3\delta(\boldsymbol{k'}-\boldsymbol{k''})} \tag{B.21}$$

$$\times\, e^{i\boldsymbol{k'}(\boldsymbol{R_L}+\boldsymbol{R_s})} e^{-i\boldsymbol{k'}\boldsymbol{R_t}} \tag{B.22}$$

$$= \frac{\Omega_C}{(2\pi)^3} \int \mathrm{d}^3k' \phi^{P*}_{lm}(\boldsymbol{k'}) \phi^Q_{l'm'}(\boldsymbol{k'}) \underbrace{\left(\sum_L e^{-i(\boldsymbol{k}-\boldsymbol{k'})\boldsymbol{R_L}}\right)}_{=((2\pi)^3/\Omega_C)\sum_{\boldsymbol{G}}\delta(\boldsymbol{G}-\boldsymbol{k}+\boldsymbol{k'})} e^{-i(\boldsymbol{k}-\boldsymbol{k'})(\boldsymbol{R_s}-\boldsymbol{R_t})} \tag{B.23}$$

$$= \frac{1}{\Omega_C} \sum_G e^{-i\boldsymbol{G}(\boldsymbol{R_s}-\boldsymbol{R_t})} f^P_l(k-G) K_{lm}(\widehat{k-G}) f^Q_{l'}(k-G) K_{l'm'}(\widehat{k-G}) \tag{B.24}$$

were we have made use of the relations introduced in Sec. B. Thus, we have arrived at an expression for the total overlap matrix elements. Subtracting the trivial result from Eq. (B.18) we find the offsite terms to be

$$\check{S}^{PQ}_{slm,tl'm'}(\boldsymbol{k}) = S^{PQ}_{slm,tl'm'} - \delta_{s,t}\dot{S}^{PQ}_{slm,tl'm'} = S^{PQ}_{slm,tl'm'} - \delta_{s,t} - \delta_{PQ}\delta_{st}\delta_{ll'}\delta_{mm'}. \tag{B.25}$$

Within the CPA program the full overlap is calculated by the `subroutine calcOverlapOffsite` in file `overlap.f90` and stored in the complex array `ovlp_k(irk,iao1,iao2)` for each $\boldsymbol{k}$-point `irk` and orbital indices `iao1` and `iao2`, respectively.

Spin-orbit coupling and spin-polarization

As we have already briefly mentioned above, all considerations so far remain correct if we include spin-orbit coupling or spin polarization. As the overlap matrix is independent of spin, the only effect of an inclusion would be an increase in dimensionality of the overlap matrix such that

$$S = \begin{pmatrix} S_{\uparrow\uparrow} & 0 \\ 0 & S_{\downarrow\downarrow} \end{pmatrix} \tag{B.26}$$

with $S_{\uparrow\uparrow} = S_{\downarrow\downarrow}$. Thus, in the actual implementation the overlap matrix is calculated in the same way for all three cases and only extended to spin space for spin-orbit coupling and spin polarization.

Appendix C

C The electronic density

As we have discussed in Sec. 1.2.3, the BEB-CPA formalism utilizes the electronic density in the locally decomposed form

$$n(\boldsymbol{r}) = \sum_{LsP} \eta^P_{Ls}\, n^P_{Ls}(\boldsymbol{r}). \tag{C.1}$$

Here a brief remark is in order: if we include spin polarization or spin-orbit coupling the n_{Ls} become matrices in spin space and an additional spin trace would appear in Eq. (C.1). In the following we omit spin indices for sake of brevity and shall point out differences to the spinfull cases where need be. In practical calculations the expression in Eq. (C.1) is not explicitly evaluated, but rather all internal calculations, including the charge self-consistency, are performed with the local species resolved density components

$$n^P_{Ls}(\boldsymbol{r}) = -\frac{1}{\pi}\frac{1}{c^P_s} \sum_{\substack{MtQ \\ lml'm'}} \phi^P_{Lslm}(\boldsymbol{r}) \int_0^{E_F} \mathrm{Im}\, \underline{\Gamma}^{PQ}_{Lslm,Mtl'm'}(\omega^+)\mathrm{d}\omega \left(\phi^Q_{Mtl'm'}(\boldsymbol{r})\right)^* \tag{C.2}$$

$$\equiv -\frac{1}{\pi} \sum_{\substack{MtQ \\ lml'm'}} A^{PQ}_{Lslm,Mtl'm'} \left(\phi^Q_{Mtl'm'}(\boldsymbol{r})\right)^* \phi^P_{Lslm}(\boldsymbol{r}). \tag{C.3}$$

As we have mentioned multiple times, a great advantage of the BEB-CPA is the preservation of translational symmetry of quantities in extended Hilbert space. Thus, the effective medium Green's function $\underline{\Gamma}^{PQ}_{Lslm,Mtl'm'}$ only depends of the difference $L - M$ and the same follows for the coefficients $A^{PQ}_{Lslm,Mtl'm'}$. If we now expand the density components in cubic harmonic

$$n^P_{Ls}(\boldsymbol{r}) = \sum_{lm} n^P_{Lslm}(r) K_{lm}(\hat{r}) \tag{C.4}$$

and follow Sec. B.1.3, we can readily compute the translation of an orbital at (M, t) to the origin of the reference orbital at (L, s). After numerous manipulations Eq. (C.4) can be expressed as

$$n^P_{Lslm}(r) = -\frac{1}{\pi} \sum_{MtQ} i^{l'} A^{PQ}_{Lsl'm',Mtl''m''} C(lm, l'm', l'''m''') \times \left[B^Q_{l''m'',l'''m'''}(r, \boldsymbol{R_M} - \boldsymbol{R_L} + \boldsymbol{R_t} - \boldsymbol{R_s})\right]^* f^{Ps}_{l'}(r) \tag{C.5}$$

where we have dropped the explicit summation over (l', l'', l''') and (m', m'', m''') for better readability. The coefficients B in Eq. (C.5) are given by

$$B^{Q}_{lml'm'}(r, \boldsymbol{R}) = \frac{2}{\pi} \sum_{l''m''} i^{l'-l''} C(lm, l'm', l''m'') K_{l''m''}(\hat{R}) \int \mathrm{d}k\, k^2 j_{l'}(kr) j_{l''}(kR) f^{Q}_{l}(k) \tag{C.6}$$

and depend on the actual translation vector. Both Eqs. (C.6) and (C.5) are computed within the `subroutine init_density` found in file `density.f90`. The former is calculated by `subroutine denCalcB` and the B-coefficients are stored in the array `coeffs_B`.
The latter is calculated within `subroutine denSpecOrb` and its symmetrized form in real space is stored in the array `orb_rad_den_r(ir,ilm,iat,itype)`. Each density component is stored according to its species `itype`, atomic index `iat` and combined (l, m)-index `ilm` on an equidistant r-grid with radial index `ir`.
In the first iteration of the CPA we do not yet have access to a Green's function and so we must calculate the densities, or more directly the A-coefficients, via the input supplied by the MBBP, i.e., orbitals, potentials and crystal structure. To be precise, they are calculated from the respective DFT bandstructure for the parent compound and substitutional end members according to Ref. [6] as

$$A^{PQ}_{Lslm,Mtl'm'} = -\frac{2\pi}{N_{\boldsymbol{k}}} \sum_{\boldsymbol{k}j} \mathrm{occup}(\boldsymbol{k}, j) e^{i\boldsymbol{k}(\boldsymbol{R_L}+\boldsymbol{R_s}-\boldsymbol{R_M}-\boldsymbol{R_t})} c^{P\boldsymbol{k}j}_{lms} \left(c^{Q\boldsymbol{k}j}_{l'm't}\right)^{*} \tag{C.7}$$

where the summation runs over all bands j with fractional occupation numbers $\mathrm{occup}(\boldsymbol{k}, j)$ at $\boldsymbol{k}$. Here $c^{P\boldsymbol{k}j}_{lms}$ are the LCAO expansion coefficients for the Bloch-basis with respect to the original DFT Kohn-Sham bands. The calculation is performed by `subroutine denCalcA_first` in `density.f90`.
After the first iteration the new electronic densities are obtained from the Green's function as

$$\begin{aligned} A^{PQ}_{Lslm,Mtl'm'} =& \frac{1}{c^{P}_{s}} \frac{1}{N_{\boldsymbol{k}}} \mathrm{Im} \sum_{\boldsymbol{k}} e^{i\boldsymbol{k}(\boldsymbol{R_L}+\boldsymbol{R_s}-\boldsymbol{R_M}-\boldsymbol{R_t})} \\ & \times \left[\oint_{\mathrm{box}} \underline{\Gamma}^{PQ}_{slm,tl'm'}(\omega) f(\omega, T) \mathrm{d}\omega - \sum_{n} \frac{2n\pi i}{\beta} \underline{\Gamma}^{PQ}_{slm,tl'm'}(\mu + i\omega_n) \right] \end{aligned} \tag{C.8}$$

where the integration runs along a rectangular path in the upper complex half plane at finite temperature T (see Sec. 1.3). In Eq. (C.8) $f(\omega, T)$ is the fermi distribution function and we correct the integral for poles at fermionic Matsubara frequencies $\omega_n = (2n+1)\pi k_B T$. For better numerical stability a Broyden mixing is performed by `subroutine broyd` in `broyd.f`, where the new charge density is mixed with that of the previous iteration.

Spin-orbit coupling

For systems with spin-orbit coupling the Broyden mixing is identical to the unpolarized case, as the electronic density does not split into spin-dependent components.

Spin polarization

In contrast, for spin-polarized calculations we have adopted a more sophisticated approach: instead of mixing the spin-up and spin-down components separately, we mix the full density $n = n_{\uparrow} + n_{\downarrow}$

and magnetization $m = n_\uparrow - n_\downarrow$ of two consecutive iterations and afterwards recover the two spin components according to

$$n_\uparrow = \frac{1}{2}(n + m) \qquad \text{and} \qquad n_\downarrow = \frac{1}{2}(n - m).$$

This approach leads to a better convergence for small differences in the respective spin components between consecutive iterations. Finally, the maximal density difference, which serves as a convergence criterion of the CPA, is calculated in `subroutine denSpecOrb`.

D Appendix D

CPA matrix elements of the Hamiltonian

Before we turn to the computation of the Hamiltonian matrix elements, a general remark needs to be made concerning the storage of the potentials within the CPA code: following the convention used in the MBPP, the radial components of the potentials in real and reciprocal space are actually calculated and stored as $r \cdot V(r)$ and $k^2 \cdot V(k)$, respectively. This has the numerical advantage of avoiding divergences. All potentials are treated in this way, expect for the exchange-correlation potential $V_{\mathrm{XC}}(k)$ which is meaningful for $k = 0$. As the analytic expressions for the matrix elements were derived by Ref. [6] in building the base CPA-code which was further developed within this work, we closely follow the outline presented there. As the matrix elements of spin-orbit coupling present one of the major extensions derived within this work, we shall treat them separately in App. E.

D.1 Potential contributions

We begin our considerations by dividing the full DFT potential into its distinguishable contributions

$$V(\boldsymbol{r}) = V_{\mathrm{Pseudo}}(\boldsymbol{r}) + V_{\mathrm{Hartree}}(\boldsymbol{r}) + V_{\mathrm{XC}}(\boldsymbol{r}). \tag{D.1}$$

The screened interaction between electrons and the positively charged ions is modeled by the pseudopotential V_{Pseudo}. As we restrict ourselves to the treatment of valence electrons, the pseudopotential includes screening effects due to the core electrons. The Hartree term V_{Hartree} describes the interaction of a single electron with the background of the total electronic density. Finally, the exchange-correlation potential V_{XC} incorporates in principle all remaining many-body effects and corrections to the kinetic term and is here treated approximately within the LDA. In the following we shall drop spin indices relevant for spin-orbit coupling and spin polarization for simplicity and shall make note to quantitative changes were need be.

D.1.1 The Pseudopotential

Following the MBPP the pseudopotential is divided into a local and nonlocal part according to

$$\begin{aligned} V_{\mathrm{Pseudo}}(\boldsymbol{r}) &= V_{loc}^{PS}(\boldsymbol{r}) + \sum_{lm} \left[V_l^{PS}(\boldsymbol{r}) - V_{loc}^{PS}(\boldsymbol{r}) \right] |lm\rangle\langle lm| \\ &= V_{loc}^{PS}(\boldsymbol{r}) + \sum_{lm} V_l^{PS,nl}(\boldsymbol{r}) \, |lm\rangle\langle lm| \end{aligned} \tag{D.2}$$

in order to construct the full ionic pseudopotential [30].

The local pseudopotential

The local term $V_{loc}^{PS}(\boldsymbol{r})$ is characterized by a long range behavior $\sim \frac{Ze^2}{r}$, which is exhibited by all angular momentum components outside the core region. In the CPA code, the local part is always chose to be the $l = 0$ component, even though the MBPP allows for a free choice via the array `vidx`. Even though it is transported into the CPA, as of now it serves no functionality there and would have to be extended to grant access to the full functionality.

The nonlocal pseudopotential

The remaining nonlocal parts $V_l^{PS,nl}(\boldsymbol{r})$ describe the angular momentum dependent contributions relevant only inside the core region. In contrast to the local contributions they depend on two sets of coordinates $\boldsymbol{r}$ and $\boldsymbol{r'}$

$$ {}^{nl}V_{Ls}^{Qs}(\boldsymbol{r}, \boldsymbol{r'}) = {}^{nl}V^{Qs}(\boldsymbol{r} - \boldsymbol{R_L} - \boldsymbol{R_s}, \boldsymbol{r'} - \boldsymbol{R_L} - \boldsymbol{R_s}) \tag{D.3} $$

which increases the complexity of the problem. Being a nonlocal operator that is evaluated between two orbitals, we need to obtain knowledge about its action on a wavefunction. Following Refs. [30] and [6], this action is given by

$$ {}^{nl}V_{00}^{Q} \left| 00Ql'm' \right\rangle = \int \mathrm{d}^3r' \, {}^{nl}V^{Q}(\boldsymbol{r}, \boldsymbol{r'}) \phi_{l'm'}^{Q}(\boldsymbol{r'}) = \sum_{lm} \int \mathrm{d}^3r' \frac{1}{r^2} \delta(r - r') \, {}^{nl}V_l^{Q}(r) K_{lm}(\hat{r}) K_{lm}(\hat{r}') \phi_{l'm'}^{Q}(\boldsymbol{r'}). \tag{D.4} $$

From this the reciprocal representation is found to be

$$ {}^{nl}V^{Q}(\boldsymbol{k}, \boldsymbol{k'}) = \frac{4\pi}{\Omega_C} \sum_l (2l+1) P_l(\hat{k} \cdot \hat{k}') \int \mathrm{d}r \, r^2 j_l(kr) \, {}^{nl}V_l^{Q}(r) j_l(k'r) \tag{D.5} $$

with the Legendre polynomials P_l and spherical Bessel functions j_l.

D.1.2 The full local potential

The full local potential, which we will need to decompose into angular momentum contributions, is comprised not only of the local part of the pseudopotential but in addition contains the Hartree und exchange-correlation terms:

$$ V^{Qs}(\boldsymbol{r}) = V_{\mathrm{Hartree}}(\boldsymbol{r}) + V_{loc}^{PS}(\boldsymbol{r}) + V_{\mathrm{XC}}(\boldsymbol{r}). \tag{D.6} $$

We must then find a decomposition of the form

$$ V_{Ls}^{Qs}(\boldsymbol{r}) = V^{Qs}(\boldsymbol{r} - \boldsymbol{R_L} - \boldsymbol{R_s}) \tag{D.7} $$

for the CPA scheme. The analysis of the local potentials works analogous to that of the local orbitals in Sec. B. However, the definition of the Fourier transformation

$$ V^{Qs}(\boldsymbol{k}) = \frac{1}{\Omega_C} \int \mathrm{d}^3r \, V^{Qs}(\boldsymbol{r}) e^{-i\boldsymbol{kr}} \tag{D.8} $$

$$ V^{Qs}(\boldsymbol{r}) = \frac{\Omega_C}{(2\pi)^3} \int \mathrm{d}^3k \, V^{Qs}(\boldsymbol{k}) e^{i\boldsymbol{kr}} \tag{D.9} $$

for the local potentials differs from that of the local basis functions in two ways: firstly, the convention has been chosen such that we find a factor Ω_C instead of its square root. Secondly, the angular momentum decomposition does not include the factor i^l and is given by

$$V^{Qs}(\boldsymbol{r}) = \sum_{lm} V^{Qs}_{lm}(r) K_{lm}(\hat{r}) \tag{D.10}$$

Using this definition the reciprocal representation of V^{Qs} may be written as

$$V^{Qs}(\boldsymbol{k}) = \frac{4\pi}{\Omega_C} \int \mathrm{d}r\, r^2 \sum_{lm} (-i)^l j_l(kr) K_{lm}(\hat{k}) V^{Qs}_{lm}(r) \tag{D.11}$$

and further simplified to

$$V^{Qs}(\boldsymbol{k}) = \frac{1}{\Omega_C} \sum_{lm} (-i)^l V^{Qs}_{lm}(k) K_{lm}(\hat{k}) \tag{D.12}$$

by introducing the radial Fourier transformation

$$V^{Qs}_{lm}(k) = 4\pi \int \mathrm{d}r\, r^2 j_l(kr) V^{Qs}_{lm}(r). \tag{D.13}$$

This definition is equivalent to that of the basis orbitals in Eq. (B.4a). As this definition differs from that used within the MBPP, imported k-dependent potentials need to be rescaled by a factor of $\frac{1}{4\pi}$ within the CPA. A translation of the origin in real space is treated analogous to that of the basis orbitals and yields

$$V^{Qs}_{Ls}(\boldsymbol{r}) = \frac{\Omega_C}{(2\pi)^3} \int \mathrm{d}^2k\, \mathrm{d}^3r' e^{-i\boldsymbol{k}(\boldsymbol{R_L})-\boldsymbol{R_s}} e^{i\boldsymbol{kr}} V^{Qs}(\boldsymbol{k}) \tag{D.14}$$

$$= \frac{1}{(2\pi)^3} \int \mathrm{d}^3k\, \mathrm{d}^3r' e^{-i\boldsymbol{k}(\boldsymbol{R_L}-\boldsymbol{R_s})} e^{i\boldsymbol{kr}} V^{Qs}(\boldsymbol{r'}) e^{-i\boldsymbol{kr'}}. \tag{D.15}$$

D.1.3 The Hartree potential

As the Hartree potential describes the interaction of a single electron with the total electronic density its real space representation is given by

$$V_{\mathrm{Hartree}}(\boldsymbol{r}) = e^2 \int \frac{n(\boldsymbol{r'})}{|\boldsymbol{r}-\boldsymbol{r'}|}. \tag{D.16}$$

A much simpler evaluation is possible in reciprocal space, as we can Fourier transform the electronic density

$$\begin{aligned} n(\boldsymbol{k}) =& \frac{1}{\Omega_C} \int \mathrm{d}^3r\, n(\boldsymbol{r}) e^{-i\boldsymbol{kr}} \\ =& \frac{1}{\Omega_C} \sum_{Ps} \eta^P_s \sum_{lm} (-i)^l K_{lm}(\hat{k}) n^P_{slm}(k) \\ \equiv& \sum_{Ps} \eta^P_s n^P_s(\boldsymbol{k}) \end{aligned} \tag{D.17}$$

with the radial Fourier transformation $n^P_{slm}(k)$. With this we find the reciprocal representation of the Hartree potential to be

$$V_{\text{Hartree}}(\boldsymbol{k}) = 4\pi e^2 \frac{n(\boldsymbol{k})}{k^2} = e^2 \frac{4\pi}{k^2} \sum_{Ps} \eta^P_s n^P_s(\boldsymbol{k}) \equiv \sum_{Ps} \eta^{P(H)}_s V^P_s(\boldsymbol{k}). \tag{D.18}$$

We have thus found a site and species resolved decomposition of V_{Hartree} in the sense of the BEB-CPA which is directly calculated from the densities via

$$\begin{aligned} {}^{(H)}V^P_s =& \frac{1}{\Omega_C} \frac{4\pi e^2}{k^2} \sum_{lm} (-i)^l \, n^{Ps}_{lm}(k) K_{lm}(\hat{k}) \\ \equiv& \frac{1}{\Omega_C} \sum_{lm} (-i)^l \, {}^{(H)}V^{Ps}_{lm}(k) K_{lm}(\hat{k}). \end{aligned} \tag{D.19}$$

Here

$${}^{(H)}V^{Ps}_{lm}(k) \equiv \frac{4\pi e^2}{k^2} \eta^P_s n^{Ps}_{lm}(k) \tag{D.20}$$

is the species and radial angular resolved local contribution to the Hartree potential. Within the MBBP and the CPA program a unit convention has been chosen such that $e^2 = 2$. As already mentioned at the beginning of this chapter the implemented code actually computes potentials in the form $k \cdot V(k)$, so that we avoid the divergence of Eq. (D.20) as $k \to 0$. We finally come to the real space components of the Hartree potential by a radial Fourier transformation

$${}^{(H)}V^{Ps}_{lm}(r) = \frac{1}{2\pi^2} \int \mathrm{d}k \, k^2 j_l(kr) \, {}^{(H)}V^{Ps}_{lm}(k) = \frac{4\pi e^2}{2\pi^2} \eta^P_s \int \mathrm{d}k \, j_l(kr) n^P_{slm}(k) \tag{D.21}$$

which is implemented in `subroutine calcHartree` in `potential.f90`.

D.1.4 The exchange and correlation potential

As we have already discussed in Sec. 1.2.4, the most complicated contribution to the full electronic potential is the exchange and correlation term - the main difficulty being the fact that it is a nonlinear functional of the electronic density and it cannot be expressed in a closed analytic form. We must thus always resort to approximative schemes in determining its contribution. A sophisticated shape function approach was implemented for the treatment of the XC potential in the CPA code by Ref. [6] and shall be described in detail in the following. We begin by defining a radially symmetric shape function S_i

$$S_i(|\boldsymbol{r}|) = S_i(r) = S\left(\frac{r}{R_i}\right) \qquad \text{with} \qquad S(1) = 0 \tag{D.22}$$

for every site i in the medium. Each of these shape functions is then characterized by a cutoff radius R_i and two parameters $n \in \mathbb{N}$ and $\gamma \in \mathbb{R}$ such that

$$S(x) = \begin{cases} 1 & \text{for} \quad n = 0 \\ e^{-\gamma x^2} & \text{for} \quad n = 1. \\ 1 - e^{-\gamma(1-x)^n} & \text{for} \quad n \geq 2 \end{cases} \tag{D.23}$$

In principle, the functional forms of the shape functions may differ for each site, however, they actual implementation of the CPA code demands the same functional form for all types. We may now introduce a norm

$$\mathcal{N}(\boldsymbol{r}) = \sum_i S_i(\boldsymbol{r} - \boldsymbol{R_i}) \tag{D.24}$$

as the sum over all site centered shape functions evaluated at an arbitrary point $\boldsymbol{r}$. With this norm we may perform a local decomposition of the XC potential according to

$${}^{\mathrm{XC}}V_i(\boldsymbol{r} - \boldsymbol{R_i}) = V_{\mathrm{XC}}[n(\boldsymbol{r})]\frac{S_i(\boldsymbol{r} - \boldsymbol{R_i})}{\mathcal{N}(\boldsymbol{r})}. \tag{D.25}$$

If we consider the clean case, i.e. no random site occupation, we find

$$\begin{aligned} V_{\mathrm{XC}}[n(\boldsymbol{r})] &\stackrel{!}{=} \sum_i {}^{\mathrm{XC}}V_i(\boldsymbol{r} - \boldsymbol{R_i}) = \sum_i V_{\mathrm{XC}}[n(\boldsymbol{r})]\frac{S_i(\boldsymbol{r} - \boldsymbol{R_i})}{\mathcal{N}(\boldsymbol{r})} \\ &= V_{\mathrm{XC}}[n(\boldsymbol{r})]\frac{\mathcal{N}(\boldsymbol{r})}{\mathcal{N}(\boldsymbol{r})}. \end{aligned} \tag{D.26}$$

Thus, without disorder our decomposition becomes exact. In contrast, for a disordered system the site and species indices are no longer uniquely connected and so for the substituted system Eq. (D.25) becomes approximative. As we have discussed in Sec. 1.2.4, the introduction of the shape function scheme was made necessary due to some drawbacks of the simpler ASA. An important distinction from the ASA is the required overlap of the shape function to ensure that each and every point in space is covered by some shape function. The problem of double counting due to this overlap is circumvented by employing the norm in Eq. (D.25). The quality of a decomposition may be determined in two different ways: (i) via $\mathcal{N}(\boldsymbol{r})$ which should exhibit the lowest possible spatial fluctuations if evaluated at several points in the unit cell and (ii) via a comparison of the CPA band structure of the clean compound with that of the respective DFT calculation.
Now that we have found a sensible local decomposition of the XC potential, we must further decompose it in terms of angular momentum:

$${}^{\mathrm{XC}}V_s^P(\boldsymbol{r}) = \sum_{lm} {}^{\mathrm{XC}}V_{s,lm}^P(r)K_{lm}(\hat{r}). \tag{D.27}$$

Making use of the orthonormality Eq. (B.10) of the cubic harmonics we can find the radial angular components

$${}^{\mathrm{XC}}V_{s,lm}^P(r) = \int \mathrm{d}\Omega \, {}^{\mathrm{XC}}V_s^P(\boldsymbol{r})K_{lm}(\hat{r}). \tag{D.28}$$

In contrast to the other potential contributions, for which we could find analytic expressions, the ${}^{\mathrm{XC}}V_{s,lm}^P(r)$ can only be determined numerically (a consequence of the nonlinear dependence of V_{XC} on the electronic density). With the solid angle in Eq. (D.28) expressed in spherical coordinates $\mathrm{d}\Omega = \mathrm{d}\varphi\mathrm{d}\cos\theta$ the integration is carried out in two steps. First, the integration over φ from 0 to 2π

is divided into N equidistant points and performed via the trapezoidal rule [49, 50]

$$\begin{aligned}\int_0^{2\pi} \mathrm{d}\varphi\, f(\varphi) &= \int_0^{\frac{2\pi}{N}} \mathrm{d}\varphi\, f(\varphi) + \int_{\frac{2\pi}{N}}^{2\frac{2\pi}{N}} \mathrm{d}\varphi\, f(\varphi) + \cdots + \int_{(N-1)\frac{2\pi}{N}}^{N\frac{2\pi}{N}} \mathrm{d}\varphi\, f(\varphi) \\ &= \frac{2\pi}{N}\frac{f_0+f_1}{2} + \frac{2\pi}{N}\frac{f_1+f_2}{2} + \cdots + \frac{2\pi}{N}\frac{f_{N-1}+f_N}{2} \\ &= \frac{2\pi}{N}\left[\frac{f_0+f_N}{2} + \sum_{n=1}^{N-1} f_n\right], \end{aligned} \tag{D.29}$$

where $f_n = f(n\frac{2\pi}{N})$. If we make use of the periodicity of the spherical coordinates, i.e. $f_0 = f_n$, we come to

$$\int_0^{2\pi} \mathrm{d}\varphi\, f(\varphi) = \frac{2\pi}{N}\sum_{n=0}^{N-1} f_n. \tag{D.30}$$

Second, the integration over $\mathrm{d}\cos\theta$ is performed via a Gauß-Legendre quadrature [48–50, 155]

$$\int \mathrm{d}\cos\theta\, f(\theta) = \sum_{i=1}^{n} w_i f(x_i) \tag{D.31}$$

with weight factors

$$w_i = \frac{2}{(1-x_i^2)[P_n'(x_i)]^2}. \tag{D.32}$$

Here, P_i' denotes the first derivative of the Legendre polynomials and the tabulated optimal x_i for n sampling points were taken from Ref. [155]. Bringing both integration schemes together, we can reformulate Eq. (D.28) and come to an expression for the site and species resolved orbital decomposition of the XC potential:

$${}^{\mathrm{XC}}V_{slm}^{P}(r) = \sum_{i=1}^{n} w_i \frac{2\pi}{N}\sum_{j=1}^{N} {}^{\mathrm{XC}}V_s^P(\boldsymbol{r_{i,j}}) K_{lm}(\varphi_j, x_i) \tag{D.33}$$

with $x_i = (\cos\theta)_i$. Due to bench marking by Ref. [6], $N = 17$ and $n = 10$ are implemented in the CPA code. The full decomposition is carried out by `subroutine calcVxc` in file `potential.f90`, where the total configurationally averaged electronic density

$$n(\boldsymbol{r}) = \sum_{\substack{LsP \\ lm}} c_s^P n_{lm}^P(|\boldsymbol{r} - \boldsymbol{R_{Ls}}|) K_{lm}(\widehat{\boldsymbol{r} - \boldsymbol{R_{Ls}}}) \tag{D.34}$$

needed for the calculation of the total XC potential is performed by the `double precision function calcXCDen_spec`.

Spin-orbit coupling

The above computational scheme holds for systems with spin-orbit coupling, as the electronic density - and thus the XC potential - is not separated into spin components.

Spin polarization

The case of spin-polarization is treated differently: here, a separation of the electronic density according to spin components is and meaningful. Consequently, the XC potential must be calculated for each spin component separately by `subroutine calcVxc`.

D.1.5 The mixing potential

As we evaluate the potential contributions of the LCAO-CPA Hamiltonian we come across terms of the form

$$\left\langle iPlm\middle|\sum_{k\neq(i,j),R} c_k^R V_k^R\middle|jQl'm'\right\rangle \tag{D.35}$$

containing restricted sums such as in Eqs. (1.55) and (1.56). Instead of evaluating these sums directly, we take a different route: we first evaluate the unrestricted sum and later on subtract the excluded contributions. This approach not only serves as an efficient computation scheme but furthermore lends a tool to verify the proper functionality of the CPA code. As the unrestricted sum yields the crystal potential for a clean compound, i.e. a system without disorder and concentrations equal to one, the Hamiltonian matrix elements may here be compared to those of the underlying MBPP calculation of the parent compound. Additionally, the diagonalized crystal Hamiltonian may be applied in the analysis of self-energy effects in the disordered system. Following Ref. [6], the so called "mixing-potential" is given by

$$\begin{aligned} V_{\mathrm{mix}}(\boldsymbol{r}) &= \sum_{NuR} c_u^R V_{Nu}^{R_u}(\boldsymbol{r}) = \frac{\Omega_C}{(2\pi)^3}\sum_{NuR} c_u^R \int \mathrm{d}^3k\, e^{-i\boldsymbol{k}(\boldsymbol{R_N}+\boldsymbol{R_u})} e^{i\boldsymbol{kr}} V^{R_u}(\boldsymbol{k}) \\ &= \sum_{\boldsymbol{G}uR} c_u^R e^{-i\boldsymbol{GR_u}} e^{i\boldsymbol{Gr}} V^{R_u}(\boldsymbol{G}) \equiv \sum_{\boldsymbol{G}} e^{i\boldsymbol{Gr}} V_{\mathrm{mix}}(\boldsymbol{G}), \end{aligned} \tag{D.36}$$

with the lattice index N, atomic index u within the unit cell, species index R and reciprocal lattice vector $\boldsymbol{G}$. In the last step of Eq. (D.36) we have written the mixing potential in form of a Fourier series by introducing

$$\begin{aligned} V_{\mathrm{mix}}(\boldsymbol{G}) &= \sum_{uR} c_u^R e^{-i\boldsymbol{GR_u}} V^{R_u}(\boldsymbol{G}) \\ &= \frac{1}{\Omega_C}\sum_{uRlm} c_u^R e^{-i\boldsymbol{GR_u}} (-i)^l V_{lm}^{R_u}(G) K_{lm}(\hat{G}). \end{aligned} \tag{D.37}$$

In the case of a clean compound V_{mix} is obviously lattice periodic, as it reduces to the crystal potential. For a disordered system the lattice periodicity follows directly from Eq. (D.36). Making use of relations and definitions discussed in App. B, it is straightforward to derive the onsite matrix elements which take the form

$$\begin{aligned} \left\langle sPlm\middle|V_{\mathrm{mix}}\middle|sPl'm'\right\rangle = 4\pi \sum_{\boldsymbol{G}} e^{i\boldsymbol{GR_s}} V_{\mathrm{mix}}(\boldsymbol{G}) \sum_{l''m''} i^{l'+l''-l} K_{l''m''}(\hat{G}) \\ \times C(lm, l'm', l''m'') \int \mathrm{d}r\, r^2 j_{l''}(Gr) f_l^{P_s}(r) f_{l'}^{P_s}(r). \end{aligned} \tag{D.38}$$

Due to the lattice periodicity we may evaluate matrix elements between arbitrary site in $\boldsymbol{k}$-space:

$$\begin{aligned}{}^{\mathrm{mix}}H^{PQ}_{slm,tl'm'}(\boldsymbol{k}) &= \sum_{L} \left\langle LsPlm \middle| V_{\mathrm{mix}} \middle| 0tQl'm' \right\rangle e^{-i\boldsymbol{k}\boldsymbol{R_L}} e^{-i\boldsymbol{k}(\boldsymbol{R_s}-\boldsymbol{R_t})} \\ &= \frac{1}{\Omega_C} \sum_{\boldsymbol{G}\boldsymbol{G}'} e^{-i\boldsymbol{G}\boldsymbol{R_s}} e^{i\boldsymbol{G}'\boldsymbol{R_t}} f^P_l(k-G) \widehat{K_{lm}(k-G)} \\ &\quad \times V_{\mathrm{mix}}(\boldsymbol{G}'-\boldsymbol{G}) f^Q_{l'}(k-G') \widehat{K_{l'm'}(k-G')}. \end{aligned} \tag{D.39}$$

As we have discussed in App. D.1.1, we must discern between local and nonlocal contributions to the potential. In this context we must note that the above expression is only valid for the local potential and the nonlocal contribution must be treated separately. With the nonlocal pseudopotential being a nonlocal operator we find

$$\left\langle sPlm \middle| V^{nl}_{\mathrm{mix}} \middle| sPl'm' \right\rangle = \frac{\Omega_C}{(2\pi)^3} \sum_{\boldsymbol{G}uR} c^R_u \int \mathrm{d}^3k \, e^{-\boldsymbol{G}(\boldsymbol{R_s}-\boldsymbol{R_u})} \left(\phi^P_{lm}(\boldsymbol{k})\right)^* {}^{nl}V^{R_u}(\boldsymbol{k}, \boldsymbol{k}-\boldsymbol{G}) \phi^P_{l'm'}(\boldsymbol{k}-\boldsymbol{G}) \tag{D.40}$$

with

$$V^{nl}_{\mathrm{mix}} = \sum_{NuR} c^{R\,nl}_u V^{R_u}_{Nu}. \tag{D.41}$$

Due to the three dimensional integration, the derivation of matrix elements from expression Eq. (D.40) becomes quite tedious and due to the lack of further simplification must be performed in k-space. The final expression for ${}^{\mathrm{mix,nl}}H(\boldsymbol{k})$ is found to be

$$\begin{aligned}{}^{mix,nl}H^{PQ}_{slm,tl'm'}(\boldsymbol{k}) &= \sum_{L} \left\langle LsPlm \middle| V^{nl}_{\mathrm{mix}} \middle| 0tQl'm' \right\rangle e^{-i\boldsymbol{k}\boldsymbol{R_L}} e^{-i\boldsymbol{k}(\boldsymbol{R_s}-\boldsymbol{R_t})} \\ &= \sum_{\boldsymbol{G}\boldsymbol{G}'uR} c^R_u e^{-i\boldsymbol{G}\boldsymbol{R_s}} e^{i\boldsymbol{G}'\boldsymbol{R_t}} e^{i(\boldsymbol{G}-\boldsymbol{G}')\boldsymbol{R_u}} \\ &\quad \times \left(\phi^P_{lm}(\boldsymbol{k}-\boldsymbol{G})\right)^* {}^{nl}V^{R_u}(\boldsymbol{k}-\boldsymbol{G}, \boldsymbol{k}-\boldsymbol{G}') \phi^Q_{l'm'}(\boldsymbol{k}-\boldsymbol{G}'). \end{aligned} \tag{D.42}$$

Both the local and nonlocal contributions are calculated by `subroutine calcVmix2_k` and joined into the full $\boldsymbol{k}$-dependent mixing potential. The subroutine may be found in file `hloc.f90` and is stored in the complex array `vmix_k(irk,iao1,iao2)`. In contrast to the original implementation of Ref. [6], the subroutine was improved to make use of local part of the radial basis functions which lead to a drastic speed up in calculations. From the full mixing potential the onsite terms are obtained via Fourier transformation of Eqs. (D.39) and (D.42) performed by `subroutine calcMixOnsite` in file `hamilton.f90`

D.2 The Hamiltonian matrix elements

We are now in a position to evaluate the full Hamiltonian matrix elements and present them in an analytical form. As it is often convenient to have the matrix elements for both onsite and offsite terms, we shall discuss the respective contributions separately.

D.2.1 Onsite matrix elements of the Hamiltonian

We begin with the onsite Hamilton matrix elements which contain the following contributions

$$\begin{aligned}\dot{H}^{PP}_{slm,l'm'} =& \dot{T}^{PP}_{slm,l'm'} + \dot{W}^{PPP}_{slm,l'm'} \\ &+ \underbrace{\sum_{\substack{R \\ (N,u)\neq(0,s)}} \left\langle sPlm \middle| c^R_u \left(V^{R_u}_{Nu} + {}^{nl}V^{R_u}_{Nu} \right) \middle| sPl'm' \right\rangle}_{\equiv \Sigma_{\mathrm{res}}} . \end{aligned} \tag{D.43}$$

The first term in Eq. (D.43) denotes the kinetic contributions which are given by

$$\dot{T}^{PQ}_{slm,l'm'} \equiv \left\langle sPlm \middle| \hat{T} \middle| sQl'm' \right\rangle = \delta_{ll'}\delta_{mm'} \frac{\hbar^2}{2m} \frac{1}{(2\pi)^3} \int \mathrm{d}k\, k^4 f^P_l(k) f^Q_l(k). \tag{D.44}$$

Here, we have adapted the conventions chosen in MBPP, i.e., we have set $\frac{\bar{h}^2}{2m} = 1$. The pseudopotential contributions to the onsite matrix elements must once again be separated into local and nonlocal parts:

$$\dot{W}^{PRQ}_{slm,l'm'} \equiv \left\langle sPlm \middle| V^{R_s}_s \middle| sQl'm' \right\rangle + \left\langle sPlm \middle| {}^{nl}V^{R_s}_s \middle| sQl'm' \right\rangle , \tag{D.45}$$

where

$$\left\langle sPlm \middle| V^{R_s}_s \middle| sQl'm' \right\rangle = \sum_{l''m''} i^{l'-l} C(lm, l'm', l''m'') \int \mathrm{d}r\, r^2 f^{P_s}_l(r) V^{R_s}_{l''m''}(r) f^{Q_s}_{l'}(r) \tag{D.46}$$

and

$$\left\langle sPlm \middle| {}^{nl}V^{R_s}_s \middle| sQl'm' \right\rangle = \delta_{ll'}\delta_{mm'}\theta(l-1)\theta(l_{\max}-l) \int \mathrm{d}r\, r^2 f^{P_s}_l(r)\, {}^{nl}V^{R_s}_l(r) f^{Q_s}_l(r). \tag{D.47}$$

Here, the potentials carry an additional species index R which will become necessary in calculating offsite matrix elements. The last term we are left with in Eq. (D.43) contains a restricted sum which can be evaluated via

$$\Sigma_{\mathrm{res}} = \left\langle sPlm \middle| V_{\mathrm{mix}} + V^{nl}_{\mathrm{mix}} \middle| sPl'm' \right\rangle - \sum_R c^R_s \dot{W}^{PRP}_{slm,l'm'}. \tag{D.48}$$

The calculation of all onsite matrix elements for the Hamiltonian are carried out by the `subroutine calcHOnsite` in file `hamilton.f90`. Each contribution is stored in a separate complex array. In the code `vOnsite(iao1,itype,iao2)` stands for $\dot{W}$, `tOnsite(iao1,iao2)` for $\dot{T}$ and `hOnsite(iao1,iao2)` for $\dot{H}$.

D.2.2 Offsite matrix elements of the Hamiltonian

The expressions for the offsite matrix elements of the Hamiltonian

$$\begin{aligned}\breve{H}^{PQ}_{slm,tl'm'}(\boldsymbol{k}) =& T^{PQ}_{slm,tl'm'}(\boldsymbol{k}) + W^{PPQ}_{slm,tl'm'}(\boldsymbol{k}) + \left[W^{QQP}_{tl'm',slm}(\boldsymbol{k})\right]^* \\ &+ \underbrace{\sum_{(N,u)\neq(0,s),(0,t)} \left\langle sPlm\middle| c^R_u \left(V^{R_u}_{Nu} + {}^{nl}V^{R_u}_{Nu}\right)\middle| tQl'm'\right\rangle(\boldsymbol{k})}_{\equiv\Sigma_{\mathrm{res}}} \\ &- \delta_{st}\left[\dot{T}^{PQ}_{slm,l'm'} + \dot{W}^{PPQ}_{slm,l'm'} + \left(\dot{W}^{QQP}_{sl'm',lm}\right)^*\right] \\ &- \delta_{st}\left\langle sPlm\middle| V_{\mathrm{mix}} + V^{nl}_{\mathrm{mix}}\middle| sQl'm'\right\rangle \\ &+ \delta_{st}\sum_R c^R_s\left[\dot{W}^{PRQ}_{slm,l'm'} + \left(\dot{W}^{QRP}_{sl'm',lm}\right)^*\right] \end{aligned} \tag{D.49}$$

are similar to those of the onsite Hamiltonian in Eq. (D.43), however, there are a number of additional contributions to consider. The last three lines of Eq. (D.49) comprise corrections ensuring the $1-\delta_{ij}$ property of offsite quantities. As already mentioned above, an additional species index enters the onsite potential matrix elements $\dot{W}$ which is motivated by the corrections necessary in the offsite terms. We find the offsite kinetic contribution to be given by

$$T^{PQ}_{slm,tl'm'}(\boldsymbol{k}) = \frac{\hbar^2}{2m\Omega_C}\sum_{\boldsymbol{G}}(\boldsymbol{k}-\boldsymbol{G})^2 e^{-i\boldsymbol{k}(\boldsymbol{R_s}-\boldsymbol{R_t})} f^P_l(k-G)K_{lm}(\widehat{k-G}) f^Q_{l'}(k-G)K_{l'm'}(\widehat{k-G}). \tag{D.50}$$

A note about the last term in the first line of Eq. (D.49) is in order: here, we have made use of the hermiticity of the Hamiltonian and thus

$$\left\langle sPlm\middle| V^Q_t\middle| tQl'm'\right\rangle = \left\langle tQl'm'\middle| V^Q_t\middle| sPlm\right\rangle^*. \tag{D.51}$$

Originally being a term with the potential centered at the right terminal site we may now consider only terms centered at the left terminal site in following. After a tedious calculation these left centered matrix elements in reciprocal space are found to be

$$\begin{aligned}\left\langle sPlm\middle| V^{R_s}_s\middle| tQl'm'\right\rangle(\boldsymbol{k}) =& \frac{4\pi}{\Omega_C}\sum_{\substack{l''m''\\ l'''m'''}} i^{l'''-l} C(lm,l''m'',l'''m''') \\ &\times \sum_{\boldsymbol{G}} e^{-i\boldsymbol{G}(\boldsymbol{R_s}-\boldsymbol{R_t})} K_{l'm'}(\widehat{k-G})K_{l'''m'''}(\widehat{k-G}) \\ &\times f^Q_{l'}(k-G)\int \mathrm{d}r\, r^2 j_{l''}((k-G)r) f^P_l(r) V^{R_s}_{l''m''}(r) \end{aligned} \tag{D.52}$$

for the local part and

$$\begin{aligned}\left\langle sPlm\middle| {}^{nl}V^{R_s}_s\middle| tQl'm'\right\rangle(\boldsymbol{k}) =& \frac{4\pi}{\Omega_C}\sum_{\boldsymbol{k}} e^{-i\boldsymbol{G}(\boldsymbol{R_s}-\boldsymbol{R_t})} f^Q_{l'}(k-G)K_{lm}(\widehat{k-G}) \\ &\times K_{l'm'}(\widehat{k-G})\int \mathrm{d}r\, r^2 j_l((k-G)r) f^P_l(r)\, {}^{nl}V^{R_s}_l(r) \end{aligned} \tag{D.53}$$

for the nonlocal part, respectively. Thus, the total pseudopotential contribution is given by

$$W^{PRQ}_{slm,tl'm'}(\boldsymbol{k}) \equiv \left\langle sPlm\middle|V_s^{R_s}\middle|tQl'm'\right\rangle(\boldsymbol{k}) + \left\langle sPlm\middle|{}^{nl}V_s^{R_s}\middle|tQl'm'\right\rangle(\boldsymbol{k}). \tag{D.54}$$

We may now turn to the restricted sum Σ_{res} in Eq. (D.49) which can be written as

$$\Sigma_{\text{res}} = {}^{\text{mix}}H^{PQ}_{slm,tl'm'}(\boldsymbol{k}) + {}^{\text{mix},nl}H^{PQ}_{slm,tl'm'}(\boldsymbol{k}) - \sum_R \left(c_s^R W^{PRQ}_{slm,tl'm'}(\boldsymbol{k}) + c_t^R \left[W^{QRP}_{tl'm',slm}(\boldsymbol{k}) \right]^* \right). \tag{D.55}$$

Within the CPA program the above equations are evaluated by the `subroutine calcHOffsite_lr` in file `hamilton.f90`. The matrix elements for the potential W are stored in the complex array `vOffsite(irk,iao1,itype,iao2)`, while the kinetic contribution T is stored in `tOffsite(irk,iao1,iao2)` and the offsite Hamiltonian $\breve{H}$ in `hOffsite(irk,iao1,iao2)`. When considering spin-orbit coupling or spin polarization, formally spinor states must be introduced leading to additional spin indices, i.e. an increase in dimensionality of the involved matrices. However, most contributions to the Hamiltonian are independent of spin. In the practical implementation this allows us to keep most calculations involved in the evaluation of the Hamiltonian largely unmodified.
Generalizing to spin-space, the Hamiltonian will take the form

$$H = \begin{pmatrix} H_{\uparrow\uparrow} & H_{\uparrow\downarrow} \\ H_{\downarrow\uparrow} & H_{\downarrow\downarrow}, \end{pmatrix} = \begin{pmatrix} H_0 & 0 \\ 0 & H_0 \end{pmatrix} + \begin{pmatrix} \tilde{H}_{\uparrow\uparrow} & \tilde{H}_{\uparrow\downarrow} \\ \tilde{H}_{\downarrow\uparrow} & \tilde{H}_{\downarrow\downarrow} \end{pmatrix}, \tag{D.56}$$

where we have separated the Hamiltonian into a spin independent part H_0 and a spin dependent part $\tilde{H}_{\sigma\sigma'}$ with spin indices $\sigma^{(\prime)}$ in the last step. The first term consists of all contributions which need only be calculated in the "reduced dimensionality" without spin indices and are later on placed on the diagonal of the spinfull Hamiltonian. The second term denotes those contributions which directly depend on spin and can, in principal, have non-zero mixing terms $\tilde{H}_{\uparrow\downarrow}$ and $\tilde{H}_{\downarrow\uparrow}$.

Spin polarization

For the spin polarized case this contribution consists only of the XC potential, which is a functional of the spin components of the electronic density and was already discussed in App. D.1.4. Furthermore, for pure spin polarization (no additional spin-orbit coupling) no mixing terms occur and $\tilde{H}_{\uparrow\downarrow} = \tilde{H}_{\downarrow\uparrow} = 0$.

Spin-orbit coupling

For spin-orbit coupling mixing terms will in general be nonzero, i.e. $\tilde{H}_{\sigma\bar{\sigma}} \neq 0$, where $\bar{\sigma}$ denotes the opposite of σ. Here, the spin dependent contribution stems from the spin-orbit coupling potential V_{SO} which we shall discuss in great detail in the next chapter. The spin-orbit coupling part of the Hamiltonian in reciprocal space takes the form

$$\begin{aligned} {}^{SO}\mathcal{H}^{PQ\sigma\sigma'}_{slm,tl'm'}(\boldsymbol{k}) = &\sum_{\boldsymbol{GG'}\kappa\boldsymbol{u}} c^{\kappa}_{\boldsymbol{u}} e^{-i\boldsymbol{GR_s}} e^{i\boldsymbol{G'R_t}} e^{i(\boldsymbol{G}-\boldsymbol{G'})\boldsymbol{R_u}} \phi^{P*}_{lm}(\boldsymbol{k}-\boldsymbol{G}) \phi^{Q}_{l'm'}(\boldsymbol{k}-\boldsymbol{G'}) \\ &\times \sum_{l''\geq 1} v^{SO\sigma\sigma'}_{\kappa l''}(k-G, k-G'), \end{aligned} \tag{D.57}$$

with angular momentum resolved spin-orbit potential $v_{\kappa l}^{SO\sigma\sigma'}(k,k')$ of species κ and atomic concentration $c_{\boldsymbol{u}}^{\kappa}$ at lattice position $\boldsymbol{u}$.

Appendix E

Spin-orbit matrix elements

One of the main extensions added to the CPA program within this work is the development of a full SOC treatment of substitutionally disordered systems. Therefore, a detailed derivation of the appropriate CPA matrix elements of the SOC potential shall be given here.

E.1 Relativistic norm-conserving pseudopotentials

We begin our derivation with a general consideration of the spin-orbit potential in the context of norm-conserving pseudopotentials, as developed by Refs. [156], [157] and [158]. To this end, the major components of a relativistic pseudopotential are expanded in spinor eigenstates to J and L

$$\hat{V}^{PS} = \sum_{lm} \left| l+\frac{1}{2}, m+\frac{1}{2} \right\rangle V^{ion}_{l,l+\frac{1}{2}}(r) \left\langle l+\frac{1}{2}, m+\frac{1}{2} \right| + \left| l-\frac{1}{2}, m-\frac{1}{2} \right\rangle V^{ion}_{l,l-\frac{1}{2}}(r) \left\langle l-\frac{1}{2}, m-\frac{1}{2} \right|$$

with the spinor eigenstates $\left| J, m_J \right\rangle$

$$\left| l+\frac{1}{2}, m+\frac{1}{2} \right\rangle = \begin{pmatrix} \left(\frac{l+m+1}{2l+1}\right)^{\frac{1}{2}} \left| lm \right\rangle \\ \left(\frac{l-m}{2l+1}\right)^{\frac{1}{2}} \left| lm+1 \right\rangle \end{pmatrix} \qquad J = l+\frac{1}{2}, m_J = m+\frac{1}{2} \tag{E.1}$$

$$\left| l-\frac{1}{2}, m-\frac{1}{2} \right\rangle = \begin{pmatrix} -\left(\frac{l-m+1}{2l+1}\right)^{\frac{1}{2}} \left| lm-1 \right\rangle \\ \left(\frac{l+m}{2l+1}\right)^{\frac{1}{2}} \left| lm \right\rangle \end{pmatrix} \qquad J = l-\frac{1}{2}, m_J = m-\frac{1}{2} \tag{E.2}$$

With the standard angular momentum eigenfunctions $\left| lm \right\rangle$ and the vector living in spin-space $(\uparrow, \downarrow)$. The SOC pseudopotential takes the simplified block form

$$\hat{V}^{PS} = \sum_{lm} \frac{1}{2l+1} \begin{pmatrix} V^{PS}_{\uparrow\uparrow} & V^{PS}_{\uparrow\downarrow} \\ V^{PS}_{\downarrow\uparrow} & V^{PS}_{\downarrow\downarrow} \end{pmatrix}. \tag{E.3}$$

Using the abbreviation $V_{\pm} = V^{ion}_{l,l\pm\frac{1}{2}}$, the respective spin blocks are

$$
\begin{aligned}
V^{PS}_{\uparrow\uparrow} &= (l+m+1)\left|lm\right\rangle V_+ \left\langle lm\right| + \underbrace{(l-m+1)\left|lm-1\right\rangle V_- \left\langle lm-1\right|}_{m\to m+1} \\
V^{PS}_{\uparrow\downarrow} &= \underbrace{[(l+m+1)(l-m)]^{\frac{1}{2}}\left|lm\right\rangle V_+ \left\langle lm+1\right|}_{m\to m-1} - [(l-m+1)(l+m)]^{\frac{1}{2}}\left|lm-1\right\rangle V_- \left\langle lm\right| \\
V^{PS}_{\downarrow\uparrow} &= [(l+m+1)(l-m)]^{\frac{1}{2}}\left|lm+1\right\rangle V_+ \left\langle lm\right| - \underbrace{[(l-m+1)(l+m)]^{\frac{1}{2}}\left|lm\right\rangle V_- \left\langle lm-1\right|}_{m\to m+1} \\
V^{PS}_{\downarrow\downarrow} &= \underbrace{(l-m)\left|lm+1\right\rangle V_+ \left\langle lm+1\right|}_{m\to m-1} + (l+m)\left|lm\right\rangle V_- \left\langle lm\right|.
\end{aligned}
$$

Performing the indicated index shifts yields

$$
\begin{aligned}
V^{PS}_{\uparrow\uparrow} &= (l+m+1)\left|lm\right\rangle V_+ \left\langle lm\right| + (l-m)\left|lm\right\rangle V_- \left\langle lm\right| \\
V^{PS}_{\uparrow\downarrow} &= [(l+m)(l-m+1)]^{\frac{1}{2}}\left|lm-1\right\rangle V_+ \left\langle lm\right| - [(l-m+1)(l+m)]^{\frac{1}{2}}\left|lm-1\right\rangle V_- \left\langle lm\right| \\
V^{PS}_{\downarrow\uparrow} &= [(l+m+1)(l-m)]^{\frac{1}{2}}\left|lm+1\right\rangle V_+ \left\langle lm\right| - [(l-m)(l+m+1)]^{\frac{1}{2}}\left|lm+1\right\rangle V_- \left\langle lm\right| \\
V^{PS}_{\downarrow\downarrow} &= (l-m+1)\left|lm\right\rangle V_+ \left\langle lm\right| + (l+m)\left|lm\right\rangle V_- \left\langle lm\right|
\end{aligned}
$$

and we can rearrange Eq. (E.3) to give

$$
\begin{aligned}
\hat{V}^{PS} &= \sum_{l,m}\frac{1}{2l+1}\begin{pmatrix} m[V_+ - V_-]\left|lm\right\rangle\left\langle lm\right| & [(l+m)(l-m+1)]^{\frac{1}{2}}[V_+ - V_-]\left|lm-1\right\rangle\left\langle lm\right| \\ [(l+m+1)(l-m)]^{\frac{1}{2}}[V_+ - V_-]\left|lm+1\right\rangle\left\langle lm\right| & -m[V_+ - V_-]\left|lm\right\rangle\left\langle lm\right| \end{pmatrix} \\
&+ \sum_{l,m}\frac{1}{2l+1}\begin{pmatrix} [(l+1)V_+ + lV_-]\left|lm\right\rangle\left\langle lm\right| & 0 \\ 0 & [(l+1)V_+ + lV_-]\left|lm\right\rangle\left\langle lm\right| \end{pmatrix}. \qquad \text{(E.4)}
\end{aligned}
$$

With the help of

$$
\overline{V}_l(\boldsymbol{r}) = \frac{1}{2l+1}[(l+1)V_+ + lV_-] \qquad \text{(E.5)}
$$

and

$$
V_l^{SO}(\boldsymbol{r}) = \frac{2}{2l+1}[V_+ - V_-] \qquad \text{(E.6)}
$$

we can separate the spin-orbital contribution to the pseudopotential

$$
\hat{V}^{PS} = \sum_{lm}[\overline{V}_l(\boldsymbol{r})\mathbf{1} + V_l^{SO}(\boldsymbol{r})\hat{\mathbf{L}}\cdot\hat{\mathbf{S}}]\left|lm\right\rangle\left\langle lm\right|. \qquad \text{(E.7)}
$$

To see that this, in fact, gives the spin-orbit contribution we consider the action of the spin-orbit coupling operator

$$
\sum_m \hat{\mathbf{L}}\cdot\hat{\mathbf{S}}\left|lm\right\rangle\left\langle lm\right|. \qquad \text{(E.8)}
$$

For each l-component of the projection in spin space we find

$$\begin{aligned}
\sum_m \hat{\mathbf{L}}\cdot\hat{\mathbf{S}}\left|lm\right\rangle\left\langle lm\right| &= \frac{1}{2}\sum_m \begin{pmatrix} L_z & L_- \\ L_+ & -L_z \end{pmatrix}\left|lm\right\rangle\left\langle lm\right| \\
&= \frac{1}{2}\sum_m \begin{pmatrix} m\left|lm\right\rangle\left\langle lm\right| & \sqrt{l(l+1)-m(m-1)}\left|lm-1\right\rangle\left\langle lm\right| \\ \sqrt{l(l+1)-m(m+1)}\left|lm+1\right\rangle\left\langle lm\right| & -m\left|lm\right\rangle\left\langle lm\right| \end{pmatrix} \\
&= \frac{1}{2}\sum_m \begin{pmatrix} m\left|lm\right\rangle\left\langle lm\right| & \sqrt{l(l+1)-m(m+1)}\left|lm\right\rangle\left\langle lm+1\right| \\ \sqrt{l(l+1)-m(m+1)}\left|lm+1\right\rangle\left\langle lm\right| & -m\left|lm\right\rangle\left\langle lm\right| \end{pmatrix}
\end{aligned}$$

and compare to Eq. (E.4). As already discussed in Sec. B, within this work we express the basis functions in terms of cubic harmonics. However, the angular momentum eigenfunctions above are spherical harmonics Y_{lm}. Thus, we must make the connection from one to the other via a unitary transformation

$$Y_{lm}(\hat{r}) = \sum_{m_1} U^l_{mm_1} K_{lm_1}(\hat{r}) \tag{E.9}$$

with non-vanishing elements for $m = \pm m_1$ only and a transformation matrix $U^l \in \mathbb{C}$. A projector then transforms as

$$\begin{aligned}
\sum_{mm'} x^l_{mm'}\left|lm\right\rangle\!\!\left\langle lm'\right| &= \sum_{mm'} x^l_{mm'} \sum_{m_1m_2} U^l_{mm_1}\left(U^l_{m'm_2}\right)^*\left|\overline{lm_1}\right\rangle\left\langle\overline{lm_2}\right| && \text{(E.10)} \\
&= \sum_{m_1m_2} \underbrace{\sum_{mm'} x^l_{mm'} U^l_{mm_1}\left(U^l_{m'm_2}\right)^*}_{=\overline{x}^l_{m_1m_2}}\left|\overline{lm_1}\right\rangle\left\langle\overline{lm_2}\right| && \text{(E.11)} \\
&= \sum_{mm'} \overline{x}^l_{mm'}\left|\overline{lm_1}\right\rangle\left\langle\overline{lm_2}\right| && \text{(E.12)}
\end{aligned}$$

where $\left|\overline{lm}\right\rangle$ are the cubic harmonics. Under these considerations, the SOC potential becomes

$$\begin{aligned}
\hat{V}^{SO} &= \sum_{lm} V_l^{SO}(r)\hat{\mathbf{L}}\hat{\mathbf{S}}\left|lm\right\rangle\left\langle lm\right| && \text{(E.13)} \\
&= \sum_l V_l^{SO}(r)\sum_{mm'}\begin{pmatrix} [C^l_{mm'}]_{\uparrow\uparrow} & [C^l_{mm'}]_{\uparrow\downarrow} \\ [C^l_{mm'}]_{\downarrow\uparrow} & [C^l_{mm'}]_{\downarrow\downarrow}\end{pmatrix}\left|\overline{lm}\right\rangle\left\langle\overline{lm'}\right| && \text{(E.14)}
\end{aligned}$$

with

$$\begin{aligned}
[C^l_{mm'}]_{\uparrow\uparrow} &= \sum_{m_1}\frac{m_1}{2}U^l_{m_1m}\left(U^l_{m_1m'}\right)^* &&= \frac{1}{2}\hat{L}_z\left|\overline{lm}\right\rangle\left\langle\overline{lm'}\right| && \text{(E.15)} \\
[C^l_{mm'}]_{\downarrow\downarrow} &&&= -[C^l_{mm'}]_{\uparrow\uparrow} && \text{(E.16)} \\
[C^l_{mm'}]_{\uparrow\downarrow} &= \sum_{m_1}\frac{\sqrt{(l+m_1+1)(l-m_1)}}{2}U^l_{m_1m}\left(U^l_{m_1+1m'}\right)^* &&= \hat{L}_-\left|\overline{lm}\right\rangle\left\langle\overline{lm'}\right| && \text{(E.17)} \\
[C^l_{mm'}]_{\downarrow\uparrow} &= \left([C^l_{m'm}]_{\uparrow\downarrow}\right)^* &&= \hat{L}_+\left|\overline{lm}\right\rangle\left\langle\overline{lm'}\right|. && \text{(E.18)}
\end{aligned}$$

E.2 Matrix elements of spin-orbit interaction

With the help of Sec. E.1, we may now evaluate the matrix elements of the spin-orbit potential within the CPA formalism. The real space representation for the spin-orbit coupling potential in a solid is given by

$$\left\langle \boldsymbol{r} \middle| \hat{V}^{SO} \middle| \boldsymbol{r}' \right\rangle = \sum_{\boldsymbol{N}\kappa} v_\kappa^{SO}(\boldsymbol{r} - \boldsymbol{R}_{\boldsymbol{N}\kappa}, \boldsymbol{r}' - \boldsymbol{R}_{\boldsymbol{N}\kappa}) \tag{E.19}$$

where for each species κ

$$v_\kappa^{SO}(\boldsymbol{r}, \boldsymbol{r}') = \left\langle \boldsymbol{r} \middle| \hat{V}_\kappa^{SO} \middle| \boldsymbol{r}' \right\rangle = \sum_{lm} \frac{\delta(r - r')}{r^2} v_{\kappa,l}^{SO}(r) \hat{\mathbf{L}}_{\boldsymbol{r}} \hat{\mathbf{S}} K_{lm}(\hat{r}) K_{lm}(\hat{r}'). \tag{E.20}$$

Here, $\hat{\mathbf{L}}_{\boldsymbol{r}}$ acts on the r-coordinate. For each component in spin-space, this is expressed in terms of cubic harmonics as

$$[v_\kappa^{SO}(\boldsymbol{r}, \boldsymbol{r}')]_{\sigma\sigma'} = \sum_l \frac{\delta(r - r')}{r^2} v_{\kappa,l}^{SO}(r) \sum_{mm'} [C_{mm'}^l]_{\sigma\sigma'} K_{lm}(\hat{r}) K_{lm}(\hat{r}') \tag{E.21}$$

The CPA matrix-elements we wish to compute is

$${}^{SO}\mathcal{H}_{slm,tl'm'}^{PQ\sigma\sigma'}(\boldsymbol{k}) = \sum_{\boldsymbol{L}} e^{-i\boldsymbol{k}\boldsymbol{R}_{\boldsymbol{L}}} e^{-i\boldsymbol{k}(\boldsymbol{R}_{\boldsymbol{s}} - \boldsymbol{R}_{\boldsymbol{t}})} \left\langle LsPlm \middle| V_{\sigma\sigma'}^{SO} \middle| 0tQl'm' \right\rangle \tag{E.22}$$

with

$$V_{\sigma\sigma'}^{SO} = \sum_{\boldsymbol{N}\boldsymbol{u}\kappa} c_{\boldsymbol{u}}^\kappa v_\kappa^{SO\sigma\sigma'}(\boldsymbol{r} - \boldsymbol{R}_{\boldsymbol{N}} - \boldsymbol{R}_{\boldsymbol{u}}, \boldsymbol{r}' - \boldsymbol{R}_{\boldsymbol{N}} - \boldsymbol{R}_{\boldsymbol{u}}). \tag{E.23}$$

A short comment should be made about the notation used within this section: As the expressions in deriving the SOC matrix elements become quite long and tedious, we abbreviate multiple integrations in the following way

$$\int \mathrm{d}^3 r \, \mathrm{d}^3 r' \, \mathrm{d}^3 k \, \mathrm{d}^3 k' \longrightarrow \int \mathrm{d}^3(r, r', k, k'). \tag{E.24}$$

Applying the definitions and relations given in Sec. B yields

$$\begin{aligned}
{}^{SO}\mathcal{H}_{slm,tl'm'}^{PQ\sigma\sigma'}(\boldsymbol{k}) =& \sum_{\boldsymbol{L}} e^{-i\boldsymbol{k}\boldsymbol{R}_{\boldsymbol{L}}} e^{-i\boldsymbol{k}(\boldsymbol{R}_{\boldsymbol{s}} - \boldsymbol{R}_{\boldsymbol{t}})} \left\langle LsPlm \middle| V_{\sigma\sigma'}^{SO} \middle| 0tQl'm' \right\rangle \\
=& \sum_{\boldsymbol{L}} e^{-i\boldsymbol{k}\boldsymbol{R}_{\boldsymbol{L}}} e^{-i\boldsymbol{k}(\boldsymbol{R}_{\boldsymbol{s}} - \boldsymbol{R}_{\boldsymbol{t}})} \int \mathrm{d}^3(r, r') \phi_{lm}^{P*}(\boldsymbol{r} - \boldsymbol{R}_{\boldsymbol{L}} - \boldsymbol{R}_{\boldsymbol{s}}) \qquad \text{(E.25)} \\
& \times \sum_{\boldsymbol{N}\boldsymbol{u}\kappa} c_{\boldsymbol{u}}^\kappa v_\kappa^{SO\sigma\sigma'}(\boldsymbol{r} - \boldsymbol{R}_{\boldsymbol{N}} - \boldsymbol{R}_{\boldsymbol{u}}, \boldsymbol{r}' - \boldsymbol{R}_{\boldsymbol{N}} - \boldsymbol{R}_{\boldsymbol{u}}) \phi_{l'm'}^Q(\boldsymbol{r}' - \boldsymbol{R}_{\boldsymbol{t}}) \\
=& \frac{\Omega_C}{(2\pi)^6} \sum_{\boldsymbol{L}\boldsymbol{N}\boldsymbol{u}\kappa} e^{-i\boldsymbol{k}\boldsymbol{R}_{\boldsymbol{L}}} e^{-i\boldsymbol{k}(\boldsymbol{R}_{\boldsymbol{s}} - \boldsymbol{R}_{\boldsymbol{t}})} \int \mathrm{d}^3(r, r', k', k'') \phi_{lm}^{P*}(\boldsymbol{k}') e^{-i\boldsymbol{k}'(\boldsymbol{r} - \boldsymbol{R}_{\boldsymbol{L}} - \boldsymbol{R}_{\boldsymbol{s}} + \boldsymbol{R}_{\boldsymbol{N}} + \boldsymbol{R}_{\boldsymbol{u}})} \\
& \times c_{\boldsymbol{u}}^\kappa v_\kappa^{SO\sigma\sigma'}(\boldsymbol{r}, \boldsymbol{r}') \phi_{l'm'}^Q(\boldsymbol{k}'') e^{i\boldsymbol{k}''(\boldsymbol{r}' - \boldsymbol{R}_{\boldsymbol{t}} + \boldsymbol{R}_{\boldsymbol{N}} + \boldsymbol{R}_{\boldsymbol{u}})}. \qquad \text{(E.26)}
\end{aligned}$$

We now compute the reciprocal representation of the spin components of $v_\kappa^{SO}(\boldsymbol{r},\boldsymbol{r'})$ in Eq. (E.20)

$$\begin{aligned}
v_\kappa^{SO\sigma\sigma'}(\boldsymbol{k'},\boldsymbol{k''}) =& \frac{1}{\Omega_C}\int \mathrm{d}^3(r,r') e^{-i\boldsymbol{k'r}} v_\kappa^{SO\sigma\sigma'}(\boldsymbol{r},\boldsymbol{r'}) e^{i\boldsymbol{k''r'}} \\
=& \frac{1}{\Omega_C}\sum_{lmm'}\int \mathrm{d}^3(r,r')\frac{\delta(r-r')}{r^2} v_{\kappa l}^{SO}(r)[C_{mm'}^l]_{\sigma\sigma'} K_{lm}(\hat{r}) K_{lm'}(\hat{r}') e^{-i\boldsymbol{k'r}} e^{i\boldsymbol{k''r'}} \\
=& \frac{1}{\Omega_C}\sum_{lmm'}\int \mathrm{d}^3(r,r')\frac{\delta(r-r')}{r^2} v_{\kappa l}^{SO}(r)[C_{mm'}^l]_{\sigma\sigma'} K_{lm}(\hat{r}) K_{lm'}(\hat{r}')(4\pi)^2 \\
&\times \sum_{\substack{l''m'' \\ l'''m'''}} i^{l'''-l''} j_{l''}(k'r) j_{l'''}(k''r') K_{l''m''}(\hat{k}') K_{l''m''}(\hat{r}) K_{l'''m'''}(\hat{k}'') K_{l'''m'''}(\hat{r}'). \qquad \text{(E.27)}
\end{aligned}$$

Making use of Eqs. (B.10)-(B.12) we find

$$\begin{aligned}
v_\kappa^{SO}(\boldsymbol{k'},\boldsymbol{k''}) &= \sum_{lmm'}\frac{(4\pi)^2}{\Omega_C}\int d(r,r') r^2 r'^2 \frac{\delta(r-r')}{r^2} v_{\kappa l}^{SO}(r)[C_{mm'}^l]_{\sigma\sigma'} K_{lm}(\hat{k}') K_{lm'}(\hat{k}'') j_l(k'r) j_l(k''r') \\
&= \sum_{lmm'}\frac{(4\pi)^2}{\Omega_C}\int dr' r'^2 v_{\kappa l}^{SO}(r')[C_{mm'}^l]_{\sigma\sigma'} K_{lm}(\hat{k}') K_{lm'}(\hat{k}'') j_l(k'r') j_l(k''r') \\
&= \sum_l \sum_{mm'}[C_{mm'}^l]_{\sigma\sigma'} K_{lm}(\hat{k}') K_{lm'}(\hat{k}'') \underbrace{\frac{(4\pi)^2}{\Omega_C}\int dr r^2 j_l(k'r) v_{\kappa l}^{SO}(r) j_l(k''r)}_{=v_{\kappa l}^{SO}(k',k'')} \\
&= \sum_l \sum_{mm'}[C_{mm'}^l]_{\sigma\sigma'} K_{lm}(\hat{k}') K_{lm'}(\hat{k}'') v_{\kappa l}^{SO}(k',k'') = \sum_l v_{\kappa l}^{SO\sigma\sigma'}(k',k'') \qquad \text{(E.28)}
\end{aligned}$$

. Inserting Eq. (E.28) into Eq. (E.25) we arrive at

$$\begin{aligned}
{}^{SO}\mathcal{H}_{slm,tl'm'}^{PQ\sigma\sigma'}(\boldsymbol{k}) =& \frac{\Omega_C^2}{(2\pi)^6}\sum_{\boldsymbol{LNu}\kappa} c_{\boldsymbol{u}}^\kappa e^{-i\boldsymbol{kR_L}} e^{-i\boldsymbol{k}(\boldsymbol{R_s}-\boldsymbol{R_t})} \int \mathrm{d}^3(k',k'')\phi_{lm}^{P*}(\boldsymbol{k'})\phi_{l'm'}^{Q}(\boldsymbol{k''}) \\
&\times e^{-i\boldsymbol{k'}(\boldsymbol{R_N}+\boldsymbol{R_u}-\boldsymbol{R_L}-\boldsymbol{R_s})} e^{i\boldsymbol{k''}(\boldsymbol{R_N}+\boldsymbol{R_u}-\boldsymbol{R_t})} \sum_{l''} v_{\kappa l''}^{SO\sigma\sigma'}(k',k'').
\end{aligned}$$

This may be manipulated to give

$$\begin{aligned}
{}^{SO}\mathcal{H}_{slm,tl'm'}^{PQ\sigma\sigma'}(\boldsymbol{k}) =& \sum_{\boldsymbol{GG'}\kappa\boldsymbol{u}} c_{\boldsymbol{u}}^\kappa e^{-i\boldsymbol{k}(\boldsymbol{R_s}-\boldsymbol{R_t})} e^{-i\boldsymbol{k}(\boldsymbol{R_u}-\boldsymbol{R_s})} e^{-i\boldsymbol{G}(\boldsymbol{R_s}-\boldsymbol{R_t})} e^{-i\boldsymbol{G'}(\boldsymbol{R_u}-\boldsymbol{R_t})} \\
&\times \phi_{lm}^{P*}(\boldsymbol{k}-\boldsymbol{G})\phi_{l'm'}^{Q}(\boldsymbol{k}-\boldsymbol{G}-\boldsymbol{G'}) \sum_{l''} v_{\kappa l''}^{SO\sigma\sigma'}(k-G,k-G-G') \qquad \text{(E.29)}
\end{aligned}$$

by making multiple use of Eq. (B.14). We may furthermore shift $\boldsymbol{G'} \to \boldsymbol{G'} - \boldsymbol{G}$, which gives

$$
\begin{aligned}
{}^{SO}\mathcal{H}^{PQ\sigma\sigma'}_{slm,tl'm'}(\boldsymbol{k}) &= \sum_{\boldsymbol{GG'}\kappa\boldsymbol{u}} c^{\kappa}_{\boldsymbol{u}} e^{-i\boldsymbol{GR_s}} e^{i\boldsymbol{G'R_t}} e^{i(\boldsymbol{G}-\boldsymbol{G'})\boldsymbol{R_u}} \phi^{P*}_{lm}(\boldsymbol{k}-\boldsymbol{G}) \phi^{Q}_{l'm'}(\boldsymbol{k}-\boldsymbol{G'}) \\
&\quad \times \underbrace{\sum_{l''} v^{SO\sigma\sigma'}_{\kappa l''}(k-G, k-G')}_{= v^{SO\sigma\sigma'}_{\kappa}(\boldsymbol{k}-\boldsymbol{G}, \boldsymbol{k}-\boldsymbol{G'})} \\
&= \sum_{\boldsymbol{GG'}\kappa\boldsymbol{u}} c^{\kappa}_{\boldsymbol{u}} e^{-i\boldsymbol{GR_s}} e^{i\boldsymbol{G'R_t}} e^{i(\boldsymbol{G}-\boldsymbol{G'})\boldsymbol{R_u}} \phi^{P*}_{lm}(\boldsymbol{k}-\boldsymbol{G}) \phi^{Q}_{l'm'}(\boldsymbol{k}-\boldsymbol{G'}) \\
&\quad \times v^{SO\sigma\sigma'}_{\kappa}(\boldsymbol{k}-\boldsymbol{G}, \boldsymbol{k}-\boldsymbol{G'})
\end{aligned} \tag{E.30}
$$

If we look at the $C^{l}_{mm'}$ in Eqs. (E.15) - (E.18), it becomes obvious that there is no spin-orbit contribution from the $l = 0$ component. As a result, the l''-summation in Eq. (E.30) reduces to one over $l'' \geq 1$ and we arrive at the final result for the SOC matrix elements in reciprocal space

$$
\begin{aligned}
{}^{SO}\mathcal{H}^{PQ\sigma\sigma'}_{slm,tl'm'}(\boldsymbol{k}) &= \sum_{\boldsymbol{GG'}\kappa\boldsymbol{u}} c^{\kappa}_{\boldsymbol{u}} e^{-i\boldsymbol{GR_s}} e^{i\boldsymbol{G'R_t}} e^{i(\boldsymbol{G}-\boldsymbol{G'})\boldsymbol{R_u}} \phi^{P*}_{lm}(\boldsymbol{k}-\boldsymbol{G}) \phi^{Q}_{l'm'}(\boldsymbol{k}-\boldsymbol{G'}) \\
&\quad \times \sum_{l''\geq 1} v^{SO\sigma\sigma'}_{\kappa l''}(k-G, k-G').
\end{aligned} \tag{E.31}
$$

E.3 Implementation of the spin-orbit coupling Hamiltonian

Some remarks as to the implementation to Eq. (E.31) within the CPA program are in order: following the internal logic, the dimensionality of the Hamiltonian generally depends on the total number of atomic orbitals `nao` of the system under consideration.
Now, if we are to include spin-orbit coupling we must account for additional spin-degrees of freedom. As a result, the number of atomic orbitals is doubled reflecting the fact that we must now describe our system using spinors. This is implemented in such way that the range of atomic indices `iao=1,..,2*nao` is split such that `iao=1,...,nao` represent spin-up indices, while `iao=nao+1,...,2*nao` represent spin-down indices.
The calculation of the full spin-orbit coupling Hamiltonian from Eq. (E.31) is implemented in the `subroutine calcVmix2_k` and stored in the complex array `hso_k(irk,iao1,iao2,sig)` with `sig` $\in \{1,2,3\} \equiv \{\uparrow\uparrow, \uparrow\downarrow, \downarrow\downarrow\}$ and `iao=1,...,nao`. Here, the symmetry ${}^{SO}\mathcal{H}^{\uparrow\uparrow} = -{}^{SO}\mathcal{H}^{\downarrow\downarrow}$ was exploited to reduce computation time and memory cost. From this array `subroutine calcVso` in file `hamilton.f90` builds the array `vTotSO(irk,iao1,iao2)` with `iao=1,...,2*nao`, in contrast to `hso_k` above. This represents the full matrix form including spin-space - hence the increased orbital index dimensionality. In a simplified representation this corresponds to

$$
{}^{SO}\mathcal{H} = \begin{pmatrix} H_{\uparrow\uparrow} & H_{\uparrow\downarrow} \\ H_{\downarrow\uparrow} & H_{\downarrow\downarrow} \end{pmatrix}. \tag{E.32}
$$

From this, the onsite term (which is $\boldsymbol{k}$-independent) is extracted and stored in array `vOnsiteSO(iao1,iao2)` with `iao=1,...,2*nao`. Subtracting the onsite terms from the full spin-orbit potential for `iao1` and `iao2` corresponding to the same crystal site then yields the offsite terms. These are stored in `vOffsiteSO(irk,iao1,iao2)` with `iao=1,...,2*nao`.

The SOC Hamiltonian is fully incorporated into the relevant quantities used in `suborutine cpaCycleEnergy` to determine the effective medium Green's function and self-energy. Both quantities must be expanded in dimensionality to accommodate for the spin degrees of freedom introduced by SOC.
While the SOC Hamiltonian need only be computed once for the main CPA charge self-consistent calculation, it must be recomputed for each line in the band structure calculation performed by `subroutine cpaBandAlongLine` and the Fermi surface calculations in `subroutine CalcFermiSurface`. Here, only the onsite term is kept from the main calculation, as it is independent of $\boldsymbol{k}$.

Appendix F

Symmetrization

As electronic structure calculations can become quite cumbersome and computationally expensive, we should make use of the mathematical properties that characterize a crystal to reduce the operational expense as best we can. A very powerful tool that we can make use of here is symmetry.

The Bravais lattice

A Bravais lattice is defined as an infinite array of discrete lattice points that can be generated by discrete spatial translations such that the position of a generic point in three-dimensional (3D) space

$$\boldsymbol{R} = \sum_{i=1}^{3} n_i \boldsymbol{a}_i \tag{F.1}$$

is described via the linear combination of linearly independent primitive vectors a_i with integer coefficients $n_i \in \mathbb{N}$. Thus, the Bravais lattice describes the translational symmetry of a crystal. In three dimension there are 14 possible Bravais lattices grouped into seven lattice systems: triclinic, monoclinic, orthorombic, tetragonal, rhombohedral, hexagonal and cubic.

The point group

Aside from translational symmetry, a generic crystal may exhibit other symmetries such as rotational, inversion and mirror symmetries. In contrast to a translation, they leave at least one point of the crystal unmoved. These symmetries make up the crystallographic point group of which 32 exist in 3D.

The space group

Combining the translational and the point group symmetries we find the space groups. The space groups also contain screw axes (rotation about an axes and translation parallel to the axis) and glide planes (reflection of a point through a plane and translation parallel to the plane). There are 230 distinct space groups.

As we have already discussed in Sec. 1.2.3, a great advantage of the BEB-CPA formalism is the fact that all quantities in the extended Hilbert space preserve the symmetries of the underlying crystal structure. These symmetries can be exploited especially well when calculating $\boldsymbol{k}$-dependent

quantities. To calculate such quantities we must map the first Brillouin zone onto a regular $\boldsymbol{k}$-mesh. But instead of performing a calculation for all points on this mesh we can restrict ourselves to the irreducible part of the BZ, i.e., to the set of $\boldsymbol{k}$-points from which all other $\boldsymbol{k}$-points can be generated by applying the symmetry operations. The same hold for BZ integrations, for which the sum only runs over the irreducible part and a symmetrization is afterwards applied. Depending on the number of symmetries present for a specific crystal structure this exploitation can lead to a drastic speed-up. The MBBP makes extensive use of this and generates a list of all symmetries which is then imported into the CPA program. These operations are stored in the form of an atomic transformation table `iatrans(isym,iat,itype)` that contains the transformed atomic index corresponding to the action of a symmetry operation `isym` on an atomic index `iat` of the species `itype`.
To benefit from the symmetrization we must derive an analytic expression that we can apply to those quantities which involve a BZ integration, such as the electronic density or the effective medium Green's function. For the time being, we restrict ourselves to the spinless case where the derivation closely follows that given in Ref. [6] and shall discuss the symmetrization for a spinfull system in the cases of spin-polarization and spin-orbit coupling separately. Let us consider a generic symmetry operation

$$g = (D, \boldsymbol{\tau}) \qquad g[(\boldsymbol{r})] = D\boldsymbol{r} + \boldsymbol{\tau} \tag{F.2}$$

which can always be written as the combination of a rotation D and a translation τ. If g describes an inherent symmetry of the crystal it will map an atom located at site s onto another atom at site s' according to

$$g[s] = s' \qquad g[\boldsymbol{R_s}] = D\boldsymbol{R_s} + \boldsymbol{\tau} = \boldsymbol{R_{s'}} + \boldsymbol{R_L} \tag{F.3}$$

with a lattice vector $\boldsymbol{R_L}$. Next, let us consider the application of a symmetry operator to a local basis function

$$\begin{aligned}
\phi_{Lslm}(g[\boldsymbol{r}]) &= \phi_{Lslm}(D\boldsymbol{r} + \boldsymbol{\tau}) = \phi_{lm}(D\boldsymbol{r} + \tau - \boldsymbol{R_s} - \boldsymbol{R_L}) \\
&= \phi_{lm}\left(D(\boldsymbol{r} + \underbrace{D^{-1}\boldsymbol{\tau} - D^{-1}\boldsymbol{R_s}}_{=-g^{-1}(\boldsymbol{R_s})+\boldsymbol{R'_L}} - D^{-1}\boldsymbol{R_L}) \right) \\
&= \phi_{lm}\left(D(\boldsymbol{r} - \boldsymbol{R}_{g^{-1}(\boldsymbol{s})} - \boldsymbol{R_{L''}}) \right).
\end{aligned} \tag{F.4}$$

Recognizing that a symmetry operation only connects atoms of the same type (in general they must not be equivalent), we have dropped the species index. As

$$\phi_{lm}(\boldsymbol{r}) = i^l f_l(r) K_{lm}(\hat{r}) \tag{F.5}$$

we need to consider the effect of a rotation on the cubic harmonics $K_{lm}(\boldsymbol{r})$. With the help of the Wigner matrices

$$W^l_{mm'}(g) = \int \mathrm{d}\Omega \, K_{lm}(D\hat{r}) K_{lm'}(\hat{r}) \tag{F.6}$$

it can be shown that they transform as

$$K_{lm}(D\hat{r}) = \sum_{m'} W^l_{mm'}(g) K_{lm'}(\boldsymbol{r'}) \tag{F.7}$$

and so Eq. (F.4) becomes

$$\phi_{Lslm}(g[\boldsymbol{r}]) = \sum_{m'} W^{l}_{mm'}(g)\phi_{lm'}(\boldsymbol{r} - \boldsymbol{R}_{g^{-1}(s)} - \boldsymbol{R}_{\boldsymbol{L''}}) = \sum_{m'} W^{l}_{mm'}(g)\phi_{L''g^{-1}(s)lm'}(\boldsymbol{r}) \tag{F.8}$$

From these considerations we can derive the symmetrization of a generic matrix element of an operator $\mathcal{O}$ to be

$$\begin{aligned}\mathcal{O}_{s_1 l_1 m_1, s_2 l_2 m_2}(D_g\boldsymbol{k}) = \sum_{m_1' m_2'} & W^{l_1}_{m_1 m_1'}(g)\mathcal{O}_{g^{-1}(s_1) l_1 m_1', g^{-1}(s_2) l_2 m_2'}(\boldsymbol{k}) W^{l_2}_{m_2, m_2'}(g) \\ & \times e^{iD_g\boldsymbol{k}(\boldsymbol{R_{s_1}} - \boldsymbol{R_{s_2}})} e^{-i\boldsymbol{k}(\boldsymbol{R}_{g^{-1}(s_1)} - \boldsymbol{R}_{g^{-1}(s_2)})}.\end{aligned} \tag{F.9}$$

Written in a compact matrix product form this can be expressed as

$$\mathcal{O}(D_g\boldsymbol{k}) = S_g \mathcal{O}(\boldsymbol{k}) S_g^{\dagger} \tag{F.10}$$

with the matrix elements

$$S_{g,slm,s'l'm'} = \delta_{ll'}\delta_{s'g^{-1}(s)} W^{l}_{mm'}(g) e^{iD_g\boldsymbol{k}\boldsymbol{R_s}} e^{-i\boldsymbol{k}\boldsymbol{R}_{g^{-1}(s)}} \tag{F.11}$$

of the transformation matrix. From this we find the relation between a sum of these matrix elements over all $\boldsymbol{k}$-points and those $\boldsymbol{\kappa}$ of the irreducible part of the BZ

$$M = \sum_{\boldsymbol{k}} \mathcal{O}(\boldsymbol{k}) = \sum_{\boldsymbol{\kappa}} \sum_{g(\boldsymbol{\kappa})} \mathcal{O}(D_g\boldsymbol{\kappa}) = \sum_{\boldsymbol{\kappa}} \sum_{g} \frac{1}{n_{inv}(\boldsymbol{\kappa})} S_g \mathcal{O}(\boldsymbol{\kappa}) S_g^{\dagger}. \tag{F.12}$$

The subset of $\boldsymbol{k}$-points that can be generated by symmetry operations $g(\boldsymbol{\kappa})$ from $\boldsymbol{\kappa}$ are called the *star* of $\boldsymbol{\kappa}$. The sum over these operations in Eq. (F.12) can be replaced by a sum over all symmetry operations g if we account for the number of symmetry operations $n_{inv}(\boldsymbol{\kappa})$ that map $\boldsymbol{\kappa}$ onto itself, as was done in the last step of Eq. (F.12).
We now consider the special case of onsite matrix elements for which further simplifications are justified. As the onsite terms inherently have no $\boldsymbol{\kappa}$-dependency the phase factors in the transformation matrix S_g become trivial, we may perform the sum over symmetry operations independently from the sum over $\boldsymbol{\kappa}$

$$M = \sum_{g} S_g \left(\sum_{\boldsymbol{\kappa}} \frac{1}{n_{inv}(\boldsymbol{\kappa})} \mathcal{O}(\boldsymbol{\kappa}) \right) S_g^{\dagger} \equiv \frac{1}{N_g} \sum_{g} S_g \left(\sum_{\boldsymbol{\kappa}} w(\boldsymbol{\kappa}) \mathcal{O}(\boldsymbol{\kappa}) \right) S_g^{\dagger} \tag{F.13}$$

with the number of symmetry operation N_g and symmetry dependent weight factors $w(\boldsymbol{\kappa})$. In the CPA code they correspond to `nsymop` and `weight_irk`, respectively, and are supplied as input by the MBBP. Eq. (F.13) corresponds to reducing the calculation of all $\boldsymbol{k}$-dependent matrix elements to the irreducible subset $\boldsymbol{\kappa}$ weighted by $w(\boldsymbol{\kappa})$ and afterwards accounting for all other $\boldsymbol{k}$-points by symmetrizing the inner sum. This results in the implementation of the onsite symmetrization according to

$${}^{sym}M_{sl_1m_1l_2m_2} = \frac{1}{N_g} \sum_{g} \sum_{m_1' m_2'} W^{l_1}_{m_1 m_1'}(g) M_{g^{-1}(s) l_1 m_1' l_2 m_2'} W^{l_2}_{m_2 m_2'}(g) \tag{F.14}$$

with the unsymmetrized sum M. As some of the onsite quantities are defined with respect to different index structures, i.e., orbital-indices `iao` or special site-indices `ilm` two distinct subroutines have been

implemented for the respective cases. The `subroutine symmetrizeOnsiteGmat` is applied to the onsite mixing terms and the onsite effective medium Green's function, corresponding to the former case. The latter case of a generic complex onsite matrix in `iao`-space is treated by `subroutine symmetrizeOnsiteCmat`. Both symmetrization routines can be found in file `symmetry.f90` of the CPA code.
A note shall be made here about the symmetrization of the electronic density, which is performed different from the approach outlined above, as the BZ summation only occurs in the calculation of the A-coefficients (see Eq. (C.8)). These summations only run over the irreducible subset $\boldsymbol{\kappa}$ and are weighted by $w(\boldsymbol{\kappa})$, which reduce to $\frac{1}{N_{\boldsymbol{k}}}$ in the absence of symmetries. We then symmetrize the orbital radial densities $n_{Lslm}(r)$ according to

$$^{sym}n_{Lslm}(r) = \frac{1}{N_g}\sum_g \sum_{m'} W^l_{mm'}(g) n_{Lg^{-1}(s)lm'}(r). \tag{F.15}$$

This symmetrization is performed in `subroutine denSpecOrb` in the file `density.f90`.

Spin-polarization

The case of pure, non-relativistic spin-polarization can be treated analogously to the case of the spinless system. If we introduce an additional spin index into the formalism the main effect concerning the matrices of our observables will be an increase of the dimensionality such that a generic operator matrix $\hat{\mathcal{O}}$ takes the block form

$$\hat{\mathcal{O}} = \begin{pmatrix} \mathcal{O}_{\uparrow\uparrow} & 0 \\ 0 & \mathcal{O}_{\downarrow\downarrow} \end{pmatrix} \tag{F.16}$$

and we solely need to symmetrize each of the diagonal spin blocks independently. Thus, the symmetrization routine depicted for the spinless case is applied to each block individually.

Spin-orbit coupling

If we allow for spin-orbit coupling we must consider two separate cases for the form of a generic matrix operator $\hat{\mathcal{O}}$: firstly, all operators that are not affected by the SOC interaction will take the form

$$\hat{\mathcal{O}} = \begin{pmatrix} \mathcal{O}_{\uparrow\uparrow} & 0 \\ 0 & \mathcal{O}_{\downarrow\downarrow} \end{pmatrix}. \tag{F.17}$$

However, since $\mathcal{O}_{\uparrow\uparrow} = \mathcal{O}_{\downarrow\downarrow}$, the dimensionality of these matrix operators is only formally increased to account for the spin variable, as there is no effective spin-dependency. The symmetrization is thus only performed for the matrix of 'reduced' dimensionality. Within the CPA code, all spin-independent quantities are treated as in the spinless case and are symmetrized according to Eq. (F.9).
Secondly, for those matrix operators that truly become spin-dependent due to the SOC, a generic matrix will have nontrivial off-diagonal blocks, in contrast to the cases treated beforehand, i.e.,

$$\hat{\mathcal{O}} = \begin{pmatrix} \mathcal{O}_{\uparrow\uparrow} & \mathcal{O}_{\uparrow\downarrow} \\ \mathcal{O}_{\downarrow\uparrow} & \mathcal{O}_{\downarrow\downarrow} \end{pmatrix}. \tag{F.18}$$

When symmetrizing the matrix elements of a quantity that includes SOC we must not only consider real space rotations but also rotations in spin space. Thus, for every symmetry operation g of the

point group we must introduce a corresponding spin-rotation matrix $\hat{\chi}(g)$.
In deriving these spin-rotation matrices[1] we will make use of the properties of the Pauli-matrices:

$$\sigma_i\sigma_j = \delta_{ij}\sigma_0 + i\sum_{k=1}^{3}\epsilon_{ijk}\sigma_k \tag{F.19}$$

$$[\sigma_i, \sigma_j] = 2i\sum_{k=1}^{3}\epsilon_{ijk}\sigma_k \tag{F.20}$$

$$\{\sigma_i, \sigma_j\} = 2\delta_{ij}\sigma_0. \tag{F.21}$$

We begin by considering an arbitrary rotation, for which the corresponding operator can be expressed as

$$R \equiv e^{i\boldsymbol{x}\cdot\boldsymbol{\sigma}}, \tag{F.22}$$

where $\boldsymbol{\alpha}$ denotes the rotational axis and $\boldsymbol{\sigma}$ is the vector of Pauli-matrices. We can then expand the exponential function according to

$$R = \sum_{n=0}^{\infty}\frac{1}{n!}\left(\boldsymbol{x}\cdot\boldsymbol{\sigma}\right)^n. \tag{F.23}$$

Separating the sum in Eq. (F.23) into even ($n = 2k+2$) and odd ($n = 2k+1$) contributions yields (after some simple algebra)

$$R = \cos|\boldsymbol{x}| + i\sin|\boldsymbol{x}|(\hat{\boldsymbol{x}}\cdot\boldsymbol{\sigma}) \tag{F.24}$$

with $\hat{\boldsymbol{x}} = \frac{\boldsymbol{x}}{|\boldsymbol{x}|}$. The rotation operator R is unitary, i.e.,

$$R^\dagger R = \left[\cos|\boldsymbol{x}| - i\sin|\boldsymbol{x}|(\hat{\boldsymbol{x}}\cdot\boldsymbol{\sigma})\right]\left[\cos|\boldsymbol{x}| + i\sin|\boldsymbol{x}|(\hat{\boldsymbol{x}}\cdot\boldsymbol{\sigma})\right] \tag{F.25}$$

$$= cos^2|\boldsymbol{x}| + sin^2|\boldsymbol{x}|\underbrace{(\hat{\boldsymbol{x}}\cdot\boldsymbol{\sigma})^2}_{=|\boldsymbol{x}|^2=\mathbb{1}} = \mathbb{1}. \tag{F.26}$$

Thus, under a rotation the Pauli-matrices transform as

$$\tilde{\sigma}_i = R^\dagger\sigma_i R = e^{-i\boldsymbol{x}\cdot\boldsymbol{\sigma}}\sigma_i e^{i\boldsymbol{x}\cdot\boldsymbol{\sigma}} = -\sigma_i + e^{-i\boldsymbol{x}\cdot\boldsymbol{\sigma}}\left\{\sigma_i, e^{i\boldsymbol{x}\cdot\boldsymbol{\sigma}}\right\}. \tag{F.27}$$

With the help of Eqs. (F.19) and (F.24), after some manipulation, we finally find the transformation property

$$\tilde{\sigma}_i = \cos(2|\boldsymbol{x}|)\sigma_i + (1-2\cos(2|\boldsymbol{x}|))\hat{\boldsymbol{x}}_i(\hat{\boldsymbol{x}}\cdot\boldsymbol{\sigma}) + \sin(2|\boldsymbol{x}|)(\hat{\boldsymbol{x}}\times\boldsymbol{\sigma})_i. \tag{F.28}$$

This corresponds to a spatial rotation about $\alpha = 2|\boldsymbol{x}|$ and we can write

$$R(\alpha) = e^{i\frac{\alpha}{2}(\hat{\boldsymbol{x}}\cdot\boldsymbol{\sigma})} = e^{i\alpha(\hat{\boldsymbol{x}}\cdot\boldsymbol{S})}, \tag{F.29}$$

with spin vector $\boldsymbol{S} = \frac{\boldsymbol{\sigma}}{2}$.
We can express Eq. (F.28) in terms of a matrix product

$$\tilde{\sigma}_i = \sum_j \chi_{ij}\sigma_j, \tag{F.30}$$

[1] private communications with Rolf Heid

with

$$\chi_{ij} = \delta_{ij}\cos\alpha + \hat{\boldsymbol{x}}_i\hat{\boldsymbol{x}}_j(1-\cos\alpha)) + \epsilon_{ijk}\hat{\boldsymbol{x}}_k\sin\alpha. \tag{F.31}$$

Finally, given these spin-rotation matrices we can symmetrize a given matrix element with spin degrees of freedom according to

$$\begin{aligned}\mathcal{O}_{s_1 l_1 m_1 \sigma_1, s_2 l_2 m_2 \sigma_2}(D_g\boldsymbol{k}) = \sum_{m_1' m_2' \sigma_1' \sigma_2'} & \chi_{\sigma_1\sigma_1'}(g) W^{l_1}_{m_1 m_1'}(g) \mathcal{O}_{g^{-1}(s_1) l_1 m_1' \sigma_1', g^{-1}(s_2) l_2 m_2' \sigma_2'}(\boldsymbol{k}) \\ & \times \chi^*_{\sigma_2'\sigma_2}(g) W^{l_2}_{m_2, m_2'}(g) e^{iD_g\boldsymbol{k}(\boldsymbol{R}_{\boldsymbol{s_1}} - \boldsymbol{R}_{\boldsymbol{s_2}})} e^{-i\boldsymbol{k}(\boldsymbol{R}_{g^{-1}(s_1)} - \boldsymbol{R}_{g^{-1}(s_2)})}.\end{aligned} \tag{F.32}$$

The generation of the spin-rotation matrices is performed by `subroutine gen_spinrot` in file `symmetry.f90`. It is based on the corresponding subroutine written by Rolf Heid for the MBPP and adjusted to function within the CPA implementation.

Appendix G

Green's function for a nonorthogonal basis

As we have already discussed in Sec. B, the BEB-CPA formalism used in this work employs a nonorthogonal LCAO basis set. Here, we shall give a brief overview of the consequences for the Green's function formalism, closely following Ref. [6].

G.1 Field operators in a local basis

For the nonorthogonal basis set introduced in Sec. B the overlap between orbitals is given by

$$S_{ij} = \langle i | j \rangle = \int \mathrm{d}^3 r \, \phi_i^*(\boldsymbol{r}) \phi_j(\boldsymbol{r}) \tag{G.1}$$

and is nontrivial. The compound indices i and j denote both orbital and site indices. Expressed in a nonorthogonal basis the unit operator takes the form

$$\mathbb{1} = \sum_{ij} |i\rangle \left(S^{-1}\right)_{ij} \langle j| \tag{G.2}$$

and we shall henceforth abbreviate the (i,j)th matrix element of the inverse of the overlap matrix as S_{ij}^{-1}. We may define fermionic field operators $\psi^\dagger(\boldsymbol{r})$ and $\psi(\boldsymbol{r})$ that create and annihilate, respectively, an electron at position $\boldsymbol{r}$ as

$$\psi^\dagger(\boldsymbol{r}) = \sum_i \phi_i^*(\boldsymbol{r}) c_i^\dagger \qquad \psi(\boldsymbol{r}) = \sum_i \phi_i(\boldsymbol{r}) c_i. \tag{G.3}$$

Some care must be taken here as the hermitian second quantized operators $c^\dagger = (c)^\dagger$ cannot be seen as creation and annihilation operators. For the fermionic fields we find anticommutation relations equivalent to those for the orthogonal case, i.e,

$$\{\psi(\boldsymbol{r}), \psi^\dagger(\boldsymbol{r}')\} = \delta(\boldsymbol{r} - \boldsymbol{r}'). \tag{G.4}$$

For this to be true it must hold that

$$\{c_i, c_j^\dagger\} = S_{ij}^{-1}, \tag{G.5}$$

which may be confirmed by inserting Eq. (G.3) into Eq. (G.4). From this we find

$$\{\psi_i(\boldsymbol{r}), \psi_j^\dagger(\boldsymbol{r}')\} = \sum_{ij} \phi_j^*(\boldsymbol{r}')\phi_i(\boldsymbol{r})\{c_i, c_j^\dagger\} \stackrel{!}{=} \delta(\boldsymbol{r}-\boldsymbol{r}') \tag{G.6}$$

$$= \sum_{ij} \left\langle j \middle| \boldsymbol{r}' \right\rangle \langle \boldsymbol{r}|i\rangle \{c_i, c_j^\dagger\} \stackrel{!}{=} \delta(\boldsymbol{r}-\boldsymbol{r}') \tag{G.7}$$

$$= \left\langle \boldsymbol{r} \middle| \underbrace{\left(\sum_{ij} |i\rangle \{c_i, c_j^\dagger\} \langle j| \right)}_{(*)} \middle| \boldsymbol{r}' \right\rangle \stackrel{!}{=} \delta(\boldsymbol{r}-\boldsymbol{r}'). \tag{G.8}$$

Recognizing that $(*)$ must equate to $\mathbb{1}$ and comparing to Eq. (G.2), we readily find the sought-after relation. We can make the connection from the operators $c^{(\dagger)}$ to another set of hermitian operators $a^{(\dagger)}$ that do in fact act as creation and annihilation operators such that

$$a_i^\dagger |0\rangle = \big|i\big\rangle \qquad \text{and} \qquad a_i |0\rangle = 0 \tag{G.9}$$

with the vacuum state $|0\rangle$. Evaluating the vacuum expectation value of their anticommutator

$$\langle 0|\{a_i, a_j^\dagger\}|0\rangle = \langle 0|a_i a_j^\dagger|0\rangle + \underbrace{\langle 0|a_j^\dagger a_i|0\rangle}_{=0} = \big\langle i\big|j\big\rangle \tag{G.10}$$

we find the commutation relation

$$\{a_i, a_j^\dagger\} = S_{ij} \tag{G.11}$$

which reduces to δ_{ij} for an orthonormal basis. From these new operators we can no longer define field operators as they would violate Eq. (G.4), yet we can relate them to $c^{(\dagger)}$ via

$$c_i = \sum_j S_{ij}^{-1} a_j. \tag{G.12}$$

G.2 Field operators in the Bloch basis

The matrix elements in $\boldsymbol{k}$-space

$$A_{ij}(\boldsymbol{k}) = e^{-i\boldsymbol{k}(\boldsymbol{R_i}-\boldsymbol{R_j})} \sum_{\boldsymbol{L}} e^{-i\boldsymbol{k}\boldsymbol{R_L}} A_{Lij} \tag{G.13}$$

that posses the translational symmetry of the underlying lattice can be conveniently computed if we introduce Bloch orbitals of the form

$$\phi_{i\boldsymbol{k}}(\boldsymbol{r}) = \frac{1}{(2\pi)^{3/2}} \sum_{\boldsymbol{L}} e^{i\boldsymbol{k}(\boldsymbol{R_L}+\boldsymbol{R_i})} \phi_i(\boldsymbol{r}-\boldsymbol{R_L}) = \frac{1}{(2\pi)^{3/2}} \sum_{\boldsymbol{L}} e^{i\boldsymbol{k}(\boldsymbol{R_L}+\boldsymbol{R_i})} \phi_{iL}(\boldsymbol{r}). \tag{G.14}$$

They then take the form

$$\big\langle i\boldsymbol{k}\big|\hat{A}\big|j\big\rangle = \frac{1}{(2\pi)^{3/2}} e^{-i\boldsymbol{k}\boldsymbol{R_j}} A_{ij}(\boldsymbol{k}) \tag{G.15}$$

with

$$\left|i\boldsymbol{k}\right\rangle = \frac{1}{(2\pi)^{3/2}} \sum_{\boldsymbol{L}} e^{i\boldsymbol{k}(\boldsymbol{R_L}+\boldsymbol{R_i})} \left|i\boldsymbol{L}\right\rangle . \tag{G.16}$$

The field operators for the Bloch orbitals may be defined as

$$\psi_{\boldsymbol{k}}(\boldsymbol{r}) = \frac{1}{(2\pi)^{3/2}} \sum_{\boldsymbol{L}} e^{-i\boldsymbol{k}\boldsymbol{R_L}} \psi(\boldsymbol{r}-\boldsymbol{R_L}) \equiv \sum_i \phi_{i\boldsymbol{k}}(\boldsymbol{r}) c_{i\boldsymbol{k}} \tag{G.17}$$

with the commutation relation

$$\{\psi_{\boldsymbol{k}}(\boldsymbol{r}), \psi^\dagger_{\boldsymbol{k}'}(\boldsymbol{r}')\} = \delta_{\boldsymbol{k}\boldsymbol{k}'}\delta(\boldsymbol{r}-\boldsymbol{r}') \tag{G.18}$$

and

$$\{c_{i\boldsymbol{k}}, c^\dagger_{j\boldsymbol{k}'}\} = \delta_{\boldsymbol{k}\boldsymbol{k}'} S^{-1}_{ij}(\boldsymbol{k}). \tag{G.19}$$

Analogous to Sec. G.1 we find a set of creation and annihilation operators

$$a^\dagger_{i\boldsymbol{k}} \left|0\right\rangle = \left|i\boldsymbol{k}\right\rangle \qquad \{a_{i\boldsymbol{k}}, a^\dagger_{j\boldsymbol{k}'}\} = \delta_{\boldsymbol{k}\boldsymbol{k}'} S_{ij}(\boldsymbol{k}) \tag{G.20}$$

and the operator transformation relation

$$c_{i\boldsymbol{k}} = \sum_j S^{-1}_{ij}(\boldsymbol{k}) a_{j\boldsymbol{k}}. \tag{G.21}$$

G.3 The retarded Green's function

Here we shall give a brief introduction to the Green's function formalism in condensed matter physics and refer the interested reader to standard textbooks [53, 54, 159] for a more elaborate overview. A number of different definition for the retarded, time dependent Green's function may be found, here, we use the convention

$$G_{ij}(t) = -i\theta(t) \left\langle 0\right|\{a_i(t), a^\dagger_j(0)\}\left|0\right\rangle \tag{G.22}$$

with the Heaviside step function $\theta(t)$ and the annihilation (creation) operators $a^{(\dagger)}$. As we confine ourselves to noninteracting electronic Green's functions it is sufficient to evaluate the vacuum expectation value. In the Heisenberg representation a generic time dependent operator $\hat{\mathcal{O}}$ may be expressed through the full Hamiltonian operator according to

$$\hat{\mathcal{O}}_i(t) = e^{i\hat{H}t}\hat{\mathcal{O}}_i e^{-i\hat{H}t} \qquad \hat{\mathcal{O}}_i = \hat{\mathcal{O}}_i(t=0) \qquad \hat{\mathcal{O}}^\dagger_j = \hat{\mathcal{O}}^\dagger_j(t=0). \tag{G.23}$$

We assume the eigenvalue problem of $\hat{H}$ to be solved and we can always find an orthogonal eigenbasis $|n\rangle$ such that

$$\hat{H}\left|n\right\rangle = \epsilon_n \left|n\right\rangle \qquad \sum_n |n\rangle\langle n| = \mathbb{1}. \tag{G.24}$$

Under these circumstances, the retarded Green's function yields

$$G_{ij}(t) = -i\theta(t)\,\langle 0|\{a_i(t), a_j^\dagger(0)\}|0\rangle \tag{G.25}$$

$$= -i\theta(t)\sum_n \langle 0|e^{i\hat{H}t}a_i e^{-i\hat{H}t}|n\rangle\ \langle n|a_j^\dagger + a_j^\dagger e^{i\hat{H}t}|n\rangle\ \langle n|a_i e^{-i\hat{H}t}|0\rangle \tag{G.26}$$

$$= -i\theta(t)\left(\sum_n e^{-i\epsilon_n t}\,\langle 0|a_i|n\rangle\ \langle n|a_j^\dagger|0\rangle + \sum_n e^{i\epsilon_n t}\,\langle 0|a_j^\dagger|n\rangle\ \langle n|a_i|0\rangle\right) \tag{G.27}$$

$$= -i\theta(t)\sum_n e^{-i\epsilon_n t}\,\langle 0|a_i|n\rangle\ \langle n|a_j^\dagger|0\rangle \tag{G.28}$$

where we have inserted two identities $\mathbb{1}$ and made use of the action of a on the vacuum state. We can now find the spectral representation $G(\omega)$ through a Fourier transformation

$$G_{ij}(\omega) = \int \mathrm{d}t\, e^{i\omega t}G_{ij}(t) \tag{G.29}$$

$$= \sum_n \langle 0|a_i \frac{|n\rangle\langle n|}{\omega + i\delta - \epsilon_n} a_j^\dagger|0\rangle \tag{G.30}$$

$$= \langle 0|a_i\hat{G}(\omega)a_j^\dagger|0\rangle = \big\langle i\big|\hat{G}(\omega)\big|j\big\rangle \tag{G.31}$$

with the resolvent operator

$$\hat{G}(\omega) = \left(\omega + i\delta - \hat{H}\right)^{-1}. \tag{G.32}$$

Inspecting the matrix elements of the inverse resolvent operator

$$\big\langle i\big|\hat{G}^{-1}(\omega)\big|j\big\rangle = \big\langle i\big|\omega + i\delta - \hat{H}\big|j\big\rangle = S_{ij}(\omega + i\delta) - H_{ij} \tag{G.33}$$

we directly find

$$\big\langle i\big|\hat{G}^{-1}(\omega)\hat{G}(\omega)\big|j\big\rangle = S_{ij}. \tag{G.34}$$

Inserting $\mathbb{1} = \sum_{ij}\big|i\big\rangle\, S_{ij}^{-1}\,\big\langle j\big|$ yields

$$\sum_{i'j'}[(\omega + i\delta)S - H]_{ii'}S_{i'j'}^{-1}G_{j'j}(\omega) = S_{ij} \tag{G.35}$$

which can be solved explicitly as a matrix equation for G and finally yields the Green's function matrix elements

$$G_{ij}(\omega) = S\,[(\omega + i\delta)S - H]^{-1}S\Big|_{ij} \equiv S\mathcal{G}(\omega)S\big|_{ij} \tag{G.36}$$

Within this work we express quantities of interest either through G or $\mathcal{G}$, depending on which is more handy in the given context. Thus, if we evaluate an observable from the nonorthogonal-basis Green's function we must always be cautious of how this quantity is expressed in terms of the second quantized operators. In real space we can write the Green's function as

$$G(\boldsymbol{r}, \boldsymbol{r}', \omega) = \int \mathrm{d}t\, e^{i\omega t}G(\boldsymbol{r}, \boldsymbol{r}', t) = \int \mathrm{d}t\, e^{i\omega t}\,\langle 0|\{\psi(\boldsymbol{r}, t), \psi^\dagger(\boldsymbol{r}', 0)\}|0\rangle \tag{G.37}$$

and following the same line of evaluation as before we arrive at

$$G(\boldsymbol{r}, \boldsymbol{r}', \omega) = \langle 0|\psi(\boldsymbol{r})\hat{G}(\omega)\psi^\dagger(\boldsymbol{r}')|0\rangle = \sum_{ij}\phi_i(\boldsymbol{r})\mathcal{G}_{ij}(\omega)\phi_j^*(\boldsymbol{r}') \tag{G.38}$$

with the initially defined field operators. This is the expression used within the charge self-consistency.

G.4 The Bloch spectral function

One of the most important quantities for the study of substitutionally disordered systems is the Bloch spectral function $A(\omega, \boldsymbol{k})$. It provides a tool to investigate the momentum resolved effects due to disorder and contains information about the band structure such as energy shifts and band broadening. For a clean compound, the band structure is essentially obtained by solving Eq. (1.5) along a path in $\boldsymbol{k}$-space, i.e. obtaining the energy eigenvalues along that path. The ω-dependence of the associated Bloch spectral function is directly connected to said eigenvalues: it is just a set of δ-peaks centered at those eigenvalues. Since δ-peaks present a numerical fall pit, in practical implementation such δ-peaks must typically be replaced by Lorentz-peaks with a finite spectral width. This spectral width stems from the necessity of evaluating the Green's function at frequencies $\omega + i\delta$, i.e., introducing an infinitesimal imaginary part. While this width is trivially independent of $\boldsymbol{k}$ in the clean compound, the ω-dependence of $A(\omega, \boldsymbol{k})$ will generally be more complex and can be $\boldsymbol{k}$-dependent. Thus, a comparison of the Block spectral function for clean and disordered system provides level shifts and band broadening - resulting from the real and imaginary part of the self-energy due to disorder. These spectral broadenings are inversely proportional to the lifetimes of the corresponding electronic states. While they are infinite in the clean case, they become finite due to disorder and the entailed scattering of electrons from impurities.
Starting from

$$A(\boldsymbol{k}, \omega) = -\frac{1}{\pi} \operatorname{Im} G(\boldsymbol{k}, \omega) \tag{G.39}$$

and the definition of the discrete Fourier transformation

$$G(\boldsymbol{k}, \omega) = \sum_{\boldsymbol{L}} e^{-i\boldsymbol{k}\boldsymbol{R_L}} \int \mathrm{d}^3 r \, G(\boldsymbol{r} - \boldsymbol{R_L}, \omega) \tag{G.40}$$

and using Eqs. (G.38) and (G.17) we find

$$G(\boldsymbol{k}, \omega) = \sum_{L} \int \mathrm{d}^3 r \, e^{-i\boldsymbol{k}\boldsymbol{R_L}} \, \langle 0 | \psi(\boldsymbol{r} - \boldsymbol{R_L}) \hat{G}(\omega) \psi^\dagger(\boldsymbol{r}) | 0 \rangle \tag{G.41}$$

$$= (2\pi)^{3/2} \int \mathrm{d}^3 r \, \langle 0 | \psi_{\boldsymbol{k}}(\boldsymbol{r}) \hat{G}(\omega) \psi^\dagger(\boldsymbol{r}) | 0 \rangle \tag{G.42}$$

where we have once again used the field operators. Inserting the field operator definitions and using Eq. (G.15), this can further be simplified to

$$G(\boldsymbol{k}, \omega) = (2\pi)^{3/2} \int \mathrm{d}^3 r \, \sum_{ij} \phi_{i\boldsymbol{k}}(\boldsymbol{r}) \phi_j^*(\boldsymbol{r}) \, \langle 0 | c_{i\boldsymbol{k}} \hat{G}(\omega) c_j^\dagger | 0 \rangle \tag{G.43}$$

$$= \sum_{ij} e^{i\boldsymbol{k}\boldsymbol{R}_j} S_{ji}(\boldsymbol{k}) \, \langle 0 | c_{i\boldsymbol{k}} \hat{G}(\omega) c_j^\dagger | 0 \rangle \, . \tag{G.44}$$

We now make the transformation from $c^{(\dagger)}$ operators to $a^{(\dagger)}$ operators via Eqs. (G.21) and (G.12) and find

$$G(\boldsymbol{k}, \omega) = \sum_{iji'j'} e^{i\boldsymbol{k}\boldsymbol{R}_j} S_{ji}(\boldsymbol{k}) S^{-1}_{ji'}(\boldsymbol{k}) S^{-1}_{ij'} \left\langle j'\boldsymbol{k} \middle| \hat{G}(\omega) \middle| i' \right\rangle \tag{G.45}$$

$$= \sum_{ij} e^{i\boldsymbol{k}\boldsymbol{R}_i} \underbrace{\left\langle i\boldsymbol{k} \middle| \hat{G}(\omega) \middle| j \right\rangle}_{= (2\pi)^{-3/2} e^{-i\boldsymbol{k}\boldsymbol{R}_j} G_{ij}(\boldsymbol{k}, \omega)} S^{-1}_{ij} \tag{G.46}$$

where we have made use of $\sum_i S_{ji}(\boldsymbol{k})S^{-1}_{ij'}(\boldsymbol{k}) = (S(\boldsymbol{k})S^{-1}(\boldsymbol{k}))_{jj'} = \delta_{jj'}$ and relabelled the indices. Following the same route for $\left\langle i\boldsymbol{k}\middle|\hat{G}^{-1}\hat{G}\middle|j\right\rangle$ leads to

$$G_{ij}(\boldsymbol{k},\omega) = S(\boldsymbol{k})[(\omega+i\delta)S(\boldsymbol{k}) - H(\boldsymbol{k})]^{-1}S(\boldsymbol{k})\Big|_{ij} = S(\boldsymbol{k})\mathcal{G}(\boldsymbol{k},\omega)S(\boldsymbol{k})\big|_{ij} \tag{G.47}$$

which, inserted into Eq. (G.46), brings us to

$$G(\boldsymbol{k},\omega) = \sum_i \left[S(\boldsymbol{k})\mathcal{G}(\boldsymbol{k},\omega)\right]_{ii} = \mathrm{Tr}\left[S(\boldsymbol{k})\mathcal{G}(\boldsymbol{k},\omega)\right]. \tag{G.48}$$

This expression is used in calculating the Block spectral function throughout this work.

G.5 Projected spectral function

With the full information contained within the spectral function $A(\boldsymbol{k},\omega)$, we can ask ourselves whether we can disentangle these peaks to gain more insight into the disorder effects on individual bands. To this end, we can make use of the fact that the bands of the clean parent compound have well-defined eigenvectors onto which we can project the $\boldsymbol{k}$-dependent Green's function $S(\boldsymbol{k})\Gamma(\boldsymbol{k},\omega)S(\boldsymbol{k})$. This ansatz can be formulated mathematically by

$$G_n(\boldsymbol{k},\omega) = \sum_{i,j\in\mathrm{parent}} c^*_{n,i}(\boldsymbol{k})\left[S(\boldsymbol{k})\Gamma(\boldsymbol{k})S(\boldsymbol{k})\right]_{i,j} c_{n,j}(\boldsymbol{k}). \tag{G.49}$$

Here, $c_{n,j}$ is the jth orbital component of the eigenvector connected to band n. Keeping in mind that the parent compound eigenvectors only span a subspace of the extended Hilbert space, the sum over orbital indices in Eq. (G.49) is restricted. We can expect this projection technique from the extended Hilbert space down to a smaller subspace to be sufficiently accurate as long as the disorder induced band changes are not too large. Use of this projection technique is made throughout this work and has proven to be a beneficial tool in the treatment of substitutionally disordered systems.

G.5.1 Green's function integrations

In Eqs. (1.79) and (1.81) we encounter frequency integrations of the effective medium Green's function which require some special attention: the evaluation of Green's functions requires the introduction of an infinitesimal imaginary part δ to the frequency $\omega^+ = \omega + i\delta$ as discussed in Sec. 1.2.4. The specific choice of δ has direct and strong influence on the fine structure of our results. We can circumvent this problem and remove the dependency via the following scheme: first, we bring these integrals into a different form, making use of the Heaviside step function θ. They may then be written as

$$\int_{-\infty}^{\infty} \mathrm{d}\omega\Gamma(\omega)\theta(E_F-\omega) \tag{G.50}$$

and we can convert them into integral over a close contour $\mathcal{C}$ in the complex plane via the residue theorem. This removes the dependency of our results from the specific choice of parameters like δ. However, in doing so we have introduced another technical problem along the way: step functions are particularly difficult to handle numerically and often results in instabilities. It is common practice to

replace step functions such as θ by a smooth cutoff function. As we are dealing with particle numbers and electronic densities, a physically meaningful choice in this context is the Fermi distribution function

$$f(\omega, T) = \frac{1}{e^{\beta(\omega-\mu)} + 1}. \tag{G.51}$$

Here, μ is the chemical potential which depends on temperature T and obeys $\mu(T = 0) = E_F$. Furthermore, $\beta = (k_B T)^{-1}$ is the reciprocal temperature with Boltzmann constant k_B. With this replacement we have introduced an artificial temperature scale which cannot be compared to that of experiment as it is the temperature scale of a system of noninteracting electrons.
In the CPA implementation the chemical potential is calculated for two different temperatures and then extrapolated down to $T = 0$, while the charge self-consistency is only computed at the higher temperature to minimize computational time. Having removed the problem introduced by the step function θ, we encounter yet another difficulty: $f(\omega, T)$ has singularities in the complex plane at fermionic Matsubara frequencies $\omega_n = (2n + 1)\pi k_B T$ for integer n. This particular problem, however, is solved by the residue theorem which states that the poles must simply be subtracted from the integral:

$$\oint_{\mathcal{C}} \mathrm{d}\omega \underline{\Gamma}(\omega) f(\omega, T) - \sum_n \frac{2ni\pi}{\beta} \underline{\Gamma}(\mu + i\omega_n). \tag{G.52}$$

In Ref. [6] the closed contour was chosen to take the form of a rectangular box far from the real axis to ensure that all poles of the Green's function are enclosed. The precise dimensions of this box must be adjusted for each class of materials considered in practical applications. The numerical integration is carried out via the so-called Weddle-rule [160] (sixth order Newton-Cotes formula) to ensure reasonable accuracy beyond the usually applied Simpson integration [161]. This choice leads to a constraint on the frequency sampling points: they must obey $\mathrm{mod}(\texttt{\#sampling points}, 6) \stackrel{!}{=} 1$. Further simplification of the contour integral results from the symmetry of the Green's function for which (in presence of inversion symmetry) $G_{ij}(\omega*) = \Big(G_{ij}(\omega)\Big)^*$. Consequently, we may restrict ourselves to the upper complex half-plane, i.e., only half of the box.

Appendix H

Implementation of the CPA cycle

We shall now take some time to discuss the most important part of the CPA implementation: the CPA self-consistent cycle. All subroutines pertaining to this task are stored in file `cpaSolver.f90` and the main job if performed by `subroutine cpaCalcMedium`. Here, for each complex frequency the effective medium Green's function is computed along a rectangular path in the upper half of the complex frequency plane for two distinct temperatures.
As depicted in Fig. 1.2, for each complex frequency (`energy` in the code), the effective Medium Green's function $\underline{\Gamma}(\omega)$ is calculated from the offsite Hamiltonian $\underline{\breve{H}}$ and the self-energy $\underline{\Sigma}(\omega)$. This is done by `subroutine cpaCycleEnergy`, which provides a self-consistent, fully symmetrized onsite medium Green's function stored in the complex array `greenSite(tlm1,tlm2,isite)`. Additionally, it provides the $\boldsymbol{k}$-dependent kernel of

$$\underline{\Gamma}_{ii}^{PQ} = \int_{1.\mathrm{BZ}} \mathrm{d}^3 \left[\omega \mathbb{1} - \underline{\breve{H}}(\boldsymbol{k}) - \underline{\Sigma}_i\right] \tag{H.1}$$

in the irreducible part of the first Brillouin zone. This quantity is used extensively throughout the program for the computation of physical observables and stored in the complex array `greenOrbK(iao1,iao2,irk)` with orbital indices `iao<i>`.
The full effective medium Green's function in Eq. (H.1) is then evaluated back in `subroutine cpaCalcMedium` by summation over all irreducible $\boldsymbol{k}$-points and symmetrized. Further applications of `subroutine cpaCycleEnergy` occur in the determination the Fermi level in `subroutine cpaCalcFermi` and the A-coefficients in `subroutine cpa_calcDenA` for the evaluation of the charge self-consistent densities (see Sec. C).
Both these subroutines require a complex frequency integration of the Green's function and the evaluation of the latter at the fermionic Matsubara frequencies. This integration is performed numerically, and in contrast to most other integrations performed in this work, a Newton-Cotes formula of higher order than the Simpson rule [161] is necessary to achieve sufficient accuracy. To this end, an

integration according to the so-called Weddle rule [160] was implemented by A. Herbig [6]:

$$\int_a^b \mathrm{d}x\, f(x) \simeq \frac{h}{840}\left[41f(x_0) + 216f\left(x_0+\frac{h}{6}\right) + 27f\left(x_0+\frac{2h}{6}\right) + 272f\left(x_0+\frac{3h}{6}\right)\right.$$
$$+ 27f\left(x_0+\frac{4h}{6}\right) + 216f\left(x_0+\frac{5h}{6}\right) + 41f(x_1)$$
$$\left.+41f(x_1) + 216f\left(x_1+\frac{h}{6}\right) + ... + 4f(x_N)\right], \tag{H.2}$$

where $h = (b-a)/N$). A peculiarity of the Weddle rule is the condition imposed on the number of sampling points N: division of N by 6 must yield a rest of 1, i.e., $\mathrm{mod}(N,6) \stackrel{!}{=} 1$. This integration method is implemented in `subroutine cpaComplexIntegrateBox`.
Further use of `subroutine cpaCycleEnergy` is made in calculating the density of states and all orbitally projected quantities provided by `subroutine cpaDosPlot`. For a converged CPA calculation this subroutine additionally computes the self-energy later used in band structure and Fermi surface calculations. It should be noted, that this particular instance of the self-energy is calculated with a smaller infinitesimal smearing of the complex frequency that those used throughout the main program. Additionally, if the Fermi surface calculation is to be performed, the self-energy is computed at the Fermi level.
For the band structure calculations performed by `subroutine cpaBandsAlongLine` and the Fermi surface calculations performed by `subroutine CalcFermiSurface`, the CPA cycle is performed under different circumstances: while the calculations in the charge self-consistent cycle are performed on a regular $\boldsymbol{k}$-mesh, we here evaluate the Bloch spectral function $A(\boldsymbol{k},\omega)$ along a specific direction in $\boldsymbol{k}$-space. Consequently, a new $\boldsymbol{k}$-mesh has to be generated for the discretized direction. This ensures that all $\boldsymbol{k}$-dependent quantities (such as the offsite Hamiltonian, mixing potential and offsite overlap) can be recomputed for a given direction. All non-$\boldsymbol{k}$-dependent quantities that have been calculated beforehand can be reused.

Appendix I

CPA GUI documentation

In order to provide the CPA program to a broader audience not familiar with the source code a GUI has been implemented using the `Tkinter`-package of `python`. Here, we shall give a brief overview of the supplied functionalities and the mode of operation.

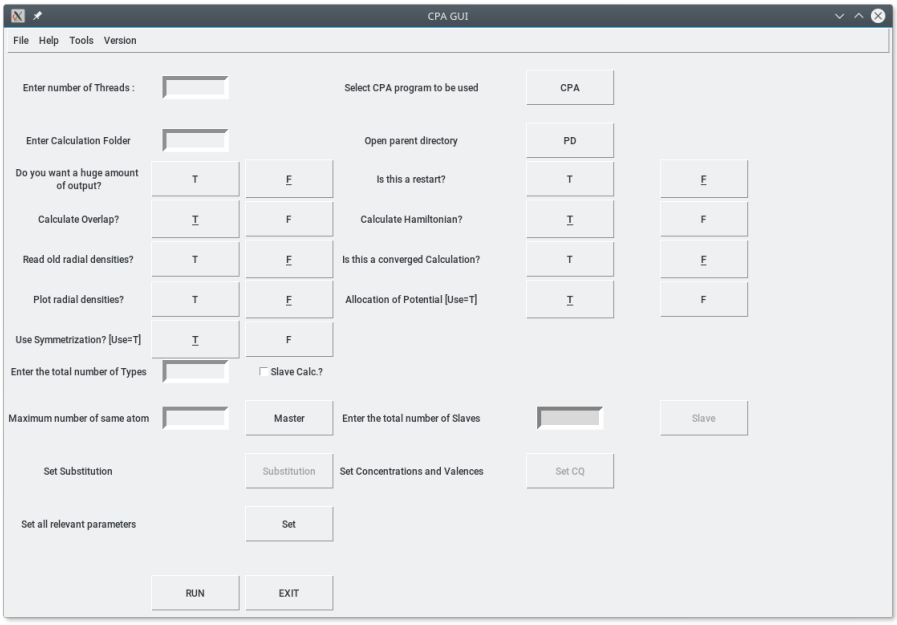

Figure I.1: Main window of the CPA GUI.

Computational parameters

In order to run a CPA calculation through the GUI a number of computational parameters must be set by the user. Aside from the specification of the number of threads to be employed in multi-threaded calculations, a path must be set to the executable `cpa`. The selection is then checked and an error message displayed in case of a faulty selection. The user must further provide the name of the folder in which to run a calculation and set the path to the parent directory via the `PD`-button. As described in App. A, a set of boolean values must be provided for the CPA program to determine the status of a

given calculation, such as a calculation restart. To this end, a set of two buttons is provided for each boolean labeled `T` (true) and `F` (false), respectively.

Setting master and slave

The CPA program makes use of so called master and slave calculations, i.e., parent compound and substituents, respectively. These are MBPP calculations which serve as input to the CPA. In order to set the appropriate paths, two variables must be given: the total number of atomic types involved (including the substituent species) and the maximum number of sites occupied by a single species. Failure to provide these will result in an error message being displayed when trying to set the paths to MBPP calculations. The path to the MBPP calculation containing the parent compound may be set via the button `Master`. The presence of substitutions must be indicated via a check-box marked `Slave Calc.?` and the number of said substitutions must be entered into the specified field. Upon correct entry, the button labeled `Slave` allows to specify paths to the MBPP folders for all Slaves. Here, a box may be checked to indicate that a certain substitution represents a vacancy, in which case no folder can be specified following the internal logic (see Sec. 2.2). Via the `CHECK` button the user may verify that all necessary paths have been set. The button `Substitions` provides an interface in which to set the actual substitutions according to L15. in App. A and `Set CQ` allows to set concentrations,valence electron numbers and cutoff radius for each substitution.

Parameter setting

The GUI allows the user to specify all parameters connected to internal routines of the CPA, such as cutoff parameters and energy intervals (see App. A) via the `Set Param` button. Aside from preset default values, the interface provides brief information about each parameter via the respective `Info` button and requires a consistency check before allowing the user to continue.

Running and exporting input files

The user is given the choice to run a calculation directly from the GUI via the `RUN` button, in which case all input is intensively checked for consistency. Additionally, under `Tools` → `Export Bash` a bash-file in style of that presented in App. A may be exported from for later use.

Appendix J

J Crystal structures and calculational details

This chapter contains all information on the crystal structures and calculational details pertaining to both MBPP and CPA calculations for all system studied in this work. Some general remarks can be made on all calculations presented within this work, while more specific details will be presented below. The MBPP calculations were carried out on a regular $k_x \times k_y \times k_z$ Monckhorst-Pack [162] $\boldsymbol{k} - mesh$ for Brillouin-zone integrations, where the k_i were chosen depending on the specific problem at hand and are given below for each case. The norm-conserving pseudopotentials were constructed after Vanderbilt [32] by Rolf Heid[1]. To construct the basis sets, for each type the appropriate local orbital-type function was chosen and plane waves up to a cutoff energy of 22 Ry was used. Using a parameterization after Perdew and Wang [163], the XC-potential was treated within the LDA.
In the CPA program, an angular momentum up to $l = 2$ was chosen, resulting in nine local basis functions per atomic type. The corresponding radial functions were generated by the LCAO-fit routine of the MBPP from the bare localized functions ${}^{\mathrm{MBPP}}f_l^P(r)$ where we have made use of the cutoff function

$$f_l^P(r) = \left[1 - e^{-\gamma_l^P\left(R_{C,l}^P - \lambda_l^P r\right)^2}\right] {}^{\mathrm{MBPP}}f_l^P(r), \tag{J.1}$$

with cutoff radius $R_{C,l}^P$ and function parameters λ_l^P and γ_l^P.
Within the CPA, the XC-potential was treated with the shape function approach described in App. D.1.4. The specific shape functions were chosen as

$$S(x) = 1 - e^{-\gamma(1-x)^n} \qquad x = \frac{|\boldsymbol{r}|}{R_C^P} \tag{J.2}$$

with $n = 6$ and $\gamma = 90$ for all sites, and the cutoff radii R_C^P are chosen individually for each calculation. Analogous to the MBPP calculations, the LDA functional after Ref. [163] was used.
As we discuss in App. G.5.1, an artificial temperature must be introduced in the computation of the chemical potential to avoid numerical instabilities in Green's function integrations. The Fermi level is found by calculating the chemical potential at two distinct temperatures $T_1 = 800$ K and $T_2 = 300$ K, and extrapolating from these values to $T = 0$ K.

[1] Private communication with Rolf Heid

J.1 Fermi surface calculations for fcc Cu, Ni, and $Cu_{1-x}Ni_x$

For both Cu and Ni in the fcc structure a lattice constant of $a = 6.8\,a_0$ was chosen (a_0 being atomic units) in Sec. 2.1.

Atomic type P	l	λ_l^P	γ_l^P	$R_{C,l}^P$
Cu	0	0.9495	0.2763	6.0
Cu	1	0.9054	0.1456	6.0
Cu	2	0.9973	0.4599	6.0
Ni	0	0.9329	0.2033	6.0
Ni	1	0.8914	0.1142	6.0
Ni	2	1.0164	0.4707	6.0

Table J.1: LCAO-fit parameters for Cu (top) and Ni (bottom).

The MBPP calculations were carried out on a regular $8 \times 8 \times 8$ Monckhorst-Pack [162] $\boldsymbol{k}$-mesh for Brillouin-zone integrations and the LCAO-fit parameters supplied by the MBPP are listed in Tab. J.1. With these, Eq. (J.1) was used to gain the radial basis functions for the CPA calculations. They are presented in Fig. J.1.
Following the notation presented in Sec. 2.1, all Fermi sheets used in the construction of the Fermi surfaces were computed for $\boldsymbol{k}_1^{\text{scan}} = (\frac{3}{8}, \frac{3}{8}, \frac{3}{4})$, $\boldsymbol{k}_2^{\text{scan}} = (\frac{3}{8}, -\frac{3}{8}, 0)$. The Fermi surfaces were constructed from multiple Fermi sheets, computed for 50 discrete sampling points along $\boldsymbol{k}_3^{\text{scan}} = (\frac{1}{2}, \frac{1}{2}, 0)$. For each sheet, the Bloch spectral function was calculated on a regular 100×100 $\boldsymbol{k}$-mesh grid.

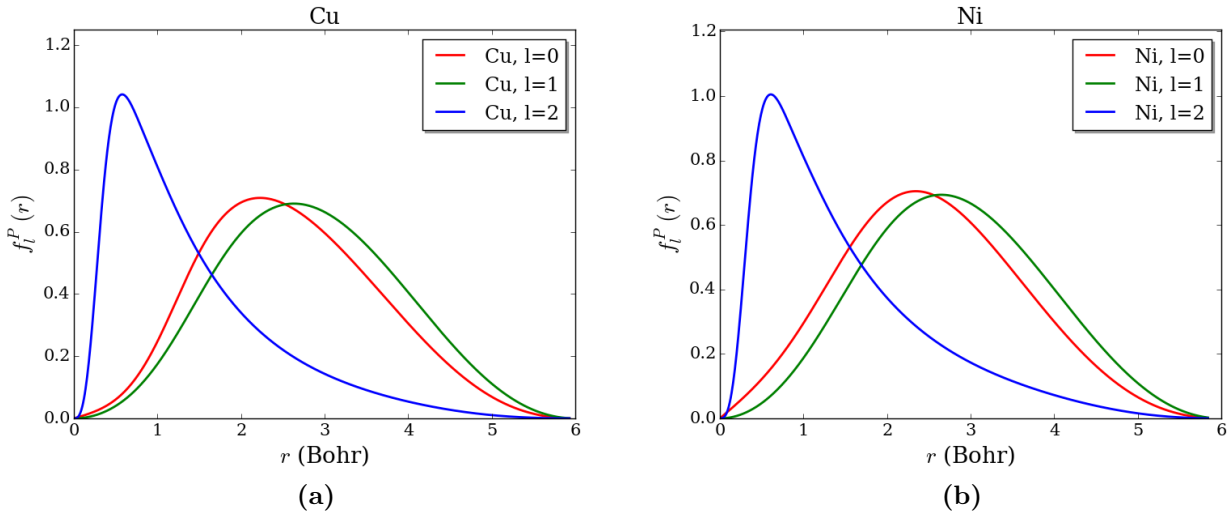

Figure J.1: Radial basis functions $f_l^P(r)$ for (a) fcc Cu, and (b) fcc Ni.

J.2 Vacancy calculations - turning bcc Fe into sc Fe

A comparison of the two structures considered in Sec. 2.2 can be found in Fig. 2.7, where for both the lattice constant $a = 5.4\,a_0$ (a_0 being atomic units) was chosen. In Fig. 2.7 (b) we find the hypothetical simple cubic structure with one atom per unit cell located at $(0,0,0)$, while Fig. 2.7 (a) shows the actual fcc crystal structure with atoms located at $(0,0,0)$ and $\frac{a}{2}(1,1,1)$. The bcc lattice is equivalent to an sc structure with two atoms per unit cell.

Atomic type P	l	λ_l^P	γ_l^P	$R_{C,l}^P$ (Bohr)
Fe	0	0.9672	0.2244	6.0
Fe	1	1.1437	1.3206	6.0
Fe	2	0.9806	1.6200	6.0
Fe1	0	0.8990	0.1841	6.0
Fe1	1	0.8418	0.1247	6.0
Fe1	2	0.9950	0.4611	6.0
Fe2	0	0.8990	0.1841	6.0
Fe2	1	0.8420	0.1248	6.0
Fe2	2	0.9950	0.4611	6.0

Table J.2: LCAO-fit parameters for sc Fe (top) and bcc Fe (bottom).

The MBPP DFT calculations for both compounds were performed on a regular $8\times8\times8$ Monckhorst-Pack [162] $\boldsymbol{k}$-mesh for Brillouin-zone integration. The basis set was constructed using one local d-type function and plane waves up to a cutoff energy of 22 Ry.

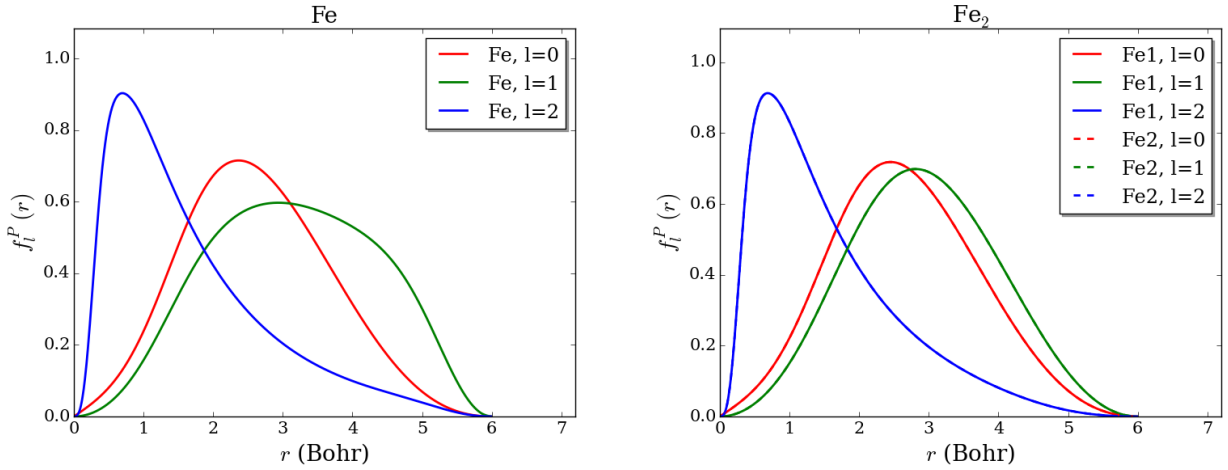

Figure J.2: Radial basis functions $f_l^P(r)$ used in the CPA calculation for angular momenta $l = 0, 1, 2$ of (a) sc Fe and (b) bcc Fe.

The radial basis functions for the CPA calculations were calculated from Eq. (J.1) with the cutoff

radii $R^P_{C,l}$ and function parameters λ^P_l and γ^P_l given in Tab. J.2. The respective radial functions resulting from the LCAO-fit are presented in Fig. J.2.
In the substitution of the central atomic site of bcc Fe (see Sec. 2.2) a finite concentration of Fe was left, i.e., the vacancy substitution was performed with $c = 99.9\%$. This is due to an internal concentration threshold $\delta c = 10^{-6}$ which must be met for the symmetry properties of a site to be kept. As the vacancy receives the symmetry properties of the to-be-substituted site, a complete substitution is not possible in practice.

J.3 Spin polarized calculations in bcc Fe, Co, and $Fe_{1-x}Co_x$

In Sec. 2.3 we have considered both Fe and Co to be in a bcc structure with a lattice constant $a = 5.4\,a_0$, i.e., with a unit cell as in Fig. 2.7 (a).

Atomic type P	l	λ^P_l	γ^P_l	$R^P_{C,l}$ (Bohr)	μ (μ_B)
Fe	0	0.8929	0.1963	6.0	2.223
Fe	1	0.8190	0.1366	6.0	
Fe	2	0.9977	0.5051	6.0	
Co	0	0.9020	0.2101	6.0	1.709
Co	1	0.8520	0.1579	6.0	
Co	2	1.0020	0.5138	6.0	

Table J.3: LCAO-fit parameters and magnetic moment for Fe (top) and Co (bottom).

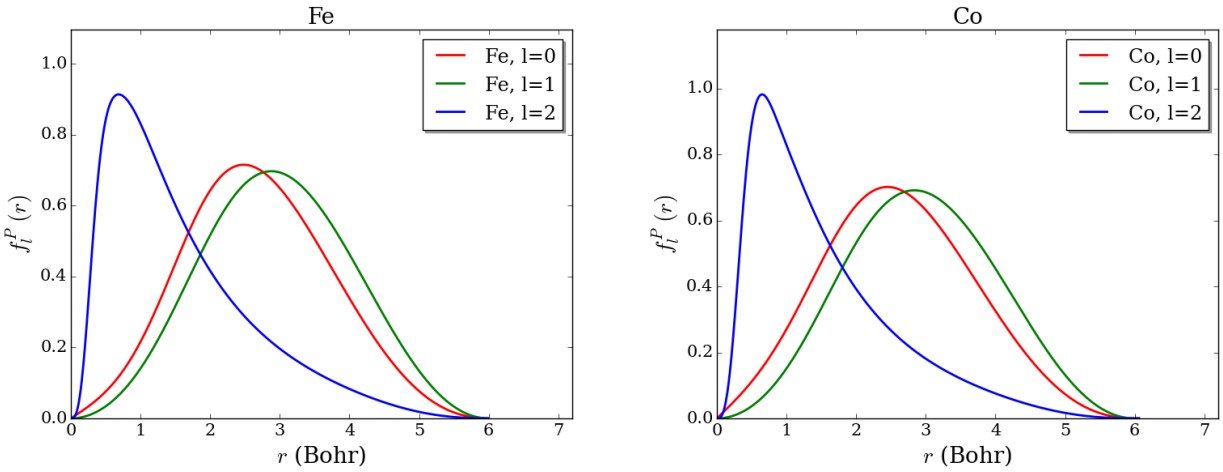

(a) **(b)**

Figure J.3: Radial basis functions $f^P_l(r)$ used in the CPA calculation for angular momenta $l = 0, 1, 2$ as produced from the LCAO-fit of the MBPP of (a) Fe and (b) Co.

The MBPP calculations were carried out using the same parameters as in Sec. 2.2 with the exception of the regular Monckhorst-Pack $\boldsymbol{k}$-mesh for Brillouin-zone integration which, in this instance, was

increased to $12 \times 12 \times 12$. For the construction of the basis set a local d-type function and plane waves up to a cutoff energy of 22 Ry were used for each end member. The LCAO-fit parameters for both atomic type used in Eq. (J.1) to compute the CPA radial basis functions are presented in Tab. J.3, along with the respective magnetic moments $\mu_{\mathrm{Fe}} = 2.223\mu_B$ and $\mu_{\mathrm{Co}} = 1.709\mu_B$. The resulting functions are depicted in Figs. J.3 (a) and J.3 (b)

J.4 Spin-orbit coupling in bcc Fe

In Sec. 2.4 we have considered Fe in a body centered cubic (bcc) structure with a lattice constant $a = 5.4\,a_0$. A schematic drawing of the corresponding unit cell may be found in Fig. 2.7 (a).

Atomic type P	l	λ_l^P	γ_l^P	$R_{C,l}^P$
Fe	0	0.8987 (0.8989)	0.1841 (0.1840)	6.0
Fe	1	0.8406 (0.8411)	0.1244 (0.1243)	6.0
Fe	2	0.9946 (0.9948)	0.4614 (0.4609)	6.0

Table J.4: LCAO-fit parameters for bcc Fe with (without) spin-orbit coupling.

The MBPP calculations were performed on a regular $12 \times 12 \times 12$ Monckhorst-Pack [162] $\boldsymbol{k}$-mesh for Brillouin-zone integration and the basis set was constructed from one local d-type function and plane waves up to a cutoff energy of 22 Ry. The LCAO-fit parameters supplied by the MBPP are listed in Tab. J.4. The radial basis function for the CPA were calculated according to Eq. (J.1) and are presented in Fig. J.4.

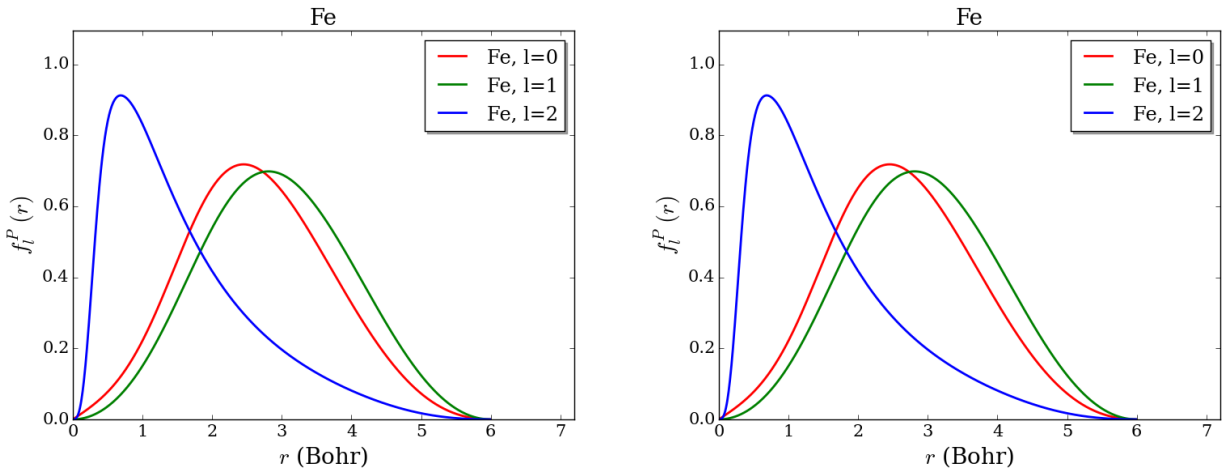

(a) **(b)**

Figure J.4: Radial basis function $f_l^P(r)$ used in the CPA calculations for angular momenta $l = 0, 1, 2$ as supplied by the LCAO-fit of the MBPP (a) without, and (b) with spin-orbit coupling.

J.5 $FeSe_{0.5}Te_{0.5}$ and substitutions

The unit cell of the iron chalcogenides in tetragonal structure is depicted in Fig. 3.2. The corresponding lattice vectors are given by

$$\boldsymbol{a}_1 = \begin{pmatrix} a \\ 0 \\ 0 \end{pmatrix} \qquad \boldsymbol{a}_2 = \begin{pmatrix} 0 \\ a \\ 0 \end{pmatrix} \qquad \boldsymbol{a}_3 = \begin{pmatrix} 0 \\ 0 \\ c \end{pmatrix} \tag{J.3}$$

and atomic positions are

$$\boldsymbol{R}_{\mathrm{Fe}_1} = \begin{pmatrix} a/4 \\ a/4 \\ 0 \end{pmatrix} \qquad \boldsymbol{R}_{\mathrm{Fe}_2} = \begin{pmatrix} -a/4 \\ -a/4 \\ 0 \end{pmatrix} \qquad \boldsymbol{R}_{(\mathrm{Se/Te})_1} = \begin{pmatrix} a/4 \\ -a/4 \\ z \end{pmatrix} \qquad \boldsymbol{R}_{(\mathrm{Se/Te})_2} = \begin{pmatrix} -a/4 \\ a/4 \\ -z \end{pmatrix}. \tag{J.4}$$

Here, a is the lattice constant, c denotes the interlayer distance, and z is the chalcogen height.
As we have shown in Sec. 3.4.1, the choice of lattice parameters has a significant impact on the band structure of FeSe. It is reasonable to assume that this will also be the case for the substituted crystal $FeSe_{1-x}Te_x$, and so it is of paramount importance to be as close to the real system as possible when we perform our CPA calculations. To this end, we rely on experimental data.

	$FeSe_{1-x}Te_x$	$x = 0$	$x = 0.483(9)$	$x = 0.516(8)$
	a (Å)	3.7688(7)	3.7913(7)	3.7948(2)
	c (Å)	5.520(1)	5.945(3)	5.986(1)
Fe1	U_{11} (Å^2)	0.0108(5)	0.0096(2)	0.0106(1)
	U_{33} (Å^2)	0.0226(6)	0.0184(5)	0.0187(2)
Se/Te	z	0.26680(9)	0.27794(9)	0.27984(7)
	U_{11} (Å^2)	0.0138(4)	0.0126(1)	0.0129(1)
	U_{33} (Å^2)	0.0184(4)	0.0365(4)	0.0368(2)
Fe2	z	–	0.6969(16)	0.6991(9)
	U_{iso} (Å^2)	–	0.0111(21)	0.0134(12)
	SOF	–	0.080(4)	0.105(3)
	wR_2 (%)	4.67	2.70	3.56
	R_1 (%)	1.92	1.49	1.53

Table J.5: Structural parameters of $FeSe_{1-x}Te_x$ determined from single-crystal x-ray diffraction.

The structural parameters for $FeSe_{0.5}Te_{0.5}$ were determined from several single crystals with a substitutional level close to $x = 0.5$ via XRD[2] using a STOE imaging plate diffraction system (IPDS-2T) equipped with Mo K_α radiation (see Tab. J.5). At room temperature, all accessible symmetry-equivalent reflections were measured up to a maximum angle $2\theta = 65°$ and resulting data was

[2]Private communication with Michael Merz

corrected for Lorentz, polarization, extinction, and absorption effects. For the respective refinements in space group $P4/nmm$, using SHELXL [164] and JANA2006 [165], around 155 averaged symmetry-independent reflections ($I > 2\sigma$) were included. All refinements converged quite well, showing excellent reliability factors (see Tab. J.5).

Compound	Atomic type P	l	λ_l^P	γ_l^P	$R_{C,l}^P$ (Bohr)
FeSe	Fe	0	0.8840 (0.8996)	0.1918 (0.2016)	6.0
	Fe	1	0.9380 (0.9423)	0.3084 (0.3251)	6.0
	Fe	2	0.9892 (0.9900)	0.5589 (0.5344)	6.0
	Se	0	0.9876 (0.9888)	1.3351 (0.9000)	6.0
	Se	1	0.9842 (0.9872)	2.5000 (0.9000)	6.0
	Se	2	1.3672 (1.3184)	0.1936 (0.2291)	6.0
FeTe	Te	0	0.9881 (0.9904)	2.2896 (0.9000)	6.0
	Te	1	1.0024 (1.0051)	2.1381 (0.9000)	6.0
	Te	2	1.2815 (1.2374)	0.3026 (0.3239)	6.0
FeI	I	0	0.9939 (0.9957)	2.3415 (0.9000)	6.0
	I	1	0.9945 (0.9991)	2.5000 (0.9000)	6.0
	I	2	1.2429 (1.2231)	0.2921 (0.3234)	6.0
FeBr	Br	0	0.9858 (-)	0.8270 (-)	6.0
	Br	1	0.9687 (-)	0.9000 (-)	6.0
	Br	2	1.1913 (-)	0.3357 (-)	6.0
NiSe	Ni	0	0.9219 (-)	0.1881 (-)	6.0
	Ni	1	1.0328 (-)	0.2753 (-)	6.0
	Ni	2	1.0078 (-)	0.5502 (-)	6.0
CuSe	Cu	0	0.9022 (-)	0.1507 (-)	6.0
	Cu	1	1.0327 (-)	0.2545 (-)	6.0
	Cu	2	0.9940 (-)	0.5555 (-)	6.0
CoSe	Co	0	0.8959 (-)	0.1957 (-)	6.0
	Co	1	0.9806 (-)	0.3141 (-)	6.0
	Co	2	0.9965 (-)	0.5590 (-)	6.0

Table J.6: LCAO-fit parameters without (with) SOC for FeSe, FeTe, FeI, FeBr, NiSe, CuSe, and CoSe.

From the refinement of the site occupancy factor (SOF) we can clearly identify a significant amount of interstitial Fe (Fe2) in the substituted compound. The amount of interstitial iron has significant impact on the magnetic and superconducting properties of the studied system and has been grounds for extensive research [63–65]. It is known to lead to the suppression of superconductivity, which would render the system unfit for the search for Majorana zero modes. However, as was shown by Ref. [64], superconductivity can persist at low interstitial content and excess iron may even be reduced from as-grown samples via annealing [119] - enhancing superconductivity. An investigation into the effects of interstitial iron on the band structure of Fe(Se,Te) was conducted in Chap. 4. Se/Te and interstitial

Fe2 sit on $2c$ Wyckoff positions with coordinates $(\frac{1}{2}, 0, z)$ whereas Fe1 sits on a special position $2a$ with coordinates $(0, 0, 0)$. The U_{ii} denote the anisotropic atomic displacement parameters (for Fe1 and Se/Te $U_{11} = U_{22}$ and $U_{12} = U_{13} = U_{23} = 0$); for interstitial Fe2 only U_{iso} is given.
The lattice parameters for the idealized $x = 0.5$ crystal, used in our electronic structure calculations, were obtained from refinement of the XRD data and are the result of averaging two $FeSe_{1-x}Te_x$ samples with $x = 0.483$ and $x = 0.516$, respectively ($a = 3.793$ Å, $c = 5.9656$ Å, and $z = 0.27885$).
For Brillouin-zone integration we have chosen a regular Monckhorst-Pack [162] $\boldsymbol{k}$-mesh of $14 \times 14 \times 18$. The basis set was constructed using one local d-type function for Fe and plane waves up to a cutoff energy of 22 Ry. We have treated the XC-potential within the LDA using a parameterization after Perdew and Wang [163].
In Tab. J.6, we have listed the LCAO-fit parameters γ_l^P and λ_l^P, and the corresponding cutoff radii $R_{C,l}^P$ for all substitutional end members used within this work. The radial functions for all end members are given in Figs. J.5 and J.6 and calculated from Eq. (J.1).

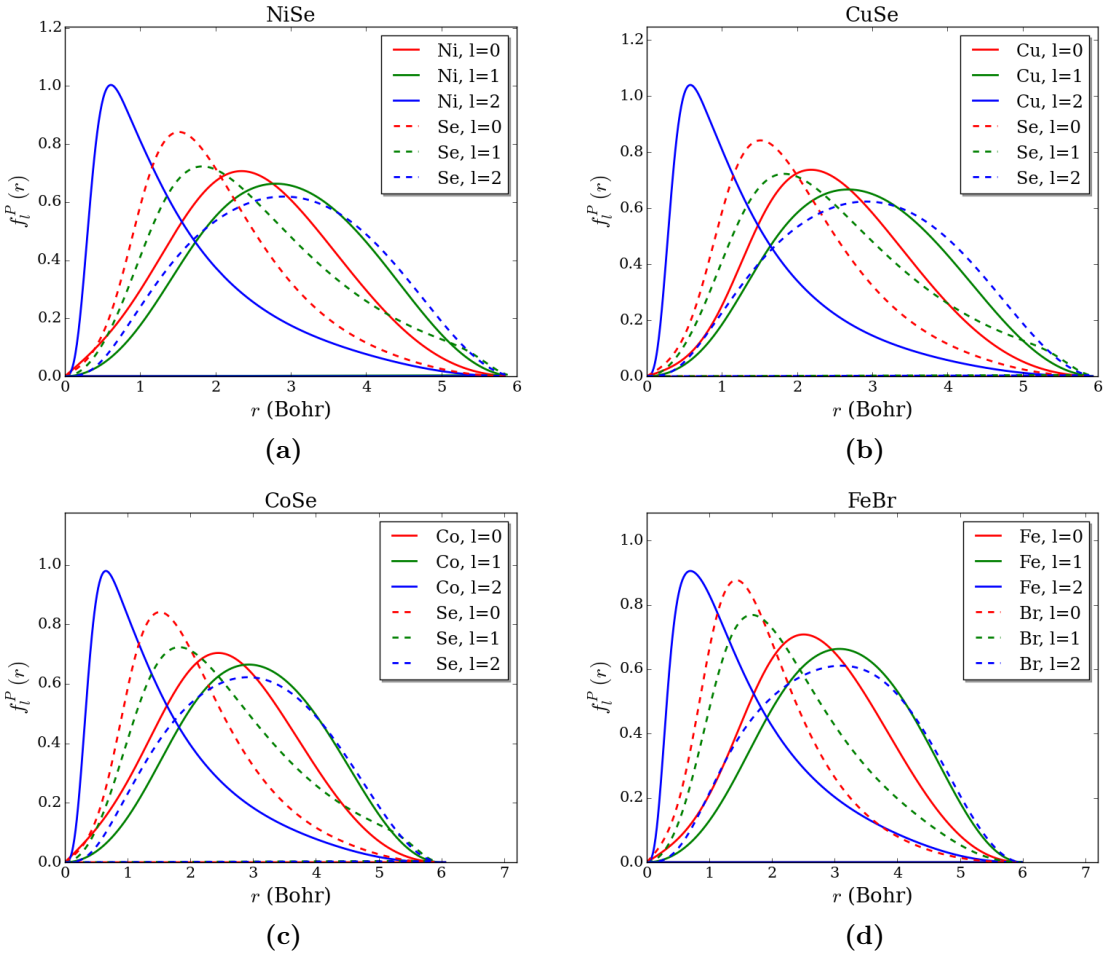

Figure J.5: Radial basis functions $f_l^P(r)$ used in the CPA calculations for angular momenta $l = 0, 1, 2$ for (a) NiSe, (b) CuSe, (c) CoSe, and (d) FeBr without SOC.

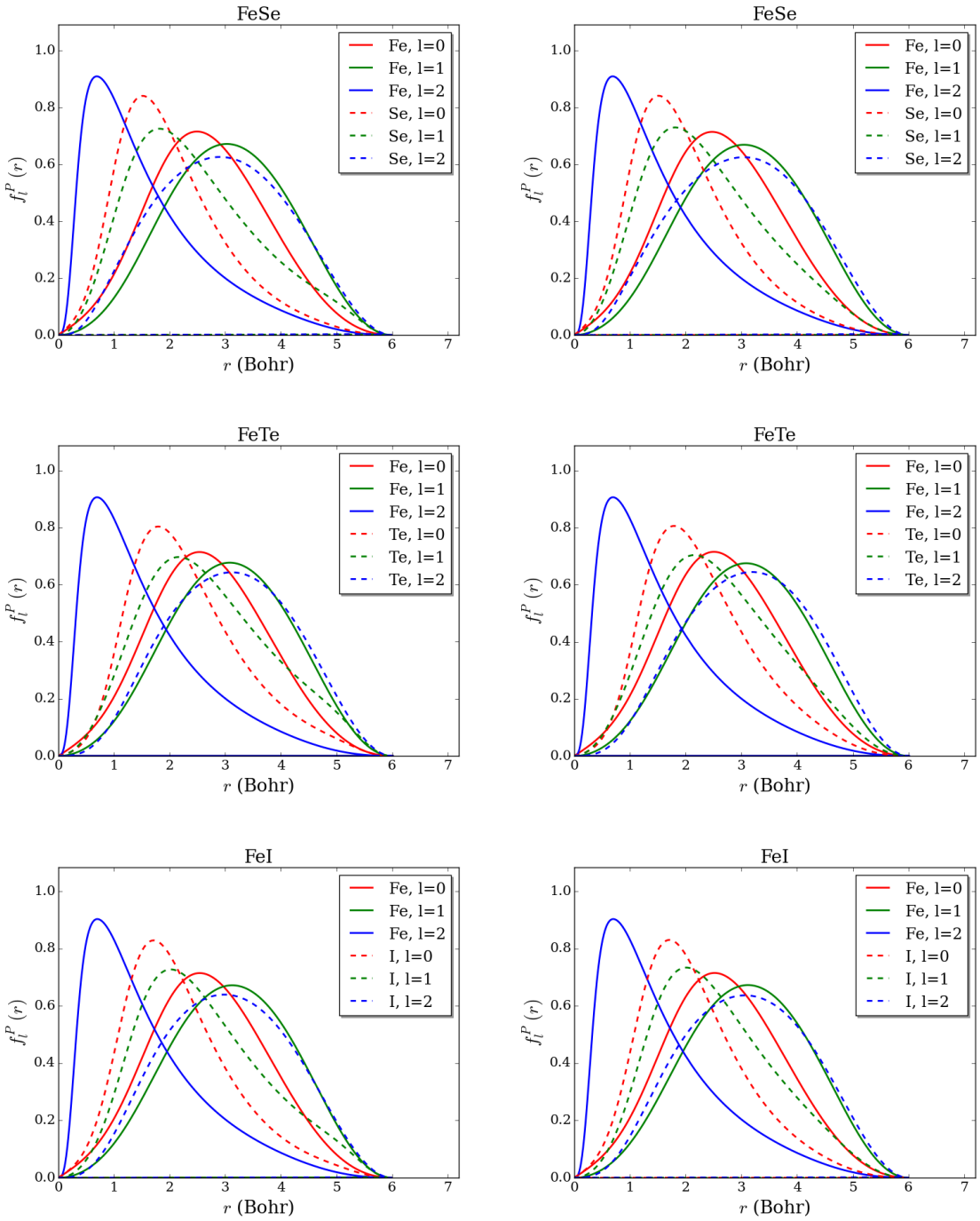

Figure J.6: Radial basis functions $f_l^P(r)$ used in the CPA calculations for angular momenta $l = 0, 1, 2$ for FeSe (top), and FeTe (middle), and FeI (bottom) without (left), and with SOC (right).

J.6 Interstitial iron in $Fe_{1+y}Se_{0.5}Te_{0.5}$

The crystal structure of $Fe_{1+y}Se_{0.5}Te_{0.5}$ was obtained via XRD[3] from a sample with $y \simeq 0.084$ interstitial iron content ($a = 3.7920$ Å, $c = 5.9430$ Å, and $z = 0.2772$). All calculations in Chap. 4 make use of this, regardless of interstitial iron content y.

Compound	Atomic type P	l	λ_l^P	γ_l^P	$R_{C,l}^P$ (Bohr)
FeFeSe(Te)	Fe	0	0.8932	0.2041	6.0
	Fe	1	0.8113	0.1399	6.0
	Fe	2	0.9887	0.4330	6.0
	Fe2	0	0.9372	0.2214	6.0
	Fe2	1	0.9819	0.2619	6.0
	Fe2	2	0.9865	0.4953	6.0
	Se (Te)	0	0.9912 (0.9917)	0.4162 (0.3436)	6.0
	Se (Te)	1	0.9988 (1.0005)	0.3981 (0.2788)	6.0
	Se (Te)	2	1.1895 (1.0776)	0.1441 (0.1758)	6.0

Table J.7: LCAO-fit parameters for FeFeSe and FeFeTe (those for Te are shown in parenthesis).

The MBPP calculations were carried out with a regular Monckhorst-Pack [162] $\boldsymbol{k}$-mesh of $12\times12\times12$ for Brillouin zone integration. The basis set was constructed with one local d-type function for each Fe and plane waves up to a cutoff energy of 22 Ry.

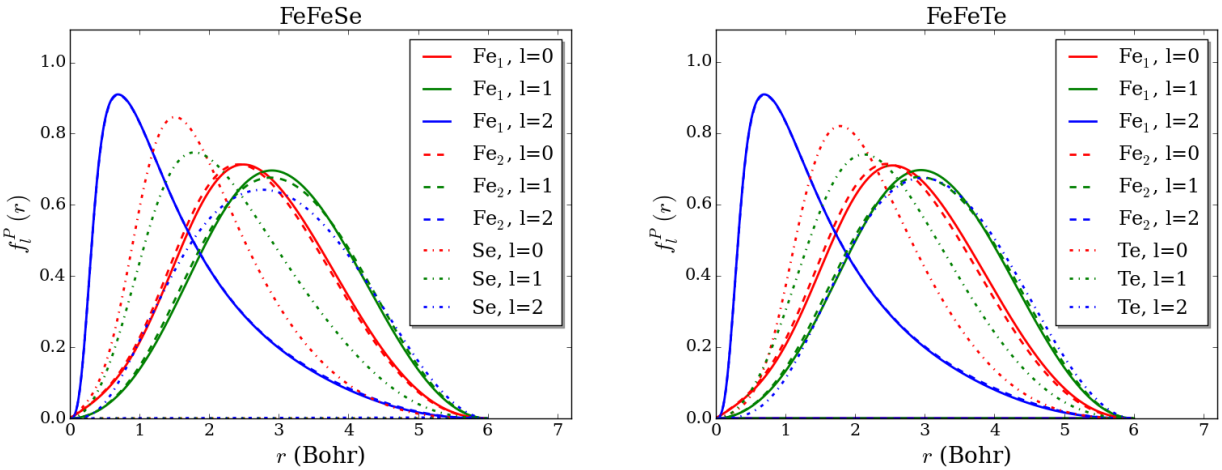

Figure J.7: Radial basis functions $f_l^P(r)$ used in the CPA calculations for angular momenta $l = 0, 1, 2$ for (a) FeFeSe, and (b) FeFeTe.

The radial basis functions for the CPA are calculated according to Eq. (J.1) with the corresponding cutoff radii $R_{c,l}^P$ and function parameters λ_l^P and γ_l^P yielded by the LCAO-fit routine (parameters are

[3]Private communication with Michael Merz

given in Tab. J.7).
As described in Sec. 2.2, the basis functions for the vacancies are chosen to be equal to the to-be-substituted type, i.e., Fe_2. The radial basis function for both end members are presented in Fig. J.7.
The Fermi surface calculations were performed on regular 50×50 $\boldsymbol{k}$-mesh grids for up to 10 discrete sampling points along $\boldsymbol{k}_3^{\text{scan}}$ (for notation see Sec. 2.1). Only one quadrant of the Brillouin zone was scanned and symmetry arguments used to complete the Fermi surfaces.
The individual Fermi surface cross sections at $k_z = 0$ for all vacancy and transition metal substitutions were computed on regular 150×150 $\boldsymbol{k}$-mesh grids.